TRANSPORTATION RESEARCH

RECORD

No. 1371

Bridges, Other Structures, and Hydraulics and Hydrology

Bridge, Culvert, and Tunnel Research

A peer-reviewed publication of the Transportation Research Board

TRANSPORTATION RESEARCH BOARD
NATIONAL RESEARCH COUNCIL

NATIONAL ACADEMY PRESS
WASHINGTON, D.C. 1992

Transportation Research Record 1371
Price: $28.00

Subscriber Category
IIC bridges, other structures, hydraulics, and hydrology

TRB Publications Staff
Director of Reports and Editorial Services: Nancy A. Ackerman
Senior Editor: Naomi C. Kassabian
Associate Editor: Alison G. Tobias
Assistant Editors: Luanne Crayton, Norman Solomon, Susan E. G. Brown
Graphics Coordinator: Terri Wayne
Office Manager: Phyllis D. Barber
Production Assistant: Betty L. Hawkins

Printed in the United States of America

Library of Congress Cataloging-in-Publication Data
National Research Council. Transportation Research Board.

Bridge, culvert, and tunnel research.
p. cm.—(Transportation research record ISSN 0361-1981; no. 1371)
"A peer-reviewed publication of the Transportation Research Board."
ISBN 0-309-05414-1
1. Bridges, Concrete—Foundations and piers. 2. Bridges—Floors. 3. Reinforcing bars—Corrosion. 4. Columns, Concrete—Testing.
I. National Research Council (U.S.). Transportation Research Board.
II. Series: Transportation research record; 1371.
TE7.H5 no. 1371
[TG340]
388 s—dc20 92-41314
[624'.2] CIP

Sponsorship of Transportation Research Record 1371

GROUP 2—DESIGN AND CONSTRUCTION OF TRANSPORTATION FACILITIES
Chairman: Charles T. Edson, New Jersey Department of Transportation

Structures Section
Chairman: Robert C. Cassano, Imbsen & Associates Inc.

Committee on General Structures
Chairman: John J. Ahlskog, FHWA, U.S. Department of Transportation
Dan S. Bechly, Amar Bhajandas, Charles H. Bryant, Martin P. Burke, Jr., Frank J. Constantino, Paul F. Csagoly, Donald J. Flemming, Theodore V. Galambos, Charles S. Gloyd, Frederick Gottemoeller, Richard P. Knight, Clellon Lewis Loveall, Dennis R. Mertz, John Minor, Roy L. Mion, Andrzej S. Nowak, William J. Rogers, Arunprakash M. Shirole, A. J Siccardi, Paul G. Steinhauser

Committee on Steel Bridges
Chairman: Charles W. Roeder, University of Washington
John J. Ahlskog, David R. Anderson, Charles J. Arnold, Alfred G. Bishara, William G. Byers, William F. Crozier, Donald J. Flemming, Dan M. Frangopol, Geerhard Haaijer, Ray W. James, Theodore H. Karasopoulos, Michael J. Koob, Andrew Lally, Albert D. M. Lewis, Ayaz H. Malik, Richard A. Parmelee, Charles G. Schmidt, Charles Seim, Robert A. P. Sweeney, John A. Van Lund, Ivan M. Viest, Gerald M. White, Stanley W. Woods

Committee on Concrete Bridges
Chairman: Wayne Henneberger, Figg & Muller Engineers Inc.
J. C. Beauchamp, Robert N. Bruce, Jr., George A. Christian, John H. Clark, John A. Corven, Anthony Ralph Cusens, Charles S. Gloyd, H. Henrie Henson, James J. Hill, Roy A. Imbsen, Michael E. Kreger, John M. Kulicki, Charles M. Minervino, Mrutyunjaya Pani, Richard A. Parmelee, Philip C. Perdikaris, Walter Podolny, Jr., Henry G. Russell, Alex C. Scordelis, S. Srinivasan, John F. Stanton, Holger S. Svensson, Robert A. P. Sweeney, Man-Chung Tang, Julius F. J. Volgyi, Jr., Allan H. Walley

Committee on Dynamics and Field Testing of Bridges
Chairman: David B. Beal, New York State Department of Transportation
Secretary: Harold R. Bosch, FHWA, U.S. Department of Transportation
Baidar Bakht, James W. Baldwin, Jr., Ian G. Buckle, C. B. Crouse, Paul F. Csagoly, Bruce M. Douglas, Thomas E. Fenske, Dan M. Frangopol, Hota V. S. Gangarao, David William Goodpasture, Ramankutty Kannankutty, F. Wayne Klaiber, Michael J. Koob, Albert N. Lin, Wallace T. McKeel, Jr., Fred Moses, Andrzej S. Nowak, Suresh G. Penjarkar, Kwok-Nam Shiu, Robert A. P. Sweeney, Ivan M. Viest, Robert C. Y. Young

Committee on Culverts and Hydraulic Structures
Chairman: A. P. Moser, Utah State University
Kenneth J. Boedecker, Jr., Thomas K. Breitfuss, Dennis L. Bunke, Bernard E. Butler, Darwin L. Christensen, Jeffrey I. Enyart, James B. Goddard, James J. Hill, Paige E. Johnson, Iraj I. Kaspar, Michael G. Katona, Carl E. Kurt, Timothy J. McGrath, John J. Meyer, John C. Potter, Edward A. Rowe, Jr., James C. Schluter, David C. Thomas, Corwin L. Tracy, Robert P. Walker, Jr.

Construction Section
Chairman: Donn E. Hancher, Texas A&M University

Committee on Construction of Bridges and Structures
Chairman: Ramankutty Kannankutty, City of Minneapolis Department of Public Works
James M. Barker, Robert M. Barnoff, Neal H. Bettigole, D. Stephen Brown, Bruce M. Douglas, Jackson L. Durkee, James J. Hill, James R. Hoblitzell, Jai B. Kim, Richard M. McClure, Franklin R. Muth, William R. Nash, Charles V. Slavis, James R. Wilder, Luis Ybanez

Frederick D. Hejl and Frank R. McCullagh, Transportation Research Board staff

Sponsorship is indicated by a footnote at the end of each paper. The organizational units, officers, and members are as of December 31, 1991.

Transportation Research Record 1371

Contents

Foreword

GangaRao et al. present the experimental findings of research on seven bridge decks, six concrete-filled and one open. Fanous et al. present the results of their investigation of the use of a folded-plate deck structure in a shell bridge system. Soltani and Kukreti summarize the results of their survey of bridges with integral abutments. Fu et al. present the results of their study of 13 isotropically reinforced bridge decks.

Meletiou and Tia developed and evaluated a field permeability test apparatus and found that the apparatus and method appear promising in providing a suitable measuring system for the rapid, convenient, and reliable determination of the in situ water permeability of structural concrete. Dutta et al. investigated five rehabilitation methods for corroding rebar [latex modified concrete (LMC)] overlay, low-slump dense concrete (LSDC) overlay, polymer impregnated concrete, LMC overlay with polymer impregnation, and LSDC with polymer impregnation and found that, compared with the untreated specimens, all five methods dramatically reduced the corrosion rate. The differences between the five methods were insignificant. Al-Qadi et al. conducted an extensive laboratory evaluation of preformed membrane systems as a chloride barrier and found that the preformed membrane systems performed better than unprotected decks.

Miller and Duwadi present the details of a research program to develop procedures for the design and construction of bridge falsework. Jahren and Rooker report the results of a fatigue study of an 80-year-old drawbridge. Elgaaly et al. describe the monitoring of the Forks Bridge in the state of Maine. Sanders and Breen present information and proposed provisions on a rational and systematic approach to anchorage zone design that could be implemented in the AASHTO Bridge Specification. Eberhard et al. give an overview of static and dynamic tests that were performed on a three-span reinforced concrete highway bridge to improve the ability of bridge engineers to assess the vulnerability of similar bridges to earthquakes. Kritzler et al. present the findings of a comprehensive study of the Chicago Transit Authority's elevated steel structures.

Coffman presents the results of a study of the seismic performance of one control and three retrofitted half-scale circular reinforced concrete columns. The retrofitted columns far outperformed the control. Bernards et al. report on the investigation of two seismic retrofitting methods (external hoops applied over the height of the column and full-height rectangular steel jacketing) applied to ⅖-scale shear-deficient columns representative of existing rectangular bridge columns. Although both methods improved performance, the rectangular steel jacket retrofit improved performance significantly over that of the as-built column. Fu and Tang propose a proof load formula for highway bridge evaluation and demonstrate that the proposed formula will ensure a relatively uniform level of bridge structural safety. Aktan et al. report on the testing of a reinforced concrete slab bridge to failure to develop procedures to allow full use of RC slab bridge capacity.

Garber et al. report on a study to assess the feasibility of applying cathodic protection to corrugated steel pipes to prevent corrosion and proved that corrugated steel pipe can be protected economically using cathodic protection. Sargand et al. present information on the response and performance of a small-diameter pipe under field conditions.

Behavior of Concrete-Filled Steel Grid Decks

HOTA V. S. GANGARAO, PENMATSA R. RAJU, AND NARSIMHA R. KOPPULA

The experimental findings of the current research on concrete-filled steel grid decks are presented. These findings are based on testing seven specimens (one open and six concrete-filled decks). Experimental tests have been conducted in elastic as well as post-yielding ranges, and consequent deflection and strain data are critically reviewed and reported. External composite action of concrete-filled steel grid decks with wide-flange steel stringers is studied and discussed. Similarly, strain incompatibility of internal composite action between steel grid deck members and concrete fill (referred to as incomplete internal composite action) is established with the aid of strain gauge readings, and the data are synthesized and presented. Analytical results, based on the orthotropic plate theory, are developed and their correlations with experimental strains and deflections are presented. Excellent correlation of theoretical results with the experimental results is noted in the elastic range.

Bridge deck maintenance and rehabilitation are major problems currently faced by the transportation industry in the United States. The aging bridge infrastructure needs billions of dollars for rehabilitation of bridge decks to bring them up to acceptable standards (*1*). The life-cycle cost of conventional reinforced concrete slab is becoming a heavy financial burden because of either frequent maintenance and repair or rehabilitation and replacement. Concrete-filled steel grid decks, on the other hand, have been used to rehabilitate many bridge decks to reduce the dead load, widen existing decks, increase the load-carrying capacity of supporting stringers, and economically rehabilitate aging bridge decks. These decks are ideal as bridge decking material in movable and long-span bridges because of their low self weight of about 40 to 60 lb/ft^2 when compared with concrete decks that weigh about 110 lb/ft^2. About 25 million ft^2 of steel grid decks is in use in the United States (*2*) (unpublished data, Bridge Grid Flooring Manufacturers Association). Concrete-filled grid decks share about 75 to 80 percent of total bridge grid deck area now in use. Concrete-filled steel grid decks have been used in many major bridges, such as the Walt Whitman Bridge (1956), Mackinac Straits Bridge (1957), Verrazano Narrows Bridge (1964), and others. Some of them have been in use for more than 60 years and have exhibited excellent performance characteristics.

Manufacturing and installation costs of concrete-filled grid decks vary from about \$20 to \$25/ft^2, depending on the type of steel grid deck, concrete filler, and other construction constraints. Open steel grid decks are either rectangular or four-way types. Steel grid decks are factory assembled and consist of main and secondary (cross) bars positioned perpendicular to each other. The bars are mechanically interlocked and welded or riveted at their intersections. Tertiary bars may be added to run in the middle of main bars. Concrete may be placed to the full depth, half depth of the grid deck with or without overlay, or just over the grid deck (exodermic). The fully filled grid deck is shown in Figure 1.

In spite of their long usage, longitudinal growth of filled grids, cupping and cracking of concrete overlay, and weld failures between stringers and filled decks have been reported as maintenance problems (*1*,*2*). In addition, there are no satisfactory analytical methods available to predict the elastic and ultimate strength behavior of concrete-filled decks under applied static loads. No satisfactory design criteria have been established to check the strength and stiffness of concrete-filled steel grid decks.

The major objective of this study is to understand the pre- and postcracking strength and stiffness behavior of fully filled concrete grid decks under out-of-plane static loads, with emphasis on internal composite action between grid bars and concrete, external composite action between filled grid and wide-flange stiffening beams, elastic and ultimate moments, and simple theoretical correlations with the experimental data. Many other important issues, including fatigue behavior, deck growth phenomenon, and improvements in stiffness, are being researched and will be published as a sequel to this work.

All new specimens (Specimens 1 through 4 and 7) are 12 ft long and 6 ft wide. The old specimens (Specimens 5 and 6) are 14 ft long and 6 and 5.5 ft wide, respectively. For all specimens, main bars run in the long direction except for Specimen 3, where main bars run in the short direction. All steel grid decks are 4.25 in. deep, but the total depth of Specimens 4 through 6 varies with overlay. Cross bars are spaced at 4 in. in all specimens, whereas main bars are spaced

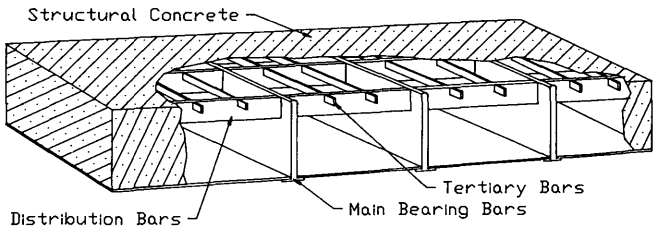

FIGURE 1 Full-depth concrete grid deck.

H. V. S. GangaRao and P. R. Raju, College of Engineering, West Virginia University, Morgantown, W. Va. 26506-6101. N. R. Koppula, Bechtel Power Corporation, Gaithersburg, Md. 20877.

TABLE 1 Description of Specimens Used for Testing

SPECIMEN NUMBER	TYPE OF GRID DECK	STATUS**	SPECIMEN SIZE	MAIN BAR DIR.	MAIN BAR SPACING	TOTAL DEPTH OF SPECIMEN	CONCRETE STRENGTH (PSI)
1	OPEN	NEW	6' X 12'	LONG	8"	4.25"	-
2	FULLY FILLED	NEW	6' X 12'	LONG	8"	4.25"	4600
3	FULLY FILLED	NEW	12' X 6'	SHORT	8"	4.25"	7300
4	FULLY FILLED WITH 2 1/8" OVERLAY	NEW	6' X 12'	LONG	8"	6.375"	4500
5	FULLY FILLED WITH 0.375" OVERLAY	OLD*	6' X 14'	LONG	6"	4.625"	4000 (ASSUMED)
6	FULLY FILLED WITH 0.19" OVERLAY	OLD*	5.5' X 14'	LONG	6"	4.44"	4000 (ASSUMED)
7	FULLY FILLED	NEW	6' X 12'	LONG	8"	4.25"	4000

*TERTIARY BARS ARE SPACED AT 6" BETWEEN THE MAIN BARS

**EXODERMIC DECK TEST RESULTS WILL BE PRESENTED AS A SEQUEL TO THIS PAPER

- CONCRETE IS NOT PRESENT

at 8 in. and 6 in. for new and old decks, respectively. Old specimens have tertiary bars at 6-in. spacing and are in the direction of main bars. No tertiary bars are present in new specimens. Concrete strength used in new specimens is indicated in Table 1. Concrete strengths of old decks are not known, because no data are available. However, for analysis purposes, concrete having 4,000 lb/in.^{2} strength is assumed. The two old specimens were removed from the Hall Station Bridge over Union Railroad at Monraville and brought to the Major Units Laboratory, West Virginia University (WVU), to find strength and stiffness of old decks. One end of each old deck was severely damaged during its removal. The severely damaged end was avoided, and testing was carried out on a 10-ft span.

About 100 tests on seven specimens have been conducted to study the elastic and ultimate behavior of concrete-filled steel grid decks. The influence of internal and external composite action on the stiffness of concrete-filled decks was studied. Experiments on flexural behavior, including transverse load distribution, load sharing, and deformations, were also carried out on open decks for comparison with concrete-filled grid decks. Experimental data were collected using four to six strain gauges and four dial gauges. Detailed information on testing can be obtained elsewhere (*3*).

OPEN VERSUS CONCRETE-FILLED DECKS

Static tests were conducted to measure the flexural stiffness of open and concrete-filled grid decks. The study reveals a substantial increase in strength and stiffness of open decks when filled with concrete (Table 2). The two-beam and three-beam experimental test set-ups were used to carry out the load tests. The two-beam set-up was the same as the three-beam set-up except for removing the central beam and retaining the end beams. In the two-beam set-up, the maximum test span of 11.5 ft for new open concrete-filled decks and 10 ft for old filled decks are used in the experiments. A 10- by 20-in. loading pad was placed at the geometric center of a deck to simulate dual truck tires and oriented so that traffic flow was parallel to the main bars. Load versus deflection curves for an open grid deck (Specimen 1), and new concrete-filled steel grid decks (Specimens 2 through 4 and 7) are presented in Figure 2 because they have similar geometric properties.

For comparison of new filled decks with old filled decks, bending stiffness of all the decks tested in the elastic range is shown in Table 2. Fully filled decks (Specimens 2 and 7) without overlays are about 2.5 times stiffer in the main bar direction than an identical open steel deck without concrete, and they are about 4 times stiffer in the main-bar direction than in the cross-bar direction because of main- and cross-

TABLE 2 Flexural Stiffness of Various Decks

Specimen number	Spanning bar & spacing	Span Ft.	Type of deck	Stiffness of the specimen (kips/in)
1	Main bar @8"	11.5	Open	9.92
2	Main bar @ 8"	11.5	Filled	22.61
3	Cross bar @ 4"	11.5	Filled	6.62
4	Main bar @ 8"	11.5	Overlaid	68.5
5	Main bar @ 6"	10	Filled	60.6
6	Main bar @ 6"	10	Filled	50.0
7	Main bar @ 8"	11.5	Filled	26.88

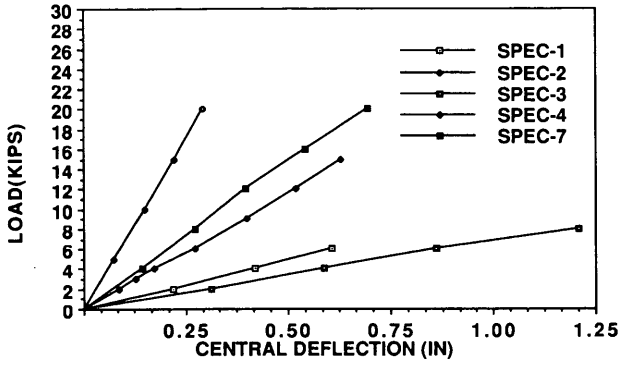

FIGURE 2 Load deflection of open and concrete-filled decks for span of 11.5 ft.

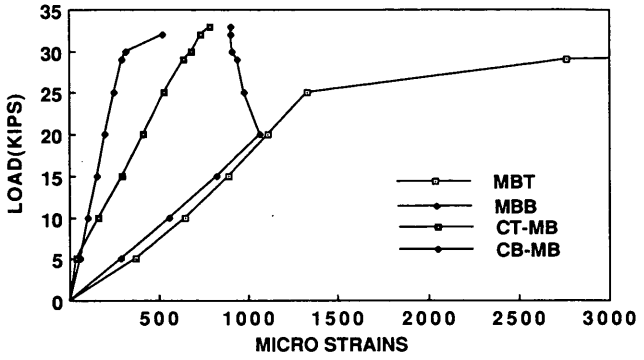

FIGURE 3 Load strains of Specimen 7 at ultimate load.

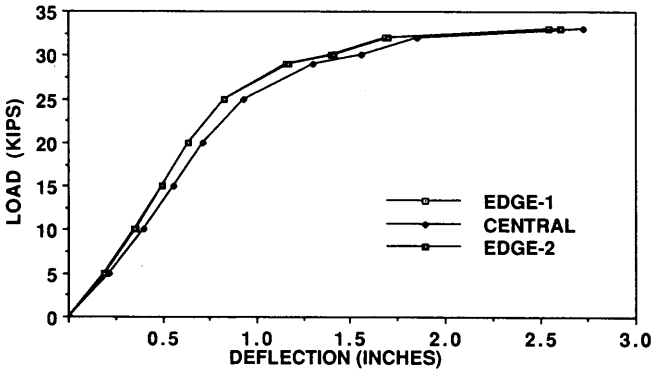

FIGURE 4 Load deflection of Specimen 7 at ultimate load. Deflections at Edges 1 and 2 are coinciding.

bar stiffness variations (i.e., the orthotropic nature of the deck system). Low stiffness is noted in Specimen 3 as it spanned in the cross-bar direction, whereas others are spanned in the main-bar direction. The flexural rigidities of the fully filled deck in main- and cross-bar directions are 26.62 $\times$ 10^3 and 7.65 $\times$ 10^3 ksi/in., respectively. The ratio of flexural rigidities in main and cross-bar directions is about 3.5, which results in greater stiffness in main-bar direction over cross-bar direction. The deck with overlay of 2⅛ in. (Specimen 4) is around 2.75 times stiffer than fully filled decks (Specimens 2 and 7). In fully filled decks, Specimen 7 showed about 18 percent higher stiffness than Specimen 2, which is attributed to the type of concrete (4,600 lb/in.^{2} versus 4,000 lb/in.^{2}) and the curing method (wrapped in plastic versus daily watering). Old concrete-filled decks are stiffer than new filled decks because of the differences in span length, main bar spacing, and tertiary bars in new and old decks.

INTERNAL COMPOSITE ACTION

Internal composite action is related to the degree of strain compatibility between the steel grid and the concrete that fills the open cells of a steel grid. The degree of strain compatibility between steel and concrete is investigated by measuring strains on both steel and concrete at the top and bottom of the deck. Typical load-versus-strain and load-versus-deflection plots for Specimen 7 are presented in Figures 3 and 4, respectively. In the precrack state, low tensile strains in concrete and high tensile strains in steel indicate poor adhesive bond between the steel grid deck and the concrete in the tension zone at the bottom of the deck. Therefore, tensile force in steel is fully accounted for, whereas tensile force in concrete is neglected.

Hairline shrinkage cracks were observed along the main bars in concrete-filled grid decks (Specimens 2, 3, and 7). The main-bar strains at the top of a deck (MBT) are about two to four times higher than the concrete strains (CT-MB) (Figure 3). Thus, strain incompatibility between steel and concrete is observed and is attributed to the lack of full adhesive bond between the steel main bars and concrete. The lack of adhesive bond is confirmed by the presence of the hairline cracks observed along the main bars in all specimens of fully filled decks except overlaid deck (Specimen 4). The cracks are believed to be caused by shrinkage of concrete between two contiguous main bars. The old decks showed better strain compatibility between steel and concrete than did new decks (Figures 3 and 5). Bulking of individual steel grid I-bars caused by rusting had filled the cracks between the steel main bar and the concrete (*2*) and thus improved adhesive bond. This phenomenon was observed in old decks. Other reasons for better compatibility in old decks are (a) main bar spacing (6 in. compared with 8 in. of new decks); (b) use of tertiary bars between main bars; (c) concrete overlay of 0.2 to 0.4 in. over the main bars, resulting in minimal shrinkage cracks; (d) type of concrete; (e) age of concrete; (f) effect of environmental loads; and (g) chloride concentration leading to corrosion. A summary of strains and neutral axes of various specimens is given in Table 3.

Strain incompatibility, as measured by the ratio of steel to concrete strain at the same location, decreased with the increase in applied load. This phenomenon is attributed to closure of cracks caused by compression on the top surface of the deck. However, the strain incompatibility (inability of steel bars and concrete to act together) in filled decks increased with repeated static tests, thus confirming poor adhesive bond between the steel grid deck and the concrete. For example, strain incompatibility in the compression zone of Specimen 7 (strains on top of steel main bar and concrete are 952 $\times$ 10^{-6} and 497 $\times$ 10^{-6}, respectively) increased from about 2 to about 3 (strains on top of steel main bar and concrete are 1,107 $\times$ 10^{-6} and 414 $\times$ 10^{-6}, respectively) as

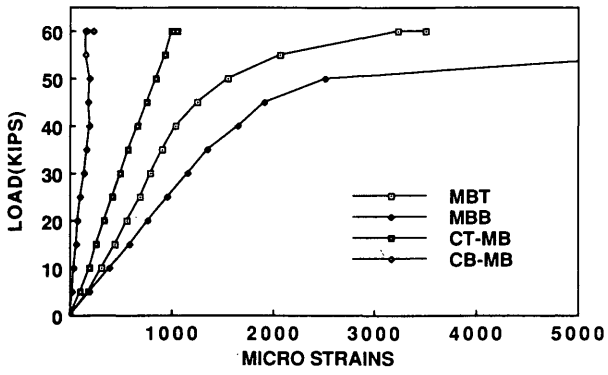

FIGURE 5 Load strains of Specimen 5 at ultimate load.

testing progressed. A similar trend was observed for all new specimens.

Concrete-filled decks were tested to study the flexural behavior in tension. It was observed from neutral axis location and strain readings that the adhesive bond effects between steel and concrete are negligible (see Table 4). Internal force equilibrium is evaluated by accounting for the degree of strain compatibility in the deck. The internal resisting (experimental) moment is arrived at from internal forces that are computed from strain gauge readings and is verified with the theoretical moment computed from the orthotropic plate theory. The experimental and theoretical moments of concrete-filled decks compared well (Table 4). Similarly, the measured deflections compared well with the theoretical deflections derived from the orthotropic plate theory. The details of ortho-

TABLE 3 Summary of Strains for Various Specimens for 10 Concentrated Loads at Mid-Span

SPECIMEN DESCRIPTION	MAIN BAR SPAN	MICRO STRAINS						TOTAL DEPTH OF DECK (IN)	N. AXIS IN MAIN BAR FROM TOP OF DECK (IN)	N. AXIS DEPTH RATIO
		COMPR.ZONE		RATIO	TENSION ZONE		RATIO			
		STEEL	CONC		STEEL	CONC				
SP-2 (M.BAR-12')	11.5"	605	228	2.65	765	56	13.7	4.25	2.07	0.487
SP-3 (M.BAR-6')	6'	267	79	3.38	315	44	7.16	4.25	2.12	0.498
SP-4 (M.BAR-12') (21/8"OVERLAY)	11.5'	386*	220	1.75	446	4	112	6.375	3.09	0.485
SP-5 (OLD DECK-1) (.38"OVERLAY)	10'	194*	248	0.78	378	44	8.59	4.44	1.725	0.373
SP-6 (OLD DECK-2) (.19"OVERLAY)	10'	232*	253	0.916	312	26	12	4.625	2.275	0.517
SP-7 (M.BAR-12')	11.5'	517	258	2	537	97	5.54	4.25	2.215	0.52

*M.BAR TOP STRAINS EXTRAPOLATED TO TOP OF CONCRETE WEARING SURFACE

TABLE 4 Comparison of Theoretical and Experimental Results for 10-kip Point Load at Center of Span (test set-up 5)

SPECIMEN NUMBER	SPAN (FT)	DEFLECTION (IN)				L.L.D MOMENT (KIP-IN) PER FOOT OF DECK	
		THEORETICAL		EXPERIMENTAL			
		CENTRAL	EDGE	CENTRAL	EDGE	THEORETICAL	EXPERIMENTAL
2	11.5	0.333	0.315	0.410	0.368	55.20	71.86
4	11.5	0.140	0.134	0.124	0.132*	55.80	70.63
5	10	0.156	0.138	0.164	0.157	47.48	54.00
6	10	0.179	0.162	0.203	0.143	50.57	51.42
7	11.5	0.335	0.315	0.344	0.305	55.20	59.66

*EDGE DEFLECTIONS ARE HIGHER BECAUSE OF SUPPORT SETTLEMENTS

tropic plate theory and the methodology to arrive at the theoretical moments and deflections are given elsewhere (*3*).

EXTERNAL COMPOSITE ACTION

The degree of external composite action of concrete-filled decks with their supporting system is measured. To evaluate this composite action, the analysis considered force equilibrium, strain compatibility, shift in neutral axis of stringer, reduction in stringer deflections, and shear lag along the deck width. Concrete-filled decks are stiffened by three wide-flange steel beams spaced at 6 ft in the short direction of the decks. Composite action was achieved between the stringers and the deck by high-strength friction grip bolts. Load-strain and load-deflection plots for composite and noncomposite behavior of the central stringer with Specimens 2 through 4 and 7 are given in another report (*3*). However, only the composite behavior of the central stringer with Specimen 7 is shown in Figures 6 and 7. Strain gauges were placed across the span direction of filled decks to measure strain variations caused by shear lag along the width of the deck. The strain variations corresponding to the distance from the central stringer are plotted for Specimens 2 and 3 in Figures 8 and 9. These plots clearly demonstrate the shear lag along the width of the deck. From strain diagrams on Specimen 7, shown in Figure 10, it is concluded that only partial composite action is achieved between flange stringers and the deck. As an example, the filled grids subjected to a concentrated load on the middle stringer are considered for the evaluation of composite action. The applied concentrated load is transversely distributed among the three stringers in proportion to the measured deflections of the stringers. The load distribution is verified from the WVU method developed from orthotropic plate theory (*4*). The experimental and theoretical transverse load distributions among the stringers correlated well with the experimental data (Table 5).

The external moment, bending, and shear deflections of the middle stringer are computed from this distributed load. Total theoretical deflection of the middle stringer is the sum of bending and shear deflections. Comparison of total theoretical deflections with measured deflections is found to be good; a maximum variation of 17 percent is noted in Table 5. The old concrete-filled grid decks (Specimens 5 and 6) were not tested for composite action with stiffening beams.

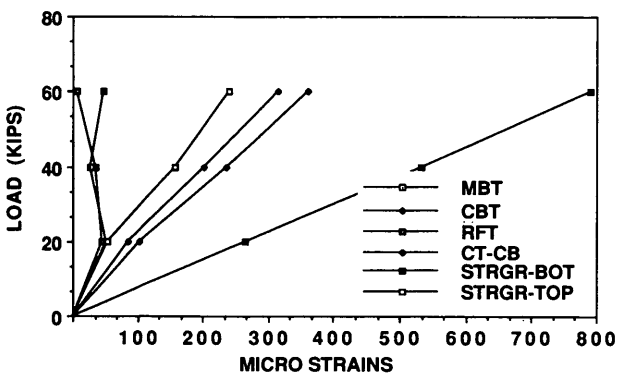

FIGURE 6 Load strains of composite stringer of Specimen 7.

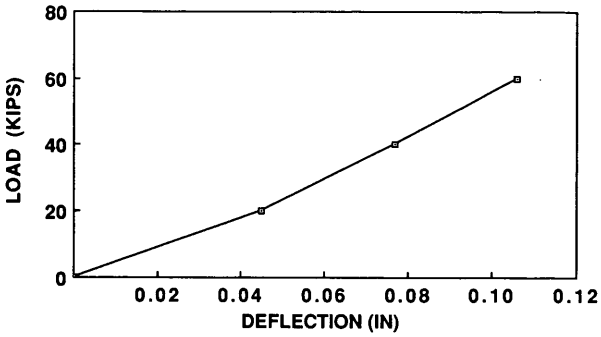

FIGURE 7 Load deflection of central stringer in Specimen 7 for composite action.

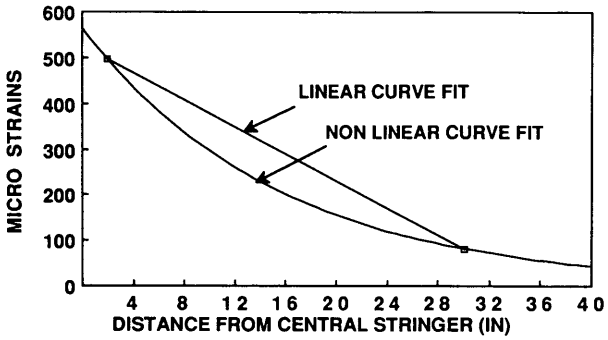

FIGURE 8 Distance strains in cross bars along the flange (filled deck) of composite stringer of Specimen 2 for a load of 40 kips on central stringer.

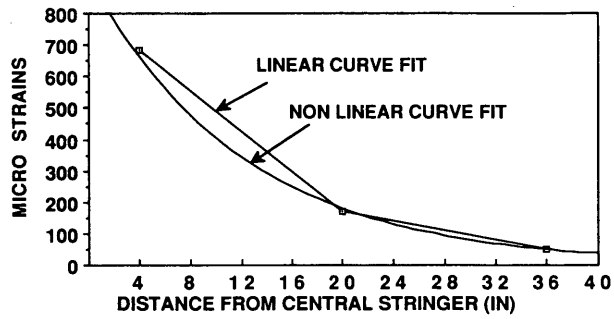

FIGURE 9 Distance strains (shear lag) in main bars along the flange (filled deck) of composite stringer in Specimen 3 for a load of 40 kips on central stringer.

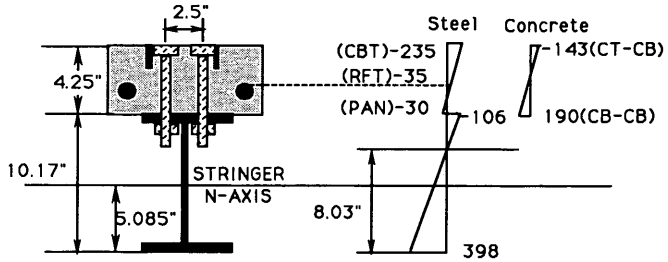

FIGURE 10 Strain diagrams for composite stringer with Specimen 7 for 30-kip load.

TABLE 5 Theoretical and Experimental Deflections of Concrete-Filled Grid Deck Composite with Wide-Flange Beams

Specimen number	Deflections (in)			
	Theory			Measured
	Bending	Shear	Total	
2	0.031	0.010	0.041	0.034
3	0.034	0.009	0.043	0.039
4	0.019	0.006	0.025	0.023
7	0.026	0.008	0.034	0.031

TABLE 6 Effective Flange Widths of Composite Stringer with Shift in Neutral Axis

Spec. No.	Shift in N.axis (in)	Effective flange width required for shift (in)	Deflections(in)			
			Theory			Experimental
			Bending	Shear	Total	
4	4.805	11.4	0.011	0.006	0.017	0.023
7	3.069	9.15	0.017	0.008	0.025	0.031

THEORETICAL EVALUATION

A simple approach was adopted to calculate the effective width of the deck for external composite action based on the shift in the neutral axis of the stringer from its centroid. The shift in the neutral axis is measured from the strain readings in the stringer for the composite case. An equivalent deck area is derived to compute the shift in the neutral axis. A composite stringer moment of inertia is computed using the equivalent area. The bending and shear deflections are computed using the composite moment of inertia. The shifts in the computed and measured deflections of the neutral axes' depths and effective flange widths are given in Table 6. The theoretical procedure is presented in another study (*3*).

ULTIMATE MOMENT

All the concrete-filled decks (Specimens 2 through 7) were tested to their ultimate load-carrying capacity. The two-beam experimental set-up was used for the ultimate loading test. The dial gauge locations were at the center, the edge of the deck, and also at the center of the edge beam. Load-versus-strain and load-versus-deflection data for all specimens were measured (*3*). Load-versus-strain gauge readings for a new filled deck (Specimen 7) and an old filled deck (Specimen 5) are shown in Figures 3 and 5. Similarly, load-versus-deflection data for these specimens are shown in Figures 4 and 11.

Open (Specimen 1), concrete flush-filled (Specimens 2 and 7) and 2⅛-in. overlaid (Specimen 4) decks have 11.5-ft spans. For these specimens, yielding of steel bars was observed at about 7, 16, 22, and 28 kips, respectively. The open deck (Specimen 1) was not tested beyond the elastic range. Therefore, load was obtained by linear extrapolation of strains.

Ultimate load tests for these specimens showed that bottom steel yielded first in all the specimens except Specimen 7.

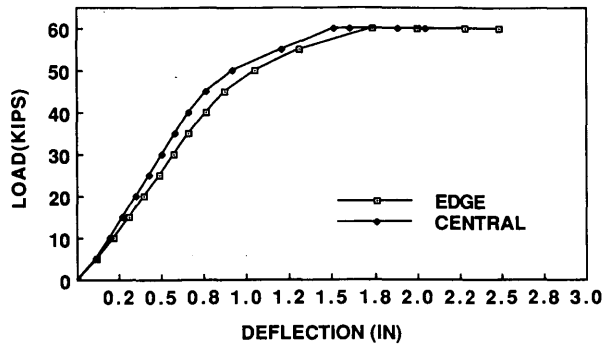

FIGURE 11 Load deflection of Specimen 5 at ultimate load.

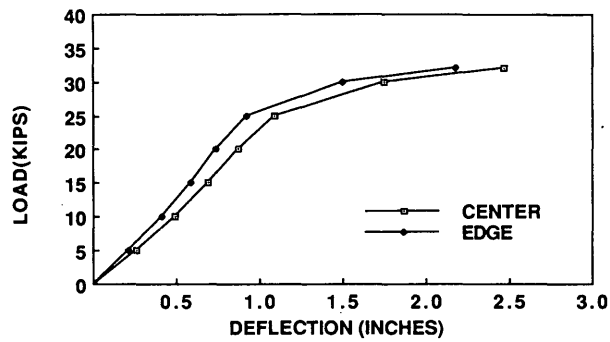

FIGURE 12 Load deflection of Specimen 2 at ultimate load.

Concrete reached its crushing value (strain of 0.003) only in Specimen 4, which has a 2⅛-in. overlay. Other fully filled concrete specimens did not reach the concrete crushing value because of strain incompatibility between steel and concrete in the compression zone.

In fully filled decks, the global deck deflections showed linearity beyond local yielding of main bars. This shows that there is a considerable degree of indeterminacy in the concrete-filled decks that leads to redistribution of loads. Post-yielding linearity is observed in up to about 50 percent and 14 percent higher loads than the initial yield loads for Specimen 2 and Specimen 7 in Figures 12 and 4, respectively. The post-yielding linearity depends on the degree of strain incompatibility.

CONCLUSIONS

1. Fully filled concrete decks were found to be about 2.5 times stiffer than the comparable open steel grid deck.
2. Concrete-filled grid decks with a 2⅛-in. overlay were about 2.75 times stiffer than the fully filled decks.
3. Concrete is found to be ineffective in the tension zone.
4. The observed strain incompatibility between main bars and concrete is two to four times in all new concrete-filled decks. However, better strain compatibility is noted in an overlaid deck through experimental results.
5. Good strain compatibility is observed in old concrete-filled decks that were in service for several years.
6. Concrete-filled grid decks stiffened by the wide-flange steel stringers are 1.5 to 2.25 times stiffer than the stringer

stiffness alone. For example, full composite action between filled decks and steel stringers can be assumed for design purposes.

7. Fully filled grid decks show some linearity beyond the local main bar yielding, which emphasizes the hyperstatic nature of concrete-filled grid decks.

8. Ultimate concrete compression strains (0.003) were attained only in overlaid concrete-filled decks. However, poor strain compatibility between concrete and steel in other new decks occurred even though yielding of steel was noted; concrete and steel grid decks cannot be treated in unison for design purposes.

9. Deflection and moments of concrete-filled decks obtained from the orthotropic plate theory compared well with the experimental results.

REFERENCES

1. H. V. S. GangaRao et al. *Behavior and Design of Open Steel Grid Decks for Highway Bridges*. Final Report. FHWA, U.S. Department of Transportation, 1988.
2. D. H. Timmer. A Study of the Concrete Filled Steel Grid Bridge Decks in Ohio. Bridge Maintenance and Rehabilitation Conference, Morgantown, W. Va., Aug. 1980.
3. H. V. S. GangaRao, P. R. Raju, and N. R. Reddy. *Experimental Investigation of Concrete-Filled Steel Grid Deck Behavior Under Static Loads*. Interim Report, Vol. 1. FHWA, U.S. Department of Transportation, 1991.
4. P. R. Raju and H. V. S. GangaRao. *Wheel Load Distributions on Highway Bridges*. Constructed Facilities Center Report 89-100, West Virginia University, Morgantown, W. Va., 1989.

Publication of this paper sponsored by Committee on General Structures.

Investigation of a Folded-Plate Bridge

FOUAD FANOUS, F. WAYNE KLAIBER, AND TAHER MERCHANT

Closing a bridge for rehabilitation or emergency repairs always causes costly delays and inconveniences the traveling public. A bridge system that is economical, relatively easy and quick to construct, and capable of withstanding the live loads and volume of today's traffic would alleviate some of these problems. As a possible solution to the nation's need for an emergency or "bypass" bridge, a new type of bridge—the shell bridge—has been developed. The feasibility and practicality of the shell bridge system have been verified through analytical and experimental investigations. The use of a folded-plate deck structure instead of a circular-shell deck structure in a shell bridge system was investigated. The obvious advantage of using a folded-plate cross section is that fabrication would be much simpler (i.e., flat form work instead of curved form work). The folded-plate bridge system was investigated analytically using the ANSYS general-purpose finite-element program. In the experimental portion of the investigation, a 1:24 Plexiglas scale model of a folded-plate bridge was fabricated and tested. The model was subjected to in-plane forces to simulate posttensioning forces and vertical forces to simulate live loading. In this preliminary investigation, the folded-plate deck structure, except for the higher transverse stresses caused by the lack of arch action, was determined to be an improvement over the circular-shell deck structure.

Because bridges are a vital element of any country's surface transportation system, the closing of a bridge for any reason (emergency repairs, strengthening, rehabilitation, etc.) always causes costly delays, detours, and inconvenience to the traveler. This is especially true in the cases of isolated bridges where the next available bridge is several miles away or bridges subjected to high volumes of traffic. To help alleviate some of these problems, a shell bridge system has been developed that is economical, relatively easy and quick to construct, and capable of carrying legal loads and today's volume of traffic. Although it is primarily intended to be used for "bypass" bridges, this system can be used with appropriate modification in permanent installations.

Several prefabricated elements and systems are available today for replacing damaged and deficient bridges relatively quickly and at a relatively low cost (e.g., precast, prestressed beams plus precast slabs). These systems are applicable for short spans; if intermediate supports are used, these systems can also be used for long multispan bridges. The shell bridge system developed in this study can be used for both short and relatively long spans without intermediate supports. The shell bridge is segmental, which eliminates many handling and transportation problems. Using the technology of segmental construction, individual shell segments are posttensioned together at the site to construct a bypass bridge of the desired span length. The shell bridge combines the advantages of prefabrication and segmental construction and also has high torsional rigidity plus arch action in the transverse direction.

Fanous et al. reported preliminary investigations of this system (*1*). In their study, 15 different cross sections were analyzed. From these, four different configurations of the integrated deck and circular shell structure (i.e., potential shell bridge cross sections) were investigated using finite-element techniques. The primary emphasis of this study was the investigation of the shell-deck connection and various methods of connecting the edge of the deck to the shell. The most efficient was the cross section with the lightest shell-deck connection (relatively long but thin) and inclined members (for connecting the edge of the deck and shell).

The second phase of the study involved the construction and testing of a 1:3 scale model shell bridge (*2*). The scale of the posttensioned reinforced concrete model was determined by available laboratory space and the minimum thickness of concrete that could be cast. The model consisted of six segments posttensioned together to create a model bridge 10 ft wide and 34 ft long. Thus, the prototype of this model would be 30 ft wide (two lanes) and more than 100 ft long, which is considerably longer than the usual simple span bridges. The primary purpose of the laboratory model testing was to determine potential construction problems and potential stress concentrations that could not be determined with finite-element analysis.

The third phase of the shell bridge investigation involved the analytical and experimental investigation of a folded-plate bridge (*3*)—one in which the shell portion of the shell bridge is replaced with plate elements (Figure 1)—to determine its behavior and response to various loading conditions. Although the transverse arch action is lost, the folded-plate structure would be much easier to fabricate (e.g., flat elements in the cross section). Although the use of folded-plate structures for bridges is a new concept, folded-plate roof structures have been used extensively when long spans without intermediate supports are required. In most situations, folded-plate roofs usually require posttensioning.

EXPERIMENTAL PHASE

Model

Plexiglas was selected for the model material; this resulted in several problems that will be discussed later. Use of the Phase II prototype bridge (length, 100 ft; width, 30 ft) and Plexiglas that was readily available (thickness, ¼ in.) resulted in a 1:24 scale model. The cross section and side view of the model are shown in Figures 2*a* and *b*, respectively. Curbs and diagonal

Department of Civil and Construction Engineering, Iowa State University, Ames, Iowa 50011.

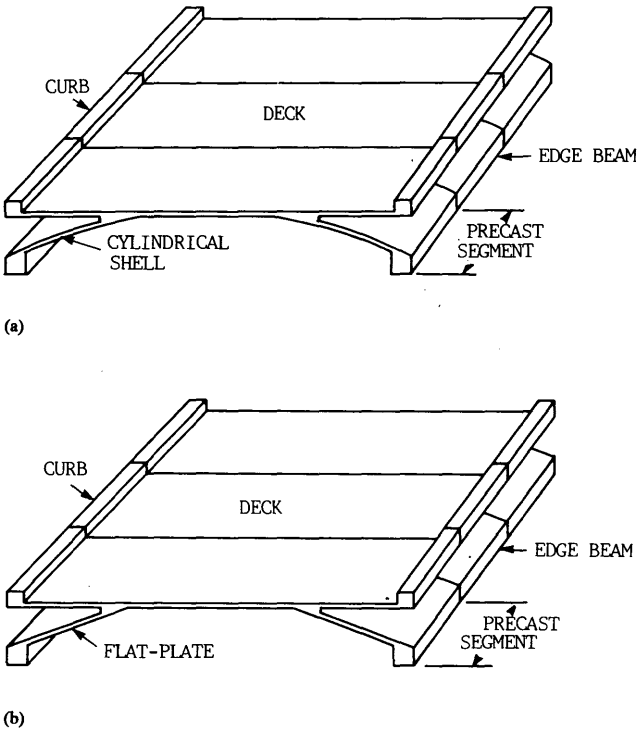

FIGURE 1 Shell bridge cross sections: (*a*) circular-shell elements and (*b*) folded-plate elements.

members were bolted to the model so it could be tested with and without curbs and diagonals.

Although the Plexiglas model was fabricated as a unit (i.e., no individual segments), posttensioning was included because it would be required in the prototype. Shown in Figure 2*a* is the location of the posttensioning applied to the model. Initially, annealed aluminum rods were used for the posttensioning; however, after repeated use, the threads would wear out. The aluminum rods were then replaced with steel rods; the higher modulus of elasticity resulted in smaller strains in the rods, which were obviously more difficult to measure accurately.

Material Properties

To determine the modulus of elasticity and Poisson's ratio of the Plexiglas, an instrumented simply supported beam, fabricated from the Plexiglas used in the model, was tested using third-point loading (*2*). Midspan transverse and longitudinal strains were recorded at 15-sec intervals. Results revealed that the rate of creep became negligible after a few minutes. Based on the test results, instantaneous Young's modulus and Poisson's ratio were determined to be 443,800 lb/in.^{2} and 0.36, respectively. After 1 min, Young's modulus of the Plexiglas was found to be 414,900 lb/in.^{2}; after 2 min it had decreased to 409,700 lb/in.^{2}. In the analytical studies, an average mod-

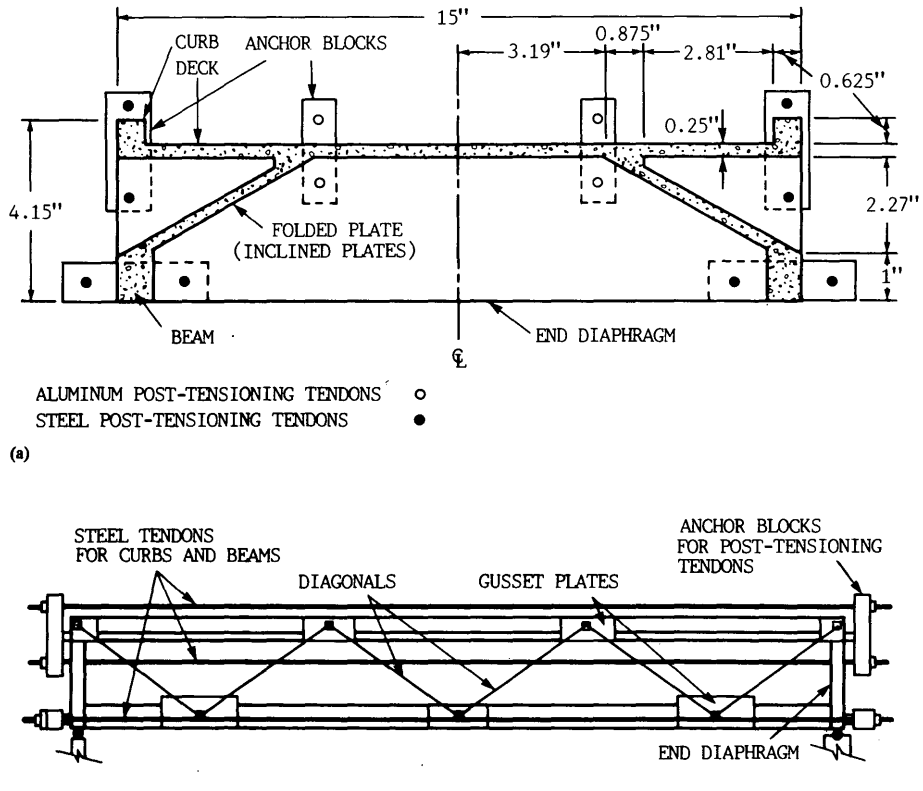

FIGURE 2 Plexiglas bridge model: (*a*) cross section of bridge and (*b*) side view of bridge model with six diagonals.

ulus of elasticity (428,000 lb/in.^{2}) and Poisson's ratio (0.36) were used.

Instrumentation

Basic instrumentation for the model consisted of electrical-resistance strain gauges (henceforth referred to as gauges) for measuring strains and mechanical dial gauges for measuring deflections. The gauges were monitored using a computer-controlled data acquisition system.

General-purpose temperature-compensate gauges were installed and waterproofed on the model as well as on the posttensioning tendons in accordance with the manufacturer's guidelines. Two gauges were mounted on each posttensioning tendon longitudinally and diametrically opposite each other so that the axial force could be measured accurately and bending strains cancelled.

Because the model is geometrically symmetric about the longitudinal and transverse axes, its response under symmetrical loading can be assumed to be symmetric. Taking advantage of the assumed symmetry, the majority of the gauges were installed on one-quarter of the model. However, to verify the assumed symmetric behavior of the bridge, 10 gauges were installed on the other quarter-sections of the model.

As will be shown, only longitudinal strains in the curbs and beams are significant; transverse strains are essentially negligible. Hence gauges were positioned so that strains could be monitored along the tops and bottoms of the curbs and beams. Along the longitudinal and transverse centerlines of the deck and near the deck-plate connection, two separate gauges perpendicular to each other were installed at points of interest to measure the longitudinal and transverse strains. This combination was used instead of rosettes to avoid gauge heating problems. Mechanical dial gauges were used to measure midspan beam and curb deflection. Space limitations (i.e., smallness of model) prevented monitoring the deflections at additional locations.

FINITE-ELEMENT ANALYSIS

Modeling

The integrated folded-plate deck bridge model was analyzed using the ANSYS finite-element program (*4*). Eight-node solid elements (STIF45 in ANSYS element library) were used to idealize the bridge deck, folded plates, anchor plates, and gusset plates (see Figure 3). These elements were also used to analyze the shell bridge structures studied in previous related work (*1*,*2*). Posttensioning tendons, the vertical and the diagonal elements connecting the shell edge beam to the deck, were modeled using three-dimensional truss elements (STIF8 in ANSYS element library).

Because of the geometrical symmetry of the bridge model about the longitudinal and transverse axes, only one-quarter of the bridge structure was modeled. Appropriate symmetry and asymmetry boundary conditions were applied at the nodes on the symmetry planes. However, for general cases of loading, four computer runs with various combinations of boundary conditions were needed. For loads symmetric with respect to one of the symmetry planes, only two runs were used. The model was analyzed considering the following configurations and was tested in Configurations 1 and 2.

- Configuration 1: Model without diagonal members connecting the deck to the folded plate.
- Configuration 2: Model with six diagonal members connecting the deck to the folded plate.
- Configuration 3: Model with 12 diagonal members connecting the deck to the folded plate.

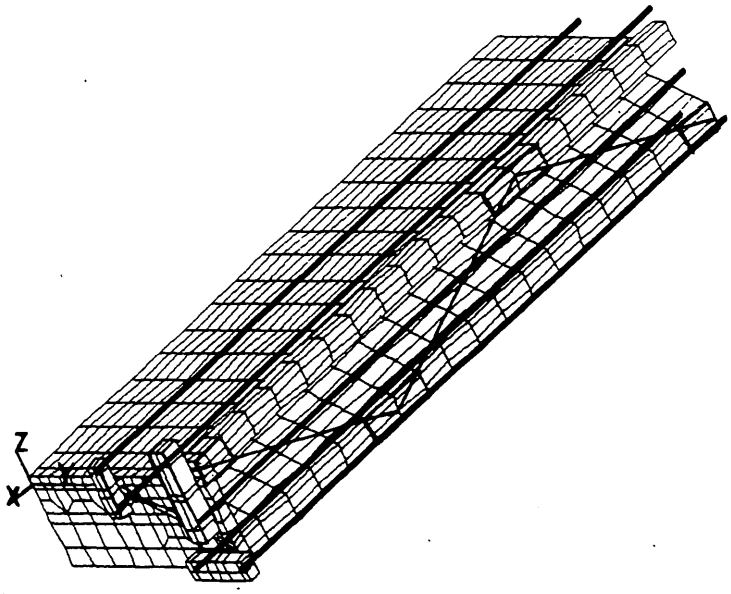

FIGURE 3 Finite-element model (perspective view) of integrated folded-plate deck bridge.

Posttensioning

In the finite-element analysis, the posttensioning forces in the tendons were included as a prestrain in the truss elements used to model the tendons. This was accomplished in steps to obtain the desired value of posttensioning force in each tendon. In the first step, the strain in each tendon was estimated using the desired posttensioning forces. However, examination of the analysis results indicated that the forces in the tendons were slightly less than desired. This lessening of the tendon forces was caused by losses in the specified prestrain because of the axial shortening of the bridge caused by posttensioning forces. The prestrain was then modified to account for these differences, and the structure was reanalyzed until the desired posttensioning forces were obtained. The final posttensioning forces applied in the analysis were used in the comparisons with experimental results.

TESTING AND RESULTS

Test Procedure

The bridge model was first tested using a 7.5-lb, single concentrated load simulating the scaled load of one axle of a standard HS20-44 truck (*5*). This load was adequate to produce strains of a magnitude sufficient to be accurately measured. Strains and deflections were recorded for the single load positioned at various locations defined by the longitudinal and transverse axes, as illustrated in Figure 4, to determine maximum deflections, shear stresses, and longitudinal and transverse strains. The model was also subjected to simulated AASHTO HS20-44 trucks positioned to produce maximum stress in the model.

Results

As previously noted, posttensioning of the tendons in the model to the desired force required adjustment to account for the creep in the Plexiglas material. Adjustments were made until the posttensioning forces were essentially stabilized. Posttensioning results (analytical versus experimental) were significantly different; the more noticeable differences occurred in the vicinity of the applied posttensioning force. These differences resulted from the higher creep that occurred in these areas and the way creep was included in the analytical model.

Response of the Model Under Single Load

Bridge Deck

The deflection of the bridge model deck at midspan with various web member configurations (Figure 2) loaded with a single load near the curb at midspan is shown in Figure 5. The difference between the measured and theoretical deflections was within 13 percent. Connecting the deck to the folded-plate edge beam reduced the overall deflection and resulted in higher torsional stiffness, as indicated by the smaller differential displacement between Edges *A* and *C* shown in Figure 5.

The transverse strains across the top of the deck at midspan when the load is placed at Points *G*1 and *G*3 (Figure 4) are shown in Figure 6. Note the excellent agreement between the finite-element analysis and the experimental results. Connecting the deck to the folded-plate edge beam reduced the magnitude of the transverse strains (Figure 6*a*). These strains were significantly reduced when the number of the diagonal members was doubled (12 diagonals versus 6 diagonals). Increasing the number of diagonals increased the stiffness of the cross section and significantly reduced the transverse strains near the connection between the folded plate and the deck. On the other hand, the distribution and magnitude of the transverse strains in the deck are essentially independent of the type of deck-edge beam connection when the load is applied at Point *G*3 (Figure 6*b*). The presence of diagonal members improved the overall structural behavior of the section under non-symmetrical loadings.

The distribution of the longitudinal strain across the top of the deck and along the bridge centerline when the load is positioned at Point *G*3 is shown in Figure 7. As can be seen, the strain distribution is not affected by the presence of the diagonal members connecting the deck to the folded plate's edge beam. Also illustrated in this figure is the overall agreement between the analytical and experimental results; however, the results differ significantly at the point of loading. This difference most likely results from idealizing the load as a true point load in the finite-element analysis instead of distributing the load, as presented in the model testing.

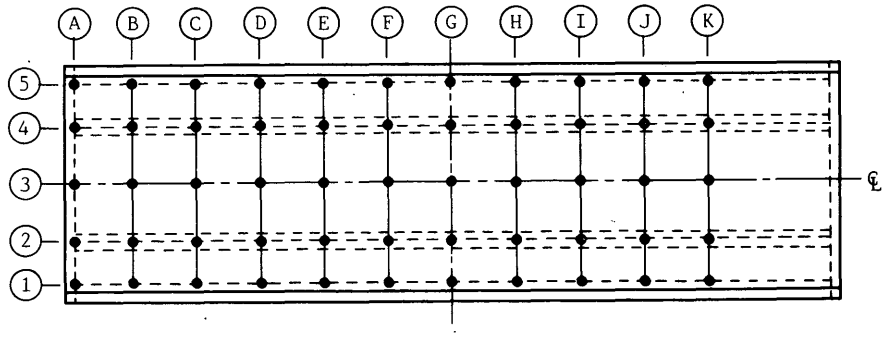

FIGURE 4 Load point locations.

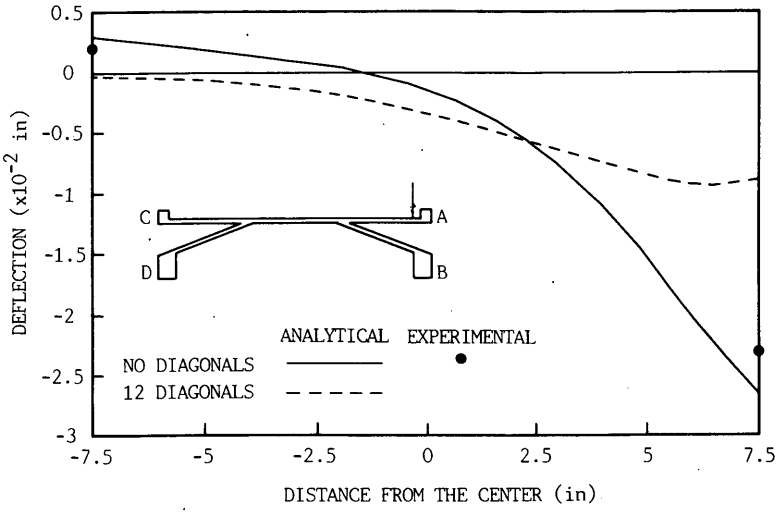

FIGURE 5 Midspan deck deflection: single load at Point *G*1.

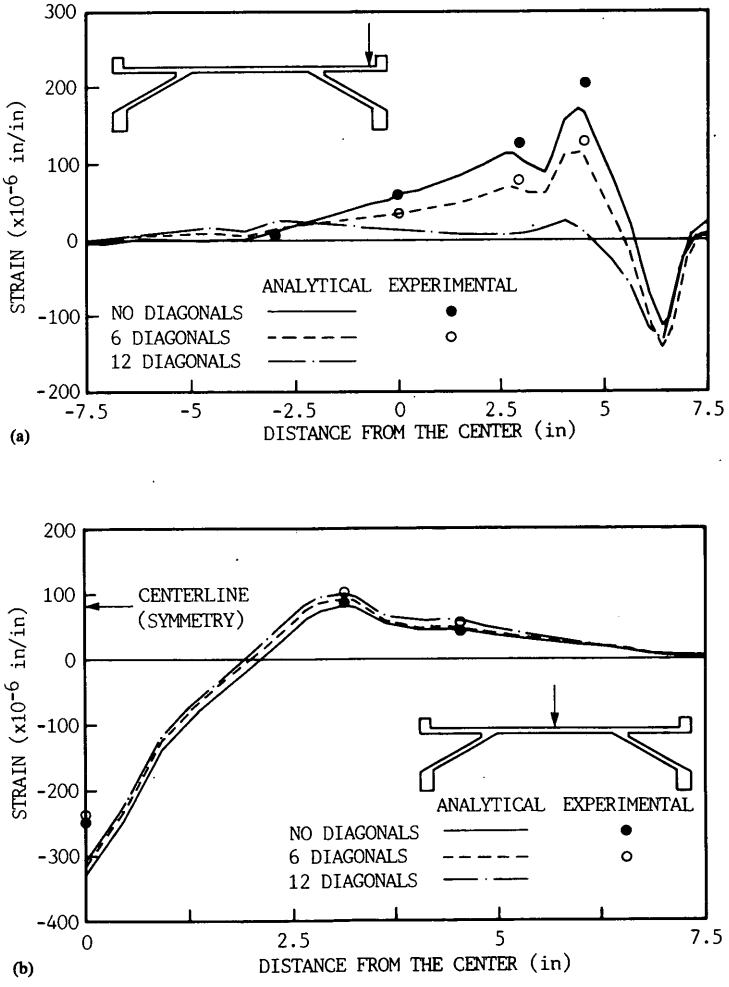

FIGURE 6 Transverse strain distribution on top of deck at midspan: (*a*) single load at Point *G*1 and (*b*) load at Point *G*3.

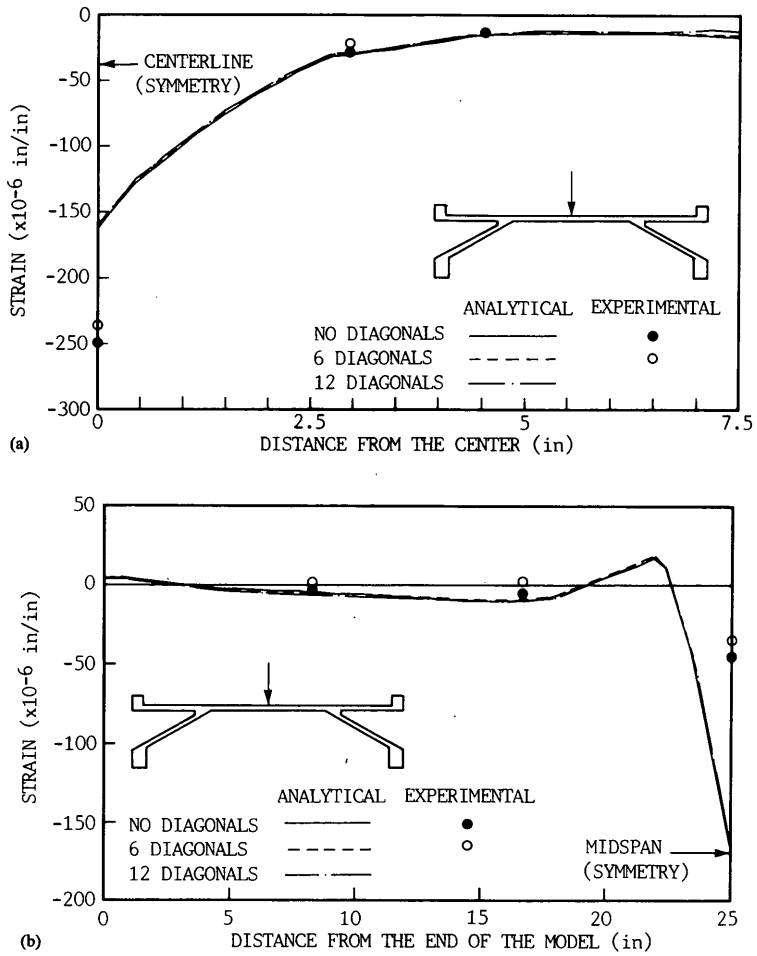

FIGURE 7 Longitudinal strain distribution on top of deck at midspan—single load at point *G3*: (*a*) strains across the deck and (*b*) strains along the bridge span.

Folded Plate

To investigate the response of the folded plate, the longitudinal and transverse strains were recorded for the single-load position at various locations along Section *G* (Figure 4). The longitudinal strain at midspan at Point *P* in the inclined plate was not significantly affected by the addition of the diagonal members, as shown in Figure 8*a*. However, adding diagonal members increased the torsional rigidity of the section and reduced the rotation of the deck-plate connection, resulting in a smaller transverse strain in the inclined plate when the load was applied near the curb (Figure 8*b*). The experimental results also illustrated that the transverse strain at Point *P* rapidly decreases as the load moves toward the other side of the deck (Figure 8*b*).

The experimental results also indicated that the maximum shear stresses in the inclined plate occurred when the load was applied at Point *B2* (Figure 5). In this case, most of the load is transferred to the supports through the inclined plates, resulting in higher shear stresses in the inclined plate near the end diaphragm. Shear stresses were determined to be essentially uniform along the width of the plate except in the regions where the plate is connected to the edge beam and the deck. The presence of diagonal members did not have a significant effect on the shear stresses in the folded plates.

Response of the Model Under Truck Loading

After verifying the analytical results with the experimental results, the model was analyzed with scaled loads equivalent to AASHTO HS20-44 truck loading at various locations. For the case of maximum bending moment, two trucks were placed side by side at midspan. The model was also analyzed under a truck loading at midspan, with each truck positioned as close to the curb as the AASHTO specifications permit to produce maximum transverse stress in the deck.

The results of these analyses are summarized in Figures 9 and 10. Although the posttensioning forces were calculated so that no tensile strain would be induced in the model, some tensile strain was induced in the top of the curb near the end diaphragm (Figure 9*a*). This strain was the result of local moment caused by applying the posttensioning force at the bottom instead of the center of the curb. The analysis dem-

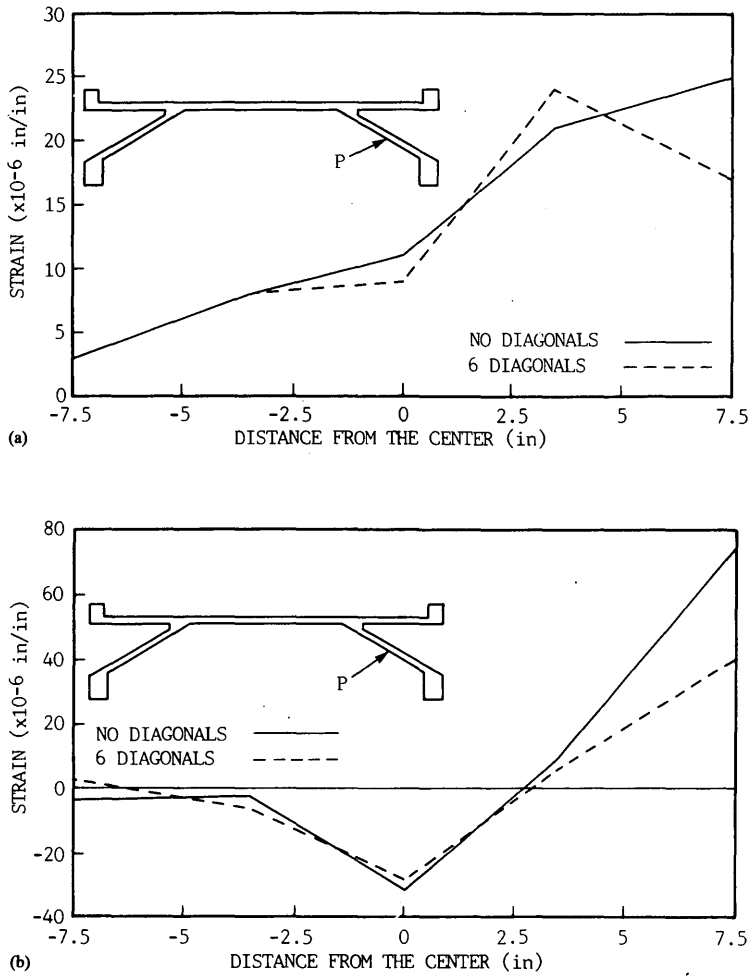

FIGURE 8 Longitudinal strain (*a*) and transverse strain (*b*) at Point *P* as single load moves along Section *G*.

onstrated that no tensile strains were induced in the bottom of the edge beam (Figure 9*b*). This verifies that the ordinary beam theory is adequate to estimate the required post-tensioning forces.

Figure 10 illustrates that the transverse strain in the top of the deck is reduced by approximately 50 percent when diagonals are used. The advantage of connecting the curb to the deck is also demonstrated. The differential deflection across the deck is minimized and the cross section is forced to act as a unit.

SUMMARY AND CONCLUSIONS

Aging, lack of maintenance, increases in legal loads, and increased traffic volumes cause more bridges to be added to the list of deficient bridges every year. Detouring traffic to avoid the problems associated with posted or closed bridges causes costly delays and inconveniences the traveling public. This paper summarizes one of the several phases of ongoing research to develop a new type of bridge that is economical, relatively easy to construct, and useful as an emergency bypass bridge. Through analytical and experimental studies, the feasibility and practicality of using an integrated folded-plate deck system were investigated. The folded-plate bridge system was analyzed using the ANSYS finite-element program. In the experimental portion of the investigation, a 1:24 Plexiglas scale model of a folded-plate bridge was fabricated and tested under forces simulating posttensioning and legal live loads.

The experimental and analytical investigations illustrate that folded-plate bridges can be constructed for short- or relatively long-span bridges. The results show that connecting the beams along the bottom edges of the folded plates to the curbs increases the stiffness of the bridge section and improves the overall behavior of this bridge system. The close agreement between the experimental and analytical results illustrates the capability of using finite element methods to analyze this complex bridge type. The performance of the model under simulated service loads also demonstrates that the folded-plate deck bridge is an alternative to some of the currently used bridge systems, except for the higher transverse stresses that were caused by the lack of arch action.

The results obtained in this investigation using a 1:24 scale model must be interpreted with care. Problems associated with using small-scale models fabricated with Plexiglas to model

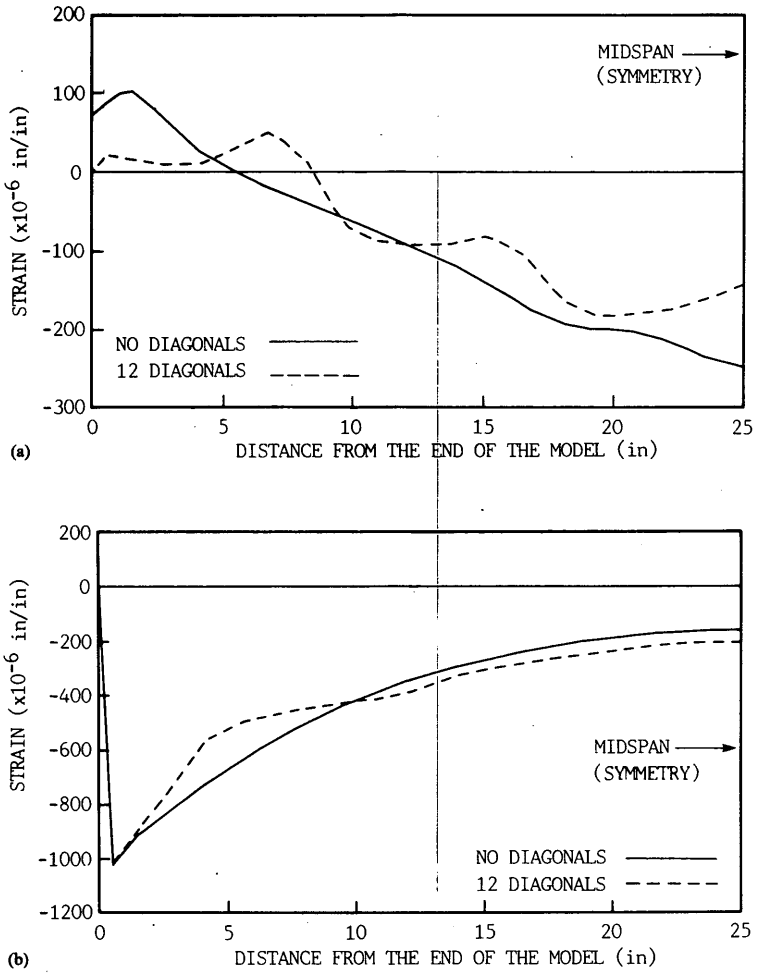

FIGURE 9 Longitudinal strain distribution along top of curb (*a*) and bottom of beam (*b*): two trucks at midspan, prestressing force applied.

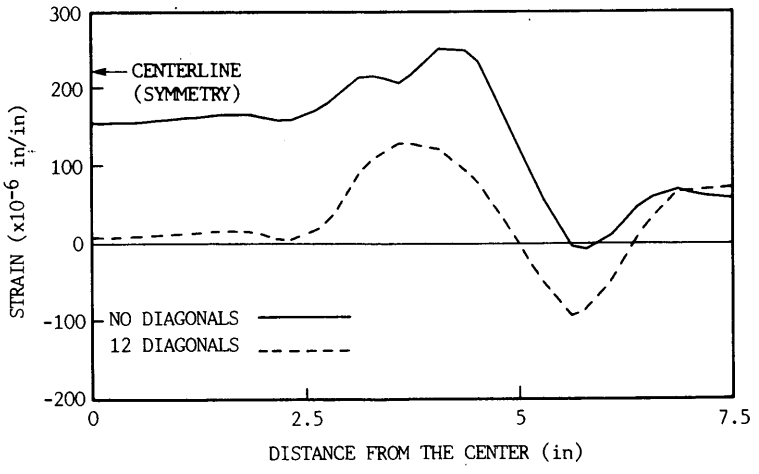

FIGURE 10 Transverse strain distribution along top of deck at midspan: two trucks at midspan, prestressing force applied.

actual structures need to be carefully considered. Research is still needed to determine the most economical fabrication and erection techniques for shell or folded-plate bridges.

ACKNOWLEDGMENTS

This research was supported by the National Science Foundation under the direction of John Scalzi. The authors also are grateful to Denise Wood for her assistance in typing this paper.

REFERENCES

1. F. Fanous, D. Andrey, and F. W. Klaiber. Analytical Investigation of Shell Structures Utilized as Emergency Bypass Bridges. In *Transportation Research Record 1180*, TRB, National Research Council, Washington, D.C., 1987, pp. 12–18.
2. W. Wassef. *Analytical and Experimental Investigation of Shell Structures Utilized as Bridges*. Ph.D. dissertation. Iowa State University, Ames, 1991.
3. T. Merchant. *Experimental and Analytical Investigations of a Folded-Plate Model Bridge*. M.S. thesis. Iowa State University, Ames, 1991.
4. G. J. DeSalvo and J. A. Swanson. *ANSYS Engineering Analysis User's Manual*, Vols. 1 and 2. Swanson Analysis System, Inc., Houston, Pa., 1989.
5. *Standard Specification for Highway Bridges*, 13th ed., American Association of State Highway and Transportation Officials, Washington, D.C., 1983.

Interpretations of the results reported here are those of the authors and do not reflect the opinions of the sponsor.

Publication of this paper sponsored by Committee on General Structures.

Performance Evaluation of Integral Abutment Bridges

ALAN A. SOLTANI AND ANANT R. KUKRETI

To establish a maximum safe length and design details for zero skew steel and concrete bridges with integral abutments, a survey of the highway departments of all 50 states was conducted. The findings of the survey include maximum lengths of integral abutment bridges being constructed, advantages and disadvantages of these bridges as perceived by the various states, and the extent of field observations done. The variation in the design assumptions and length limitations used as well as the problems associated with thermal movement experienced by the various states are discussed. A critique of the design and construction practices of the states that have pioneered the use of integral abutment bridges is also presented.

Before World War II most bridges with an overall length of 50 ft or more were constructed with some form of expansion joints. Periodic inspection of these bridges has revealed that the expansion joints tend to freeze and close and, therefore, do not operate as intended. Closer inspection of such bridges has also revealed that no serious distress was associated with the freezing or closing action of the joints.

Studies conducted by the Ohio Department of Highways have shown that the increase in internal stress in the approach slabs and not in the bridge slabs has been the main cause of bridge failures (*1*). Such a problem could be resolved easily by providing adequate expansion joints in the approach pavements without any expansion joints on the bridge at all. This has led to the advancement of the case for the construction of continuous bridges. Bridges in which the girders are fixed at the abutments, thereby requiring no expansion joints at the abutment, are called integral abutment bridges. Presented are findings of a survey conducted to evaluate the current design practices and performance of such bridges.

BACKGROUND

Most bridges in the world are constructed with some form of expansion joints. An example of these bridges is shown in Figure 1, and a detail of an abutment in which such a joint is provided is shown in Figure 2. This type of an expansion joint at the abutment causes the water from the backfill and roadway to penetrate into the bearing areas and onto the bridge seats. The joints could then potentially be forced to close, resulting in broken backwalls, sheared anchor bolts, and damaged roadway expansion devices. These problems and the maintenance costs associated with them have accelerated the development of integral abutments in the United States.

The routine use of integral abutments to tie the bridge superstructure to the foundation piling began in the United States about 30 years ago. The states of Kansas, Missouri, Ohio, and Tennessee are some of the early users. This method of construction has steadily grown more popular. In addition to being aesthetically pleasing, integral abutment bridges offer the advantage of lower initial costs and lower maintenance costs, because they eliminate expensive bearings, joint material, piles for horizontal earth loads, and leakage of water through the joints. An example of a bridge with integral abutments is shown in Figure 3. In this type of bridge, the thermal stresses are transferred to the substructure via a rigid connection in which the abutment contains sufficient bulk to be

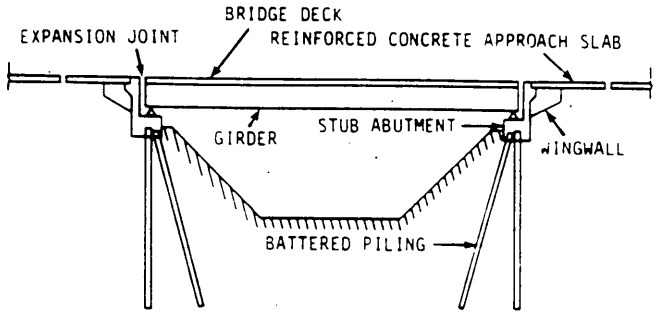

FIGURE 1 Cross section of bridge with expansion joints.

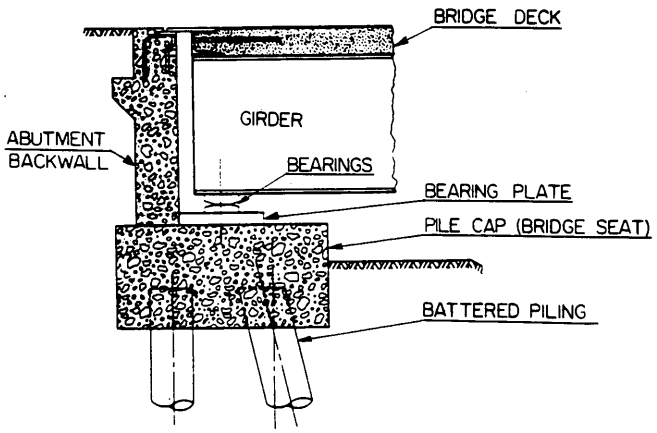

FIGURE 2 Abutment detail of bridge with expansion joints.

A. A. Soltani, Oklahoma Department of Transportation, 200 N.E. 21st Street, Oklahoma City, Okla. 73107. A. R. Kukreti, School of Civil Engineering and Environmental Science, University of Oklahoma, Norman, Okla. 73019.

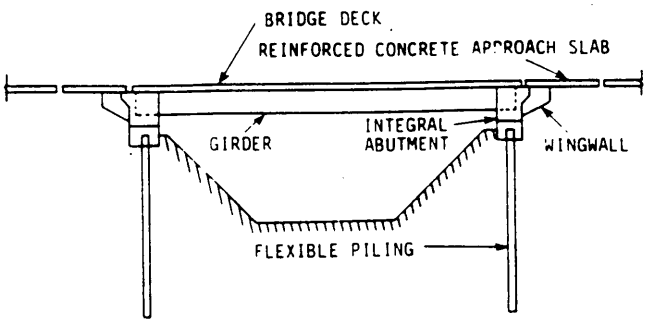

FIGURE 3 Cross section of bridge with integral abutments.

considered a rigid mass. Various construction details have been developed by the various states to accomplish the transfer; a few of these are shown in Figure 4. A positive connection to the girder ends is generally provided by vertical and transverse reinforcing steel. This connection provides a mechanism for full transfer of temperature variation and live load rotational displacements to the abutment piling. Also, because of the confinement of the bridge slab between the two abutments, the horizontal displacements can be transferred to the end of either the abutment or the approach slab, where the approach slab is tied to the abutment. This is because, in this type of design, the bridge acts as a rigid frame.

The semi-integral abutments, as shown in Figure 5, are designed to minimize the transfer of rotational displacements to the piling. They do, however, transfer horizontal displacements and also allow elimination of the deck expansion joints. Rotation is generally accomplished by using a flexible bearing surface at a selected horizontal interface in the abutment. Allowing rotation at the pile top generally reduces the pile load.

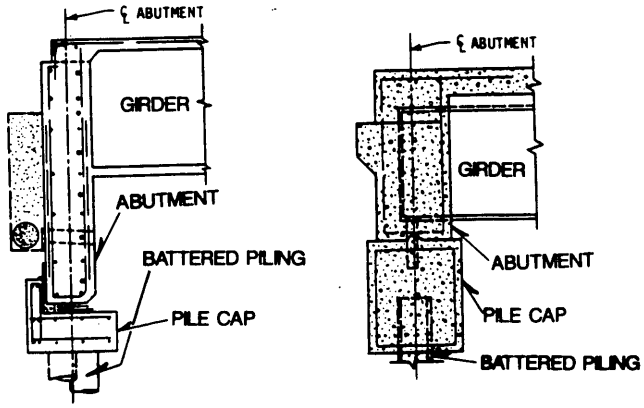

FIGURE 5 Details of semi-integral abutment used by various states.

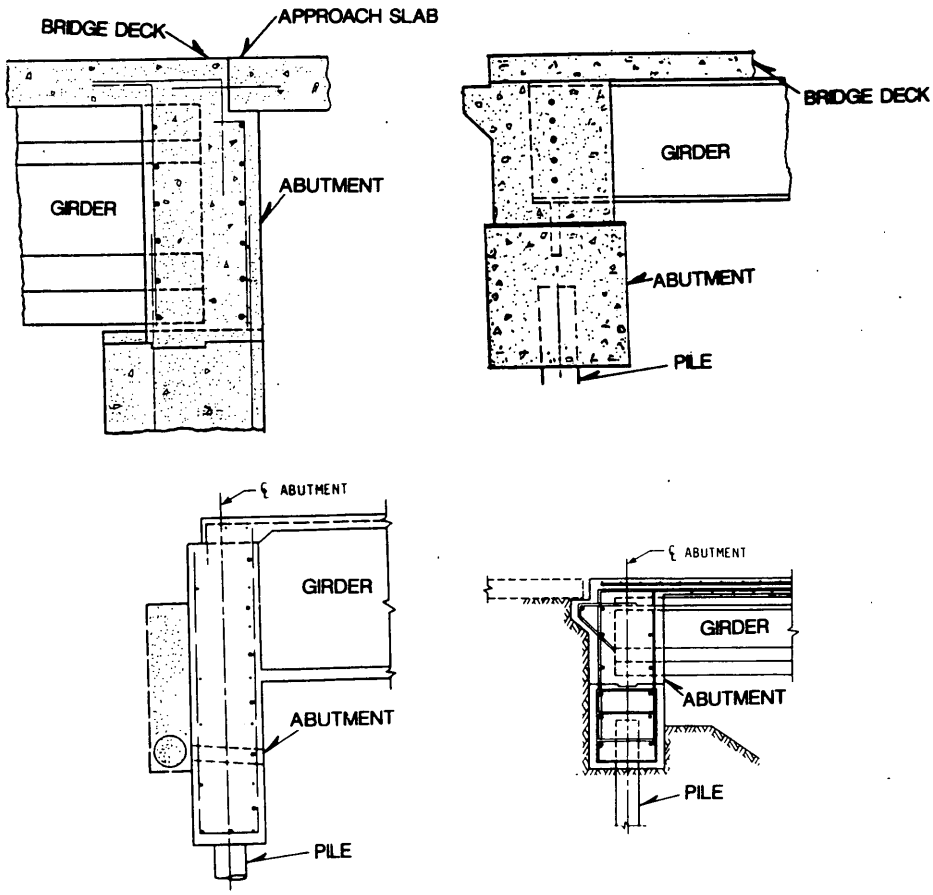

FIGURE 4 Details of integral abutment used by various states.

REVIEW OF STUDIES AND CONSTRUCTION DETAILS

Many surveys have been conducted concerning the use of integral abutments (*2–5*). These surveys indicate that there are significant variations in the design limitations and criteria currently followed. Many states have not felt comfortable using a system that does not contain some "free space" to accommodate the displacements caused by temperature changes.

Today, more than 80 percent of the state highway agencies have developed design criteria for bridges without expansion joint devices. Most of the states initially used integral abutments for bridges that were less than 100 ft long. Later, allowable lengths were gradually increased on the basis of good performance of the connection details used. However, the increased lengths have varied in the different states.

Full-scale field testing and sophisticated national design methods were not commonly used as a basis for increasing the allowable length. This led to wide variations in criteria for the use of integral abutments from state to state. FHWA recommends integral abutments for steel bridges less than 300 ft long (*6*). For pre- or posttensioned concrete bridges and for unrestrained bridges (i.e., bridges on which the abutments are free to rotate, such as a stub abutment connected to a row of piles or an abutment hinged to the footing), FHWA recommends a 600-ft maximum (*5*).

The limits of allowable horizontal movement that will cause objectionable pile stresses have not been established. In fact, the value constituting an objectionable pile stress has not yet been defined. This partly explains the wide variation in the design criteria used for integral abutment bridges by the various state highway agencies.

A survey of 50 states and a review of the literature have shown that little theoretical or experimental work has been conducted to establish limits or to develop design procedures for integral abutment bridges. Iowa State University is one of the few institutions conducting some field and model tests but has not yet concluded these studies.

SURVEY QUESTIONNAIRE AND RESULTS

To develop a design procedure and related construction details for integral abutment bridges, it is imperative to understand not only the state of the art as far as analysis and design are concerned but also the current practices followed by the various highway agencies. These practices have been developed by observing the actual performance of such bridges constructed over the years. Also, a thorough understanding of the problems that these agencies have encountered, in particular the "phobia" surrounding the design and detailing of integral abutment bridges, is important; one could either suggest solutions to these problems or at least be able to explain them. Only then could a practical design—one that could be acceptable and used by most state agencies—be possible.

To develop a design procedure and related construction details, it is imperative to know the disadvantages as well as the advantages of the current details used by the various state agencies. The construction details that have shown signs of failure need to be studied and scrutinized to find shortcomings and ways to improve them.

Other problems that need to be addressed are (a) how the states compensate the active and, most importantly, the passive soil pressure behind the abutments and (b) whether they leave a free space behind the abutments to allow for thermal expansion and, if so, what construction details they have used.

A survey questionnaire was prepared to obtain this information from the departments of transportation across the United States. It was also intended to collect additional information about the history of these bridges in each state to determine whether field testing had been conducted or is currently being conducted to monitor their performance. States were requested to confine their answers to 90-degree bridges and to send a copy of their design procedure and standard details for integral abutment bridges. After the responses were obtained and analyzed, some departments were contacted on the telephone for additional information.

Summary of Responses Obtained

Of 38 responses received, 29 indicated that their states either were using or had used integral-type abutments. A few states, such as Florida, Pennsylvania, and Virginia, were just beginning to use them; their first integral abutment bridges were constructed in the 1980s. On the basis of a review of the survey results, several states were contacted later for additional information to gain a better understanding of successful design details and assess the performance of relatively long integral abutment bridges.

The results of the correspondence and the telephone conversations with the bridge engineers are presented in Table 1. Each column in this table corresponds directly to the survey questionnaire that was sent to all 50 states. The following information corresponds to each column of Table 1:

- Column 1. STATE: name of the state supplying the information.
- Column 2. USE: whether integral abutment-type bridges are being used (Y = yes; N = no).
- Column 3. TYPE: type of road normally using integral abutment-type bridges (1 = state; 2 = county; 3 = all).
- Column 4. LENGTH: the span length each state uses for integral abutment-type bridges. The following code numbers are used to categorize various span lengths:

1 = <200 ft	5 = 500–600 ft
2 = 200–300 ft	6 = 600–700 ft
3 = 300–400 ft	7 = 700–800 ft
4 = 400–500 ft	8 = >800 ft

- Column 5. EXP. JTS: if expansion joints are used in the approach slabs, at what distance they are from the abutments.
- Column 6. PILE CAP: Whether pile caps are used (Y = yes; N = no).
- Column 7. 1st IAB: year the first integral abutment-type bridge was constructed in the state.
- Column 8. LONGEST: length of the longest integral abutment-type bridge constructed with the following materials: (1) steel, (2) cast in place, and (3) pre- or posttensioned.

TABLE 1 Summary of Responses

STATE	USE	TYPE	LENGTH								EXP JTS	PILE CAPS	1ST IAB	LONGEST			BKF MAT	DIS ADV
			1	2	3	4	5	6	7	8				1	2	3		
ALABAMA	N																	
ARIZONA	Y	3	x								NO	Y	76	296		162	G	10,14
ARKANSAS	N																	6
CALIFORNIA	Y	3	x	x							YES	Y	50	240	260	240	G	10,14
COLORADO	Y	3	x	x	x						200'	Y	75			450	G	4
FLORIDA	Y	1	x								0'	Y	85		200		N.A.	N.A.
GEORGIA	Y	3		x		x					N.A.	Y	77	340		477	N.A.	N.A.
HAWAII	N		x	x							N.A.	N.A.	67			100	N.A.	3
IDAHO	Y	3	x	x							50'	Y	72	266	262	521	G	5,2,4
ILLINOIS	Y	3	x								20'	Y	86	230	100	250	G	6
INDIANA	Y	3	x								YES	Y	72		150		G	NONE
IOWA	Y	3	x	x							YES	Y	64		130	300	G	2,3
LOUISIANA	N																	
MICHIGAN	N	2		x							YES	Y	70	250			G	N.A.
MINNESOTA	Y	3	x								YES	Y	60	200			G	2,3
MISSISSIPPI	N		x										40	30	40		N.A.	N.A.
MISSOURI	Y	1	x	x	x	x	x				50'	Y	60's	500	600		N.A.	2
MONTANA	Y	3	x	x							0'	Y	N.A.	150	108	230	G	4
NEBRASKA	Y	1		x							0'	Y	69	464		260	G	13
NEVADA	Y	3	x	x	x						0'	Y	74	294		530	G	NONE
NEW JERSEY	N																	
NEW HAMPSHIRE	N																	
NEW MEXICO	Y	3	x	x	x	x					NO	Y	77	250		450	G	16
N. CAROLINA	N																	
N. DAKOTA	Y	1	x	x		x					20'	N	60	350	100	450	G	1,2,3
OKLAHOMA	Y	1	x	x							15'	Y	79		279	210	G	10
OREGON	Y	3	x	x							NO	Y	30		385	420	G	3
PENNSYLVANIA	Y	1	x	x							YES	Y	86			250	G	8
S. CAROLINA	Y	1	x								20'	Y	74	220	150			N.A.
S. DAKOTA	Y	3	x	x	x						20'	Y	48	354	324		N.S.	NONE
TENNESSEE	Y	3	x	x	x	x	x	x	x	x	0'	Y	70	416	460	927	G	NONE
TEXAS	N																G	
UTAH	Y	3	x	x	x						NO	Y	50's	450	150	400		9
VIRGINIA	Y	1	x								NO	Y	82	180			G	2,15
WASHINGTON	Y	1	x								NO	Y	20		350		G	11,7
W. VIRGINIA	N																	
WISCONSIN	Y	3		x							NO	Y	70	100	150	300	W.G.	7
WYOMING	Y	3	x	x							NO	Y	60	356	199	172	G	N.A.
																	G	

- Column 9. BKF MAT: type of material used behind the abutments (*G* = granular, *W.G.* = washed gravel; *N.S.* = no specification; and *N.A.* = no answer).
- Column 10. DIS-ADV: disadvantages of integral abutment-type bridges. The numbers are the disadvantages listed separately in Table 2 as perceived by the various states.

Trends Observed in the Responses

Most of the states that use integral abutments, as reflected in Table 2, have developed specific guidelines (policies) concerning allowable bridge lengths. The basis of these guidelines, however, is largely empirical. It was hoped that these guidelines would have been developed according to results of some rational analysis and design procedures or experiments conducted to find anticipated movement of the bridge or approach slab and the pile stresses. However, it was found from the responses that all states used empirical data to arrive at the maximum allowable bridge lengths. It is evident that much of the progress in the use of integral abutments resulted from successive extension of limitations based on acceptable performance of prototype installations. The following points are summarized from the responses to the survey questionnaire and subsequent correspondence and telephone conversations with several states:

1. Most of the states cited the reason for using integral abutments as cost savings. They pointed out that typical bridge designs that use integral abutments require less piling, have simpler construction details, and eliminate expensive expansion devices. Some states indicated that their primary reason for using integral abutments was that they eliminate the problems encountered with use of expansion joints. A few respondents pointed out that simplicity of construction and lower maintenance costs were their primary motives for using integral abutments.

2. The span length and limitations currently being used for bridges with integral abutments are given in Table 1. In summary, for states that use this type of design, the acceptable range of limitations is as follows: steel, 200 to 300 ft; concrete, 300 to 400 ft; and prestressed concrete, 300 to 450 ft. A few states, such as Idaho, Missouri, Nevada, Tennessee, and Utah, use longer limitations for each structure type. Typically they have been building integral abutment bridges longer than most other states and have had good success with them. The move toward the use of integral abutment bridges for longer spans is based on the excellent performance observed for shorter-span bridges and the maximum benefit from what many regard as a very-low-maintenance, dependable abutment design. The difference in concrete and steel length limitations reflects the greater sensitivity of steel in reacting to temperature changes. Although the coefficients of expansion (α) are nearly equal for both materials (for concrete $\alpha_c = 60 \times 10^{-7}$ in./in./°F and for steel $\alpha_s = 65 \times 10^{-7}$ in./in./°F), the relatively large mass of most concrete structures makes them less reactive to ambient temperature changes. This is reflected in the design temperature variation specified by AASHTO (*6*), which states:

> Provision shall be made for stresses or movements resulting from variations in temperature. The rise and fall in temperature shall be fixed for the locality in which the structure is to be constructed and shall be computed from an assumed temperature at the time of erection. Due consideration shall be given to the lag between air temperature and the interior temperature of massive concrete members or structures.

3. Almost all states indicated that a free-draining backfill material be used behind the abutments. One major problem seems to be to achieve a 95 percent compaction requirement of backfill. This requirement eliminates settlement of the approach slab.

4. Most states reported that construction and maintenance costs are lower if integral abutments are used. The following are some comments made about construction and maintenance problems using integral abutments:

a. Field placement of precast beams could be a problem, since cranes cannot get close to the abutments because the backfill is not placed until after the beams are placed.

b. The proper compaction of backfill is critical.

c. Careful consideration at the end of the bridge is necessary.

d. The effects of elastic-shortening after posttensioning should be carefully considered.

TABLE 2 Disadvantages of Integral Abutment Bridges as Perceived by Various State Departments of Transportation

1.	Increased earth load can cause abutment cracking.
2.	Skew over 20° cannot be accommodated.
3.	Can only be applied to short bridges.
4.	Cracks developed in the asphalt backface of the abutments, as a result of which a bump at the end of bridge or approach slab could appear.
5.	Integral abutment bridges are limited to pile supported abutments, and drill shafts cannot be used.
6.	Lack of rational method for predicting behavior. Also, thermal stresses are unknown.
7.	Temporary shoring will be required in precast bridges.
8.	Crane cannot go close to place precast beams, since backfill is put in after the beams have been placed. Therefore, cranes with large booms are required.
9.	Good details for tying the approach slab to the abutment are not available.
10.	Longer than normal approach slab is required.
11.	Limits future modifications, such as widening.
12.	Cracks in slab, end diaphragm or wingwalls are possible.
13.	Wingwalls cannot be tied to the abutment.
14.	Erosion of the approach embankment caused by water intrusion.
15.	Field problems exist when constructing a bridge on a steep slope.

e. Wingwalls may need to be designed for heavier loads to prevent cracking.

f. Adequate pressure relief joints should be provided in the approach slab to avoid overstressing of the abutments.

g. Positive tie connection between the approach slab and abutment may be necessary to avoid opening in cold weather.

Review of Design and Construction Details in Selected States

To become more familiar with the designs and construction practices of various highway agencies in the United States, a critique of integral abutment bridge developments in a few selected states (pioneers in designing such bridges) is summarized in this subsection.

Tennessee

Numerous integral abutment bridges have been constructed and their field performance has been evaluated in Tennessee. In an unpublished memorandum, Edward Wasserman, of the Tennessee Department of Transportation (DOT), wrote:

> In Tennessee DOT, a structural engineer can measure his ability by seeing how long a bridge he can design without inserting an expansion joint.

He also explained that in the past 20 years, nearly all their new highway bridges with spans ranging several hundred feet long have been designed with no expansion joints, even at the abutments. The largest bridges include a 927-ft prestressed concrete bridge, a 416-ft steel bridge, and a 460-ft cast-in-place concrete bridge. Details of a typical bridge are shown in Figure 6. The Tennessee DOT reports (*7*):

> We have found neither the deck elongation nor the superstructure stresses to be abnormal. All measured stress data were lower than predicted. Exactly why, we don't know, but we think we have some of the answers. One factor appears to be creep in concrete. If concrete is expanded or contracted slowly, as by temperature, it creeps. Stresses due to shrinkage/expansion don't reach the level predicted. To make theory better fit reality, in the case of concrete we have reduced its thermal modulus of elasticity to one-third that's used for dynamic loads.
>
> In addition, temperature cycling of concrete bridges appear to reach lower peaks than in steel. Apparently concrete's greater mass provides a heat sink. Thus, its temperature tends not to rise as high nor as low as theory predicts. We design Tennessee bridges in concrete for a temperature range of 20° to 90°F, and steel superstructure bridges for a range of 0° to 120°F. Based on these ranges and thermal coefficients of expansion for respective materials, we design for 0.505 inch of movement per 100 feet of span in concrete, and 0.936 inch of movement per 100 feet of span in steel.

To demonstrate this procedure, the 2,800-ft-long Kingsport bridge in Tennessee can be chosen as an example, in which the center of the bridge is assumed to be neutral or fixed. The total movement of the superstructure of this bridge, which is made of concrete, is obtained by multiplying 1,400 (equals span) by 0.505 (equals rate of expansion), which yields the total movement at each abutment equal to 7.07 in. This bridge has performed within this range since 1978 (*8*).

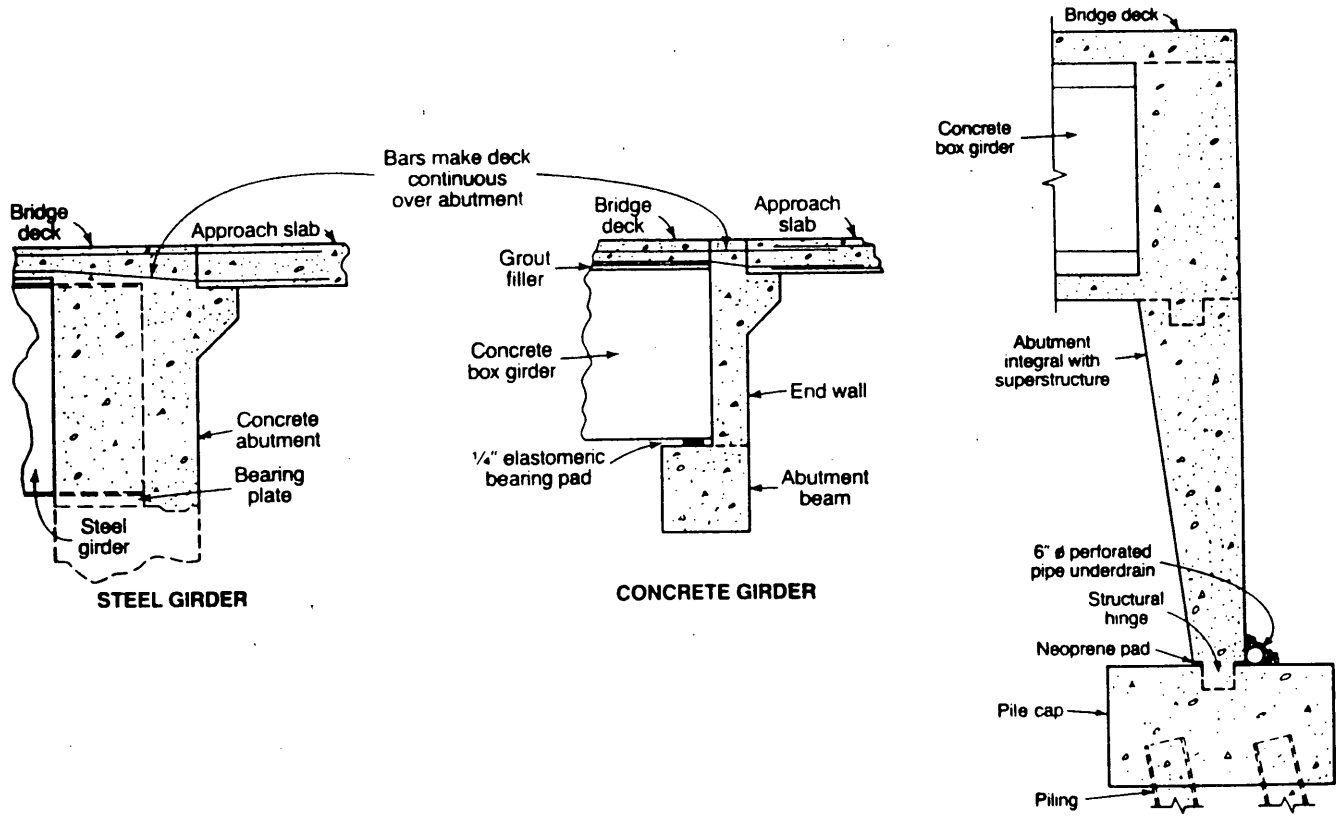

FIGURE 6 Typical details of integral abutment bridge construction used in Tennessee.

Tennessee DOT also explains (*7*) that when they are asked, "How do you set about to reduce or eliminate expansion joints?" they give the following explanations:

1. "We take advantage of pile translation and rotation capabilities."
2. "By modifying foundation conditions, if feasible."
3. "By taking advantage of reduced modulus of elasticity of concrete for long-term loads (1,000,000 psi versus 3,000,000 psi)."
4. "By allowing hinges to form naturally or constructing them."
5. "Employing expansion bearing, where necessary."

Where there is a concrete pavement approaching a concrete deck, Tennessee DOT installs a compression seal joint between them. But where the interface is asphalt to concrete, they believe that no special treatment is necessary. Regarding this, they point out: "This will eventually cause some local pavement failure and a 'bump,' which is a minor problem compared to joint maintenance." In summary, Tennessee's 20-year experiment with integral abutment bridges has proven that, for thermal movements up to 2 in., both immediate construction savings and long-term maintenance savings can be realized by total elimination of joints.

California

One of the reasons for the popularity of jointless bridges in California is their performance during the 1971 San Fernando earthquake. During this earthquake, the jointless abutment-approach fill concept suffered less overall damage than the jointed abutment-type bridges. Also, because of initial cost and inherent problems with expansion joints, especially at abutments, California DOT has pointed out (*9*):

> It has been general practice in California since 1971 to construct highway structures without expansion joints. Consequently, most structures less than 350 feet long built since that time are jointless. California also has over 100 jointless structures with lengths exceeding 350 feet. Even on most structures with expansion joints, the abutments are jointless.

California DOT has indicated (G. D. Mancarti, Memo to Designers):

> The major benefits of integral abutment are its low initial cost, its effectiveness on absorbing seismic loads and its ability to accommodate structurally, relatively large thermal movements. Reinforced concrete bridges up to 400 feet in length have shown no evidence of structural distress of the abutments from thermal movements.

Because water intrusion has been the main problem with this design, California DOT connects the approach slab directly to the abutment and extends it over the wingwalls. Also, an underlying drainage system is provided to give additional insurance. California's limitation on bridge movement (including temperature, creep and long-term prestressed shortening) is a maximum of 1 in. at the expansion joint between the approach slab and the adjoining pavement.

South Dakota

South Dakota has extensive experience in the use of integral abutments, particularly for steel bridges. It is also one of the first states to conduct a full-scale testing program to evaluate the performance of integral abutment bridges. A brief review of this program is presented in this section.

In this testing program they have measured the magnitude of the stresses induced by thermal movements in the girder and the upper portion of the steel-bearing piles of integral abutment-type bridges. A full-scale model representing the end portion of a typical highway bridge was constructed and tested to simulate the following four construction stages:

Stage 1: Girder welded to piles only.
Stage 2: With an integral abutment in place.
Stage 3: With abutment and slab.
Stage 4: Backfill completed.

For each stage, the test specimen was subjected to a series of predetermined longitudinal movements via hydraulic jacks to simulate expansion and contraction caused by temperature changes. The fact that the test specimen was designed and constructed as a full-scale model that represents the end portion of an actual bridge confirmed this approach as a field study instead of as a model study (*3*). Many variables (e.g., compressive strength of concrete, placement of steel) that normally would be under tight control in the laboratory were not controllable in the field. In addition, a single concentrated load was applied to the girder to simulate the thermal stresses, which in reality should have been applied by a distributed load. This certainly would have introduced some inaccuracy into the results. The conclusions based on these test results were as follows:

1. The induced movement and shear force in the girder, caused by temperature changes alone, are usually smaller than the overstress allowance made by AASHTO (*6*) for combined loadings.
2. The integral abutment acts as if it were a rigid body.
3. Thermal movements larger than 0.5 in. may cause yielding in the steel piling.

More studies are required to prove the accuracy of the last conclusion. This contradicts the practices followed, with complete success, by the states of Tennessee and North Dakota, which recommend 7 in. and 4 in. of expansion, respectively.

Another point (*3*) is that the stresses at the various parts of the test specimen, in Stage 4, were of greater magnitude during the expansion cycle than during the contraction cycle. This result was attributed to the passive soil resistance of the backfill to expansion and to the fact that the active soil pressure actually helps contraction, even making the differences between the two actions more pronounced.

North Dakota

North Dakota has been constructing integral abutment bridges for more than 30 years. It is also the only state that has tried to eliminate the effect of passive soil pressure behind the

abutments. Following is a brief summary of a field study (*10*) conducted by the North Dakota State Highway Department in November 1981.

The bridge studied had integral abutments, piers, concrete box girders, and a concrete deck. The bridge, 450 ft long, was made up of six 75-ft spans. Expansion joint material was placed between the back side of the abutment and the soil backfill, as shown in Figure 7, and compressible material (Type R Zerolite with compressive strength range of 5 to 10 lb/in.^{2}) was placed on the webs of the abutment piles, as shown in Figure 8.

The equation the North Dakota DOT uses to calculate temperature change, ΔT, is

$$\Delta T = T_1 - T_2 + (T_3 - T_1)/3 \quad (1)$$

where

T_1 = air temperature at dawn on the hottest day,
T_2 = air temperature at dawn on the coldest day, and
T_3 = maximum air temperature on the hottest day.

This temperature change will result in the change in length, ΔL, of the bridge given by

$$\Delta L = L \alpha \Delta T \quad (2)$$

where

L = original length of bridge and
α = coefficient of thermal expansion of the bridge deck material.

An interesting point noted by the North Dakota DOT was that, after 1 year, the gap had closed by 0.5 in. on the north abutment and 0.75 in. on the south abutment. The abutment-to-backfill gap is a questionable measure of abutment movement inasmuch as the soil backfill may move into the opening, depending on the ability of the expansion joint material to expand and fill the gap.

At the time of maximum change in bridge length, the south abutment had moved out by 1.96 in. and the north abutment had moved out only by 0.74 in. Therefore, North Dakota DOT concluded that the total change in the bridge length will not result in equal movement at each abutment.

Pile stresses were studied for the case in which the maximum abutment movement (1.96 in.) occurred. North Dakota DOT had concluded that the yielding took place in less than the top 1 ft of the piles, and at the highest stress point (top of the pile) the yielding occurred only on the outer one-fourth depth of each of the flanges. In other words, the stress at the top of the pile is sufficient to initiate a yield stress in the steel but not sufficient to cause the formation of a plastic hinge (*11*).

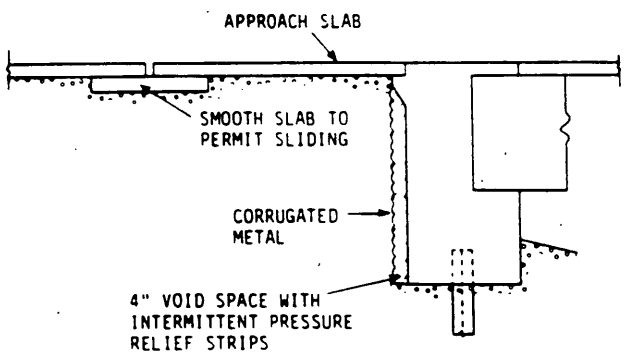

FIGURE 7 North Dakota integral abutment system with pressure relief strips.

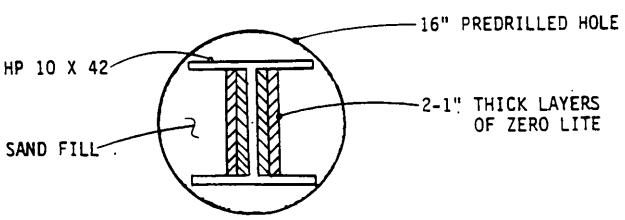

FIGURE 8 North Dakota abutment pile with compressible material on web.

Iowa

Iowa began building integral abutments on concrete bridges in 1964. One of the first bridges was constructed on Stange Road over the Squaw Creek in Ames (*12*). This prestressed beam bridge is about 230 ft long with no skew and is shown in Figure 4. Inspection of this bridge indicates no major cracks and apparent distress in the abutment walls, wingwalls, and beams caused by the thermal movement. The Iowa DOT reported (*12*) that inspection has been made yearly on 20 integral abutment bridges for about 5 years after their construction. Some of these bridges were skewed up to 23 degrees. The inspections were terminated because no stress or problems were found relating to the lack of expansion joints in the superstructure.

Iowa's designs are based on an allowable bending stress of 55 percent of yield plus a 30 percent overstress, because the loading is caused by temperature effects (*12*). The movement in the piles is found by a rigid joint frame analysis, which considers the relative stiffness of the superstructure and the piling. The piles are assumed to have an effective length of 10.5 ft; the soil resistance is not considered. Their analysis has shown that the pile deflection is about ⅜ in. (*12*).

CONCLUSION

Although the objective of this study was to investigate the methods of analysis and design details that have been implemented by the various DOTs in the United States to overcome the problems related to integral abutment bridges, it is apparent that this topic has not yet been resolved. Many research studies have been conducted recently, and work is continuing at Iowa State University. The findings of the recent research studies agree in most part with the findings presented. Some of the state DOTs have effectively solved most of the problems and have been successful in constructing long bridges with integral abutments.

One problem that no state, except North Dakota, has addressed deals with the effect of passive soil pressure that acts

behind the abutments during the bridge deck expansion. Further study of their design approach is warranted.

Most states are using integral abutments in designing their bridges. The study shows that design practices followed by most state DOTs are too conservative, and much longer bridges could be constructed. However, some rational analysis is still necessary to make this design more acceptable.

ACKNOWLEDGMENTS

This study is the result of 2 years of research on integral abutment bridges and their effects on approach slabs and the adjacent pavement. The authors wish to express their gratitude to the bridge engineers in those states who have helped by responding to the survey questionnaire and the follow-up letters and telephone calls. Specifically, they wish to express their gratitude to James Schmidt of the Oklahoma Department of Transportation for helping research the required materials.

REFERENCES

1. M. P. Burke, Jr. The World's Most Expensive Pavement Expansion Joints. Presented at Ohio Transportation Engineering Conference, April 4, 1972, pp. 65–68.
2. L. F. Greimann, A. M. Wolde-Tinsae, and P. S. Yang. Skewed Bridges with Integral Abutments. In *Transportation Research Record 903*, TRB, National Research Council, Washington, D.C., 1983, pp. 64–72.
3. H. W. Lee and M. B. Sarsam. *Analysis of Integral Abutment Bridges*. South Dakota Department of Highways, Pierre, March 1973, 135 pp.
4. J. H. Emanual. *An Investigation of Design Criteria for Stresses Induced by Semi-Integral End Bents*. University of Missouri, Rolla, MO., 1972.
5. *Integral, No-Joint Structures and Required Provisions for Movement*. Federal Aid Highway Program Manual, T 5140.13, FHWA, U.S. Department of Transportation, 1980.
6. *Standard Specification for Highway Bridges*, 13th ed. AASHTO, 1983.
7. *Structural Memorandum No. 45*. Tennessee Department of Transportation.
8. C. L. Loveall. Jointless Bridge Decks. *Civil Engineering*, Nov. 1985, pp. 64–67.
9. C. F. Steward. *Long Highway Structures Without Expansion Joints*. Final Report. California Department of Transportation, May 1983.
10. J. L. Jorgenson. *Behavior of Abutment Piles in an Integral Abutment Bridge*. North Dakota State University, Nov. 1981.
11. J. L. Jorgenson. Behavior of Abutment Piles in an Integral Abutment in Response to Bridge Movements. In *Transportation Research Record 903*, TRB, National Research Council, Washington, D.C., 1983, pp. 72–79.
12. A. M. Wolde-Tinsae, L. F. Greimann, and B. V. Johnson. Performance of Integral Bridge Abutments. IABSE Proceedings P-58/83. *IABSE Periodica 1/83*, Feb. 1983.

Publication of this paper sponsored by Committee on General Structures.

Long-Term Serviceability of Isotropically Reinforced Bridge Deck Slabs

GONGKANG FU, SREENIVAS ALAMPALLI, AND FRANK P. PEZZE III

Isotropically reinforced bridge decks have the potential to reduce costs to bridge owners for both construction and maintenance. For long-term serviceability evaluation, 13 such decks in New York State, with reinforcement ratios of 0.36 and 0.24 percent, have been inspected annually for the past 5 years; 4 of them have been load tested annually since they were constructed, the longest life being 8 years. Generally they have performed satisfactorily. Maximal stresses of bottom transverse rebars under 16-kip wheel loads over the years have always been below allowable levels based on conservative analyses. Rebar stresses in both the isotropic and AASHTO decks in New York State increase with age for the first year or two and remain relatively constant thereafter. Comparison of top-surface transverse cracking between the New York isotropic decks and North Carolina AASHTO decks indicates that the various reinforcement arrangements result in similar cracking severity.

In the United States, reinforced concrete (R/C) bridge deck slabs are designed on the basis of the flexural failure mode, according to the current AASHTO design code (*1*). However, extensive research has shown punching shear to be the dominant failure mode for slabs. This is attributed to flexural strength enhancement by the presence of membrane-compressive force in the slab, induced by its transverse boundary constraints, which is referred to as the "arching action" or the "dome effect." Based on varied research findings (*2–5*), Ontario had adopted an empirical design of isotropically reinforced deck slabs with a minimum reinforcement ratio of 0.3 percent in each face (*6*). This requires significantly less flexural steel than is required in the AASHTO code. Attracted by reductions in construction cost and probability of rebar corrosion resulting from this deck design of light reinforcement, researchers and state agencies in the United States have devoted notable efforts in this area over the past decade. A number of states have built or planned experimental isotropic deck slabs.

Slab capacity increase by arching action was noted as early as 1909 (*7*). Most early research in this area was oriented toward building-floor applications. Early work in this field has been briefly reviewed by several authors (*8–13*).

Behavior and strength of R/C bridge decks under static load are obviously of essential interest to bridge designers and owners. Modern studies of R/C bridge deck slabs in this area began at Queen's University in Ontario, Canada (*2,3,5,14*). They demonstrated excessive reserve strength of conventional R/C decks designed in accordance with the AASHTO provisions (*1*) by ⅛-scale models, and dominant punching failure of both isotropic and AASHTO orthotropic decks. After examining isotropic decks of various reinforcement ratios, they recommended an isotropic deck design with a minimum reinforcement ratio of 0.2 percent that possessed an adequate safety factor. Their findings were later confirmed by full-scale bridge testing (*15,16*), with 0.3 percent reinforcement adopted by the Ontario code (*6*). In the United States, Beal (*17,18*) confirmed these previous findings by testing ⅙-scale models and full-scale bridge decks containing isotropic and AASHTO orthotropic reinforcement. He also concluded that rebar stresses under the AASHTO design wheel load (20.8 kips) were lower than those predicted by the AASHTO code, and that ultimate strengths were six times larger than the design load in 0.25 percent reinforced isotropic deck models. Fang et al. (*8,9*) tested a full-scale isotropic deck model with about 0.4 percent reinforcement in each layer under simulated vehicle wheel loads. They found significant compressive membrane forces after cracking of the deck under load, with the deck behaving linearly up to a wheel load three times the AASHTO design load. Perdikaris and Beim (*10,11*) also confirmed adequate safety factors for isotropic decks by testing ⅙- and ⅓-scale deck models with 0.3 percent reinforcement, as well as their failure by punching shear. Puckett et al. (*19*) recently tested two full-scale decks—one reinforced according to the AASHTO code and the other 0.3 percent isotropically according to the Ontario code (*6*)—under vehicular loads at numerous locations. They found that bottom transverse rebars between girders experienced highest stresses under these loads. Jackson and Cope (*13*) tested two ½-scale models of isotropic deck to examine global load effects under wheel loads simulating critical vehicle loading cases. One deck had approximately 20 percent more reinforcement than is required by the Ontario code; the other was lighter. They found that the empirical design approaches of isotropic reinforcement appeared to be satisfactory, although global transverse moments could have large effects on deck behavior at various load levels.

Besides static strength, R/C deck fatigue strength has also been studied by several researchers. Batchelor et al. (*4,20*) performed fatigue tests on isotropic and orthotropic deck models of ⅛ scale under a sinusoidal concentrated load. They found that failure under fatigue load was always by punching shear. On the basis of their test results, they recommended an endurance limit of 0.4 (a fatigue load factor of 2.5) for an isotropic deck design with 0.2 percent reinforcement. Using fixed pulsating and stepwise moving loads, Okada et al. (*21*) and Sonoda and Horikawa (*22*) tested (a) full-scale models and panels sawed from distressed orthotropic decks and (b) 1.32 percent (top and bottom) isotropically reinforced slab models of ⅓ scale. First they found that moving load was substantially

Engineering Research and Development Bureau, New York State Department of Transportation, State Campus, Albany, N.Y. 12232.

more damaging than fixed pulsating load with respect to slab flexural and shear resistance. Fang et al. (*8,9*) tested a full-scale isotropic deck model with about 0.4 percent reinforcement under fixed pulsating 26-kip loads. They concluded that 5 million cycles of this pulsating load did not deteriorate the deck significantly. Perdikaris and Beim (*10,11*) first used constant rolling wheel load in their fatigue tests of ⅙-scale isotropic deck models with 0.3 percent reinforcement. The constant rolling wheel load resulted in a gridlike crack pattern on the model bottom surface, as often observed on decks in service (*10,11,21*). They also found that the constant rolling wheel load simulating real traffic loading is much more deteriorative than the fixed pulsating wheel load. It was concluded that the isotropic decks possess higher ductility and fatigue strength under constant rolling wheel load than the AASHTO orthotropic decks. Agarwal (*23*) reported a study of testing 14 Ontario isotropic and AASHTO bridge decks built for comparison in the early 1980s. He found that after a number of years of service, the slab panels displayed no visible signs of distress under wheel loads far exceeding factored loads specified by the codes (*1,6*). He further concluded that the major parameters affecting strength and stiffness are slab thickness, girder type, and girder spacing.

These results show that empirically designed isotropic decks with less steel possess adequate strengths higher than is conventionally predicted, but their long-term serviceability is subject to further examination. In general, service fatigue conditions of R/C bridge decks are much more severe than the laboratory environment in which most of these experimental studies were conducted. This is caused by thermal effects resulting from environmental temperature fluctuation, application of deicing chemicals, freeze-thaw cycling, damage cumulation caused by interaction of these deteriorating factors, and so forth. It is extremely difficult, if not impossible, to simulate these influencing factors in a laboratory. This paper presents a study partially sponsored by FHWA to examine long-term serviceability of full-scale isotropic deck slabs. It is intended to evaluate isotropic deck slabs based on their continuous in-service behavior.

SCOPE

Upon confirmation of previous research results regarding strength of isotropic decks, New York State experimented with an empirical isotropic deck design (*18*). Its cross section is shown with two rebar spacings—namely, 8 or 12 in. at centers with reinforcement ratios (of steel to effective cross section) of 0.36 and 0.24 percent, respectively (Figure 1). To take advantage of potential mass production of the reinforcing mat, the following provisions (*18*) applied:

1. A maximum girder spacing of 10 ft (i.e., a maximum ratio of girder spacing to deck thickness of 14.1) with no fewer than four girders.
2. Grade 60 steel with the top-mat epoxy coated,
3. Structural concrete Type E (water-cement ratio of 0.44; air content of 6.5 percent; slump, 3 to 4 in.; sand, 35.8 percent; and cement, 648 lb/yd^3) according to current New York State construction specifications (*24*),
4. Longitudinal bars parallel to girders and transverse bars parallel to the skew angle up to 30 degrees,

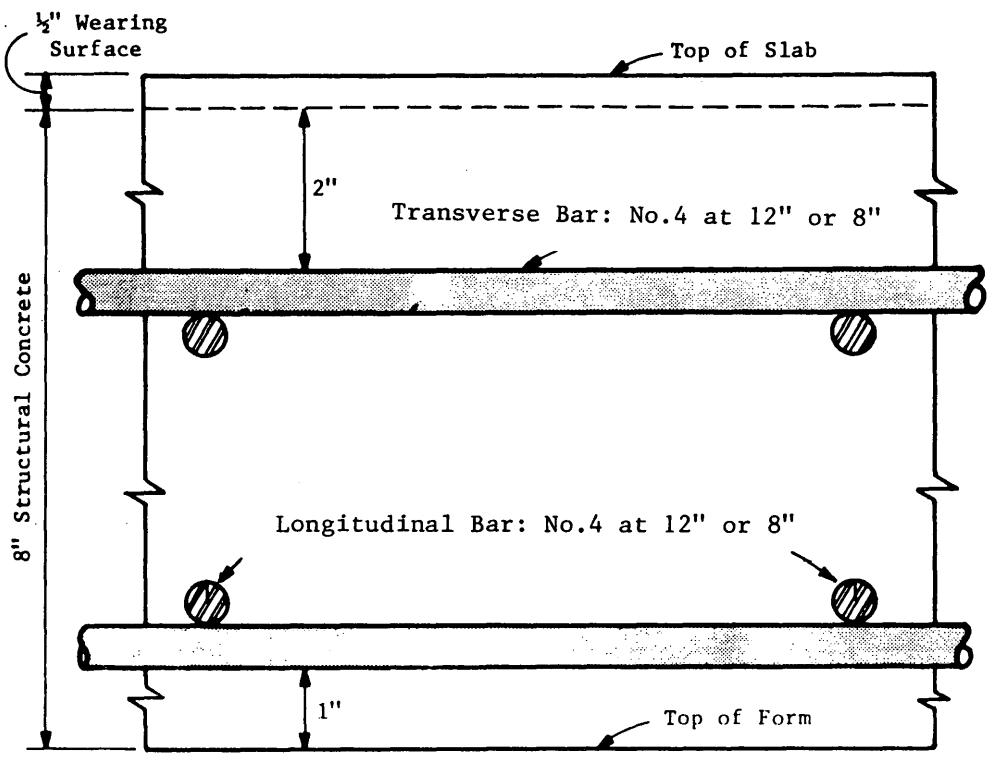

FIGURE 1 Standard cross section of isotropic decks in New York State.

5. Additional reinforcement for fascia overhang and negative moment areas according to the AASHTO specifications (*1*), and
6. Permissible metal stay-in-place forms according to New York State's current practice.

Since 1982, a total of 29 such isotropic decks have been constructed on bridges of multiple steel girders with diaphragms or cross bracings. Thirteen relatively older decks of the 29 are covered by the present study. Their locations are shown in Figure 2. Note that there are two bridges (sites) each at locations on Route 104 and the Hutchinson River Parkway. More details of the experimental isotropic decks are given in Table 1, including year built, average daily truck traffic, and structural features. As indicated in Table 1, 4 of the 13 bridges are instrumented with electrical resistance strain gauges.

Serviceability of concrete structural components refers to various aspects of their behavior under service conditions, such as deflection and stress level induced by service load, cracking behavior, and surface conditions affected by concrete cracking, spalling, and delamination. In this study, rebar stress levels under vehicular service load and surface conditions of the bridge decks were chosen for the serviceability evaluation. Stress level provides direct information on distress condition and available fatigue strength, and surface condition relates to corrosion probability with respect to accessibility of corrosive deicing chemicals to rebars. Deflection was not used as a criterion here because points of interest are not always accessible on a bridge in service without specially built equipment.

To obtain stress under wheel loads, the four instrumented experimental decks were load tested annually from construction until the present or until failure of aged strain gauges in the decks. Since 1986, when the oldest experimental deck (Site 1) had been in service for 4 years, the 13 experimental decks have been inspected annually to examine and record their surface condition with respect to serviceability.

LOAD TESTS AND REBAR STRESS UNDER SERVICE LOAD

Instrumentation and Load Test

Three types of load were applied to obtain deck rebar strain/stress under the AASHTO wheel load: (a) a single concentrated load distributed over an 8- × 20-in. plate by jacking a truck's rear axle (referred to as the simulated wheel load test); (b) a stationary vehicular wheel load at various longitudinal locations across the bridges (referred to as the static influence line test); and (c) a moving vehicular wheel load across the bridges at crawl speed (referred to as the dynamic influence line test). The wheel loads were applied along the centerline between two interior girders to produce maximum strain/stress in the instrumented rebars. Each loading was generally applied three times to produce replicates to eliminate possible instrumental error and accommodate unavoidable variations in vehicular loading. The simulated wheel load test was discontinued in 1987 because its results were regarded as having little value with respect to service load effects, considering the load's unrealistic distribution area and magnitude. Rebar strain readings in the static influence line test were recorded by a static data-acquisition system of 99 channels, whereas those in the dynamic influence line test used a dynamic data-acquisition system of eight channels at a speed

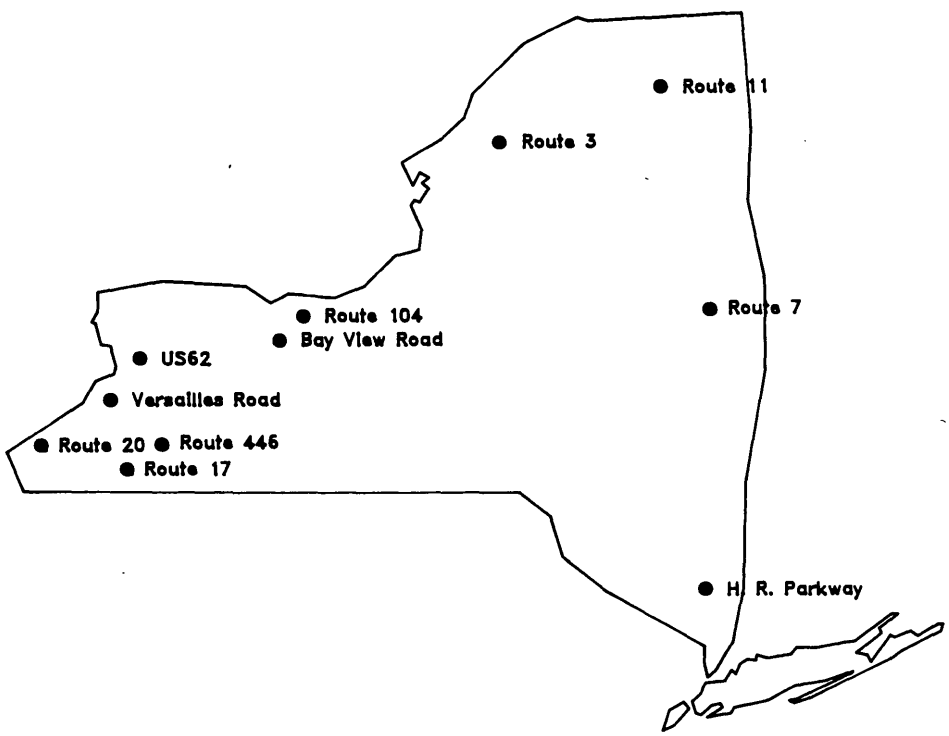

FIGURE 2 Locations of isotropic bridge decks in New York State.

TABLE 1 Background Data on New York State Isotropic Decks

Site	Location	Rebar Pattern[a]	Year Built	Truck Volume[b]	Skew, deg	Span Type	Span Length, ft	Girder Spacing
1a*	Bay View Rd	A	1982	NA	14	S	60,60,48,38	8'9"
1b*	Bay View Rd	12	1982	NA	14	S	60,38	8'9"
1c*	Bay View Rd	8	1982	NA	14	S	60,38	8'9"
2a*	Rte 7	A	1983	1300	50	S	131	10'0"
2b*	Rte 7	12	1983	1300	50	S	131	10'0"
2c*	Rte 7	8	1983	1300	50	S	131	10'0"
3*	Rte 20	12	1987	480	0	C	1030	9'10"
4	HR Parkway SB	12	1985	0	R	S	145	8'3"
5	HR Parkway NB	12	1986	0	R	S	144	8'0"
6	Rte 3	12	1986	280	12	S	176	10'0"
7	Rte 104 EB	12	1985	1050	8	S	150	9'0"
8	Rte 104 WB	12	1985	1050	8	S	150	9'0"
9	Rte 17	12	1986	1700	9	S	140	8'3"
10	US 62	12	1986	860	0	C	322	9'0"
11	Rte 446	12	1986	280	20	S	103	9'6"
12	Versailles Rd	12	1986	50	0	C	411	7'0"
13*	Rte 11	12	1988	470	0	C	756	9'0"

*Instrumented decks, R = skew varies because girder spacing varies from end to end, C = continuous, S = simple, NA = not available.

[a]A = AASHTO grid, 12 = 12x12 grid, 8 = 8x8 grid.

[b]Estimated annual daily truck traffic, from traffic volume reports of the Data Services Bureau, New York State Department of Transportation.

NOTES: Sites 1, 7, and 8 had removable forms. Sites 4, 5, 6, 9, 10, 11, and 12 have metal stay-in-place forms (SIPFs). Sites 3 and 13 have SIPFs with 0.2 and 0.1 percent, respectively, of the form area removed at gage locations. Site 2 has SIPFs, with 20 percent of the form area removed at the 12x12 grid gage location, 34 percent at the AASHTO grid gage location, and 17 percent at the 8x8 grid gage location.

of 25 samples per second. The dynamic influence line test was used to reduce test time, compared with the static influence line test. The two different influence line tests produced consistent results.

Figures 3 through 6 show instrumentation details for the four instrumented experimental decks, including types and locations of strain gauges. They were selected to monitor rebar strain/stress in critical areas. The instrumented bars are 4 to 6 ft long, including 15 in. at each end for overlapping with regular rebars. It is shown that Sites 1 and 2 have AASHTO orthotropic and the two isotropic (8- and 12-in. grid) reinforcement arrangements for behavior comparison. They are respectively referred to as Sites 1a, 1b, 1c, 2a, 2b, and 2c, as presented in Table 1.

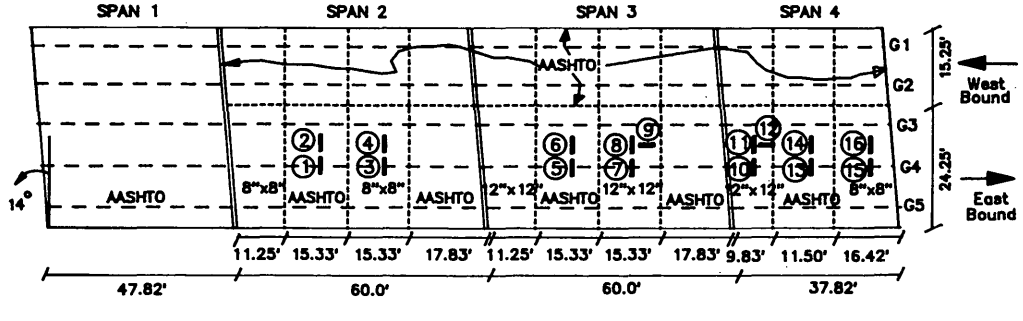

NOTES:

1. All spans are simply supported.
2. — = gage locations.
3. 16 four-arm strain gages of self-temperature compensating type for rebar uniaxial strain. Top transverse bars over girder G4: Nos. 1, 3, 5, 7, 10, 13, 15. Bottom transverse bars at center of interior bay: Nos. 2, 4, 6, 8, 11, 14, 16. Bottom longitudinal bars at center of interior bay: Nos. 9, 12.

FIGURE 3 Gauge locations at Site 1 (Bay View Road).

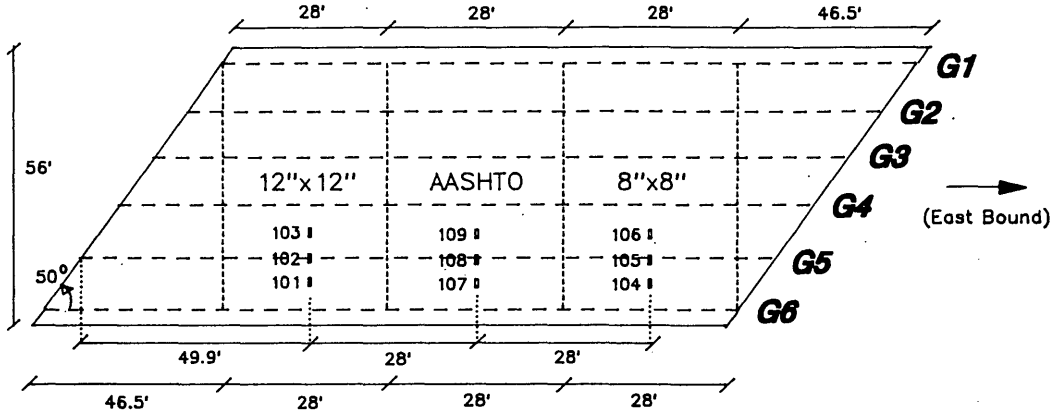

NOTES:

1. The span is simply supported.
2. ▮ = gage locations.
3. 9 four-arm strain gages of self-temperature compensating type for rebar uniaxial strain. Bottom transverse bars at center of fascia bay: Nos. 101, 104, 107. Top transverse bars over girder G5: Nos. 102, 105, 108. Bottom transverse bars at center of interior bay: Nos. 103, 106, 109.

FIGURE 4 Gauge locations at Site 2 (Route 7).

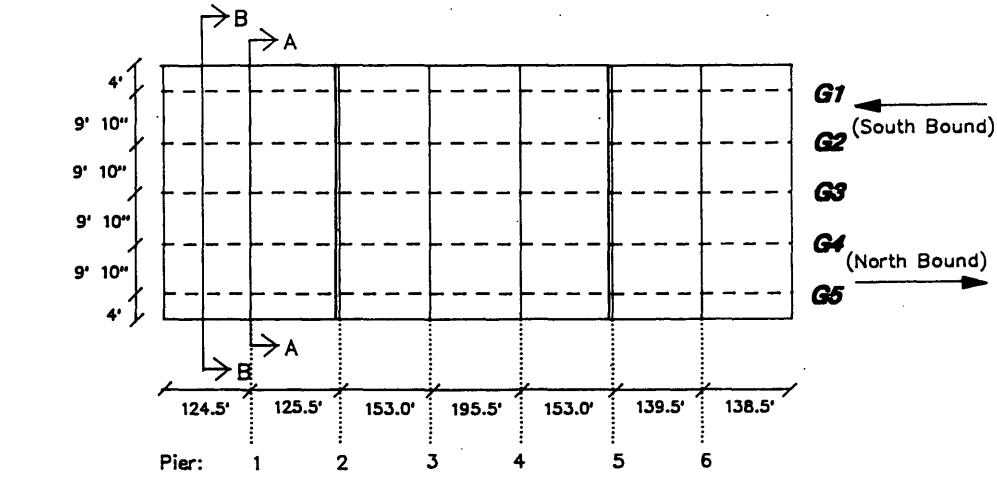

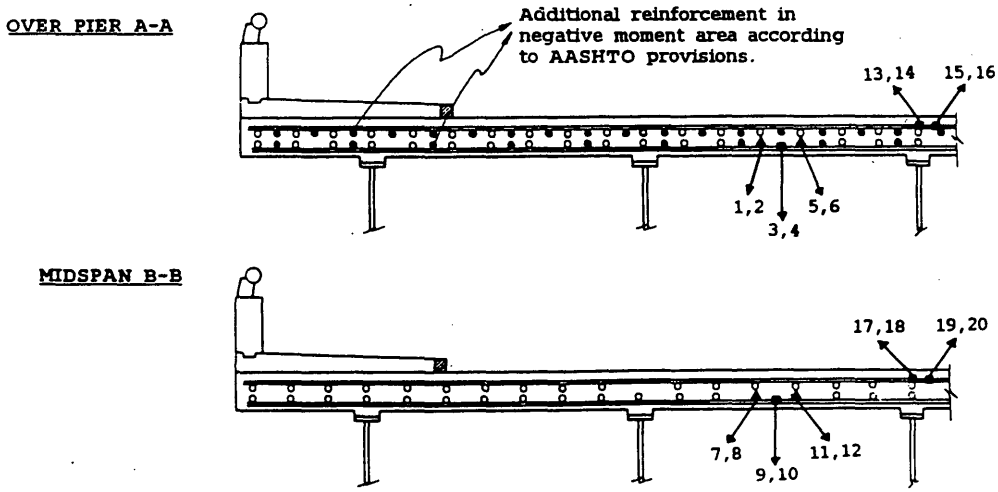

Notes:

■ Gage on Transverse Rebar
▲ Gage on Longitudinal Rebar
Total of 20 weldable single-arm strain gages of self-temperature compensating type. At each location, two gages on diametrically opposite sides of a rebar for uniaxial strain.

FIGURE 5 Gauge locations at Site 3 (Route 20).

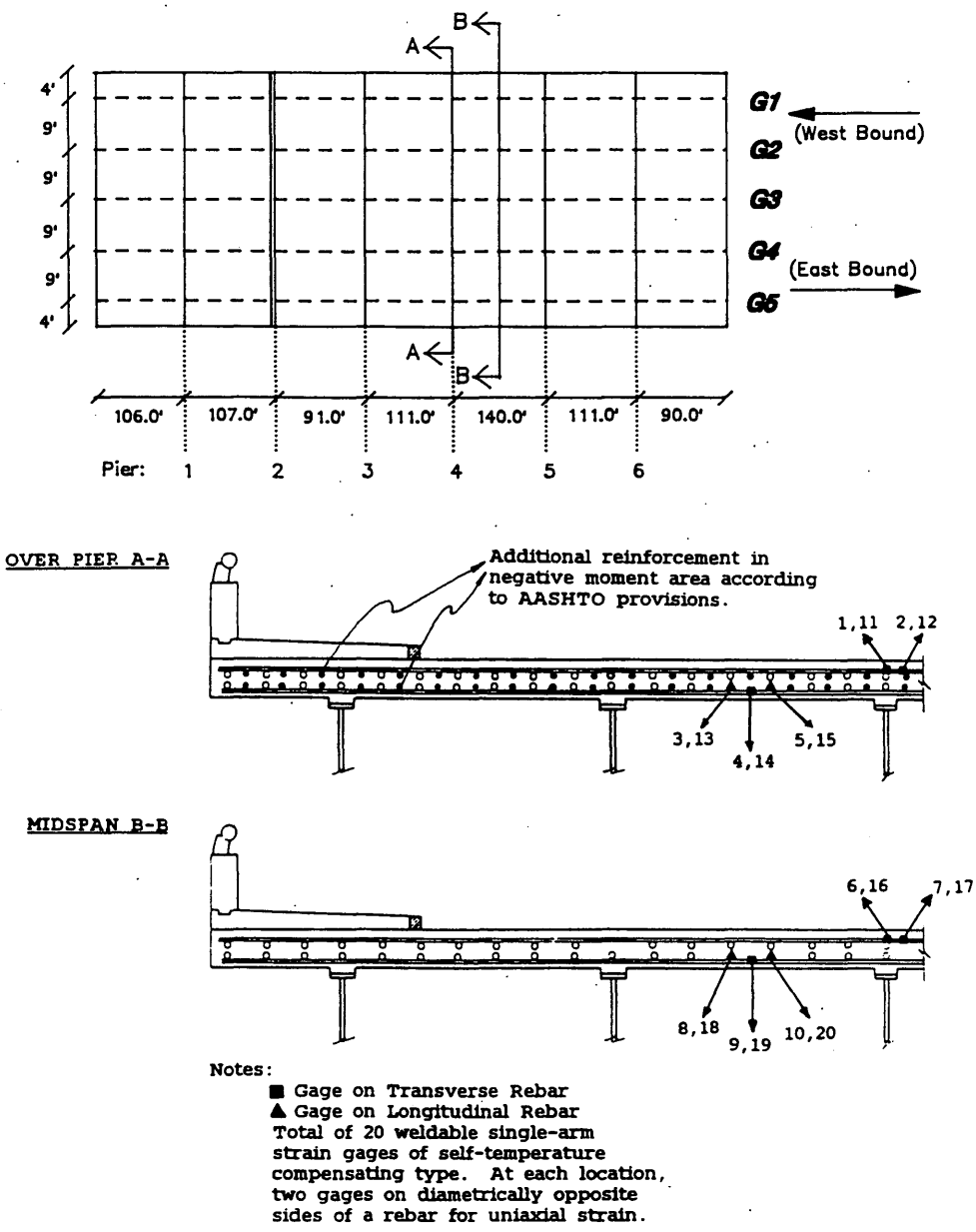

FIGURE 6 Gauge locations at Site 13 (Route 11).

Rebar Stress Under Service Load

Figure 7*a* and *b* shows typical rebar stress influence lines, obtained in a dynamic influence line load test at Site 3 (Route 20) in 1990. They show rebar stresses at sections of midspan and pier (Figure 5 shows more details of gauge locations). In the test a two-axle truck applied load, with front and rear axles of 15 and 30 kips, respectively, at a spacing of 15 ft. The truck was driven on the southbound side of the bridge, from Pier 2 to the south abutment, at a speed of about 10 mph. This section of the bridge is continuous over Pier 1 (Figure 5). The stresses obtained under the load were then linearly scaled to a vehicular load of 16-kip rear wheels. The abscissa in both figures is the distance from the front axle to the starting point near Pier 2. Figure 7*a* and *b* shows that the dynamic effects of the moving vehicle were minimized by the crawl speed. The figure also shows that rebar stresses consist of two components: global and local contributions. The local contribution is described by two sharp peaks induced by the front and rear wheels. The global one is demonstrated by curves of relatively lower slopes before and after the sharp peaks, which describe the deck's participation in load carrying as part of the bridge's cross section. In these two figures, the local effect in maximum rebar stresses is shown to be greater than the global effect.

In Figure 7*a*, stress of the bottom transverse bars (average of Gauges 9 and 10) at midspan section was contributed mainly by the global stress, except between distances of 170 and 210

ft. When the loading vehicle was on the adjacent span (between Piers 2 and 1), the bottom transverse bar at midspan was subjected to very low negative (compressive) stresses. This stress became positive (tensile) when the vehicle was on the gauged span (between Pier 1 and the south abutment). It is also shown in Figure 7*a* that the top transverse bars over an interior girder (Gauges 17 and 19) had much lower stresses than the bottom transverse one and yet experienced combined global and local effects. Rebar stresses at Gauges 7, 8, 11, 12, 18, and 20 are not shown here because of failure due to age, but previous results showed that their maximums were as negligibly low as about 0.64 ksi (*25*).

Figure 7*b* shows similar superposition of global and local effects of the vehicular wheel loads at the Pier 1 section indicated in Figure 5. It is seen that longitudinal bar stresses (Gauges 1, 5, and 6) were more localized than those of the transverse bars (Gauges 3 and 4), as indicated by the sharper peaks. Figure 7*b* also shows that the bottom longitudinal bars experienced higher stress than the bottom transverse bar. This stress was caused by the presence of a transverse crack on the top surface at the pier section. Without this crack, previous stress data showed that the opposite was true (*25*). Nevertheless, the highest stress shown in Figure 7*a* and *b* is lower than 3 ksi, apparently far below an allowable level.

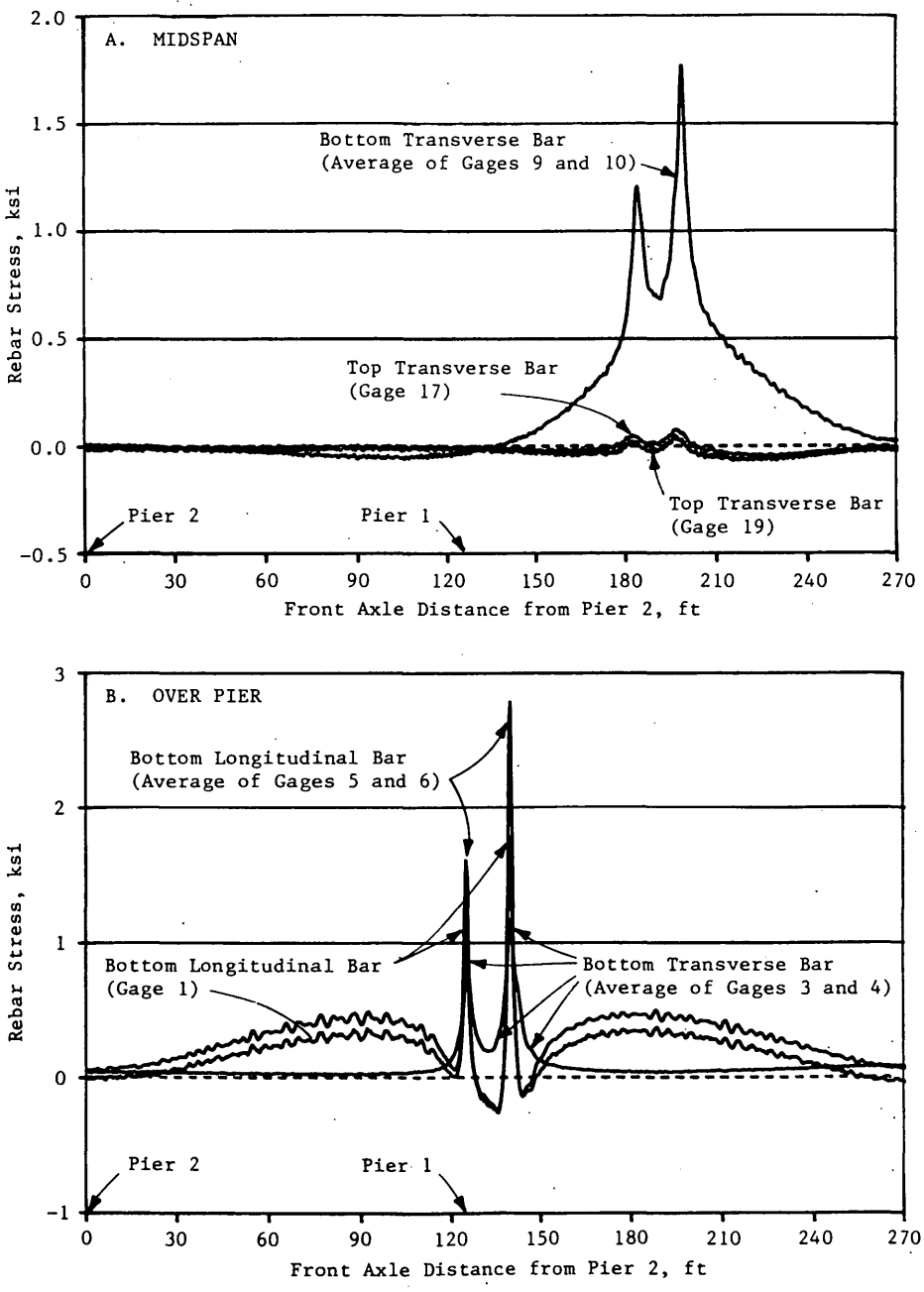

FIGURE 7 Site 3 influence lines under vehicular 16-kip rear wheel load.

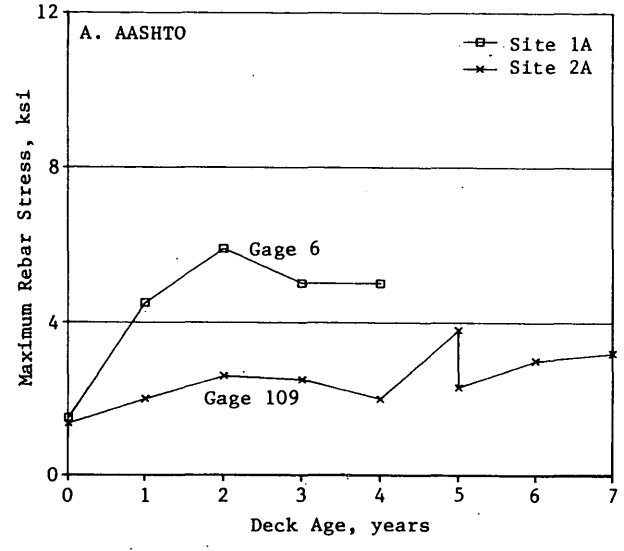

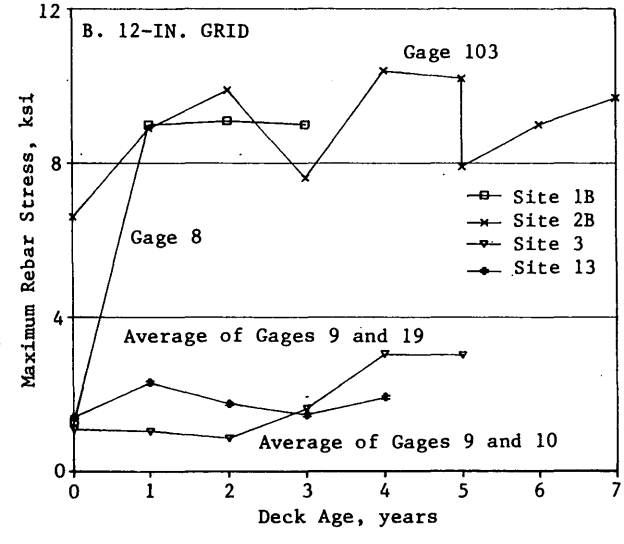

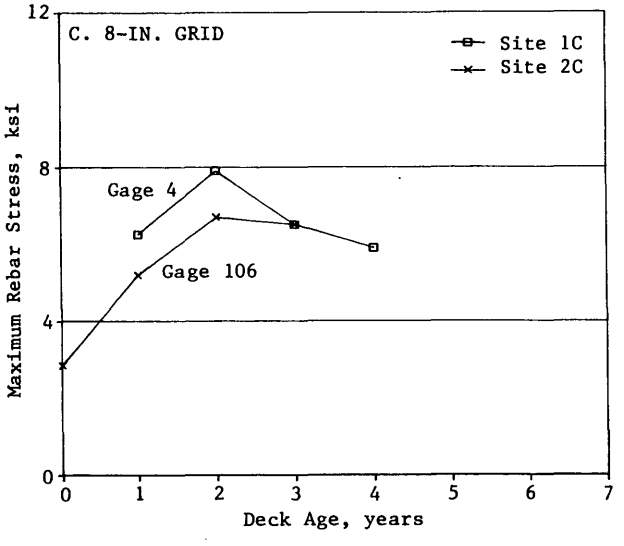

FIGURE 8 Maximum rebar stresses on bottom transverse bar under 16-kip wheel load.

TABLE 2 Comparison of Isotropic Deck Rebar Stresses

	12x12 Grid				8x8 Grid	
Live-Load Stress, ksi	Site 1b	Site 2b	Site 3	Site 13	Site 1c	Site 2c
Allowable[a]	14.3	12.9	14.6	14.6	15.7	14.8
Measured[b]	9.1	10.4	1.6	2.3	7.9	6.7

[a]Allowable live-load stress = (24 ksi - dead-load stress)/1.3.
[b]Measured live-load stress = maximum stress under vehicular 16-kip wheel load obtained in the load tests.

Stress at Gauges 2, 13, 14, 15, and 16 was not obtained in the 1990 test because of their failure. It is noted that by 1990 this deck had been in service for 4 years. Previous rebar stresses were lower than those presented in Figure 7*a* and *b*.

Figure 8*a*, *b*, and *c* demonstrates evolution of maximal stresses in bottom transverse bars with deck age, for the three reinforcement arrangements. Comparison of these curves shows that the 12-in. grid experienced higher stress than the other two patterns of reinforcement at Sites 1 and 2. This is expected since less steel was used in the 12-in. grid. It is noted that, at a deck age of 5 years, two tests were performed in Site 2 (Route 7), and two stress readings were recorded in Figure 8*a* and *b*. These different readings characterize variation of the stress results over deck age as shown in these figures. This variation is attributed to several factors: uncertainty in paths of the loading vehicle, possible nonlinearity in deck load-response relationship under various levels of applied loads, and/or possible electrical noise influencing data recording. This variation is unavoidable in a field-testing environment and is not a cause for concern. Despite the variation, a clear tendency is observed in Figure 8*a* through *c* that rebar stresses increased in the first year or two of service and remained relatively constant thereafter, regardless of reinforcement arrangements.

The global maximum stresses of 12-in. and 8-in. grid decks shown in Figure 8*b* and *c* are listed in Table 2. Using a simplified model of transversely continuous beam and the AASHTO allowable stress method (*1*), dead-load stresses in the transverse rebar were found for the instrumented decks, under a uniformly distributed dead load of 142 lb/ft^2 (accounting for weights of the deck, stay-in-place forms, and future overlay). Allowable live-load rebar stresses are computed as the differences between a total allowable stress of 24 ksi for Grade 60 steel and the dead-load stresses, with the maximum impact factor 1.3 by the AASHTO code considered conservatively. These are also listed in Table 2 for comparison. On the basis of the conservative analyses, measured maximal stresses are all lower than allowable levels for the two isotropic reinforcement arrangements.

GENERAL INSPECTION

Since 1986, the 13 experimental isotropic decks have been inspected for possible deterioration affecting serviceability.

They are examined for cracking, spalling, and delamination by visual and sonic (chain-drag) methods. Both top and bottom deck surfaces are inspected. No spalling or delamination have been observed. Generally, cracking is judged to be minor and the decks have performed satisfactorily (*26*).

At Sites 1 and 2, a few bottom transverse cracks highlighted by efflorescence are seen from the ground. These cracks appear in similar intensities in all sections regardless of reinforcement (AASHTO, 12-in. or 8-in. grids). Sites 7 and 8 have more intensive bottom transverse and longitudinal cracks, which are highly visible. These two sites will be discussed further, along with top surface inspection data. These four are the only bridges among the 13 addressed here with forms either completely or partially removed so that their bottom surface could be inspected. Top surface cracking at all the sites will also be discussed in more detail.

Cracking on upper deck surface is classified in three types according to direction of extension: transverse, longitudinal, or diagonal. Transverse cracks are defined as perpendicular to traffic flow and longitudinal as parallel to traffic flow. All others are noted as diagonal. Examination and recording of cold-joint cracking at the ends of concrete pours were discontinued in 1989, because this was considered unavoidable and irrelevant to reinforcement arrangement. Crack density, defined as crack length per unit area (inches per square yard), is used for quantitative measurement of cracking severity.

Transverse cracking was predominant and longitudinal much less frequent (64 and 32 percent, respectively, in 1990). Figure 9 relates total crack densities for individual decks to age. Top surface cracking generally increases with age in both isotropic and AASHTO decks. Note, however, that crack densities actually decreased with age once for Sites 2a, 6, and 13, apparently because of either inexperience of the inspectors or reduction of crack visibility by less moisture near the deck surface at inspection time. Since most observed cracks are hairline or narrower, these two factors did affect inspection results for crack density. Although Sites 1, 7, and 8 have relatively higher crack densities, the decks are generally performing satisfactorily.

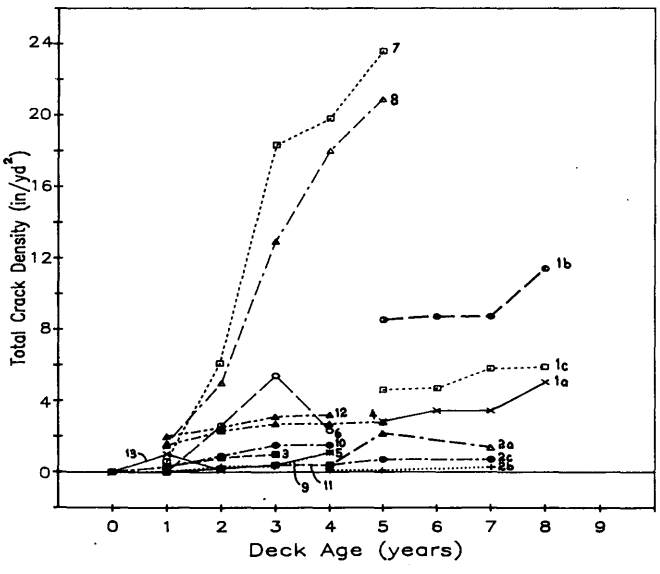

FIGURE 9 Total crack densities on top surface of experimental decks.

Site 1 experienced the third highest crack density (Figure 9). Note that this bridge was subjected to the simulated wheel loads in early tests of as high as 30 kips over an 8- × 20-in. area. Most cracks observed here are near loading plate areas.

Figure 9 also shows that Sites 7 and 8 experienced the highest crack densities; 65 and 62 percent are transverse, and 31 and 36 percent longitudinal, respectively. These two bridges were constructed simultaneously by the same contractor in 1985. A special investigation attempted to identify causes of this relatively severe cracking. Two cores were taken in 1990 from Site 7 (Route 104 eastbound). Core 1 was at an intersection of longitudinal and diagonal cracks (also of longitudinal and transverse bars), and Core 2 over a longitudinal crack (also over a longitudinal bar) along the centerline between two interior girders. Epoxy coating of top bars in both cores was found to be intact; no corrosion was observed. In Core 1, the crack extended from the top surface about one-quarter into the deck's depth. Multiple aggregate fractures were found in Core 2, with a crack penetrating its full depth; this indicates that the longitudinal cracking was load related and occurred after the concrete developed its strength. Early concrete strengths at both sites were also found to have been sought by the contractor for early opening of the bridges. Generally this is done for the contractor's convenience for moving heavy construction equipment. Such movements may have caused the observed longitudinal cracks. Construction records also show that at each site two of eight tested slumps exceeded the maximum specified allowable level (*24*). Higher slump may cause more transverse cracking due to more severe concrete shrinkage. It was concluded that higher crack densities at Sites 7 and 8 were caused mainly by improper construction procedures and possible overloading.

In an investigation of North Carolina's AASHTO R/C decks (*27*), 72 bridges were inspected solely to determine the severity of transverse cracking. Of these, 15 were multiple-steel-girder bridges in a service age range comparable with that of New York's experimental decks, with results used here for comparison. Crack severity in that study was defined as a weighted number of cracks per unit of longitudinal length [cracks per linear foot (CLF)] equal to the total number of major transverse cracks plus 0.25 total number of minor transverse cracks per span length. Major cracks were defined as those propagating from at least one edge of the pavement to the roadway centerline, and minor, as shorter cracks. New York's crack density data were then converted to CLF values. In Table 3, New York's 12-in. grid isotropic decks and North Carolina's AASHTO decks are compared. This comparison shows that the highest AASHTO deck CLF is 0.266 versus 0.247 for the isotropic decks. Excluding the abnormal cases (Sites 7 and 8 in New York and 64-32-045E in North Carolina), average CLFs for the isotropic and AASHTO decks are 0.030 and 0.031, respectively. Their standard deviations are also equivalent (Table 3). Table 3 shows that transverse cracking severities of the isotropic and the AASHTO decks are generally equivalent.

TABLE 3 Comparison of Transverse Cracking

New York 12x12 Isotropic Decks				North Carolina AASHTO Decks		
Site	Location	Age, years	CLF*	Bridge	Age, years	CLF*
1	Bay View Rd	8	0.114	1835-44-088	3	0.000
2	Rte 7	7	0.007	231-32-020	9	0.000
3	Rte 20	3	0.014	53-44-015	3	0.000
4	HR Parkway SB	5	0.062	264-40-010	9	0.000
5	HR Parkway NB	4	0.026	64B-32-010	5	0.000
6	Rte 3	4	0.004	95-44-083N	3	0.026
7	Rte 104 EB	5	0.247	64B-32-010	5	0.013
8	Rte 104 WB	5	0.200	264-40-010	9	0.055
9	Rte 17	4	0.018	1655-40-060	3	0.008
10	US 62	4	0.021	8-60-030	1	0.053
11	Rte 446	4	0.000	95-44-083N	3	0.075
12	Versailles Rd	4	0.063	64-32-045E	4	0.266
13	Rte 11	2	0.001	85-60-100N	4	0.104
				85-60-090N	5	0.055
				220-55-012N	4	0.041
Mean**			0.030	Mean***		0.031
Standard Deviation**			0.036	Standard Deviation***		0.034

*CLF = cracks per linear foot = (total major transverse cracks + total minor transverse cracks/4)/span length.
**Excluding Sites 7 and 8.
***Excluding Site 64-32-045E.

CONCLUSIONS

The strength of empirically designed isotropic decks has been verified in previous research as adequate for current wheel loading. Their long-term serviceability, when subjected to severe service fatigue conditions remains an issue to be addressed. Thirteen experimental isotropic decks in New York State have been examined periodically by both load test and general inspection over their service lives, with the longest open for 8 years. No spalling or delamination has been found and cracking is judged to be minor. Isotropic decks experienced crack severity comparable with that of AASHTO decks. Maximum rebar stresses in the isotropic decks under the AASHTO wheel load of 16 kips are always lower than allowable levels on the basis of conservative analyses. Transverse cracking severity of the isotropic and AASHTO decks is found to be equivalent. Maximal transverse rebar stresses under the 16-kip wheel load increased for the first year or two of service and remained relatively constant thereafter, regardless of reinforcement patterns.

ACKNOWLEDGMENTS

The study presented here was partially supported by FHWA. The assistance and cooperation of New York State Department of Transportation personnel over the years are gratefully appreciated. Discussions with D. B. Beal and M. J. Loftus were particularly useful.

REFERENCES

1. *Standard Specifications for Highway Bridges*, 13th ed. AASHTO, Washington, D.C., 1983.
2. B. E. Hewitt. *An Investigation of the Punching Strength of Restrained Slabs with Particular Reference to the Deck Slabs of Composite I-Beam Bridges*. Ph.D. dissertation. Queen's University at Kingston, Ontario, Canada, March 1972.
3. B. E. Hewitt and B. deV. Batchelor. Punching Shear Strength of Restrained Slabs. *Journal of the Structural Division*, ASCE, Vol. 101, No. 9, 1975, pp. 1837–1853.
4. B. deV. Batchelor, B. E. Hewitt, and P. Csagoly. An Investigation of the Fatigue Strength of Deck Slabs of Composite Steel/Concrete Bridges. In *Transportation Research Record 664*, TRB, National Research Council, Washington, D.C., 1978, pp. 153–161.
5. B. deV. Batchelor, B. E. Hewitt, P. Csagoly, and M. Holowka. Investigation of the Ultimate Strength of Deck Slabs of Composite Steel/Concrete Bridges. In *Transportation Research Record 664*, TRB, National Research Council, Washington, D.C., 1978, pp. 162–170.
6. *Ontario Highway Bridge Design Code*, 2nd ed. Ministry of Transportation and Communications, Downsview, Ontario, Canada, 1983.
7. C. A. Turner. Advance in Reinforced-Concrete Construction: An Argument for Multiple-Way Reinforcement in Floor-Slabs. *Engineering News*, Vol. 6, No. 7, 1909, pp. 178–181.
8. I.-K. Fang. *Behavior of Ontario-Type Bridge Deck on Steel Girders*. Ph.D. thesis. University of Texas at Austin, 1985.
9. I.-K. Fang, J. Worley, N. H. Burns, and R. E. Klingner. Behavior of Isotropic R/C Bridge Decks on Steel Girders. *Journal of Structural Engineering*, ASCE, Vol. 116, No. 3, 1990, pp. 659–678.
10. P. C. Perdikaris and S. Beim. RC Bridge Decks under Pulsating and Moving Load. *Journal of Structural Engineering*, ASCE, Vol. 114, No. 3, 1988, pp. 591–607.
11. P. C. Perdikaris and S. Beim. *Design of Concrete Bridge Decks*. Report FHWA/OH-88/004. Department of Civil Engineering, Case Western Reserve University, Cleveland, Ohio, 1988.
12. J. A. Puckett, J. D. Lohrer, and R. D. Naiknavare. *Evaluation of Bridge Deck Utilizing Ontario Bridge Deck Design Method: Instrumentation and Testing of Two Reinforced Concrete Bridge Decks*, Vol. 2. Report FHWA/WY-89-002. Department of Civil Engineering, University of Wyoming, Laramie, and Wyoming Highway Department, July 1989.

13. P. A. Jackson and R. J. Cope. The Behavior of Bridge Deck Slabs under Full Global Load. In *Developments in Short and Medium Span Bridge Engineering '90* (B. Bakht, R. A. Dorton, and L. G. Jaeger, eds.), Toronto, Ontario, Canada, 1990, Vol. 1, pp. 253–265.
14. P. Y. Tong and B. deV. Batchelor. Compressive Membrane Enhancement in Two-way Bridge Slabs. In *Cracking, Deflection, and Ultimate Load of Concrete Slab System* (E. G. Nawy, ed.), ACI Special Publication SP-30, Paper SP30-12. American Concrete Institute, 1971, pp. 271–286.
15. M. Holowka. *Testing of a Trapezoidal Box Girder Bridge*. Report RR221. Ministry of Transportation and Communications, Downsview, Ontario, Canada, Nov. 1979.
16. M. Holowka and P. Csagoly. *Testing of a Composite Prestressed Concrete AASHTO Girder Bridge*. Report RR222. Ontario Ministry of Transportation and Communication, July 1980.
17. D. B. Beal. Load Capacity of Concrete Bridge Decks. *ASCE Journal of Structural Division*, ASCE, Vol. 108, No. 4, 1982, pp. 814–832.
18. D. B. Beal. *Reinforcement for Concrete Bridge Decks*. Research Report 105. Engineering Research and Development Bureau, New York State Department of Transportation, July 1983.
19. J. A. Puckett, R. D. Naiknavare, and J. D. Lohrer. *Evaluation of Bridge Deck Utilizing Ontario Bridge Deck Design Method: Review of Experimental and Analytical Research in Lightly Reinforced Bridge Decks*, Vol. 1. Report FHWA-WY-89-002. Department of Civil Engineering, University of Wyoming, Laramie, and Wyoming Highway Department, July 1989.
20. B. deV. Batchelor and B. E. Hewitt. Are Composite Bridge Slabs Too Conservatively Designed?—Fatigue Studies. In *Fatigue of Concrete*. ACI Special Publication SP41, Paper SP41-15. American Concrete Institute, 1974, pp. 331–346.
21. K. Okada, H. Okamura, and K. Sonoda. Fatigue Failure Mechanism of Reinforced Concrete Bridge Deck Slabs. In *Transportation Research Record 664*, TRB, National Research Council, Washington, D.C., 1978, pp. 136–144.
22. K. Sonoda and T. Horikawa. Fatigue Strength of Reinforced Concrete Slabs Under Moving Loads. *Proc., IABSE Colloquium, Fatigue of Steel and Concrete Structures*, Lausanne, Switzerland, Vol. 37, 1982, pp. 455–462.
23. A. C. Agarwal. Load Testing of New Concrete Bridge Deck Slabs. In *Developments in Short and Medium Span Bridge Engineering '90* (B. Bakht, R. A. Dorton, and L. G. Jaeger, eds.), Toronto, Ontario, Canada, 1990, Vol. 1, pp. 277–289.
24. *Standard Specifications: Construction and Materials*. New York State Department of Transportation, Albany, Jan. 1985.
25. S. Alampalli and G. Fu. *Influence Line Tests of Isotropically Reinforced Bridge Deck Slabs*. Client Report 54. Engineering Research and Development Bureau, New York State Department of Transportation, Sept. 1991.
26. F. P. Pezze and G. Fu. *1990 Visual Inspection of Isotropic Bridge Decks*. Client Report 51. Engineering Research and Development Bureau, New York State Department of Transportation, May 1991.
27. G. R. Perfetti, D. W. Johnston, and W. L. Bingham. *Incidence Assessment of Transverse Cracking in Concrete Bridge Decks: Structural Considerations*. Vol. II. Report FHWA/NC/85-002. Center for Transportation Engineering Studies, North Carolina State University at Raleigh, June 1985.

Publication of this paper sponsored by Committee on General Structures.

Permeability Evaluation of Concrete Bridge Structures Exposed to Marine Environment in Florida

CONSTANTINE A. MELETIOU AND MANG TIA

A field permeability test (FPT) apparatus and method were developed and evaluated in both the laboratory and the field. The developed prototype FPT apparatus and method were used in the testing and evaluation of in-service marine structures in conjunction with other standard tests. The developed FPT apparatus and method appear promising in providing a suitable measuring system for the rapid, convenient, and reliable determination of the in situ water permeability of structural concrete. There appears to be a linear relationship between the charge (in coulombs) passed through a concrete material as measured by the rapid chloride permeability test (AASHTO T277-83) and its corresponding water permeability, with a coefficient of determination, R^2, of 0.90. There was an apparent relationship between permeability and durability of concrete in service. The concrete material that exhibited durability problems also demonstrated high permeability. The FPT method was demonstrated to be able to provide a relative measurement of permeability that can be used as an indication of the quality and performance characteristics of structural concrete.

Long-term durability of concrete structures in a marine environment has been a great concern to civil engineers in recent years as an increasing number of cases of premature deterioration of such structures have been reported throughout the country and the world. To ensure long-term durability of concrete structures, attention must be given to the quality of the concrete material with regard to those factors that may affect its performance under the given exposure conditions.

Concrete exposed to a marine environment may deteriorate as a result of the combined action of chemical and physical forces. These include chemical action of seawater constituents on the cement hydration products, alkali-aggregate expansion, crystallization pressure of salts within the concrete matrix, frost action in cold climates, corrosion of embedded steel in reinforced or prestressed members, and physical erosion due to wave action and floating objects. Attacks on concrete tend to increase the concrete permeability, which in turn makes the concrete material progressively more susceptible to further action by the same destructive agents, as well as to other types of attack (*1*).

Permeability has been regarded by experts in the field to be a fundamental material property governing the durability of concrete, particularly in structures exposed to a marine environment (*2,3*). Mehta (*2*) reviewed the case histories of several concrete structures that had exhibited deterioration after long-term exposure to seawater. These case histories clearly showed that although physical and chemical interactions between seawater and constituents of portland cement took place, serious deterioration did not occur unless seawater was able to penetrate the interior of the concrete. The author concluded that "permeability rather than the chemistry of concrete was thus identified as the most important factor in long-term durability" (*3*). The author pointed out that structural cracking does not lead to corrosion as long as the remaining concrete is impermeable, especially if the concrete is fully submerged. Mehta also stated in his conclusions that harmful chemical attack can be limited to the surface by rigorous implementation of well-known measures to ensure low permeability of concrete.

Since the durability of concrete in a marine structure is greatly affected by its permeability, it is logical that the permeability of the in-service concrete should be used to assess its durability. However, currently there is no convenient and effective method that can be used for this purpose. There is a great need to develop such a method. This paper presents the research work conducted at the University of Florida to address this area of need.

OBJECTIVES OF THE STUDY

The primary objectives of this research study were the following:

1. To develop a field permeability test (FPT) apparatus and method for reliably and conveniently determining the permeability of in-service concrete;
2. To test and evaluate the developed FPT apparatus and method and establish, through laboratory and field experimentation, an effective and efficient testing procedure;
3. To implement the FPT apparatus and method in the testing of existing marine structures to determine the in situ permeability of concrete under actual field conditions; and
4. To investigate and attempt to establish any relationships that may exist between the results of the rapid chloride permeability tests and the results of the FPTs.

The development and evaluation of the FPT apparatus and method as stated in Objectives 1 and 2 have been presented in detail previously (*4*); therefore, they will be only briefly summarized in this paper. The work pertaining to Objectives 3 and 4 is presented in greater detail.

Department of Civil Engineering, University of Florida, Gainesville, Fl. 32611.

RESEARCH METHODOLOGY AND TESTING PROGRAM

The testing and analysis program of this study include the following major tasks:

1. The developed prototype FPT apparatus was tested in both the laboratory and actual field installations to evaluate its performance characteristics, to ensure that it is operating properly and satisfactorily, and to establish an effective testing procedure.
2. FPTs were run at various locations on in-service concrete bridges situated at or near the coast of Florida. In situ measurements of moisture content of the tested concrete were also made. Relevant design and construction information on the tested structures were obtained, when available.
3. Rapid chloride permeability tests were performed on concrete samples that were cored from selected test locations.
4. A comparative analysis of the experimental data obtained from the field and laboratory tests was performed to establish possible relationships among the results from the various tests.

FIELD TESTING PROGRAM

Selected Concrete Bridge Structures

In-service marine concrete structures, mainly bridges that are located at or near the coastal regions of Florida, are classified as being exposed to extremely aggressive or highly corrosive environments and thus were targeted for testing for a "worst-case scenario." The selection of these structures was primarily based on current needs and accessibility of the test sites. An attempt was made to test a variety of bridge types ranging from high-profile monumental bridge structures to small highway bridges. This variety offered the opportunity to test and evaluate concrete bridge structures of various ages, designs, and functions and utilizing various materials and construction methods. The following 13 concrete bridge structures in Florida were selected and tested: in the Florida Keys, Seven-Mile Bridge, Long Key Bridge, Bahia Honda-Southbound Bridge, Bahia Honda-Northbound Bridge, Spanish Harbor Bridge, Niles Channel Bridge, and Niles Channel Old Bridge; B. B. McCormick Bridge, Jacksonville; SR-206 Bridge, Crescent Beach; Seabreeze Causeway Bridge, Daytona Beach; Broward River (SR-105) Bridge, Jacksonville; Horse Creek Bridge and Horse Creek Old Bridge, Melbourne.

Six of these bridges are located on the Florida Atlantic Intracoastal Waterway (FAIW), whereas the other seven are located in the Florida Keys. The majority of these bridges were designed for a service life of 50 years, although the Seven-Mile and the Long Key bridges were designed for a life of 75 years.

A Florida Class IV concrete, specified to have a maximum allowable water–cement ratio of 0.41, and epoxy-coated reinforcing steel bars were used in the construction of the Seven-Mile, Long Key, and Niles Channel bridges. Cathodic protection(CP) systems were installed on a total of 20 pile columns of the B. B. McCormick Bridge and on the east-end pile caps (footers) of the SR-206 bridge. Conductive coating was applied to 60 piles and conductive concrete applied to 10 piles of the Seabreeze Causeway Bridge; conductive coating was also applied to the underdecking beams and end walls of the Horse Creek Bridge and to approximately 45 piles of the Broward River Bridge. The majority of these CP systems were installed and energized after concrete deterioration was detected and were used as remedial systems to reduce further corrosion.

Figures 1 and 2 show the extent and severity of concrete deterioration of some of the in-service concrete bridge structures tested in this study. Concrete cracking due to corrosion of the embedded steel reinforcement and subsequent spalling of concrete cover is the most predominant type of concrete deterioration encountered in marine concrete bridge structures in Florida. Figure 1 shows a severely deteriorated pile from the B. B. McCormick Bridge substructure located on the FAIW in Jacksonville. Extensive vertical cracking of concrete is seen from the steel corrosion. The corrosion of the embedded steel reinforcement in the pile is in an advanced state and the steel can readily be seen through the gap created in the material because of localized loss of concrete cover. This is a typical pattern of concrete distress that is demonstrated in the form of continuous vertical cracking running parallel to the edge of the pile and extending several feet above the high-tide level into the splash zone. The tidal zone,

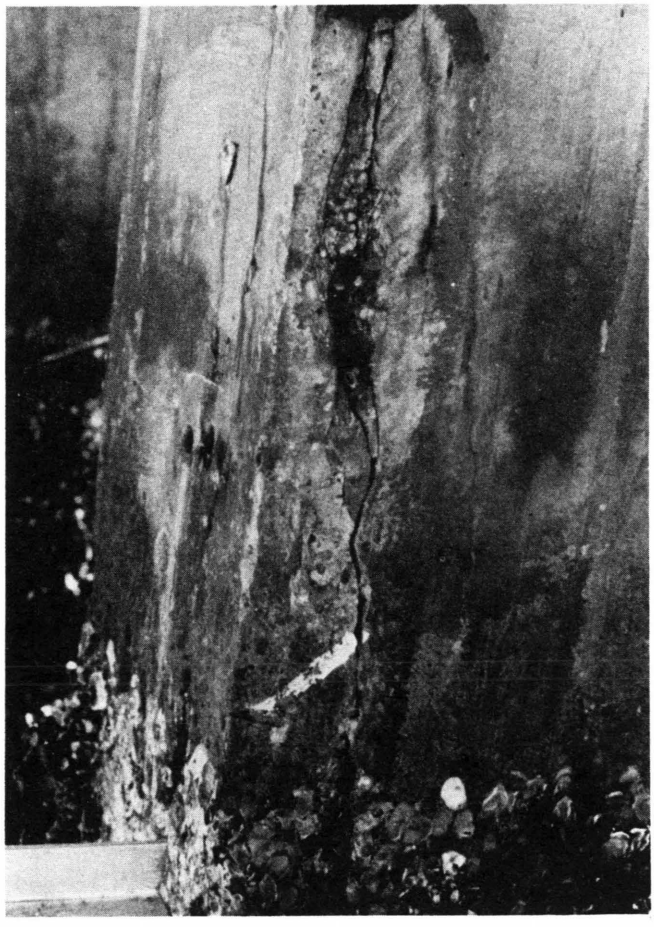

FIGURE 1 Excessive vertical cracking and spalling of concrete in a pile (B. B. McCormick Bridge, Jacksonville).

defined as the region between the low- and high-tide levels, can easily be identified by the existence of various formations of marine organisms that extend to the high-tide level, above which the splash zone begins.

The extent and severity of concrete deterioration of in-service bridge structures in Florida are clearly manifested in Figure 2, which shows a massive structural element of the Seven-Mile Bridge substructure located in the Florida Keys, which is considered to be an extremely aggressive (highly corrosive) environment. Corrosion of the embedded steel reinforcement in this case is in the most advanced state in which decomposition of the material and disbondment from the surrounding concrete are accompanied by a complete loss of concrete cover, which in turn can lead to severe structural damage. In this particular pier, the concrete deterioration extends to about 9 ft above the tidal zone. This is contrary to the general observation that the most severe deterioration is likely to take place in the tidal zone where the concrete is exposed to various types of physical and chemical forces. As demonstrated in Figure 2, concrete deterioration caused by corrosion or other chemical and physical attacks is not a phenomenon that is encountered only in the tidal zone and that can readily be repaired or treated locally; it is a more extensive problem that has the potential to cause severe structural damage.

FIGURE 2 Excessive steel corrosion and extensive concrete spalling in a pier (Seven-Mile Bridge, Florida Keys).

Field Permeability Tests

The field testing operations included (a) site selection, (b) preparation of test location, (c) determination of size and location of the embedded reinforcing steel, (d) coring of test holes for FPT, (e) extraction of concrete cored samples for chloride permeability testing, (f) determination of moisture content of site concrete, (g) performance of FPTs, and (h) patching of cored concrete.

In situ permeability tests were performed on the selected concrete bridges using the developed FPT apparatus (*4*,*5*). FPTs were performed on structural elements such as partially submerged piling, pile columns, piers, pile caps, footers, bascules, and so forth, at various locations, elevations, and orientations. The majority of the structural elements tested were part of the substructure of these concrete bridges and were accessible only by water. Therefore, the flow measurements for the in situ permeability tests were taken remotely by means of the FPT instrumentation unit that was carried on and operated from a boat.

In situ permeability tests were run at several locations on the bridge substructures. Tests were run on the undeteriorated portion of a generally deteriorated element. Thus, the tested concrete was representative of the concrete material of the member. The surface of in situ concrete at the prepared test sections was cleaned of any marine organisms or other irregularities if the selected test location was within the tidal or splash zone. The FPTs were performed by inserting the FPT probe in a ⅞-in.-diameter, 6-in.-deep hole drilled perpendicular to the concrete surface, sealing off the middle section of the test hole by means of the double-packer mechanism of the probe, and applying high pressure (150 to 500 lb/in.^{2} of gravity) to force the water to permeate radially into the concrete mass, as shown in Figure 3. The rate of flow of water into the test section (i.e., the injection rate) was constantly monitored by a manometer attached to the FPT instrumentation unit, which also contained the central control panel with the appropriate hydraulic quick-connections, flow valves, pressure regulator, and test gauge. Flow measurements were taken at regular intervals for as long as it was required to

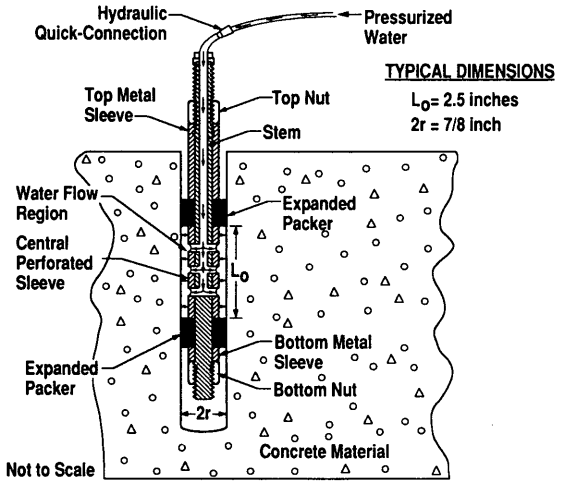

FIGURE 3 Schematic diagram of the FPT probe and setup.

reach a steady-state flow rate condition. The apparent coefficient of permeability of the concrete was determined from the steady-state flow rate by means of the following equations:

$$K = \frac{Q}{2\pi L_0 h} \sinh^{-1}\left(\frac{L_0}{2r}\right) \quad \text{for } r \leq L_0 < 10r \tag{1}$$

or

$$K = \frac{Q}{2\pi L_0 h} \ln\left(\frac{L_0}{r}\right) \quad \text{for } L_0 \geq 10r \tag{2}$$

where

K = coefficient of permeability (in./sec or cm/sec);
Q = steady-state flow (in.^{3}/sec or cm^3/sec);
h = applied pressure head (in. or cm);
$2r$ = diameter of test hole (in. or cm); and
L_0 = length of test section [in. or cm (see Figure 3)].

The derivation of Equations 1 and 2 can be found elsewhere (*4*,*5*). These equations are usually referred to as the Packer/Lugeon equations and are the ones used by the U.S. Bureau of Reclamation for in situ determination of rock mass permeability. For the FPT setup used, the length of the test section, L_0, was always between r and $10r$; thus, Equation 1 was used in computing the coefficient of permeability in an FPT.

The relative moisture content of the concrete site at each test location was measured before, during, and after testing by means of a nondestructive portable moisture meter at four diagonal points around the test hole. Since the accuracy of the moisture meter had not been investigated, the main purpose of using the moisture meter was to determine the relative change in moisture content during the test rather than to measure the moisture content of the concrete accurately. If the concrete was relatively dry, a vacuum preconditioning and subsequent presaturation of the test section were applied for approximately 30 min before any permeability testing. The concrete test section was saturated to the extent that further saturation would not affect the results of the FPT. It is estimated that in this condition the concrete was fully saturated to a minimum depth of 0.4 in. (1 cm) from the wall of the test hole.

The FPTs were conducted by one person and an assistant; test measurements were completed usually within 2 hr from the commencement of the actual test run. The entire FPT operation, including coring, preconditioning, testing, and patching of concrete, was completed within approximately 2 to 3 hr. The FPT apparatus demonstrated satisfactory performance; no major problems were encountered in any of the field installations.

LABORATORY TESTING PROGRAM

The standard test method for rapid determination of the chloride permeability of concrete (AASHTO T277-83) was employed in this study to further evaluate the concrete material of the in-service bridge structures under investigation. Cored concrete samples were obtained from selected test locations where FPTs were performed. However, to minimize the disruption to the concrete structures tested, 1.75-in.-diameter cores instead of the standard 3.75-in.-diameter cores were obtained. Figure 4 shows an actual concrete core obtained from one of these test locations as well as a prepared specimen as used in the chloride test. Since the 1.75-in. actual diameter of these cores was smaller than the standard 3.75-in.-diameter normally used in this test, the dimensions of the inside diameter of the applied voltage cell were modified to fit the outside diameter of the prepared field specimens. Figure 5 shows the modified applied voltage cell that was fabricated and used in this study.

During the preliminary testing of some of the cores using the modified applied voltage cell, temperatures as high as 180°F were observed within the first 2 hr of test duration. Thus, an additional modification was made to the rapid chloride test. The level of applied voltage was reduced from the standard 60 V to 30 V to avoid equipment failure caused by the observed higher-current flows through the tested concrete samples.

Because of these modifications, the results obtained from the rapid chloride permeability test were adjusted accordingly to take into account the reduced cross-sectional area of the concrete specimens and the reduced applied voltage. The test measurements were normalized to correspond to standard

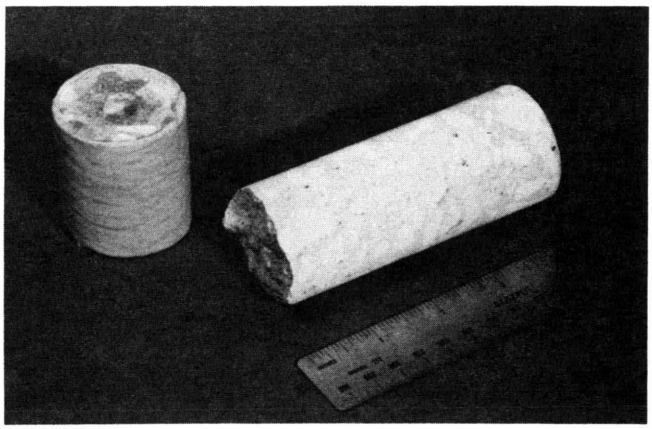

FIGURE 4 Field concrete core (*right*) and prepared specimen (*left*).

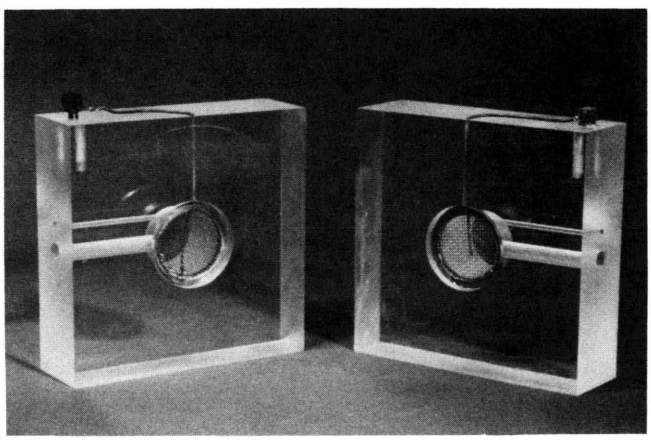

FIGURE 5 Modified applied voltage cell.

results by applying an adjustment factor C_a, determined as follows.

The electrical resistivity ρ of any material is defined as the resistance between opposite faces of a unit specimen of the material according to the following equation:

$$\rho = RA/L \tag{3}$$

where

R = electrical resistance of specimen,
A = cross-sectional area of specimen, and
L = length of specimen.

According to Ohm's law,

$$I = V/R \tag{4}$$

where I is the electrical current and V is the applied voltage. Since the length of the concrete specimens used in the chloride test device was constant (2 in.) and the resistivity of the concrete material during the testing was assumed to remain constant, the relationship between the standardized and modified chloride test results can be represented by the following simple equation:

$$I_{60}/I_{30} = V_{60}A_{60}/V_{30}A_{30} = C_a \tag{5}$$

where I_{60}, V_{60}, A_{60} are test parameters at the standard 60-V potential level and I_{30}, V_{30}, A_{30} are test parameters at the reduced 30-V potential level.

For the modified test setup used, the adjustment factor C_a was computed to be 9.18. This adjustment factor was used to normalize the test results obtained from the modified chloride test to correspond to the standard chloride permeability test results (in coulombs) as interpreted by AASHTO T277-83.

TEST RESULTS

FPT Results

Repetitive FPTs were performed on the same test sections to evaluate the repeatability of the test results. Representative results for various structural elements are displayed in Table 1. The data show that the measured permeability coefficients have a maximum percent difference ranging from about 3 to 28 percent. The results obtained from these replicate tests indicated that the FPT method demonstrated acceptable repeatability under actual field conditions. However, much higher variations were observed among the mean coefficients of permeability obtained from FPTs performed at various test locations on structural elements having the same design or concrete type, or both. Table 2 displays representative test results from FPTs performed at various test locations. As can be seen from these data, the maximum percent difference in such cases ranged between about 5 and 684 percent. The highest variation among the permeability coefficients of the same class of concrete was obtained from FPTs performed on three different test sections from a girder of the SR-206 Bridge at Crescent Beach, which was built in 1975. From a total of 57 individual FPTs run on the 13 selected concrete bridges,

TABLE 1 Results of FPTs Performed at the Same Test Section

CONCRETE BRIDGE STRUCTURE TESTED	TYPE OF STRUCTURAL ELEMENT	PERMEABILITY COEFFICIENT (xE-9 cm/sec) 1st TEST	RE-TEST	MAXIMUM PERCENT DIFFERENCE
SEVEN MILE	PIER STRUT	1.90	1.85	2.70
	"	6.69	8.09	-17.30
BAHIA HONDA - NORTHBOUND	FOOTER CAP	5.25	6.21	-15.46
B. B. McCORMICK	PILE COLUMN	10.00	9.50	5.26
	"	45.70	35.60	28.37
	"	47.20	45.20	4.43
	ONSHORE PIER	41.70	34.80	19.83
		22.80	24.01	-5.04
SEABREEZE CAUSEWAY	BASCULE	25.80	20.80	24.04
	"	24.60	19.20	28.12

the lowest registered value of permeability coefficient, 0.94×10^{-9} cm/sec, was the one obtained from a test section on a V-pier cap of Pier 103 at the Long Key Bridge. Overall, the permeability coefficients of the tested site concretes were, on average, two to four orders of magnitude higher than the coefficients obtained from FPTs performed on laboratory-prepared concretes of similar quality (*5,6*).

Chloride Permeability Test Results

Rapid chloride permeability tests were performed in the laboratory on a number of cored concrete specimens (1.75 in. in diameter) obtained from the selected bridge structures under investigation. The concrete cores used in this series of tests were obtained from structural elements that already had been tested for their relative water permeability by means of the developed FPT apparatus. These cores were obtained from locations as close as possible (within 12 in.) to the tested FPT sections.

The field-cored concrete specimens were sectioned in 2-in. slices and subsequently conditioned and prepared for testing according to the procedure stipulated by AASHTO T277-83. As many as three 2-in. slices were cut from the top (A), middle (B), and bottom (C) sections of long field cores, when possible. The middle (B) section of concrete cores, corresponding to the region of concrete material tested with the FPT, was used in these tests for comparative purposes. The test measurements were analyzed according to the standard procedure, and the adjustment factor C_a was applied to convert the chloride permeability results (in coulombs) to correspond to standard values. The results from this series of laboratory chloride permeability tests are presented in Table 3.

The maximum percent difference between the values of the charge passed (in coulombs) of replicate test specimens taken

from the top, middle, and bottom sections of field concrete cores ranged between about 1 and 242 percent. A relatively high variation was also observed among the values of structural elements having the same design or concrete class, or both, as in the case of the water permeability results. In 80 percent of the cases, the relative chloride permeability (in terms of coulombs) of the tested concrete material was higher for concrete specimens cut from the bottom or the middle sections of cores as compared with those cut from the top. Although a definite relationship quantifying this effect was not achieved during this research study, this trend, along with the discrepancies in the test results obtained for the same class of concretes, indicated a significant variation in the quality and durability characteristics of the tested concretes. One possible explanation for the high variation of the results of the rapid chloride permeability tests is that they are affected by the chloride ion contents of the test concrete. Since the cores contained variable amounts of chloride ions, high variations in the test results were obtained.

TABLE 2 Results of FPTs Performed on Various Structural Elements of the Same Type and Concrete Material

CONCRETE BRIDGE STRUCTURE TESTED	TYPE OF ELEMENT TESTED	TEST SECTION	MEAN COEFFICIENT OF PERMEABILITY (xE-9 cm/sec)	MAXIMUM PERCENT DIFFERENCE
SEVEN MILE	STRUT	1	1.875	294.13
	"	2	7.390	
LONG KEY	PIER CAP	1	0.940	162.77
	"	2	2.470	
	"	3	2.360	
BAHIA HONDA - SOUTHBOUND	FOOTER	1	7.210	533.38
	"	2	27.760	
	"	3	6.650	
	"	4	42.120	
BAHIA HONDA - NORTHBOUND	"	1	5.730	550.09
	"	2	23.930	
	"	3	37.250	
SPANISH HARBOR	PILE	1	3.880	6.89
	"	2	3.630	
NILES CHANNEL	FOOTER	1	1.460	21.92
	"	2	1.780	
NILES CHANNEL - OLD	WALL	1	51.030	30.41
	"	2	66.550	
B. B. McCORMICK	PILE	1	9.750	470.37
	"	2	40.070	
	"	3	46.200	
	"	4	14.500	
	"	5	19.800	
	"	6	8.100	
	"	7	37.730	
	"	8	23.400	
SR206 - CRESCENT BEACH	GIRDER	1	12.000	684.31
	"	2	1.530	
	"	3	5.650	
SEABREEZE CAUSEWAY	BASCULE	1	23.300	109.91
	"	2	11.100	
	"	3	21.300	
BROWARD RIVER	PILE	1	8.030	304.73
	"	2	32.500	
HORSE CREEK	BEAM	1	10.640	4.51
	"	2	7.970	
	"	3	11.120	
HORSE CREEK - OLD	WALL	1	5.910	13.87
	"	2	6.730	

Correlation Between the Results of the FPT Method and AASHTO T277-83

The results obtained from the developed FPT method and the standard AASHTO T277-83 were compared to identify any possible relationships between them. Since the center of

TABLE 3 Results of Rapid Chloride Permeability Tests

CONCRETE BRIDGE	TYPE OF ELEMENT	SPECIMEN No.	CHARGE PASSED (COULOMBS) ACTUAL (M)	ADJUSTED (S)	MAX. % DIFF.
SEABREEZE CAUSEWAY	BASCULE	1B	420.2	3,857.4	N/A
		2B	822.2	7,547.9	N/A
B. B. McCORMICK	PILE	3B	372.8	3,422.3	N/A
	PIER	4B	289.6	2,658.9	N/A
BROWARD	BASCULE	5B	209.3	1,921.7	N/A
OLD HORSE CREEK	WALL	6A	230.0	2,111.8	0.76
	"	6B	231.8	2,127.9	
	"	7A	344.0	3,158.2	N/A
	"	8B	211.1	1,937.8	127.45
	"	8C	480.1	4,407.5	
NEW HORSE CREEK	BEAM	9A	298.0	2,735.3	178.68
		9B	572.1	5,252.2	
		9C	830.4	7,622.7	
		10A	251.8	2,311.0	242.02
		10B	861.0	7,904.1	
NILES CHANNEL	STRUT	11A	637.9	5,855.6	35.02
	"	11B	861.2	7,906.2	
OLD NILES CHANNEL	WALL	12A	2000.9	18,368.1	21.22
	"	12B	1650.7	15,153.1	
	"	13B	1985.6	18,227.6	N/A
SP.HARBOR	PILE	15A	1139.2	10,457.5	N/A
BAHIA HONDA SOUTH BOUND	FOOTER	16B	1002.8	9,205.7	9.79
	"	16C	1101.0	10,107.2	
	"	17B	1240.7	11,390.0	46.83
	"	17C	845.0	7,757.5	
CONCRETE BRIDGE	TYPE OF ELEMENT	SPECIMEN No.	CHARGE PASSED (COULOMBS) ACTUAL (M)	ADJUSTED (S)	MAX. % DIFF.
BAHIA HONDA NORTH BOUND	FOOTER	18B	845.2	7,758.6	46.29
	"	18C	1236.4	11,350.1	
	"	19A	863.4	7,926.2	26.22
	"	19B	1089.8	10,004.4	

Key:

(M) = Test results using the Modified Applied Voltage Cell with a reduced 30-volt potential level

(S) = Estimated equivalent charge corresponding to coulomb values as interpreted in the Standard AASHTO T277-83 method

N/A = Not Applicable

Note:

According to the standard AASHTO T277-83 method:

Charge Passed (coulombs)	Chloride Permeability
>4,000	High
2,000-4,000	Moderate
1,000-2,000	Low
100-1,000	Very Low
<100	Negligible

the flow region in a typical FPT was located about 3 in. from the surface of the concrete, the chloride permeability test results obtained from the specimens cut from the middle of concrete cores (B-series) corresponding to the FPT section were used for comparison. The comparison of the results from these two tests is presented in Table 4.

A linear regression analysis between these two variables was performed. The results of the regression analysis were as follows:

$$Q_{RCP} = 247.7167K_{FPT} + 1834.190$$

$$R^2 = 0.90$$

Standard Error of the Slope = 22.01 (6)

TABLE 4 Comparison of Results Obtained from the FPT and Rapid Chloride Permeability Test

CONCRETE BRIDGE STRUCTURE TESTED	TYPE OF STRUCTURAL ELEMENT	CHLORIDE PERMEABILITY B-SERIES (COULOMBS)	MEAN WATER PERMEABILITY COEFFICIENT (xE-9 cm/sec)
SEABREEZE CAUSEWAY	BASCULE	3,857.4	11.10
	"	7,547.9	21.30
B. B. McCORMICK	PILE	3,422.3	9.75
	PIER	2,658.9	8.10
BROWARD RIVER	BASCULE	1,921.7	6.08
HORSE CREEK - OLD	WALL	2,127.9	5.91
	"	1,937.8	6.73
HORSE CREEK - NEW	BEAM	5,252.2	10.64
	"	7,904.1	7.97
NILES CHANNEL	STRUT	7,906.2	14.70
NILES CHANNEL - OLD	WALL	15,153.1	51.03
	"	18,227.6	66.55
BAHIA HONDA - SOUTHBOUND	PIER. FOOTER	9,205.7	27.76
	"	11,390.0	42.12
BAHIA HONDA - NORTHBOUND	"	7,758.6	23.93
	"	10,004.4	37.25

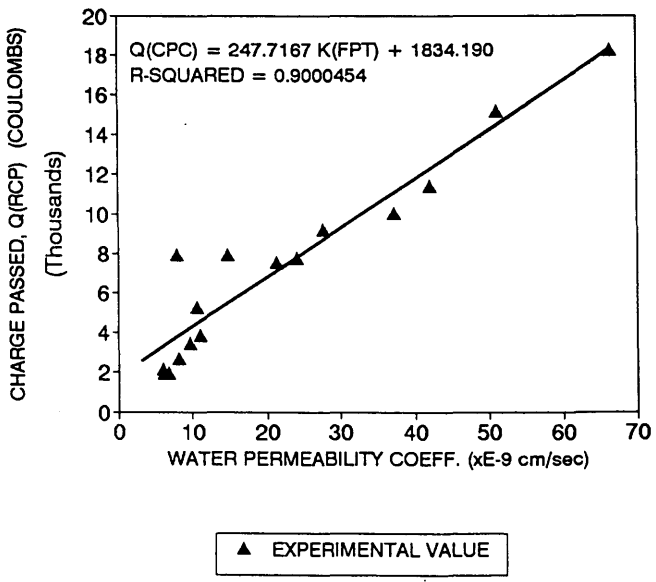

FIGURE 6 Correlation between charge passed and water permeability coefficient.

where Q_{RCP} is the charge passed (in coulombs) measured by the rapid chloride permeability (RCP) test method and K_{FPT} is the coefficient of permeability as determined by the FPT method. Figure 6, which is a graphical representation of these results, suggests that it is possible to assume a linear relationship between the respective chloride and water permeability values as determined by the two methods. Although limited experimental values were considered in this analysis, the obtained coefficient of determination (R^2) of 0.90 indicates a strong correlation between the two quantities.

DISCUSSION OF RESULTS

The evaluation of the in-service concrete structures investigated in this study was performed from the concrete material point of view and with respect to the physical property of permeability. Comparison of the results obtained from FPTs performed on the selected in-service concrete structures with those obtained from water permeability tests on laboratory-prepared concrete specimens of similar quality and materials indicates that the site concretes exhibited very high water permeabilities (*6–8*).

According to the notes in the standard AASHTO T277-83 procedure (*9*), conventional portland cement concrete of low *w/c* ratio (less than 0.4), which corresponds to the Florida Class IV concrete used in some of the previously mentioned bridge structures, typically is expected to have low chloride permeability corresponding to a total charge passed ranging between 1,000 and 2,000 coulombs, as indicated in Table 3. However, only 7 percent of the tested concrete specimens produced results that were within this range, whereas 28 and 66 percent of the specimens exhibited moderate and high chloride permeabilities, respectively. All of the concrete specimens extracted from bridge structures located in the Florida Keys region exhibited high chloride permeabilities. The highest registered charge passed through a tested concrete material—18,368 coulombs—was obtained from a concrete core extracted from the arch wall at the Old Niles Channel Bridge. This value was about 360 percent higher than the upper limit of charge passed corresponding to high chloride permeability according to AASHTO T277-83. This bridge was built in 1906, and the concrete material at the test location was determined to have a chloride content of approximately 100 lb/yd^3 at the time the FPTs were performed (*8*). Based on the high quantities of charge passed through the majority of the tested concretes and the observed high variation of values obtained from duplicate specimens tested with the rapid chloride permeability method, could indicate that there was a significant variation in the quality and durability characteristics of the concrete with respect to chloride permeability.

Although the site concrete was sound both at the particular locations where the FPTs were performed and where cored samples were extracted and did not exhibit any visual signs of deterioration, the results obtained from the field and laboratory testing programs indicated poor durability characteristics with respect to permeability. The results further suggest that there seems to be an apparent relationship between the condition of structural concrete and its permeability. Concrete bridge structures that demonstrated durability problems also exhibited high permeability of the concrete material. For ex-

ample, the permeability values obtained from a number of piles from B. B. McCormick Bridge, which has exhibited severe concrete deterioration (Figure 1), were substantially higher than those obtained from the piles from Horse Creek Bridge, which has shown no concrete deterioration (Table 2). It is believed that the relatively high permeability of the concrete contributed significantly to the severe deterioration of some elements in these bridge structures by allowing the intrusion of deleterious substances present in the marine environment into the concrete.

CONCLUSIONS

In this study, an FPT apparatus and method were developed and evaluated in both the laboratory and the field. The developed prototype FPT apparatus and method were used in the testing and evaluation of in-service marine structures in conjunction with the standard rapid chloride permeability test and laboratory water permeability test.

On the basis of the experimental findings of the field and laboratory testing programs, the major conclusions of this research study are summarized as follows:

1. The developed FPT apparatus and method appear promising in providing a suitable measuring system for the rapid, convenient, and reliable determination of the in situ water permeability of structural concrete. The repeatability of the FPT results under actual field environment was shown to be acceptable.
2. There appears to be a linear relationship between the charge passed (coulombs) through a concrete material as measured by the rapid chloride permeability test (AASHTO T277-83) and its corresponding water permeability, with a coefficient of determination, R^2, of 0.90.
3. There appears to be a relationship between permeability and durability of concrete in service. The concrete material that exhibited durability problems also demonstrated high permeability.
4. The deterioration of concrete in the tested bridge structures was primarily caused by corrosion of the embedded steel reinforcement, which was caused by the intrusion of chloride ions. It is believed that the high permeability of the in situ concrete material significantly contributed to this effect.
5. A high variation in permeability was observed between concrete bridge structures specified to have the same concrete class. Since permeability is greatly affected by the microstructure of the concrete, high variations in permeability test results are usually expected, especially for in-service concrete. It is recommended that a sufficient number of tests be performed and that the data be statistically analyzed to account for such variations.
6. The FPT method can provide a relative measurement of permeability that can be used as an indication of the quality and performance characteristics of structural concrete.

ACKNOWLEDGMENTS

The Florida Department of Transportation (FDOT) and FHWA are gratefully acknowledged for providing financial support for this study. The cooperation of Jamshid Armaghani, the technical coordinator for this study, Rodney Powers, and Ivan Lasa of the FDOT Materials Office is duly acknowledged. The collaboration of David Bloomquist and his significant contribution in the design and development of the FPT apparatus are most gratefully acknowledged. Ed Dobson, Danny Richardson, and Patrick Upshaw provided their valuable technical support in this study.

REFERENCES

1. P. K. Mehta. *Concrete, Structures, Properties, and Materials*, Chapter 5. Prentice-Hall, Inc., Englewood Cliffs, N.J., 1986, pp. 105–169.
2. P. K. Mehta. Durability of Concrete in Marine Environment—A Review. *Performance of Concrete in Marine Environment*, SP-65. American Concrete Institute, Detroit, Mich. 1980, pp. 1–20.
3. P. K. Mehta. Durability of Concrete Exposed to Marine Environment—A Fresh Look. *Concrete in Marine Environment*, SP-109. American Concrete Institute, Detroit, Mich. 1988, pp. 1–23.
4. C. A. Meletiou, M. Tia and D. Bloomquist. Development of a Field Permeability Test Apparatus and Method for Concrete. *American Concrete Institute Materials Journal*, Vol. 89, No. 1, Jan.–Feb. 1992, pp. 83–89.
5. C. A. Meletiou. *Development of a Field Permeability Test for Assessing the Durability of Concrete in Marine Structures*. Ph.D. dissertation, University of Florida, Gainesville, 1991.
6. M. Tia et al. *Field and Laboratory Study of Modulus of Rupture and Permeability of Structural Concretes in Florida*. Final Report, UF Project 491-450423412. Department of Civil Engineering, University of Florida, Gainesville, Aug. 1990.
7. P. Soongswang, M. Tia, D. Bloomquist, C. A. Meletiou, and L. Sessions. An Efficient Test Set-Up for Determining the Water-Permeability of Concrete. In *Transportation Research Record 1204*, TRB, National Research Council, Washington, D.C., 1988, pp. 77–82.
8. P. Soongswang, M. Tia, and D. Bloomquist. Factors Affecting the Strength and Permeability of Concrete Made with Porous Limestone. *ACI Materials Journal*, Vol. 88, No. 4, July–Aug. 1991, pp. 400–406.
9. Standard Method of Test for Rapid Determination of the Chloride Permeability of Concrete. AASHTO T277-83. In *Standard Specification for Transportation Materials and Methods of Sampling and Testing*, 14th ed. AASHTO, Washington, D.C., 1986.
10. *Concrete Chloride Content Ledger*, Vol. 1. Florida Department of Transportation, March 1978–July 1981.

DISCUSSION

KENNETH A. SNYDER
National Institute of Standards and Technology, Gaithersburg, Md. 20899.

I would like to present several points for review by the authors.

1. I feel that a key element in the presentation was the omission of laboratory water permeability measurements performed on the field specimens. I acknowledge that laboratory tests were performed to correlate the results of the portable permeability meter (PPM) and standard laboratory water permeability tests. I would agree that the results were very encouraging. However, field tests performed on 3-ft-diameter columns are more suspect to experimental problems than tests performed on 6- × 6- × 12-in. specimens; I am only guessing at the size of specimens on the basis of the presentation slides.

The primary concern is saturation. I would venture to guess that the 6- × 12-in. prisms were properly cured in saturated lime water. Therefore, the entire life of the specimen was spent submerged, and, hence, fully saturated. I don't believe that "vacuum saturating" a 3-ft-diameter column for one-half hour is sufficient to ensure saturation, not to mention an extreme experimental hurdle to be performed correctly.

2. The authors' experimental apparatus contains a feature that leads to skepticism of the results. When the fluid in the middle region is pressurized, the greatest pressure gradient exists between the middle region and the two regions in the cored hole immediately above and below the middle pressurized region. This suggests that the immediate tendency of the fluid would be to flow back into the core. This behavior is different from the spherical geometry the authors mentioned in the presentation. If no fluid is found in the regions immediately above and below the middle region then there could be additional shortcomings of the assumptions used in the permeability calculation. The lack of fluid would indicate that the fluid does not penetrate the concrete very far, suggesting a cylindrical geometry rather than a spherical one.

3. I would also like to discuss the mathematical development of the authors' equations to calculate permeability from the flow. I realize that the nature of TRB dissuades from discussing involved mathematical development and, therefore, I realize that my questions already may have been addressed in a technical publication.

There was no mention of a time dependence to the solution of the permeability calculation. I believe you mentioned that spherical symmetry was assumed along with an infinite medium. If one assumes an infinite medium, then the pressure gradient must be zero to satisfy the boundary conditions and, hence, there should be no flow. Practically, one accepts that there must be a pressure gradient at the core wall the instant the pressure is applied. However, as fluid moves out into the concrete the "rising edge" of the pressure gradient must be moving out also. This should continue until the rising edge reaches the outside surface of the object under test. All the while, the flow from the probe would slowly diminish because of the changing pressure gradient. I believe that the authors simply stated that the flow was recorded until a steady state was reached.

4. An additional aspect of the test that should be considered is the extent of the test. Consider the depth to which the fluid (I assume water) penetrates the system, which can be roughly approximated from the following calculation. The volume-averaged Darcy equation can be expressed in differential form:

$$\langle \mathbf{v} \rangle = -\frac{k}{\mu} \nabla \langle \mathbf{p} \rangle$$

Consider that the closest region of atmospheric pressure is just a few centimeters away above and below the probe's middle section. Assuming an applied pressure of 100 lb/in.^{2} and a reasonably permeable sample, the velocity of the fluid penetrating the concrete would still be very small:

$$\langle \mathbf{v} \rangle = \frac{10^{-16}\text{m}^2}{10^{-3}\ \text{kg/m sec}} \frac{7 \times 10^5\ \text{N/m}^2}{2 \times 10^{-2}\text{m}} = 4 \times 10^{-6}\ \text{m/sec}$$

Over the course of 1 hr the fluid would advance only approximately 1.5 cm. Since this is the greatest pressure gradient the fluid would experience, it is an upper limit of the maximum penetration.

5. The oil industry is very interested in determining the permeability of underground rock formations to estimate, among other things, the productivity of a potential oil well. The development of a meter to measure the in situ permeability holds a keen interest for them. When one considers the immeasurable person hours and dollars spent by petroleum engineers trying to develop such a device, which has still eluded them, it is a good idea to look with a critical eye at any new developments of such a device.

AUTHORS' CLOSURE

The development of the FPT apparatus and method used in this study has been presented in detail in a previous paper by the authors (*1*); the answers to most of the questions raised by the discussant can be found therein. The derivation of the analytical equation relating the flow rate measured in the FPT and the water permeability of the concrete is presented as follows.

It is assumed that the mass concrete is infinite in size and that a steady-state flow condition has been reached.

The following parameters are defined:

R = radius of influence (i.e., the effective radius of the flow region under study) and
$\Phi(R)$ = the potential at a distance R from the center of the sphere.

The discharge, Q, at any radial distance ρ from the source at the center of the sphere is

$$Q = 4\pi\rho^2 v_\rho = 4\pi\rho^2 \frac{\partial \Phi}{\partial \rho}$$

$$\frac{\partial \Phi}{\partial \rho} = \frac{Q}{4\pi\rho^2} \tag{1}$$

where $4\pi\rho^2$ is the surface area of the sphere and v_ρ is the radial velocity.

By integrating Equation 1,

$$\int \partial\Phi = \int \frac{Q}{4\pi\rho^2}\, \partial\rho$$

we obtain the potential, Φ, as

$$\Phi = -\frac{Q}{4\pi\rho} + C \tag{2}$$

Equation 2 indicates that in the case of spherical flow the potential varies inversely with the radius of influence.

To determine the constant of integration, C, in Equation 2, the boundary conditions at the hole should be defined as follows: $\rho = r$ and $\Phi = \Phi_0$. Therefore, by solving Equation 2 with respect to C we get

$$C = \Phi_0 + \frac{Q}{4\pi r} \tag{3}$$

By applying the boundary conditions and substituting the expression for C in Equation 3 into Equation 2, we get

$$\Phi = \frac{Q}{4\pi}\left(\frac{1}{r} - \frac{1}{\rho}\right) + \Phi_0 \tag{4}$$

where $r \leq \rho \leq R$.

The following parameters are also defined: $2r$ = diameter of test hole and $L_0 = 2L$ = length of test section. According to Girinsky (*2*), the discharge, Q, can be assumed to be constant along the test section, and the discharge per unit length can be expressed as

$$\frac{dQ}{d\eta} = \frac{Q}{2L} \Rightarrow dQ = \frac{Q}{2L}\,d\eta \tag{5}$$

Assuming Equation 2 to represent the potential at any point in the flow region,

$$d\Phi = \frac{dQ}{4\pi\rho} \tag{6}$$

For a cylindrical coordinate system,

$$\rho = [r^2 + (z - \eta)^2]^{1/2} \tag{7}$$

By combining Equations 5 through 7 we get

$$d\Phi = \left(\frac{Q}{2L}\right)d\eta\left(\frac{1}{4\pi\rho}\right) \Rightarrow d\Phi = \left\{\frac{Q}{8\pi L[r^2 + (z - \eta)^2]^{1/2}}\right\}d\eta$$

Set the limits of integration from $(L_0/2)$ to $+ (L_0/2)$ (note that $L_0 = 2L$):

$$\Phi(r, z) = \frac{Q}{8\pi L}\int_{-L}^{+L} \frac{d\eta}{[r^2 + (z - \eta)^2]^{1/2}} \tag{8}$$

$$\Rightarrow \Phi(r, z) = \frac{Q}{8\pi L}\left[\sinh^{-1}\left(\frac{z + L}{r}\right) - \sinh^{-1}\left(\frac{z - L}{r}\right)\right] \tag{9}$$

According to Harr (*3*), the equipotential surfaces given by Equation 9 are seen to be ellipsoids.

By assuming $z = 0$ and substituting $L_0 = 2L$, Equation 9 becomes

$$\Phi(r) = \frac{Q}{2\pi L_0}\sinh^{-1}\left(\frac{L_0}{2r}\right) \approx \frac{Q}{2\pi L_0}\ln\left(\frac{L_0}{r}\right) \tag{10}$$

where

$$\sinh^{-1}(x) = \ln [x + (x^2 + 1)^{1/2}]$$

and if $x >> 1$, $\sinh^{-1}(x)$ is approximately equal to $\ln(2x)$.

Finally, if we substitute in Equation 10 $Kh = \Phi$ and solve with respect to the permeability K, we obtain

$$K = \frac{Q}{2\pi L_0 h}\sinh^{-1}\left(\frac{L_0}{2r}\right) \quad \text{for } r \leq L_0 < 10r \tag{11a}$$

and

$$K = \frac{Q}{2\pi L_0 h}\ln\left(\frac{L_0}{r}\right) \quad \text{for } L \geq 10r \tag{11b}$$

where K is the coefficient of permeability and h is the applied pressure head.

Equations 11a and b relate the measured flow rate in the FPT to the coefficient of permeability of the concrete tested. For the FPT setup used, the length of the test section, L_0, is always between r and $10r$, and thus Equation 11a is used in computing the coefficient of permeability in the FPT.

The equation is based on the assumption that a steady-state flow condition has been reached. Thus, the recommended testing procedure requires that the FPT be run until an apparent steady-state flow condition has been reached. As stated in the paper, the concrete test sections were presaturated to the extent that further saturation would not affect the results of the FPT. It might be true that at the apparent steady-state condition, the test concrete had not been completely saturated and the flow had not reached its true steady-state condition. However, for practical purposes, since the test results do not change appreciably after that point, the determined permeability should be very close to the true permeability.

REFERENCES

1. C. A. Meletiou, M. Tia, and D. Bloomquist. Development of a Field Permeability Test Apparatus and Method for Concrete. *American Concrete Institute Materials Journal*, Vol. 89, No. 1, Jan.–Feb. 1992, pp. 83–89.
2. N. K. Girinsky. Determination of the Coefficient of Permeability." *Gosgeolizdat*, 1950.
3. M. E. Harr. *Groundwater and Seepage*. McGraw-Hill, Inc., 1962, pp. 259–262.

The opinions and findings of this paper reflect only the views of the authors and do not necessarily reflect the official views of the sponsoring agencies.

Publication of this paper sponsored by the Committee on Concrete Bridges.

Comparison of Treatment Methods Involving Polymer Impregnation for Abating Corrosion in Overlaid Bridge Decks

TAPAS DUTTA, RICHARD E. WEYERS, AND IMAD L. AL-QADI

To investigate the corrosion of the reinforcing steel (rebars) in bridge decks, concrete laboratory specimens with rebars were cast and subjected to a chloride environment. The corrosion potential and rate were monitored with Cu-$CuSO_4$ half-cell and three electrode linear-polarization (3 LP) devices. When active corrosion had been initiated, five rehabilitation treatment methods were applied to the corroding specimens: latex-modified concrete (LMC) overlay, low-slump dense concrete (LSDC) overlay, polymer-impregnated concrete, LMC overlay with polymer impregnation, and LSDC with polymer impregnation. The monomer system used was 90 percent methyl methacrylate (MMA), 10 percent trimethylolpropene trimethacrylate and 0.5 percent of the above monomer mix of azobisiobutyronitrile. The impregnated specimens were grooved and dried to 230°F before impregnation and subsequent polymerization. The posttreatment corrosion rates were used for analyzing the effectiveness of the various treatment methods. The treatment methods investigated were able to reduce the corrosion rate dramatically compared with untreated specimens. However, the difference in effectiveness among the five methods was insignificant.

Premature deterioration of reinforced concrete bridge decks was first recognized by highway agencies in the late 1950s. An initial study determined that the principal cause was spalling, which resulted from corrosion of the reinforcing steel caused by the high chloride content of the concrete and moisture intrusion (*1,2*). The major source of chlorides is the deicing salts applied to the roadways during winter. In 1970, more than 9 million tons of deicing salts were used in the United States (*3*), increasing to 12 million tons by 1979 (*4*). A second source of chlorides is sea water in direct contact and from spray on bridge components in a marine environment.

By the 1970s, highway agencies had begun to identify the enormous cost involved in the repair and rehabilitation of deficient bridges. It was found that the number of bridges that became deficient each year far exceeded the actual number of bridges that were repaired in the same time frame. As a result, an increasingly large backlog of deficient bridges was created with each passing year. A recent cost estimate of the rehabilitation of bridges deteriorated by corrosion was placed at $20 billion, at an annual increase rate of $0.5 billion (*5*).

T. Dutta, California Department of Transportation, 120 South Spring Street, Los Angeles, Calif. 90012. R. E. Weyers and I. L. Al-Qadi, Virginia Polytechnic Institute and State University, Blacksburg, Va. 24061.

An early response to the bridge deck deterioration problems was to modify the design parameters. The cover depth was increased up to 3 in., which prolonged the time it took the chloride ions to reach the top mat of rebars. By reducing the ratio of water to cement to between 0.40 and 0.45, chloride permeability of concrete was reduced and, hence, the rate of diffusion of chloride ions was diminished. These methods did not stop the corrosion process, however, but the time to initiate the corrosion of the rebars was extended.

Rigid overlay systems on bridge decks have been used for some time as a rehabilitation technique. The most commonly used rigid overlays are latex-modified concrete (LMC), low-slump dense concrete (LSDC), and polymer concrete (PC). These overlay systems are also applied to new bridge decks as a means of corrosion protection.

Electrochemical chloride removal in conjunction with the injection of materials such as penetrating sealants and corrosion inhibitors has been used recently. When corrosion inhibitors such as calcium nitrite are injected into concrete they encapsulate the steel and act as a barrier to chloride ions. The application of coating materials, such as epoxy coating rebars, has been extended to include parapet, substructure, and superstructure components of bridges. However, this method has not proved completely successful over long periods of time in severe environments such as the Florida Keys. The application of waterproofing membranes along with an asphaltic concrete wearing surface has also been in use as a protection technique. Impressed current systems and galvanic cathodic protection systems have demonstrated their capability of arresting the corrosion of steel in concrete.

The only nonelectrochemical method to abate corrosion of steel in concrete bridge decks is deep impregnation. Deep impregnation (depths of 3 to 4 in.) of monomer into concrete and subsequent in situ polymerization abates corrosion where it has started and prevents the start of corrosion in the steel. A deep grooving method of concrete bridge decks that was developed by Weyers and Cady (*6,7*) resulted in the feasibility of polymer impregnating entire bridge decks. The monomer that was used in that study is MMA. The polymer encapsulates the concrete around the reinforcing steel and fills most of the void spaces, thereby stopping the flow of current, and consequently prevents the onset or continuation of any corrosion activity. Therefore, W/C and slump will not have any effects, whereas the percentage of air will affect the amount of monomer used.

PREPARATION OF SPECIMENS AND INITIATION OF CORROSION

Eighteen laboratory concrete specimens were cast. The concrete mix used is in accordance with Virginia A4AE bridge concrete mixture. They were 12 in. long and 10 3/8 in. wide. Each specimen had two triad of rebars (Figure 1). To minimize the effects of manufacturing oil and existing rust on the rebars, the rebars were cleaned by soaking them in a hexane solution for about 20 min and then wiped clean. The rebars were then dried in an oven at 240°F for 10 min. To prevent corrosion from taking place at the exposed ends, the two ends were covered with electroplating tape so that the uncovered length of each rebar was 6.5 in. Thus, the exact surface area exposed for corrosion was known; hence, corrosion rates could be normalized to a square foot of surface area of the rebar.

A thermocouple Type *T* junction was taped at the bottom center point of each top righthand rebar of each specimen. Type *T* plugs were attached to the other ends. Five treatment methods were used and one set of control specimens were not subjected to any treatment. Triplicate specimens were cast for each treatment and for the controls. Therefore, a total of 18 specimens were cast. The two-letter codes assigned to each group were as follows:

- CO: Specimens acted as controls, untreated,
- LM: Specimens overlaid with LMC,
- LS: Specimens overlaid with LSDC,
- PC: Specimens with polymer impregnation,
- PM: Specimens overlaid with LMC and polymer impregnation, and
- PS: Specimens overlaid with LSDC and polymer impregnation.

The sides were coated with epoxy to prevent moisture loss and salt ingress from the sides. Plexiglass dikes 1 in. high and 5/16 in. thick were fixed on top of each specimen using silicon rubber. Glass covers were used on the specimens to minimize moisture loss during wet cycles. A resistor of 100 Ω was connected between the top rebar and the bottom right rebar of each triad. A jumper cable was fitted between the two bottom rebars of each triad, resulting in a macrocell cathode-to-anode area of 2.

Before the first wet cycle, potential and temperature readings were taken. Temperature readings were measured by a digital Type *T* thermocouple meter. Potential readings were taken with a copper-copper sulfate (CSE) half cell in accordance with the ASTM C-876 procedure. The interpretation of the potential values are given in ASTM C-876 and summarized as follows:

- If the potential is more positive than −200 mV CSE, there is a probability of more than 90 percent that there is no active corrosion present.

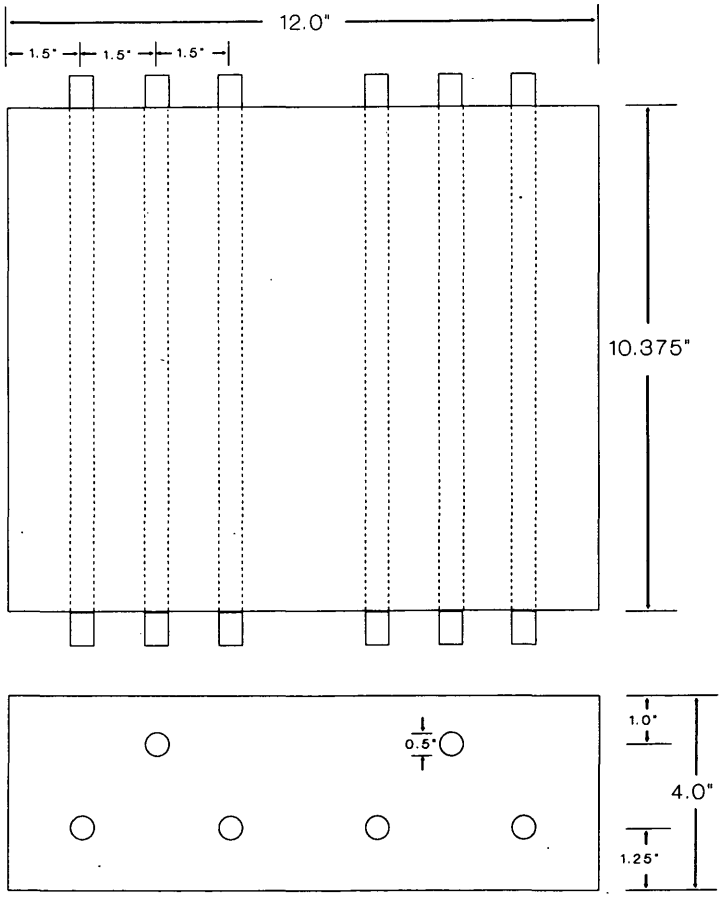

FIGURE 1 Plan and elevation of specimens.

- If the potential is between −200 mV CSE and −350 mV CSE, corrosion activity is uncertain.
- If the potential is more negative than −350 mV CSE, there is a probability of more than 90 percent that there is active corrosion present.

The three-electrode linear polarization device (3LP) manufactured by Kenneth C. Clear, Inc., was used to monitor the corrosion current. The corrosion rate of metal is directly proportional to the corrosion current (Faraday's first law). The 3LP device impresses a current in the reverse direction and polarizes the corrosion current. Knowing the impressed current and the corresponding value of the potential, the corrosion current is obtained using the Stern-Geary equation. A description of the test procedure is given in the 3LP manual (*8*). Interpretation of the obtained corrosion current (I_{corr}) values is given in the 3LP manual as follows:

- $I_{corr} < 0.2$ mA/ft^2 → no corrosion damage is expected.
- I_{corr} between 0.2 and 1.0 mA/ft^2 → corrosion damage is possible in 10 to 15 years.
- I_{corr} between 1.0 and 10 mA/ft^2 → corrosion damage is expected in 2 to 10 years.
- $I_{corr} > 10$ mA/ft^2 → corrosion damage is expected in 2 years or less.

Five days after the concrete was placed, the first wet cycle was started. A 6 percent (by weight) sodium chloride solution was used as the source of chloride ions for the concrete. The wet cycle extended for a period of 3 days. At the end of that period, the solution was removed from the specimens using a wet-dry shop vacuum. During the dry cycle the ambient temperature was raised to 120°F using several infrared lamps. The high temperature dried the concrete and made it moisture hungry so that the penetration of salt solution during the next wet cycle was at a higher rate. The duration of the dry cycle was 4 days.

During the ponding period, chloride contents of some selected specimens were determined at various depths with a specific ion probe test method developed by James Instruments, Inc. (*9*). The results obtained by the specific ion probe method are correlated to that obtained by the standard AASHTO test method (T-260-78) (*10*).

Literature review indicates that several different values of chloride ion concentration have been suggested as a threshold value for the initiation of corrosion. The authors have considered the value of 1.2 lb/yd^3 of chloride ions in concrete as a requirement to initiate the corrosion based on the research performed by FHWA (*11,12*).

Treatment activities were started when it was determined that there was active corrosion in most of the top rebars, all the potentials were more negative than −350 mV, the mean corrosion current was 4.2 mA/ft^2 with most of the values being over 2 mA/ft^2, and the chloride contents at the rebar level of selected test specimens were greater than 1.2 lb/yd^3.

TREATMENT PROCESS

During the treatment processes, the salt water ponding of all 18 specimens was suspended. Twelve forms were made to accommodate the 2-in. height overlay. LMC overlays were applied to the LM and PM series, whereas the LS and PS series were overlaid with LSDC. After the moist curing period (14 days), the sides of the overlays were coated with epoxy. Specimens from the PC, PM, and PS series were grooved in preparation for polymer impregnation. In an earlier study by Weyers and Cady (*7*), an empirical formula was developed to determine the grooving parameters: groove spacing, groove depth, and groove width for optimum polymer impregnation.

For all the specimens, the groove width was 0.75 in. and the edge-to-edge distance between grooves was 2.5 in. Considering the groove parameters already noted, there were three grooves on each specimen. The depth of impregnation was 0.5 in. below the top rebars and the depth of the grooves was 0.5 in. above the top rebars. Two depths of impregnation were involved. The specimens of the PC series had the original cover depth of 1 in., and the final depth of polymer penetration was 2 in. For these specimens, the depth of groove was 0.5 in. The overlaid specimens (PM and PS series) had a cover depth of 3 in.; the final depth of polymer penetration for these specimens was 4 in. The groove depth for the overlaid specimens was 2.5 in. A masonry saw was used to cut along the groove lines that had been marked with a permanent ink marker. Concrete between the cut lines was then chipped out with a mason's chisel.

A drying temperature of 230°F, at 0.5 in. below top rebar, was used. Polymer impregnation of concrete was used successfully at this temperature (*13*). Three propane-fired infrared heaters, placed side by side, were used to dry the specimens. To monitor the temperature at a depth of 0.5 in. below the top rebar level, high-temperature Type *T* TC wires were encased in ceramic tubing and inserted into a hole made in the bottom of the specimens to such a depth that the TC junction was 0.5 in. below the top rebar. Nine specimens at a time were set up below the heaters at a distance of 9 in. from the heaters. Fiberglass insulation, 3.5-in. thick, was wrapped around the specimens. The fiberglass was supported by a layer of sand and gravel. The specimens were insulated to prevent the entry of heat from the sides. The TC wires were insulated to enable the TJ junction to measure the temperature at the proper location. A metal sheet with rectangular holes the same size as the specimens' surfaces was placed over the specimens to ensure that only their top surfaces were exposed to the heaters. Along with the nine specimens, three cylinders (4 in. in diameter and 8 in. long) cast from the same concrete mix design were also dried. The cylinders were used to determine the rate of polymer impregnation through the concrete. Two probes were used to record the shaded ambient temperature and the temperature at the surfaces of the specimens.

Temperatures were recorded at regular intervals after the heaters were turned on. After 70 min of heating, the internal temperatures of two specimens reached 230°F. Because the internal temperatures of the other seven specimens were substantially lower, the heaters could not be turned off. To remedy the situation, the two adequately heated specimens were covered with a metal sheet to prevent further heating of these specimens. The heaters were turned off at 150 min, when most of the specimens had the internal temperatures at the requisite value. Because concrete acts as a heat sink, the internal temperatures of all the specimens continued to rise

(between 5°F and 10°F) until a thermal equilibrium was established. Additional temperature readings were taken for about 5 hr. The specimens were then covered with a layer of fiberglass insulation and left to cool for about 12 hr before impregnation was started.

The ends of the grooves in the nine specimens were sealed with epoxy putty that does not dissolve in MMA. The putty was also used to make 1-in.-high dikes on the three cylinders. The specimens and the cylinders were covered with plastic sheets taped around the edges with duct tape. A slit was made in the middle of each plastic cover. The slits were covered by duct tape.

A mixture of 90 percent MMA and 10 percent trimethylolpropene trimethacrylate (TMPTMA) was prepared by weight. Then 0.5 percent azobisiobutyronitrile (Azo), of the above mixture, was added. The monomer was ponded on the top surface of the specimens and cylinders using a 20-ml pipette and placed through the slit in the plastic cover. The slit was kept covered after the monomer was placed.

The three cylinders had impregnation times of 6, 14, and 23 hr. During that period more monomer was added as needed when all existing monomer had diffused into the concrete. After the designated impregnation time for each cylinder was reached, the residual monomer was drawn off with the pipette. The cylinders were then placed in a hot water bath at 185°F for polymerization of the monomer. They were kept in the bath for 4 hr. The cylinders were taken out of the bath and cut longitudinally in half using a masonry saw. The cut cylinders were then etched with muriatic acid. The acid etches all portions of the concrete except the area of impregnation. Thus, the depth of impregnation of the cylinders could be visually distinguished.

The depth of polymer impregnation in concrete is a function of the square root of time of impregnation (*13*). Using this relation, the data obtained from the acid etching of the three cylinders indicated that the time corresponding to the required depth is 16 hr. Accordingly, the specimens were allowed to be impregnated for a period of 16 hr using the same procedure. At the end of that period, the residual monomer was drawn off with a pipette and the specimens were polymerized in a water bath at 185°F for 24 hr. At the end of the 24 hr, the specimens were taken out of the water bath. The specimens' grooves in the PM and PS series were filled with latex-modified mortar (LMM). Application of salt solution was resumed with the same wet and dry cycles used before treatments. Posttreatment potential and corrosion current measurements were taken periodically.

EXPERIMENT RESULTS AND ANALYSIS

After a number of potential and 3LP readings were taken, it was observed that the ambient temperature at the time of measurement had a significant effect on the resultant readings. The higher the temperature, the higher was the 3LP reading and the more negative the potential value. To analyze the data without developing a temperature correction factor, all readings were taken at room temperature, 72°F.

The potential values and the corresponding 3LP corrosion current values before and after treatments indicated that posttreatment potential values did not reflect very accurately the corrosion activity in the specimens. Although the corrosion current (I_{corr}) values in the treated specimens showed very little active corrosion, the corresponding potential values for most specimens were well into the 90 percent active corrosion region, more negative than −350 mV (*14*). The I_{corr} value is a more direct measure of corrosion activity than the potential value that is based on a probability function.

A total of 323 pairs of potential and corresponding I_{corr} values were used in a simple linear regression model (SLR) analysis. The SLR analysis resulted in an F-observed value of 219.845 and a p value of 0.001. This means that at the 5 percent significant level, the statistical test was significant and the F-observed value was well into the rejection region. Thus, there is a relationship between potential and I_{corr}. However, R^2 (the coefficient of determination) was 0.4065 and Pearson correlation coefficient was 0.64. This means that about 40 percent of the variation in I_{corr} could be predicted from the potential in the given sample data or the population. These values suggest that the relationship between potential and I_{corr} was not very strong. In view of the above results, only I_{corr} values were used for comparative analysis.

For comparing the effectiveness of the various treatment methods, the percent change in each posttreatment value was computed on the basis of the last pretreatment value as follows:

$$\Delta = \{(B - P)/B\} \times 100 \quad (1)$$

where

Δ = percent change,
B = last pretreatment I_{corr} in mA/ft², and
P = present I_{corr} in mA/ft².

Therefore, a positive Δ value indicates that the corrosion rate has decreased from its pretreatment level, whereas a negative Δ value signifies a higher corrosion level compared with its pretreatment value.

At Day 181 after the application of the overlays, the control specimens (CO) had a Δ value of −223.4 percent, demonstrating the extreme deteriorated condition of the untreated specimens, as shown in Figures 2 through 4. The latex (LM and PM) and polymer-impregnated (PC) groups demonstrated values of over +50 percent at Day 181, as presented in Figures 2 and 4, respectively. The low-slump (LS and PS) group was well below +50 percent improvement level, as shown in Figure 3. However, they remained in the positive range, indicating that the treatments had the desired effect of reducing corrosion levels. The low-slump overlay specimens had a value of +22.7 percent, whereas the low-slump overlay with polymer impregnation had a slightly higher value of +36.2 percent. However, at 41 days after overlays, all treated specimens, except for the polymer-impregnated specimens, had negative Δ values. A possible explanation is that a time lag is required before the overlays cause a decrease in the corrosion rates.

The absolute difference in the Δ between the last and first values may be a useful measure of the effectiveness of each treatment procedure. Table 1 summarizes this relationship. The maximum value of this measure was 91.03 percent for the LSDC specimens, and the minimum value was 42.30 percent for the polymer-impregnated specimens with no well-

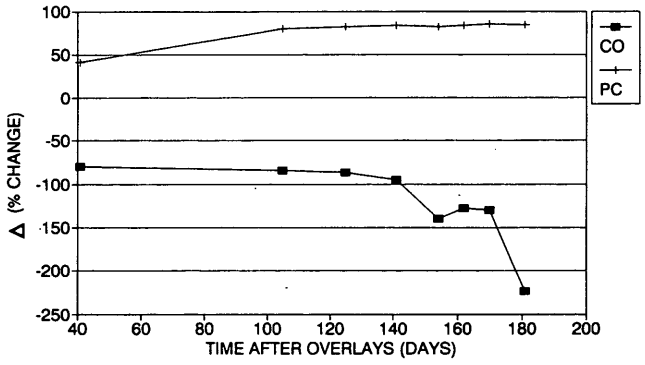

FIGURE 2 Percent change in I_{corr}-latex group.

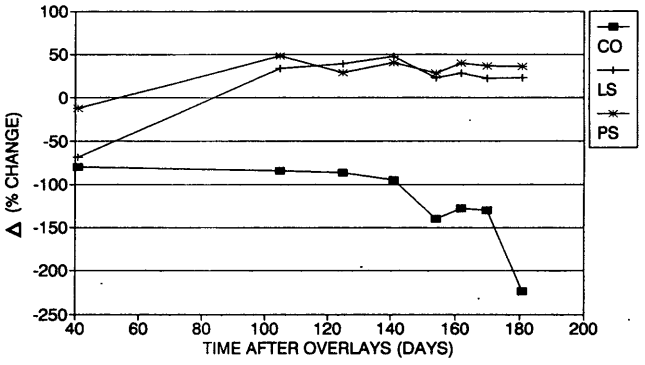

FIGURE 3 Percent change in I_{corr}-low-slump group.

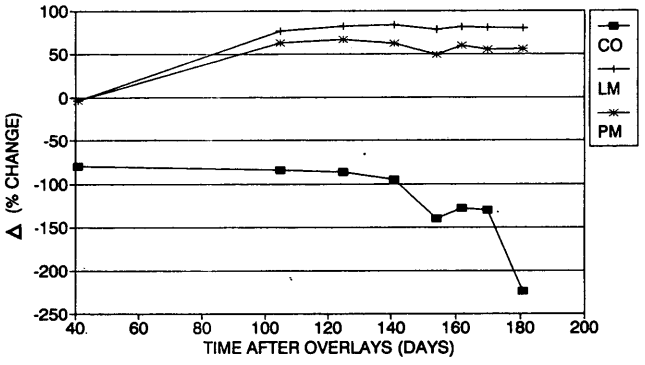

FIGURE 4 Percent change in I_{corr}-polymer-impregnated group.

defined trend among the three groups. This indicates that there was no appreciable difference in the effectiveness of any treatment method. The specimens with only overlays demonstrated higher values than polymer-impregnated overlays, which suggests that impregnation had decreased the effectiveness of the overlays in abating corrosion.

However, it was found that of both series with overlays and polymer impregnation, the PM series (LMC overlaid-polymer impregnation) and the PS series (LSDC overlaid-polymer impregnation) had the highest pretreatment corrosion rates of 4.99 mA/ft^2 and 4.92 mA/ft^2, respectively. It is conceivable that the higher corrosion rates had an effect on the "absolute difference" in Δ values. It is reasonable to expect that any

TABLE 1 Measures for Evaluating Effectiveness of Treatments

SPECIMEN (GROUP)	PRE-TREAT. Icorr (mA/SQ FT)	CHANGE @ DAY 41 (%)	CHANGE @ DAY 181 (%)	ABSOLUTE DIFF. (%)
LATEX				
LM	1.76	-3.37	+79.85	83.22
PM	4.99	-2.89	+55.84	58.73
LOW SLUMP				
LS	2.82	-68.35	+22.68	91.03
PS	4.92	-12.55	+36.19	48.74
POLYMER IMPREGNAT.				
PC	2.07	+41.73	+84.03	42.30

treatment method would be more effective if the initial corrosion rate were low compared with a relatively high initial corrosion rate.

By comparing the actual Δ values, the low-slump group appears to be less effective than the other two groups. However, this measure might not be an accurate representation of the situation, because it does not indicate the "degree" of the Δ.

The values of the Δ at Day 41 (see Table 1) indicate that the low-slump group had been least effective in abating corrosion at this age. The specimens that had been overlaid with LSDC (LS) had an unusual high negative Δ value (−68.35 percent) compared with the Δ values of the control specimens at the same time (−79.47 percent). The much-lower negative Δ value (−12.55 percent) of the specimens with LSDC overlaid-polymer impregnation (PS) could probably be attributed to the polymer impregnation. However, this value for the PS series was more negative than for the other groups. The higher pretreatment corrosion rates could not be considered as a possible cause, because the specimens with LMC overlaid-polymer impregnation (PM) also had similar high pretreatment corrosion rates. In the case of the PM series, the Δ at Day 41 was −2.89 percent, which was comparable to the −3.37 percent value for the LMC-overlaid specimens (LM).

A possible explanation for the apparently lower effectiveness of the low-slump group is that the low design slump of LSDC overlay resulted in an imperfect compaction after the overlay was placed. The LSDC overlay had a rough surface, which suggests the presence of more void spaces, resulting in increased permeability for more rapid ingress of chloride ions after treatment.

CONCLUSIONS AND RECOMMENDATIONS

This study concluded that there was insignificant difference in the effectiveness of the five treatment methods used in this investigation: LMC overlay, LSDC overlay, polymer impregnation, LMC overlay with polymer impregnation, and LSDC overlay with polymer impregnation. However, the treatments involving low-slump dense concrete overlay might be less effective as a corrosion abatement technique compared with the other four methods investigated.

Therefore, long-term studies should be performed to investigate the nature of corrosion activities after treatment methods had been applied. This would lead to the development of life-cycle models for various bridge deck rehabilitation techniques covered in the present study. Other practical factors could be considered in a future study of the effectiveness of the treatment methods used in this study: the influence of traffic volume and axle load.

REFERENCES

1. *Durability of Concrete Bridge Decks*. Report 5. Portland Cement Association, U.S. Bureau of Public Roads & Ten State Highway Agencies, 1969.
2. *Durability of Concrete Bridge Decks*. Final Report. Portland Cement Association, U.S. Bureau of Public Roads & Ten State Highway Agencies, 1970.
3. J. E. Slater. *Corrosion of Metal in Association with Concrete*. STP 818, ASTM, Philadelphia, Pa., 1983.
4. F. O. Wood. Survey of Salt Usage for Deicing Purposes. In *Automotive Corrosion by Deicing Salts*. National Association for County Engineers, Houston, Tex., 1981, pp. 25–35.
5. Strategic Highway Research Program—Research Plan. Final Report. Technical Research Area 43, Washington, D.C., May 1986, pp. 48–67.
6. R. E. Weyers and P. D. Cady. Development: Deep Grooving—A Method for Impregnating Concrete Bridge Decks. In *Transportation Research Record 962*, TRB, National Research Council, Washington, D.C., 1984, pp. 14–18.
7. R. E. Weyers, and P. D. Cady. Application: Deep Grooving—A Method for Impregnating Concrete Bridge Decks. In *Transportation Research Record 962*, TRB, National Research Council, Washington, D.C., 1984, pp. 19–21.
8. *3LP Package—Test Procedure, Data Analysis, Procedure, and General Information*. K. C. Clear, Inc., Boston, Va. June 1988.
9. *Test Model CL 500, Instruction Manual*. James Instruments, Inc., Chicago.
10. S. E. Herald. *The Development of a Field Procedure for Determining the Chloride Content of Concrete and an Analysis in the Variability of the Effective Diffusion Constant*. M.S. thesis. Virginia Polytechnic Institute and State University, Blacksburg, Sept. 1989.
11. K. C. Clear. *Reinforcing Bar Corrosion in Concrete: Effect of Special Treatments*. Report SP-49. American Concrete Institute, Detroit, Mich., 1975, pp. 71–82.
12. K. C. Clear. *Time-to-Corrosion of Reinforcing Steel in Concrete Slab*. Report FHWA RD-76-70. FHWA, U.S. Department of Transportation, 1976.
13. J. A. Manson, W. F. Chen, J. W. Vanderhoff, H. C. Mehta, P. D. Cady, D. E. Kline, and P. R. Blankenhorn. *NCHRP Report 190: Use of Polymers in Highway Concrete*. TRB, National Research Council, Washington, D.C., 1978.
14. T. Dutta. *Evaluation of the Effectiveness of Deep Polymer Impregnation as a Corrosion Abatement Technique for Overlaid Bridge Decks*. M.S. thesis. Virginia Polytechnic Institute and State University, Blacksburg, April 1991.

This paper represents the views of the authors only, and is not necessarily reflective of the views of the National Research Council, the views of the Strategic Highway Research Program (SHRP), or SHRP's sponsor. The results reported here are not necessarily in agreement with the results of other SHRP research activities. They are reported to stimulate review and discussion within the research community.

Publication of this paper sponsored by Committee on General Structures.

Preformed Membrane Performance Under Control Conditions

IMAD L. AL-QADI, RICHARD E. WEYERS, AND N. LALITH GALAGEDERA

Recently, preformed membrane systems have been used extensively in the United States and Europe as a preventive technique to reduce the corrosion in reinforced steel in bridge deck structures. However, the membrane integrity and effectiveness have not been addressed sufficiently. Therefore, an extensive laboratory investigation was conducted to evaluate the membrane effectiveness as a chloride barrier. A total of 48 typical bridge deck slabs were cast in the laboratory: 36 of them were 5 × 5 ft and 12 of them were 5 × 4 ft. A total of four slabs were control, another 4 were overlaid with hot-mix asphalt, and the rest (40 slabs) were covered with three types of preformed membranes and overlaid with hot-mix asphalt. The membranes were installed with various perforation sizes and frequencies. The slabs were exposed to 9 months of deicing (2.3 percent salt) application simulating the average of two winters of salt application in the New England states. Also, twelve 1- × 1-ft specimens were cast for preliminary evaluation. Ultrasonic pulse velocity was used as a nondestructive testing technique to evaluate the installed membranes. Ground truth cores were obtained and powdered concrete samples at three different depths were taken to measure the chloride contents. A statistical model was developed to predict the membrane status using the transit time measured by ultrasonic-pulse velocity. Chloride contents of the unprotected slabs were found to be relatively high compared with those of the protected ones. The perforation-per-unit area in the membrane system was correlated with the chloride content, and a hole size of ¼ in. was found to be a critical size.

The severity of the bridge corrosion problem led to the advent of the 1972 policy (*1*) that requires that deck protective systems be applied to all federally aided structures. This policy resulted in many experimental techniques for both the construction of new bridges and the rehabilitation of existing structures, including membrane installation overlaid with hot-mix asphalt. Membrane systems can be classified as sheet systems and liquid systems. Liquid systems consist of one or two components of moisture or chemically curing solutions that are applied to the concrete surface. Sheet systems include the various preformed factory-manufactured rolls that are bonded to bridge decks to form a continuous membrane.

Membranes have been used extensively for the past two decades in the United States, especially in the New England states. Installation of membrane systems was one of the most convenient methods to comply with the FHWA requirements (*1*). However, a few problems were identified that prevent membranes from achieving their main objective as chloride barriers. These problems include temperature effects during application, membrane installation, blistering, irregularities in the concrete surface, wearing surface application, water absorption, and water and chloride transmission.

In a recent study (*2*), 22 states indicated use of membrane systems as standard in their bridge decks; among them Illinois, Vermont, and Kansas have conducted experimental field studies (*3–6*). An extensive study was performed on bridge deck membrane systems in Vermont on 69 different bridge decks; evaluating 33 different membrane systems (*7,8*). The membranes' performance was evaluated on the basis of the analysis of chloride-contaminated samples. The investigation concluded that membranes, in general, performed well over the investigated period, 14 years, and only 7 percent of the collected concrete samples revealed chloride contamination at 1- to 2-in. depths. The use of membrane systems on old bridge decks was investigated in Kansas over a period of 16 years (*5*). Most of the membrane systems installed performed well, including a membrane installed on a 50-year-old bridge deck. LaCroix (*6*) in his study on 20 bridges over a period of 7 years concluded that using membrane systems for at least 4.5 years is considered economical. In general, the three study cases supported the use of membrane systems as chloride barriers.

Although many studies have been conducted to investigate the membrane properties in the laboratory (*9,10*), no laboratory studies were performed to study the performance (integrity and effectiveness) of installed membrane systems under controlled conditions. This study investigated the integrity and effectiveness of preformed membranes as chloride barriers. The integrity and effectiveness are interrelated membrane properties. If the membrane remains whole, there is a high probability that it will be an effective chloride barrier. However, the bonding to the bridge deck and the hot-mix asphalt overlay are important factors. Although the integrity of the membrane is breached, the membrane may still effectively extend the corrosion initiation time. The study investigated the effectiveness of three types of preformed membranes and developed a methodology to evaluate the membrane effectiveness nondestructively.

SPECIMEN PREPARATION

Twelve specimens, 1 ft × 1 ft × 8 in., were cast using Virginia A4AE bridge deck concrete mixture (*11*). Each specimen was reinforced with three No. 4 rebars. Type A membranes (which consist of a bottom layer of rubberized asphalt with adhesive qualities, a polypropylene barrier sheet, and a top layer of rubberized asphalt-wax) with slits (⅛ in., ¼ in., and ⅜ in.) cut on the center, were placed on nine specimens. The specimens were overlaid with 2.5 in. of hot-mix asphalt, Virginia

Department of Civil Engineering, Virginia Polytechnic Institute and State University, 200 Patton Hall, Blacksburg, Va. 24061.

S-5 (*11*). The mix design for the hot-mix asphalt is presented in Table 1. The three remaining specimens were considered control specimens and were not overlaid with hot-mix asphalt; however, membrane was installed on one of them. The 12 specimens were cast to evaluate nondestructive testing methods.

A total of 48 large-scale typical bridge deck slabs were cast. Thirty-six slabs, 5 ft × 5 ft × 7.6 in., were cast with removable wooden forms. Twelve slabs, 5 ft × 4 ft × 9.6 in. were cast using galvanized steel-in-place (SIP) bridge deck forms. The total thickness, 9.6 in., includes a 2-in. SIP-thick form. The slabs were reinforced with No. 5 at 8-in. spacing and No. 4 at 12-in. spacing for the top and bottom rebar mats. The two reinforcing mats were electrically isolated. A reinforcing wire coated with epoxy was connected to the center reinforcing bars of the top and bottom mats. A type T thermocouple was also cast into the center of the slabs at a depth of the center No. 5 rebar in the bottom and top mat. The top cover depth of the slabs is 2 in., and the bottom cover depth is 1 in.

After 7 days of curing, four types of standard preformed membranes were placed on 40 slabs: A, B, C, and D. Preformed membrane A consists of a bottom layer of rubberized asphalt with adhesive qualities, a polypropylene barrier sheet, and a top layer of rubberized asphalt-wax. Preformed membrane B consists of a nonwoven fibrous mat between two layers of bituminous and synthetic resins. Preformed membrane C consists of an impregnated fiberglass mesh between layers of a bituminous mastic. Membrane D is the same as membrane A except that it was installed on 5- × 4-ft SIP slabs. The membrane systems were placed according to the manufacturers' recommendations.

The patterns of membrane installation are presented in Figure 1. Nine slabs from each series, with membranes, were punched with various perforation sizes and frequencies. The tenth slab from each series had a sound membrane without perforations. Three hole sizes were used, ⅛ in., ¼ in., and ⅜ in., at three perforation frequencies, 0.5 percent, 1.0 percent, and 2.0 percent. All holes were located in a 1-ft² area at the center of each slab. Perforation sizes and frequencies are presented in Table 1, and a schematic diagram is presented in Figure 2. The eight remaining slabs were considered control slabs without preformed membranes. Four slabs, one from each series, were reinforced concrete without overlay, and the other four, one from each series, were reinforced concrete overlaid with hot-mix asphalt.

The sides of all slabs, at the concrete-asphalt interface, were coated with epoxy. A water-tight electrical box mounted on each slab housed the top and bottom rebar mat thermocouple, and a 10-Ω resistor was used to complete the electrical circuit between the mat. A 1-in.-high dike was placed on each slab surface 1 in. from the edges, and the areas outside the dikes were sealed with a Thoroseal, cement, lime, latex and quick-plug mixture. All slabs were covered with rooftops built from wood and covered with tar paper and plastic sheets to prevent any rainwater from ponding on the surfaces.

TESTING PROGRAM

The testing program included an investigation of the temperature effect on membranes, deicing salt application, nondestructive testing application, and investigating the pre-

TABLE 1 Membrane Perforation Size and Frequency

Series	Template	Membrane "A"	Membrane "B"	Membrane "C"	Membrane "A"
1	59 @ 1/8"	A1	B1	C1	D1
2	117 @ 1/8"	A2	B2	C2	D2
3	235 @ 1/8"	A3	B3	C3	D3
4	15 @ 1/4"	A4	B4	C4	D4
5	29 @ 1/4"	A5	B5	C5	D5
6	59 @ 1/4"	A6	B6	C6	D6
7	7 @ 3/8"	A7	B7	C7	D7
8	13 @ 3/8"	A8	B8	C8	D8
9	26 @ 3/8"	A9	B9	C9	D9
10	None	A10	B10	C10	D10
11	None (Asp + Con)	A11	B11	C11	D11
12	None (Con)	A12	B12	C12	D12

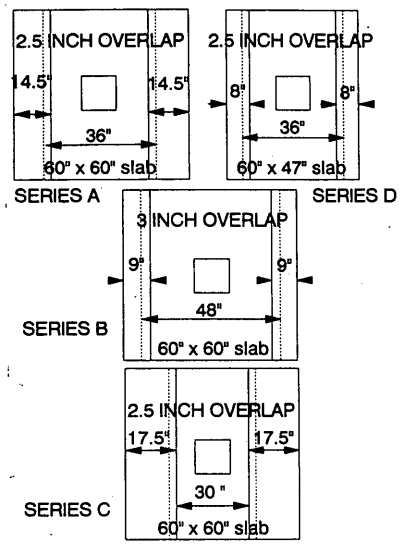

FIGURE 1 Membrane placement and series.

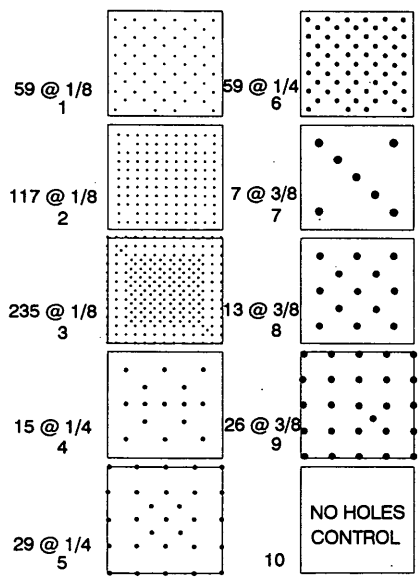

FIGURE 2 Schematic diagram of the membrane perforation frequencies and sizes.

formed membrane effectiveness using chloride content analysis of concrete samples.

Temperature Effect on Preformed Membranes

The temperature effect on preformed membranes was studied in two phases. The first one was preparing 4-in.-diameter membranes (from the three studied membrane types) and exposing them to various temperature levels. The temperature range used was 220°F to 270°F to simulate the laying and compaction temperature of the hot-mix asphalt in the field. A membranes showed a flow within the membrane system in which thin and thick spot areas were formed. These spots led to development of tiny holes in the membrane. B membranes experienced some shrinkages, especially at the edges. These shrinkages led to an uneven surface similar to a blistered membrane. C membranes showed minimum shrinkage and minimum flow within the system.

The second phase involved the preparation of 12 Marshall specimens overlaying membranes with various hole sizes and patterns. A ¼-in.-thick plexiglass sheet, which is temperature resistant up to 350°F, was placed over the Marshall mold's base. Membrane was placed over the plexiglass piece, which was used to evaluate the membrane holes through it. The following holes in the membranes were used: 1 × ⅛ in., five at ⅛ in. (ϕ), 1 × ⅜ in., and three at ⅜ in. (ϕ). The hot-mix asphalt, the same mixture as that for the slab overlay, was placed and compacted for 50 blows using an automatic Marshall compactor. The compaction was performed on one side; no compaction was performed on the plexiglass side.

For membrane A, the holes, five at ⅛ in. (ϕ) and 1 × ⅛ in., remained almost the same size after compaction. However, the three at ⅜ in. (ϕ) and 1- × ⅜-in. holes were increased dramatically in size. The bonding of the membrane to the hot-mix asphalt was satisfactory. The five at ⅛ in. (ϕ) and the 1- × ⅛-in. holes in membrane B remained almost the same after compaction, except that some tiny holes were developed in the second case. The three at ⅜-in. (ϕ) holes were almost the same, whereas an increase was noticed in the size of the 1- × ⅜-in. hole, and a development of tiny holes also occurred. The bonding of the membrane to the hot-mix asphalt was satisfactory. All holes in membrane C were almost the same size before and after the compaction, and the bonding to the hot-mix asphalt was satisfactory.

In general, membrane C performed the best in this experiment. However, an important factor was not studied at this stage: the bonding to portland cement concrete.

Deicing Salt Application

The 48 slabs were subjected to sodium chloride (NaCl) application. Each slab was ponded twice a week for 9 months, a total of 72 pondings. The slabs were salted at a rate of 11.4 tons/lane-mi/year using a solution of 0.25 lb of salt in 10.83 lb of water (2.3 percent); this rate simulates the average salt application rate for the New England states: Connecticut, 7.63; Maine, 6.40; Massachusetts, 18.34; New Hampshire, 13.49; and Vermont, 11.31 tons/lane-mi/year. During the deicing application period, the temperature of top and bottom rebar mats was measured monthly. The potential drop across the 10-Ω resistor was also measured monthly to monitor the corrosion activity.

Development of a Nondestructive Testing Methodology

No nondestructive testing method has been reported to determine defects in membrane systems. However, many nondestructive testing techniques have been used to detect defects in bridge decks (*12–17*). Three methods were used for feasibility study in this investigation: pulse radar, infrared system, and ultrasonic pulse velocity (V-meter).

A pulse radar using 1-GHz frequency was used to detect the holes in the membrane systems installed on the slabs. Because of the small thickness of the membrane sheets, the pulse radar was unable to detect any of the defects in the membranes. This can be explained by the low frequency used considering the membrane thickness and the similarity in dielectric properties between the membrane and the hot-mix asphalt.

Infrared technology was also unsuccessful because this technology is highly dependent on the surface condition and, therefore, will not be reliable in detecting any changes in the subsurface.

The ultrasonic pulse velocity (V-meter) evaluated has a frequency range of 20 to 500 kHz; the transmitter and receiver are operated at 54 kHz. The V-meter indicates the time taken for the earliest part of pulse sent by the transmitter and received by the receiver. The V-meter was first evaluated for 1- × 1-ft specimens using the direct method in which transducers are placed on the opposite sides of the specimen (top and bottom surfaces). In this method the path length is the specimen thickness; therefore, the method is the most accurate. The measurements were taken at three different positions. The average velocity for the nine specimens with preformed membrane and asphaltic concrete was 13,311 ft/sec. The maximum standard deviation between the three positions is 237, whereas the standard deviation of the pulse velocity among the nine specimens is 453. The average pulse velocity for the concrete specimen is 16,174 ft/sec, and its standard deviation is 42, whereas for concrete and membrane it is 14,969 ft/sec with a standard deviation of 18.

The successful use of the V-meter in the direct method led to the next stage of investigating its feasibility in the indirect method (both transducers on the same surface), which includes three different positions and four different distances between transmitter and receiver: 3.5, 5.0, 6.0, and 7.0 in. The study measured the transmittal time and detected the waveform. The measurements at the 3.5-in. distance were the most consistent and repeatable. However, because the measurements might be affected by the edge diffraction for 1- × 1-ft specimens, the measurements were repeated for the large-scale slabs.

On the large-scale slabs (only indirect method used), the 3.5-in. distance was also found to be the most repeatable and consistent. Therefore, a distance of 3.5 in. between transducers was used throughout the study. This distance is short enough to prevent the effect of reflected pulses from the bridge bottom and large enough to prevent detecting waves from the surface. According to Galan (*18*), the distance be-

tween transducers should be at least 0.9 the wavelength in the material. The average apparent velocity of the slabs is 13,311 ft/sec at a frequency of 54 kHz. Therefore, the apparent wavelength is 3.0 in. Thus, the minimum distance between transducers should be 2.7 in. This condition is satisfied by using a 3.5-in. distance.

The waveform was studied for the specimens and slabs. Voltage-time relationships for direct and indirect methods were obtained (*11*). A good correlation was found between the largest absolute amplitude and defects of the membrane for the specimens (1 × 1 ft) using the direct method. However, a lower correlation was found for the indirect method. The absolute amplitude is also affected by surface conditions. Therefore, no further analysis of this technique is discussed. However, using a network analyzer might indicate a better analysis of the waveform.

OVERALL INVESTIGATION

After 72 deicing applications on the slabs, half-cell potentials were measured for all the slabs. A grid was drawn on each slab to obtain an average of 20 to 25 half-cell potential measurements. An average of the CSE potential values for each slab is presented in Table 2. Potentials were measured through the overlay for slabs A1 through D11. The CSE potential values indicate corrosion initiation or uncertain corrosion activities in the unprotected slabs compared with a 90 percent probability of no corrosion activities in the protected slabs. This interpretation is in accordance with ASTM C 876-87.

Nondestructive Testing Investigation

V-meter measurements were taken for all slabs. The measurements were obtained at the center of each slab and at another two locations: at the overlap position and at the same distance from the center but perpendicular to the previous measurement (refer to Figure 2 for the overlap locations). The measurement at the center was labeled A, the second B, and the third C. The three measurements are presented in Table 3. After all the measurements were taken, ground truth cores were obtained. A water-cooled 3-in. diamond-core drill bit was used to drill through the hot-mix asphalt in the 40 slabs—A1 through D10. Two cores were extracted from each slab, one at the center where the V-meter measurements were taken and the other at one of the other two V-meter measurement locations; such as, at Slab A1 the second core was made at point B whereas the second core was extracted at point C for Slab A2.

The membranes were carefully evaluated in place and then removed and evaluated again. The criterion for membrane evaluation was a rating from 0 to 10. The 0 indicates an extremely deteriorated membrane with no bonding to the asphalt layer or to the concrete surface. The 10 indicates an excellent membrane condition with very strong bonding to the asphalt layer and the concrete surface. The rating from 7 to 10 indicates that membrane is in a good condition; the rating from 3 to 7 indicates that membrane is in a moderate condition and tiny holes or debonding, or both, exist that may affect the membrane performance; however, the membrane is generally in a satisfactory condition. A rating below 3 in-

TABLE 2 Average Potentials for Slabs

Slab I.D.	Average Potential (-mV)	Stand. Dev.	Median Potential	Min. Potential (-mV)	Max. Potential (-mV)	Temp Top Mat (F)	Temp Bottom Mat (F)	Slab I.D.	Average Potential (-mV)	Stand. Dev.	Median Potential	Min. Potential (-mV)	Max. Potential (-mV)	Temp Top Mat (F)	Temp Bottom Mat (F)
A1	145.3	1.1	146.0	143.0	146.0	----	87.9	B1	146.8	11.6	149.0	120.1	172.1	----	88.8
A2	229.9	1.5	229.9	225.0	233.0	93.7	88.7	B2	107.7	10.1	109.1	86.7	128.9	95.3	93.3
A3	141.2	16.5	137.0	110.7	192.9	73.0	72.1	B3	129.5	46.3	109.5	97.3	278.3	72.5	72.5
A4	187.4	2.4	187.0	183.0	192.0	71.6	71.7	B4	104.9	17.0	106.3	34.5	126.2	81.8	----
A5	----	----	----	----	----	----	----	B5	102.4	17.2	104.5	70.3	127.3	98.2	91.5
A6	120.2	6.4	118.5	110.2	137.3	----	----	B6	127.2	12.7	130.3	90.0	144.8	90.6	84.3
A7	204.0	18.1	203.0	166.2	241.0	76.2	74.1	B7	----	----	----	----	----	95.0	----
A8	163.1	4.8	163.3	154.7	170.3	92.3	90.7	B8	158.9	13.0	157.8	132.3	194.4	97.5	90.5
A9	132.4	8.3	132.0	117.7	162.9	91.5	84.9	B9	----	----	----	----	----	----	----
A10	183.3	11.0	183.0	146.5	205.0	93.5	82.4	B10	121.7	9.4	122.4	97.5	136.0	----	97.7
A11	58.8	13.4	58.3	34.0	95.0	88.7	85.2	B11	81.1	23.1	72.2	37.9	118.9	86.0	79.8
A12	191.6	46.4	181.0	116.5	300.0	----	----	B12	116.3	6.3	116.9	100.8	129.0	98.9	89.9
C1	146.3	16.5	150.0	114.0	172.4	99.3	93.3	D1	147.9	21.9	155.3	103.6	182.6	----	----
C2	158.1	14.9	157.6	127.6	190.6	88.1	----	D2	114.4	17.7	116.8	57.6	142.6	105.4	97.1
C3	162.5	2.1	162.2	158.6	167.5	72.5	72.1	D3	81.5	13.2	78.0	65.3	116.4	103.6	95.5
C4	91.4	1.9	91.6	87.6	94.9	72.8	----	D4	126.5	19.1	132.3	85.9	154.6	104.0	95.2
C5	119.9	25.6	125.1	108.2	135.9	74.4	73.5	D5	117.0	18.8	119.7	70.1	140.1	103.4	95.9
C6	159.3	10.5	156.8	147.1	186.9	88.2	82.7	D6	115.2	14.6	110.8	98.8	138.4	102.0	95.1
C7	284.3	34.3	271.0	243.0	349.0	87.2	81.1	D7	128.9	19.0	121.5	110.4	173.8	103.4	92.6
C8	138.7	11.0	141.0	107.8	158.1	94.8	----	D8	70.0	35.0	64.9	11.8	174.4	----	98.9
C9	----	----	----	----	----	----	----	D9	----	----	----	----	----	----	----
C10	102.2	12.7	104.7	61.5	121.0	91.2	----	D10	158.3	9.8	157.0	140.7	179.2	98.2	89.2
C11	100.5	19.6	110.3	49.9	121.5	----	86.1	D11	100.9	48.8	106.9	20.6	198.2	----	92.6
C12	220.0	17.6	222.0	185.5	253.0	107.2	96.2	D12	345.1	80.5	316.5	266.0	511.0	----	88.3

---- Bad Connection

TABLE 3 V-Meter Measurements and Membrane Evaluation

Slab I.D.	Position A V-Meter Reading (10E-6 sec)	Membrane Rating	Position B V-Meter Reading (10E-6 sec)	Membrane Rating	Position C V-Meter Reading (10E-6 sec)	Membrane Rating	Slab I.D.	Position A V-Meter Reading (10E-6 sec)	Membrane Rating	Position B V-Meter Reading (10E-6 sec)	Membrane Rating	Position C V-Meter Reading (10E-6 sec)	Membrane Rating
A1	19.2	5.0	19.1	5.0	22.3	—	C1	19.0	5.0	20.6	6.0	20.3	—
A2	19.6	5.5	20.1	—	21.5	7.0	C2	19.2	5.0	20.9	—	21.1	6.5
A3	19.8	5.0	21.1	7.5	20.6	—	C3	18.6	4.5	20.9	6.5	20.3	—
A4	19.3	5.0	22.5	8.0	20.7	6.0	C4	19.6	5.0	20.1	—	21.3	7.0
A5	20.5	5.5	23.0	8.5	19.7	—	C5	18.6	4.5	20.2	6.0	19.6	—
A6	19.9	5.5	20.5	—	23.1	8.5	C6	17.5	3.5	18.9	—	19.6	5.5
A7	18.4	4.5	21.3	7.0	20.8	—	C7	18.1	4.0	20.8	6.5	21.2	—
A8	19.5	5.0	17.7	—	18.5	5.0	C8	19.4	5.5	20.5	—	21.4	7.0
A9	17.3	3.5	19.1	5.0	17.0	—	C9	18.1	4.5	21.5	7.0	22.1	—
A10	21.1	6.5	17.4	—	20.7	6.0	C10	20.4	6.0	19.3	—	20.8	6.5
B1	18.5	4.5	21.2	7.0	22.5	—	D1	18.5	4.5	20.7	6.0	20.5	—
B2	20.4	5.5	20.6	—	22.2	7.0	D2	19.6	5.0	23.1	—	20.3	6.0
B3	17.5	3.5	22.4	8.0	22.0	—	D3	18.9	5.0	20.0	6.0	21.2	—
B4	19.2	5.0	20.0	—	20.6	6.0	D4	19.9	5.5	21.5	—	20.2	6.0
B5	19.4	5.0	20.0	5.5	19.8	—	D5	19.2	5.0	21.9	6.5	20.1	—
B6	20.1	5.5	20.8	—	20.9	6.0	D6	18.3	4.0	19.9	—	19.3	6.0
B7	17.3	3.5	20.7	6.0	19.4	—	D7	18.0	4.0	21.5	7.0	21.5	—
B8	19.0	5.0	19.1	—	22.6	8.0	D8	18.0	4.0	19.4	—	19.3	5.5
B9	17.5	3.5	23.4	8.5	18.1	—	D9	18.6	4.5	19.8	5.5	19.0	—
B10	20.7	6.0	18.0	—	18.6	4.0	D10	20.1	6.0	20.6	—	20.2	6.0

— No Cores Obtained

dicates that the membrane is ineffective as a chloride barrier. The factors considered in the evaluation were the membrane condition, its deterioration, and the bonding to the asphalt and concrete layers. This approach was used because of the inability of the V-meter to detect small holes in membranes; however, the V-meter was found to be sensitive to debonding. Eventually, any holes that exist in membranes will lead to debonding because the air void in hot-mix asphalt is always between 3 and 5 percent; therefore, chloride and water will penetrate through the holes and cause the debonding of membrane from the concrete surface. The results are presented in Table 3.

The perforations in Membranes A and C remained almost the same size; however an enlargement in the hole size in Membrane B was occasionally noticed. Membrane C had the fewest changes in hole sizes. This observation was in agreement with the tests performed earlier to investigate the temperature effects. In general, the performance of the three membrane types was satisfactory regarding their condition; however, the bonding to the asphalt or concrete, or both, was varied. Membrane B experienced best bond to the concrete, whereas Membrane A bonded the best to the asphalt concrete. The bonding of Membrane C was the worst. This explains the unchanged hole sizes of Membrane C in the slabs and in Marshall specimens after laying down the hot-mix asphalt.

Regression analysis was performed to correlate the membrane rating and the V-meter measurements. The following model was developed:

$$\text{Memrate} = -10.6 + 0.816\ \text{V-meter} \quad (1)$$

where Memrate is the membrane rating and V-meter is the V-meter measurement in microseconds.

The R^2-value of the above model is 85.9 percent (r = 92.7 percent), which indicates a good correlation between the membrane rating and the V-meter measurements. Also, the root mean square error, 0.447, indicates a strong correlation between the dependent and independent variables. A plot of the membrane rate versus V-meter measurement is presented in Figure 3. The level of significance for the two-tailed t-test concluded that both the slope and the constant are significant. Figure 3 also presents the 95 percent prediction interval of the regression model.

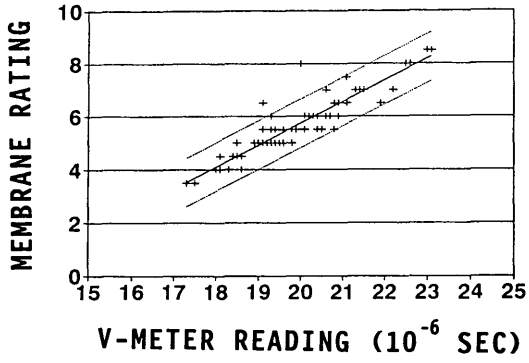

FIGURE 3 Membrane rating and V-meter measurement model with 95 percent prediction interval.

Chloride Content Measurements

After the membranes were removed from the cored locations in the slabs, half-cell potentials were taken directly at the concrete surface. The difference in potentials for a particular slab directly over the concrete or through the hot-mix asphalt overlays is insignificant (see data presented in Tables 2 and 4), which indicates that membrane sheets were able to provide continuity to measure half-cell potentials. However, they were sound enough to reduce the penetration of water and chloride as noted when the cores were removed; the salted water was accumulating between the membrane and the asphaltic layer, which may also explain the poor bonding between the asphalt layers and membranes.

Chloride contents were measured for each slab. Powdered concrete samples were obtained using a ⅛-in. vacuum bit that held the concrete powder in a collection unit. For a detailed procedure of collecting concrete samples, see Herald et al. (*19*). The concrete samples were obtained at three depths: 0 to ½, ½ to 1, and 1 to 1 ½ in. deep. The three depths are referred to as 1, 2, and 3, respectively. The chloride content was determined in each sample using the procedure developed by Herald et al. (*19*). The chloride contents in pounds per cubic yard of concrete and membrane ratings are presented in Table 5. The concrete samples for slabs A1, A2, and A4 were taken 5 days after the preformed membranes were removed. During that period, salted water was covering the holes, which again indicated the feasibility of membrane as a chloride barrier. The concrete samples obtained from these locations showed a high chloride content. Slab A11 indicated low chloride content, which was caused by some leak at the interface of the layers, whereas Slab A10 indicated a chloride content higher than expected. In general, the higher the percent of the perforation, the higher the chloride content. The chloride measurements at Depth 2 indicated that a hole size of ⅜ in. generally leads to a more chloride-contaminated concrete.

In Series B slabs, the chloride contents at B positions were the lowest. Position B is the location where membrane sheets overlap. This indicates that a thicker membrane is a better chloride barrier. However, an opposite observation was noticed in Series C: the overlap locations were more contaminated. This observation is in agreement with an earlier finding that membrane C demonstrated the least bonding. However, the membrane in Series C performed satisfactorily as a chloride barrier and indicated less chloride contamination compared with that of Series A and B. Of note here is that a membrane was installed on slab C11 by mistake. The membrane existence was first detected by the V-meter and then verified during the concrete sampling. The control slabs experienced a very high chloride content compared with that of the other protected slabs. The identification A, B, C, D, or E was used in control slabs to indicate that concrete samples were obtained at random locations.

The results of the effects of the hole size for all membranes are presented as an average for a specific location in Table 6. The average results showed that a ¼ in. hole is a critical size when considering the average chloride content (*1*). The chloride contents of the slabs with membranes of a hole size of ¼ in. and larger are two to three times the chloride content of the slabs with membranes of hole sizes of ⅛ in.

To study the effect of perforation, the chloride contents were investigated considering the perforation percent regardless of the hole size and frequency (Table 7). The effect of perforation was very pronounced for Series C slabs, which is the only series in which the hole size did not change after overlaying the hot-mix asphalt and that showed the least bonding to asphaltic overlay and concrete surface. This effect was obvious for the chloride measurements at the three depths for that series. The chloride at Depth 2 for the other series showed a correlation with the perforation percent. However, no correlation was observed when the chloride was considered at Depth 3. The reasons for the variation are that some of the slabs were not completely leveled, the hot-mix asphalt-layer thickness was varied, and some of the hole sizes were changed after laying the asphalt concrete. In general, the chloride contents in Series A and B slabs were high compared with that of Series C and D slabs. However, when all the

TABLE 4 Potential Measurement of Evaluated Slabs Directly on Concrete Surfaces

Slab I.D.	Position A	Position B	Position C	Slab I.D.	Position A	Position B	Position C
A1	-180.0	-157.0	----	B1	-162.0	-165.0	----
A2	-225.0	----	-227.0	B2	-107.0	----	-105.0
A3	-161.0	-173.0	----	B3	-168.0	-164.0	----
A4	-197.0	-196.0	-196.0	B4	-135.0	----	-128.0
A5	----	----	----	B5	-78.0	-90.0	----
A6	-143.0	----	-146.0	B6	-137.0	----	-147.0
A7	-208.0	-205.0	----	B7	-168.0	-142.0	----
A8	-179.0	----	-189.0	B8	-164.0	----	-107.0
A9	-177.0	-176.0	----	B9	-95.0	-99.0	----
A10	-189.0	----	-178.0	B10	-124.0	----	-115.0
C1	-153.0	-154.0	----	D1	-165.0	-146.0	----
C2	-161.0	----	-160.0	D2	-111.0	----	-84.0
C3	-158.0	-169.0	----	D3	-54.0	-140.0	----
C4	-121.0	----	-117.0	D4	-115.0	----	-140.0
C5	-125.0	-120.0	----	D5	-96.0	-147.0	----
C6	-161.0	----	-151.0	D6	-82.0	----	-52.0
C7	-229.0	-229.0	----	D7	-130.0	-143.0	----
C8	-149.0	----	-146.0	D8	-74.0	----	-49.0
C9	----	----	----	D9	-78.0	-94.0	----
C10	-115.0	----	-110.0	D10	-186.0	----	-205.0
				D11	-89.0	-87.0	----

TABLE 5 Chloride Content of Evaluated Slabs

Slab	Cl (1) (lb/cu.yd)	Cl (2) (lb/cu.yd)	Cl (3) (lb/cu.yd)	Membrane Rating	Slab	Cl (1) (lb/cu.yd)	Cl (2) (lb/cu.yd)	Cl (3) (lb/cu.yd)	Membrane Rating
A1-A	12.988	25.903	31.871	5.0	B1-A	3.813	0.724	1.053	4.5
A1-B	18.329	11.493	6.433	5.5	B1-B	0.705	0.024	0.009	7.0
A2-A	12.088	1.955	0.772	5.5	B2-A	0.595	0.934	0.487	5.5
A2-C	9.668	2.537	0.791	7.0	B2-C	1.033	0.595	0.934	7.0
A3-A	0.731	<0.04	<0.04	5.0	B3-A	3.504	1.558	1.558	3.5
A3-B	0.397	<0.04	<0.04	7.5	B3-B	1.278	0.993	0.993	8.0
A4-A	17.193	7.572	3.267	5.0	B4-A	2.190	0.212	<0.04	5.0
A4-B	7.766	0.753	0.849	8.0	B4-C	4.953	1.536	1.195	6.0
A5-A	1.303	<0.04	<0.04	5.5	B5-A	5.607	1.134	1.033	5.0
A5-B	2.094	<0.04	<0.04	8.5	B5-B	2.494	0.895	0.800	5.5
A6-A	6.238	<0.04	<0.04	5.5	B6-A	1.603	---	1.093	5.5
A6-C	3.010	0.415	<0.04	8.5	B6-C	4.575	0.954	1.154	6.0
A7-A	1.281	<0.04	<0.04	4.5	B7-A	2.442	1.013	0.974	3.5
A7-B	2.069	<0.04	<0.04	7.0	B7-B	3.065	0.954	1.033	6.0
A8-A	3.194	0.528	0.694	5.0	B8-A	3.194	0.528	0.694	5.0
A8-C	3.493	0.528	0.583	5.0	B8-C	3.493	0.528	0.583	8.0
A9-A	2.354	0.113	0.063	3.5	B9-A	2.606	0.230	0.732	3.5
A9-B	3.034	0.334	<0.04	5.0	B9-B	1.667	0.675	0.510	8.5
A10-A	6.520	0.180	0.163	6.5	B10-A	2.796	0.351	0.456	6.0
A10-C	3.179	0.457	0.096	6.0	B10-C	1.024	0.601	0.564	4.0
A11-A	0.548	0.096	0.096	---	B11-A	2.660	0.403	0.299	---
A11-B	1.907	0.282	0.047	---	B11-B	0.984	0.403	0.492	---
A12-A	10.612	1.362	0.299	---	B12-A	8.682	0.546	---	---
A12-B	15.188	2.484	0.475	---	B12-B	12.693	0.656	0.163	---
A12-C	8.680	3.854	0.404	---	B12-C	12.763	2.660	0.113	---
A12-D	13.348	5.488	1.427	---	B12-D	9.667	0.675	0.163	---

Slab	Cl (1) (lb/cu.yd)	Cl (2) (lb/cu.yd)	Cl (3) (lb/cu.yd)	Membrane Rating	Slab	Cl (1) (lb/cu.yd)	Cl (2) (lb/cu.yd)	Cl (3) (lb/cu.yd)	Membrane Rating
C1-A	ERR	ERR	ERR	5.0	D1-A	0.488	0.104	<0.04	4.5
C1-B	0.230	0.247	0.385	6.0	D1-B	0.506	0.087	<0.04	6.0
C2-A	0.213	0.299	0.113	5.0	D2-A	0.561	0.380	0.275	5.0
C2-C	0.213	0.333	0.196	6.5	D2-C	0.711	0.206	0.155	6.0
C3-A	2.005	0.528	0.474	4.5	D3-A	0.654	0.362	0.292	5.0
C3-B	0.846	0.247	0.063	6.5	D3-B	0.432	0.398	1.027	6.0
C4-A	0.403	0.196	0.213	5.0	D4-A	1.278	0.309	0.223	5.5
C4-C	2.553	0.316	0.247	7.0	D4-C	0.206	0.155	0.257	6.0
C5-A	0.368	0.528	0.368	4.5	D5-A	0.673	0.327	0.104	5.0
C5-B	1.488	0.456	0.583	6.0	D5-B	0.808	0.327	0.309	6.5
C6-A	1.554	0.385	0.456	3.5	D6-A	0.292	0.189	0.071	4.0
C6-C	0.656	0.299	0.130	5.5	D6-C	0.172	0.172	<0.04	6.0
C7-A	0.350	0.524	0.000	4.0	D7-A	0.172	0.223	0.488	4.0
C7-B	0.687	0.687	0.761	6.5	D7-B	0.344	0.240	0.104	7.0
C8-A	1.070	0.780	0.780	5.5	D8-A	0.155	0.121	0.257	4.0
C8-C	0.837	0.687	0.669	7.0	D8-C	0.172	<0.04	0.104	5.5
C9-A	0.687	0.614	0.507	4.5	D9-A	0.344	0.292	<0.04	4.5
C9-B	1.464	0.560	0.524	7.0	D9-B	0.309	0.275	0.189	5.5
C10-A	0.578	0.650	0.542	6.0	D10-A	0.257	0.071	0.087	6.0
C10-C	0.507	0.507	0.650	6.5	D10-C	0.415	0.275	0.155	6.0
C11-A	1.336	0.780	0.560	---	D11-A	0.598	<0.04	0.054	---
C11-B	1.336	0.669	0.385	---	D11-B	0.926	0.087	0.054	---
C12-A	15.097	13.304	7.182	---	D12-A	9.012	1.153	---	---
C12-B	20.455	7.884	1.729	---	D12-B	11.944	2.094	0.170	---
C12-C	22.019	12.139	5.589	---	D12-C	10.524	2.810	0.291	---
C12-D	22.563	8.632	2.740	---	D12-D	10.962	3.970	1.303	---
C12-E	18.704	7.645	2.152	---	D12-E	11.944	1.217	0.052	---

TABLE 6 Average Chloride Content for Slabs at a Specific Location

Position On Slab	Avg. Cl (1) (lb/cu.yd)	Std	Avg. Cl (2) (lb/cu.yd)	Std	Avg. Cl (3) (lb/cu.yd)	Std
1A	1.533	1.604	0.417	0.240	0.472	0.428
1B	0.472	0.193	0.421	0.377	0.275	0.157
2A	0.444	0.177	0.550	0.279	0.275	0.145
2C	0.641	0.342	0.354	0.165	0.118	0.067
3A	1.730	1.152	0.629	0.590	0.590	0.586
3B	0.747	0.369	0.432	0.354	0.550	0.472
4A	1.297	0.739	0.236	0.055	0.157	0.086
4C	2.555	1.942	0.668	0.613	0.550	0.444
5A	1.985	2.127	0.511	0.405	0.393	0.385
5B	1.730	0.625	0.432	0.314	0.432	0.283
6A	2.437	2.272	2.083	0.145	0.432	0.425
6C	2.123	1.785	0.472	0.295	0.354	0.464
7A	1.061	0.904	0.472	0.369	0.393	0.389
7B	1.533	1.093	0.472	0.354	0.472	0.417
8A	1.887	1.325	0.472	0.240	0.629	0.200
8C	2.005	1.521	0.432	0.252	0.511	0.216
9A	1.494	0.991	0.314	0.189	0.354	0.299
9B	1.612	0.963	0.472	0.165	0.314	0.204
10A	2.555	2.492	0.314	0.220	0.314	0.200
10C	1.336	1.097	0.472	0.114	0.354	0.252

series are considered, the chloride contents at all depths are proportional to the perforation percent, as presented in Table 7. The chloride content drops dramatically from Depth 1 to Depth 2; however, the decrease in chloride content between Depths 2 and 3 is insignificant.

To investigate the effect of membrane type on the chloride content a regression analysis was performed. Considering chloride contents at Depth 1, R^2 was 10 percent (r = 32 percent); for chloride content at depth 2, R^2 was 38 percent (r = 62 percent); and for chloride at depth 3, R^2 was 50 percent (r = 71 percent). These values are considered low, and no strong correlation exists between the membrane type and the chloride content.

FINDINGS AND CONCLUSIONS

To investigate the integrity and effectiveness of preformed membrane systems, a comprehensive laboratory investigation was conducted. Three types of preformed membranes were installed on large-scale slabs and studied under controlled conditions. The membranes were perforated with various hole sizes at varying frequencies and percent of perforation per unit area. The slabs were overlaid with hot-mix asphalt and exposed to deicing salt ponding. The potential drop in the slabs and temperature were monitored throughout the study. The effects of temperature on membrane systems were also investigated. An evaluation of nondestructive testing methods was performed, and the ultrasonic pulse velocity measurements were strongly correlated with membrane status. Concrete powder samples were obtained from two locations of each slab at three depths to determine chloride contents.

Findings

The temperature was found to have an effect on the preformed membrane sheets. At 220°F to 275°F, Membrane A showed liquidity within the system and an increase in the hole sizes at ⅜ in. Membrane C experienced some shrinkages at the edges of the membrane sheet without any changes in the hole sizes, whereas Membrane B performed the best but showed an increase in the hole sizes at ⅜ in.

The ultrasonic pulse velocity (indirect method) was able to detect debonding and defects of the membrane systems, whereas pulse radar and infrared failed to identify the membrane systems in the slabs. A statistical model was developed to correlate the ultrasonic pulse velocity and the membrane status for the large-scale slabs with a correlation of 92.7 percent (R^2 = 85.9).

A major difference was found in the chloride contents between the protected and unprotected slabs. The unprotected slabs experienced a high chloride content compared with the protected slabs. The chloride content results indicated that the chlorides were relatively higher at the overlapping location for C membranes, which indicates its weak bonding property, whereas B membranes that showed high bonding property resulted in relatively less chlorides at the overlapping locations. The hole size of ¼ in. was observed as a critical size. The percent of perforation was found to correlate with the amount of chloride content. However, the effect of membrane type was found to be minimum.

TABLE 7 Relationship Between Average Chloride Content and Perforation

PERCENT HOLES (%)	AVG. Cl (1) (LB/CU.YD)	STD DEV	AVG. Cl (1) (LB/CU.YD)	STD DEV	AVG. Cl (1) (LB/CU.YD)	STD DEV
0.5 (SERIES A)	----	----	----	----	----	----
1.0 (SERIES A)	2.240	0.943	0.275	0.236	0.373	0.334
2.0 (SERIES A)	3.105	2.311	0.079	0.035	0.039	0.020
0.5 (SERIES B)	2.791	0.711	0.629	0.342	0.708	0.464
1.0 (SERIES B)	3.145	2.056	0.865	0.263	0.747	0.224
2.0 (SERIES B)	2.555	0.770	0.904	0.668	1.140	0.338
0.5 (SERIES C)	0.354	0.197	0.393	0.134	0.197	0.114
1.0 (SERIES C)	0.550	0.377	0.550	0.193	0.432	0.275
2.0 (SERIES C)	1.415	0.558	0.511	0.094	0.472	0.020
0.5 (SERIES D)	0.708	0.421	0.236	0.083	0.236	0.177
1.0 (SERIES D)	0.472	0.220	0.275	0.114	0.236	0.075
2.0 (SERIES D)	0.432	0.169	0.393	0.244	0.118	0.102
0.5 (ALL SERIES)	1.297	1.124	0.377	0.287	0.342	0.366
1.0 (ALL SERIES)	1.533	1.655	0.507	0.318	0.444	0.307
2.0 (ALL SERIES)	1.887	1.627	0.432	0.425	0.472	0.464

Conclusions

This study concluded that membrane systems will protect the bridge decks by reducing the chloride and water intrusion. The following conclusions resulted from this study.

1. The use of membrane sheets is a desired technique to protect bridge deck structures.
2. Holes in preformed membranes increased chlorides and water intrusion; however, the effectiveness of membranes is significantly affected by perforation of a hole size of ¼ in. or larger.
3. The membrane integrity is affected by its bonding to the concrete surface and hot-mix asphalt overlay.
4. Membrane A had the strongest bonding to the asphaltic overlay, whereas membrane B had the strongest bonding to the concrete. Although Membrane C showed the weakest bonding, the system was least affected by the overlay application.
5. The membrane status can be evaluated in place nondestructively using the indirect ultrasonic pulse velocity method that can be used in a developed model to predict the membrane status.

ACKNOWLEDGMENT

The authors would like to express their thanks to Mike Otegui, Marcia Votour, and Chuck Subllet for their assistance in collecting the data.

REFERENCES

1. *NCHRP Synthesis of Highway Practice 57: Durability of Concrete Bridge Decks*. TRB, National Research Council, Washington, D.C., May 1979.
2. W. P. Chamberlin. *Summary of the Field Survey Questionnaire*. SHRP C-103 Project, Task 1. Strategic Highway Research Program, Washington, D.C., June 1989.
3. R. I. Frascoia. Performance of Waterproofing Membranes on New and Rehabilitated Bridge Decks. Presented at 4th Annual International Bridge Conference and Exhibition, Bridge Deck Rehabilitation Seminar. Pittsburgh, Pa., June 22–24, 1987.
4. R. I. Frascoia. *Performance of Waterproofing Membranes on Chloride Contaminated Bridge Decks*. Interim Report 90-3. State of Vermont Agency of Transportation Materials and Research Division, Feb. 1990.
5. I. I. Bukavatz and C. F. Crumpton. Kansas's Experience with Interlayer Membranes on Salt-Contaminated Bridge Decks. In *Transportation Research Record 962*, TRB, National Research Council, Washington, D.C., 1984.
6. J. E. LaCroix. Bridge Deck Condition Survey Phase V. Long-Term Performance Evaluation. Report 100. Illinois Department of Transportation, Feb. 1985.
7. R. I. Frascoia. Field Performance of Experimental Bridge Deck Membrane Systems in Vermont. In *Transportation Research Record 962*, TRB, National Research Council, Washington, D.C., 1984.
8. R. I. Frascoia. *Evaluation of Bridge Deck Membrane Systems and Membrane Evaluation Procedures*. Report 77-2. State of Vermont Agency of Transportation Materials and Research Division, 1977.
9. A. R. Price. *A Field Trial of Waterproofing Systems for Concrete Bridge Decks*. Report 185. Transportation and Road Research Laboratory, Berkshire, United Kingdom, 1989.
10. A. R. Price. *Laboratory Tests on Waterproofing Systems for Concrete Bridge Decks*. Report 248. Transportation and Road Research Laboratory, Berkshire, United Kingdom, 1990.
11. I. L. Al-Qadi, R. E. Weyers, N. L. Galagedra, and P. D. Cady. *Condition Evaluation of Concrete Bridges Relative to Reinforcement Corrosion. Volume 4: Deck Membrane Effectiveness and a Method for Evaluating Membrane Integrity*. Final Report. Strategic Highway Research Fund, Washington, D.C., 1992.
12. R. G. Liptai and D. O. Harris. Acoustic Emission—An Introductory Review. *Materials Research and Standards*, Vol. 11, No. 3, March 1971, pp. 8–10.
13. I. L. Al-Qadi, P. E. Sebaaly, and J. C. Wambold. New and Old Technology Available for Pavement Management System to Determine Pavement Condition. In *Pavement Management Implementation*. Special Technical Publication 1121. ASTM, Philadelphia, Pa., 1991.
14. R. F. Paetzold, G. A. Mutzkanin, and A. DeLos Santos. Surface Soil Water Content Measurement Using Pulsed Nuclear Magnetic Resonance Techniques. *American Journal of Soil Science Society*, Vol. 49, No. 3, pp. 537–540.
15. D. Manning and F. B. Holt. Detecting Deterioration in Asphalt Overlaid Bridge Decks. In *Transportation Research Record 899*, TRB, National Research Council, Washington, D.C., 1984.
16. T. Chung, C. R. Carter, D. C. Manning, and F. B. Holt. *Signature Analysis of Radar Waveforms Taken on Asphalt Covered Bridge Decks*. Report ME-84-01. Canada Ministry of Transportation and Communications. June 1984.
17. G. Clemena. Non-Destructive Inspection of Overlaid Bridge Decks with Ground Penetrating Radar. In *Transportation Research Record 899*, TRB, National Research Council, Washington, D.C., 1984.
18. A. Galan. *Combined Ultrasound Methods of Concrete Testing*. Elsevier Science Publishing Company, Inc., New York, 1990.
19. S. E. Herald, M. Henry, I. L. Al-Qadi, R. E. Weyers, M. A. Feeney, and S. F. How Lum. *Chloride Content of Concrete*. Report 9133. Pennsylvania Transportation Institute, Pennsylvania State University, University Park, Pa., Aug. 1991.

This paper represents the views of the authors only, which are not necessarily reflective of the views of the National Research Council or the views of the Strategic Highway Research Program (SHRP) or its sponsor. The results reported here are not necessarily in agreement with the results of other SHRP research activities. They are reported to stimulate review and discussion in the research community.

Publication of this paper sponsored by Committee on General Structures.

Design and Construction of Falsework on Federal Lands Highway Projects

DONALD W. MILLER AND SHEILA R. DUWADI

FHWA has developed a research program to address bridge falsework design and construction. This program was initiated as a result of the findings from the investigation into the collapse of a bridge carrying the future eastbound lanes of Maryland Route 198 over the southbound lanes of the Baltimore-Washington Parkway on August 31, 1989. It was determined by the collapse review board that existing procedures for design and construction of bridge falsework were, at best, suspect. To guide and direct this program, FHWA formed the Scaffolding, Shoring, and Forming Task Group. Members of the task group represent state highway departments, contractors, manufacturers/suppliers, professional societies, TRB, and the federal government. Their task is to collect and develop a comprehensive design and construction specification relative to the use of temporary works for bridges.

On the morning of August 31, 1989, the final concrete placement for the top deck slab of a posttensioned concrete box girder bridge being constructed to carry the future eastbound lanes of Maryland Route 198 over the southbound lanes of the Baltimore-Washington Parkway was under way. Concrete placement for the top slab of the Maryland Route 198 bridge over the Baltimore-Washington Parkway started at about 2 a.m. so that the 154 yd^3 of concrete for the top deck could be placed and finished in the cool, early-morning temperatures. Suddenly and without warning, the supporting falsework collapsed. On the basis of concrete delivery tickets, 132 yd^3 of concrete had been placed at the time of the collapse. This left 16 to 20 ft of deck on the east end of the bridge remaining to be placed. The falsework consisted of three simple-span sections: a 35-ft roadway span and two 28-ft abutment spans. The superstructure construction was supported by timber formwork on steel longitudinal support beams that were supported by manufactured metal shoring towers, as shown in Figure 1. This scenario is becoming all too familiar in the bridge design and construction workplace of today. With an increase in the use of manufactured support systems, the design and construction of falsework are becoming more complex and critical parts of bridge construction.

The collapse of the falsework initiated a great deal of concern within FHWA and Congress as to the safety of current practices relative to falsework for bridges. The collapse occurred at about 6:50 a.m. during morning rush hour on the Parkway. Nine construction workers and five commuters were injured, with one sustaining serious injuries as a result of the collapse. There were no fatalities.

D. W. Miller, FHWA, 21400 Ridgetop Circle, Sterling, Va. 22170. S. R. Duwadi, Turner-Fairbank Highway Research Center, 6300 Georgetown Pike, McLean, Va. 22101.

FALSEWORK FAILURES

A number of other collapses have occurred since the Baltimore-Washington Parkway incident. On April 24, 1990, falsework for the Lake Street/Marshall Avenue bridge near St. Paul, Minn., collapsed, killing one worker. An estimated 300 tons of steel and 1,100 tons of concrete fell into the Mississippi River. According to the state bridge engineer, the failure was related to human design error.

On June 18, 1990, the falsework supporting one section of a 63-ft welded plate tub girder being erected at N-370 and US-75 in Bellevue, Nebr., collapsed, dropping the girder. There were no injuries. On the basis of investigation and analysis, the falsework collapse was initiated by lateral loads on the falsework caused by strong southwest winds. The failure of the falsework was progressive, ending with the collapse of the girder. The progressive failure sequence was simulated through transverse frame failure modeling. Wells Engineering, Inc., who investigated the cause of the collapse, ran an analysis of the falsework system. They found that some members could be expected to yield at wind speeds of 34 mph. Progressive collapse could be expected at certain joints at wind speeds of 37 mph. The Offutt Air Force Base Weather office verified winds in excess of 35 mph and gusting during the evening of June 18.

On July 13, 1990, the US-45 bridge under construction over Spring Brook in Antigo, Langrade County, Wisc., collapsed, as placement of deck concrete was nearing completion. The cause of the collapse is believed to be shear failure of the 48 bolts connecting the deck form supports to substructure abutment walls. This initial failure led to subsequent shear failure of all but one of the remaining bolts.

On October 10, 1990, at 1:18 a.m., a section of the superstructure falsework for an elevated connector ramp of the I-880/SR-238 interchange in San Leandro, Calif., collapsed. Three workers were injured, but there were no fatalities. The accident occurred during the erection of a falsework beam over an existing ramp. The cause of the collapse was determined by Caltrans to be related to erection errors.

RESEARCH PROGRAM

One of the recommendations made by the Collapse Review Board for the investigation into the Maryland Route 198 falsework collapse, and subsequently supported by Congress, was that FHWA should develop a research project on manufactured falsework assemblies. The study should be structured to improve present specifications and result in new guidelines

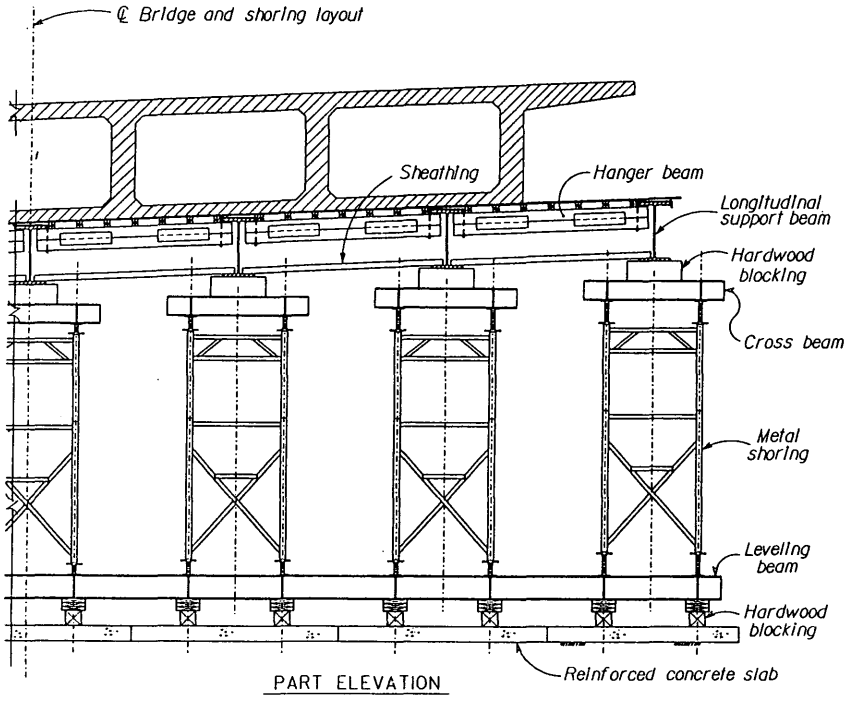

FIGURE 1 Superstructure construction for concrete girder bridge carrying Maryland Route 198 over Baltimore-Washington Parkway.

for design review and field inspection. There is also a pressing need for technical information on the various horizontal and vertical forces that interreact in shoring tower arrangements.

To implement this recommendation and to encourage cooperation, FHWA established the multidisciplinary Scaffolding, Shoring, and Forming Task Group to develop and guide the program. The Task Group includes representatives from FHWA; AASHTO; Associated General Contractors; American Road and Transportation Builders Association; TRB; the Scaffolding, Shoring, and Forming Institute; and ASCE.

The first task undertaken by the Task Group was to contract with a consulting firm to perform a synthesis of all existing codes and specifications dealing with bridge temporary works in the United States and abroad. This task was necessary because no national standards currently exist. In investigating the Maryland Route 198 collapse, it was felt that some industry practices relative to the safe use of metal shoring were not well documented and, consequently, not available to the engineers involved for consideration in reviewing the system used. Therefore, the Task Group felt that they needed to know the extent of temporary works design aids available in the worldwide engineering community before they could develop a concise manual addressing the design and construction of temporary works. The synthesis documents both the state of the art and the state of the practice. It also looked for any gaps or inconsistencies in existing specifications. After a vast amount of literature on temporary works was reviewed, it was found that on a worldwide basis, there are no major gaps in the understanding of temporary structures. However, the existing worldwide standards are not entirely adaptable to U.S. codes and construction practices and the proprietary shoring systems common to the U.S. construction industry. Despite the available information, the mistakes that contributed to prior falsework failures continue to be repeated. This suggests that although there may be no gaps in the understanding of temporary works, there is a problem with getting this information to the people doing the work.

Based on a review of current state practices, it is evident that design review and inspection procedures vary considerably from one state to another. This review covered all 50 states, the District of Columbia, Puerto Rico, and 12 Canadian provinces. As would be expected, states that are active in constructing cast-in-place concrete highway bridges are generally found to have comprehensive specifications and design guidelines, compared with those that mostly construct beam-type bridges. However, even in states that design and construct mainly beam-type bridges, a significant number of bridges are being built using cast-in-place construction methods that require extensive falsework. A clear need exists to develop unified design criteria and standards for temporary structures.

The second task undertaken by the Task Group was to develop a standard specification for bridge temporary works. The specification is written as a generic specification that can be used and modified by any state. It defines responsibilities of the parties involved at the time of bidding. Among other issues, it states that the contractor is responsible for designing and constructing safe and adequate temporary work systems. The selection of material suitable for falsework is the responsibility of the contractor, but subject to the engineer's review and approval. The contractor shall certify that the manufactured devices have been maintained in a condition to safely carry their rated loads. Each piece of manufactured shoring shall be clearly identified with regard to working load capacity. Working drawings shall be prepared by the con-

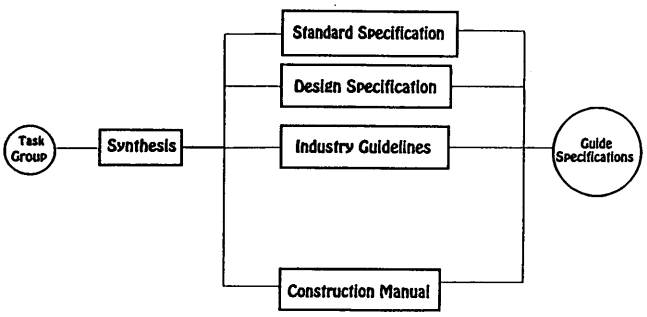

FIGURE 2 FHWA bridge temporary works research program.

tractor under the guidance of a registered professional engineer. Before placing concrete, the contractor shall have a professional engineer inspect the falsework and certify that the system is safe and erected in conformance with the approved working drawings.

The third task recognized by the Task Group was the need for a clear, practical design specification based on the best current technology (see Figure 2). A preliminary outline of the areas to be covered was developed by the group and given to a consultant for development. The design specifications will be modeled as much as practical around AASHTO's *Standard Specifications for Highway Bridges*. A comprehensive commentary will also be developed to record the origin and clarify the intent of the key provisions of the specifications. Temporary structures will include, as a minimum, scaffolding, shoring, forming, and cofferdams.

The fourth task to be undertaken was to ask the private-industry members of the Task Group to develop a set of criteria acceptable to the industry about instituting a certification program for individuals and companies involved with the design, handling, and erection of manufactured falsework assemblies.

The final task is to deal with the development of a construction manual. Realizing that some states do have good construction manuals, this task has been deferred until more work is done on the design specification development.

SUMMARY

The primary reason for this study was the collapse of the falsework on the Maryland Route 198 bridge over the Baltimore-Washington Parkway and subsequent recommendations by the Collapse Review Board to develop better specifications and guidelines. However, numerous other falsework collapses have occurred since then. Some have been design related, whereas others have been the result of poor construction practices.

The end product of the FHWA program is to develop a standard specification and a design manual on bridge temporary works with comprehensive commentaries, a synthesis of all codes and specifications dealing with the subject, and a construction manual if a need exists. These will be developed with input from representatives of AASHTO, private industry, and FHWA.

The guidelines and specifications developed will be applicable both to construction projects under the direct supervision of the Federal Lands Highway Office of FHWA and to projects carried out by the states with federal-aid highway funds. The end objective is to improve construction site safety.

Publication of this paper sponsored by Committee on Construction of Bridges and Structures.

Fatigue Life Study for a Railroad Bascule Bridge

CHARLES T. JAHREN AND JOHN A. ROOKER

A fatigue study was undertaken for an 80-year-old drawbridge whose members receive cyclic loading from both draw-span movements and trains. Although the study was a modest effort, a significant amount of information was obtained. Fatigue loading was evaluated by drawing a traffic sample from the railroad's data base and modifying the results in accordance with historical records. Critical bridge members were identified using a three-dimensional linear elastic analysis, and their cyclic stresses were corroborated by the results of experimental work. Then the remaining fatigue life of these members was estimated. The results show that many of the members have a remaining fatigue life of substantial length.

The fatigue life of bridges is a point of concern for the safe and efficient operation of railroads. At a time when wheel loads and traffic are increasing, many important railroad bridges have reached an age of 60 to 100 years. Unnecessary or premature replacement of a bridge is undesirable because the cost is high and funding is scarce. However, because of potential safety problems and the possibility of disrupted service, fatigue life should not be overestimated. When replacement is necessary, an early prediction for the end of the service life should be provided so that sufficient lead time is available for financial planning and budgeting.

This paper describes a fatigue study for an 80-year-old drawbridge whose members receive cyclic loading from both draw-span movements and trains. Although it was a modest effort, the study included both analytical and experimental work. The results indicate that many of the structural members have a remaining fatigue life of substantial length. This illustrates that significant information can be obtained from a modest research effort.

BACKGROUND

The subject of this study is Burlington Northern's (BN) Bridge 4, a 200-ft-long, double-track bascule bridge located in Seattle, Washington. The design was by the Strauss Trunnion Bridge Company. The node numbering system for the analysis and other dimensions are given in Figure 1. When the bridge draws, the moving leaf tilts up on the main trunnion. A counterweight is connected to the moving leaf through a series of links and hinges such that the top chord is in tension and the bottom chord is in compression unless a train is on the bridge. The bridge was built in 1913 of riveted steel with built-up members and has a Cooper's rating of E55 based on an allowable stress of 16 ksi. Present American Association of Railway Engineers (AREA) (*1*) design criteria call for bridges to be designed to a Cooper's rating of E80.

Primarily used by time-sensitive intermodal trains, the bridge is at a critical location in BN's Pacific Northwest railroad network. A closure would be very disruptive because trains would have to make time-consuming detours. Because of age, load rating, critical location, and expected increases in high-axle-load intermodal traffic, it was desirable to know the potential for fatigue cracking and the members that are most likely to be affected. The study focused on the bridge's moving leaf; neither the machinery nor the counterweight truss and tower were investigated.

To estimate fatigue life, it is necessary to have information on the loads, the resulting cyclic stresses, and the fatigue resistance. In past studies on other bridges, estimates for loads have been developed from traffic surveys and historical records (*2–4*); estimates of cyclic stresses were obtained from structural analysis (*2,5*) and field instrumentation (*3,4,6,7*); and fatigue resistance was based on AREA or AASHTO S-N relationships. Current research is providing additional information on railroad load spectrums and bridge fatigue behavior (*8*).

The fatigue loads for this study were based on a sample of 72 trains drawn from traffic that crossed the bridge during the 6-month period starting in March 1989. The sample consisted primarily of intermodal and general freight trains with a few coal or grain trains (Table 1). Later in the study, adjustments were made in the cyclic stresses to account for historical changes in wheel loads. These adjustments will be described later.

A three dimensional linear-elastic structural analysis provided cyclic stress information that was corroborated by the results of a limited field instrumentation effort. Based on the results of the structural analysis, critical members were selected for further analysis, and the AREA and AASHTO S-N relationships were used to provide estimates of fatigue resistance.

LOAD EVALUATION

As part of normal record-keeping activities, before a train departs, a list of cars is drawn up and entered into a computer data base. For each rail car, the list gives the serial number, gross weight, contents, destination, and a code that denotes the type of car (Figure 2). BN's car type code has four characters and is referred to as a GST code. The identification

C. T. Jahren, Department of Civil Engineering, University of Washington, 121 More Hall FX-10, Seattle, Wash. 98195. J. A. Rooker, Geiger Engineers, 110 Prospect Street, Bellingham, Wash. 98225.

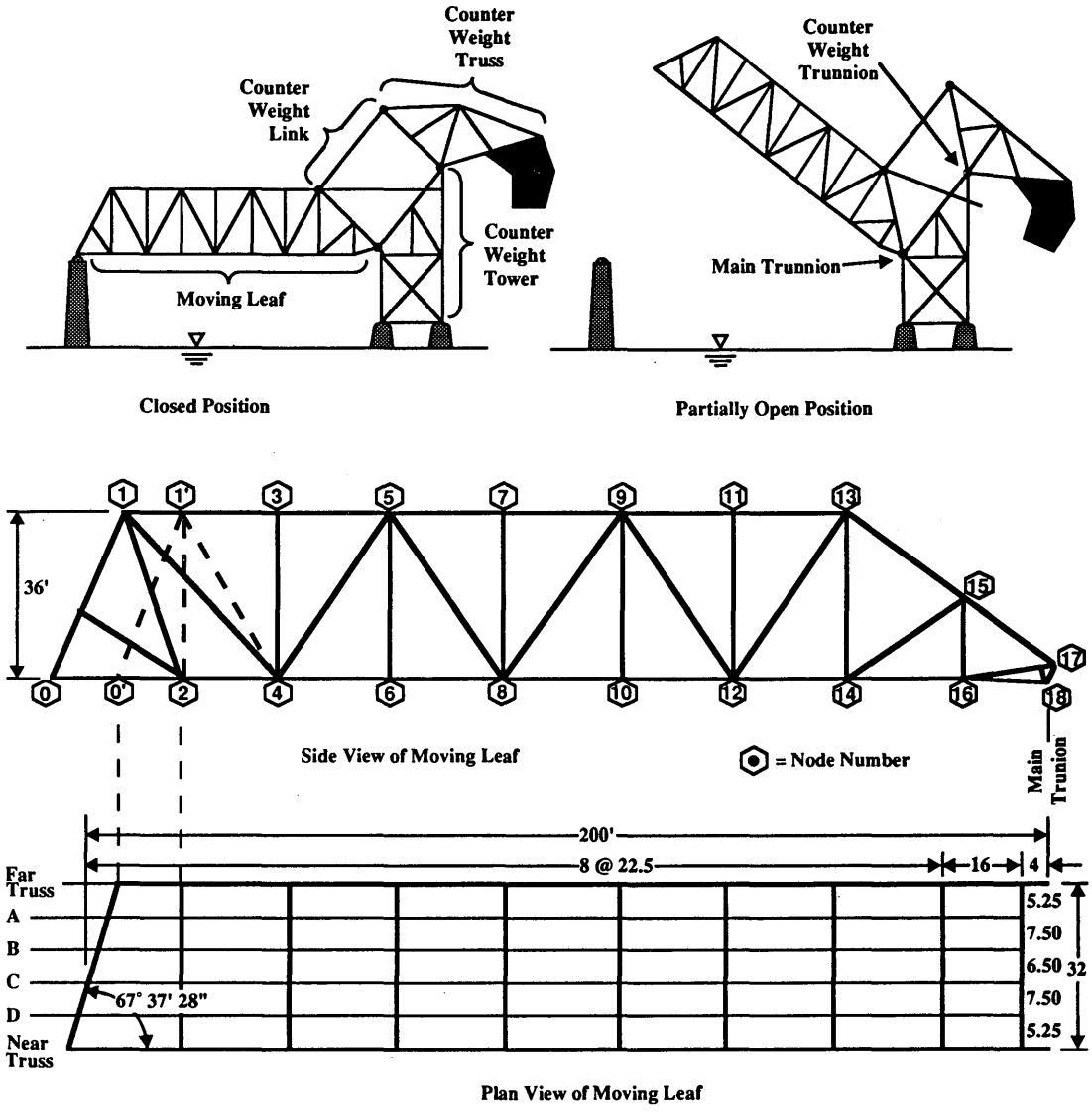

FIGURE 1 BN Bridge No. 4 (drawings not to scale).

TABLE 1 Sample of 72 Trains, 1988–1989

Train Type	No. of Trains	Percent	Trailing Tonnage	Percent
Intermodal (all types)				
Empty	11	15	22,346	14
Single stack	15	21	35,766	22
Double stack	4	6	9,571	6
Total	30	42	67,683	42
General freight	27	38	68,125	42
Grain/coal	9	12	26,016	16
Locomotives[a]	6	8	79	0
Total	72	100	161,903	100
Average train			2,249	

[a]Locomotives running light without a train.

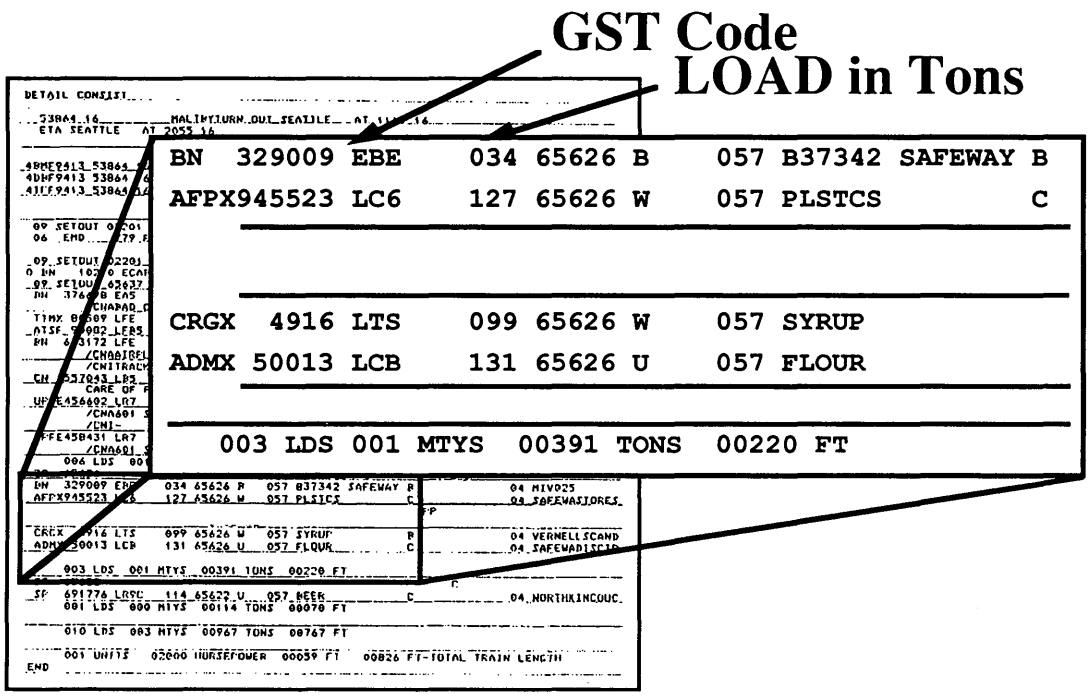

FIGURE 2 Train list from data base.

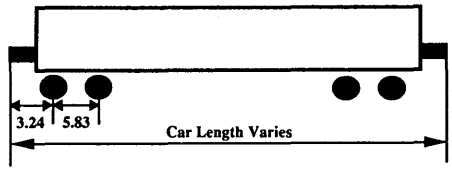

(a) Freight Car (Wheel Load Varies)

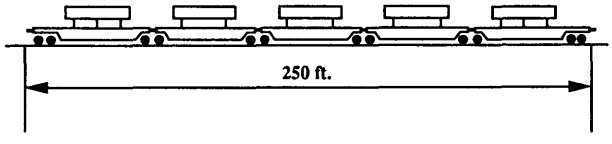

(b) Five Unit Articulated Intermodel Car (Wheel Load Varies)

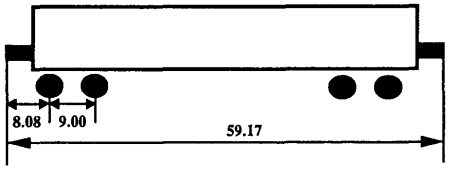

(c) Four Axle Locomotive (Wheel Load = 33 Kips)

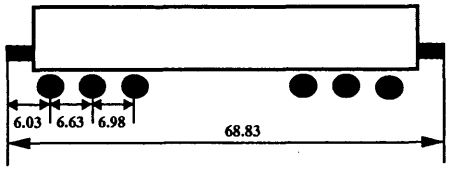

(d) Six Axle Locomotive (Wheel Load = 33 Kips)

FIGURE 3 Rail car and locomotive geometry.

number and length of each locomotive are also given. A FORTRAN program was developed that reads the gross weight and GST code for each car and generates a load string that gives estimated axle loads and spacings.

The axle loads were estimated by dividing the gross weight of the car equally among its axles. An exception was the five-platform articulated intermodal car having load platforms that share axles (Figure 3*b*). For these cars, the gross weight refers to the combined gross weight of all platforms. Each axle in an articulated wheel set was assigned one-tenth of the gross weight of the car, whereas each axle in an end wheel set was assigned one-twentieth of the gross weight.

It is possible to estimate the axle spacing from the GST code, because the length of the car may be inferred from the GST code to an accuracy of ± 5 ft and because the location of the axles in relation to the end of a rail car is consistent (Figure 3*a*). The program read the GST code, consulted a list that provided axle geometries for each car code, and computed the axle spacing.

Although there are many types of locomotives with various load characteristics, this program modeled two basic types of locomotives. Locomotives $\leq$ 62 ft long were assigned four axles (Figure 3*c*), and locomotives $>$ 62 ft long were assigned six axles (Figure 3*d*). Wheel loads were from 31 to 34 kips, depending on the length of the locomotive.

Because the resulting load string is based on several estimates, it is appropriate to discuss whether its quality is sufficient for use in fatigue studies. The gross car weight is entered by a clerk who scans a shipping document to find the weight of the contents and then guesses the tare weight of the rail car. Rail cars are rarely weighed before shipping and, for a variety of reasons, the net weight on the document may not be the actual weight of the contents. Furthermore, the contents of the rail car may be unevenly loaded. Despite these

shortcomings a weigh-in-motion comparison for three trains showed that these load models were useful for fatigue studies. Lists were obtained for the three trains and converted to a load string. Using the process described in the next section, the equivalent stress range for the midspan of a typical stringer was calculated for each train. Individual wheel loads were obtained for the same trains from the weigh-in-motion scale. Then the wheel loads from the list were replaced by the wheel loads from the weigh-in-motion scale and the stress range calculation was repeated. The differences ranged from 2 to 7 percent. If a sample contains several such trains, the difference of the whole sample is likely to be much smaller.

ANALYSIS OF STRESS CYCLING

As part of the effort to account for cyclic stresses, a three-dimensional model of the bridge was developed using the SAP 90 (*9*) structural analysis program (*10*). Except as noted later, the bridge was modeled as a rigid frame because the truss joints were heavy gusseted connections. The stringer-to-floor-beam connections had moments released in the major and minor axis because the actual connections were clip angles that joined only the webs of the members. Moments were also released for light cross-bracing members. Supports at the trunnion end (Node 17) were restrained against translation and rotation, except for rotation about the trunnion axis. The effect of the counterweight link was modeled by imposing forces in the appropriate location (Node 13) and direction. For the dead load condition, the support at the open end of far truss (Node 0) had no restraints, and the support for the near truss had only a vertical restraint that was required for structural stability; the force in the latter was negligible. For the live load condition, both the near and far trusses had vertical supports at the open end (Node 0). The dead load was modeled as the gross section of the bridge members, a line load to account for the track components, and a scaling factor to account for connection plates and other components that were not modeled.

The cyclic loading caused by draw span movement was modeled by rotating the moving leaf about the axis of the trunnion, making necessary alterations to the counterweight forces and recording the change in dead load stress for each member. Burlington Northern's records indicate that current draw span usage is 255 lifts per month. Historical records could not be found for past draw span movement, so for this study the number of lifts was increased to 300 per month (274,000 from 1913 to 1989) to cover uncertainty for the number of past lifts. The tensile portions of the member stress ranges in the far truss that exceed 3 ksi for a 60-degree lift are shown in Figure 4*a*. These stress cycles represent the largest stress cycle in the member when both bending moment and axial force are considered. Similar stresses were found in the near truss.

The tensile portions of the member stress ranges in the far truss that exceed 3 ksi for two 6-axle locomotives (Figure 3*d*) are shown in Figure 4*b*. For some members, the locomotive and draw span stress cycles are additive when trains cross the bridge between lifts. For example, end post Member 13-15 (Figure 5*a*) has a dead load stress of 5.0 ksi. Unlike end post

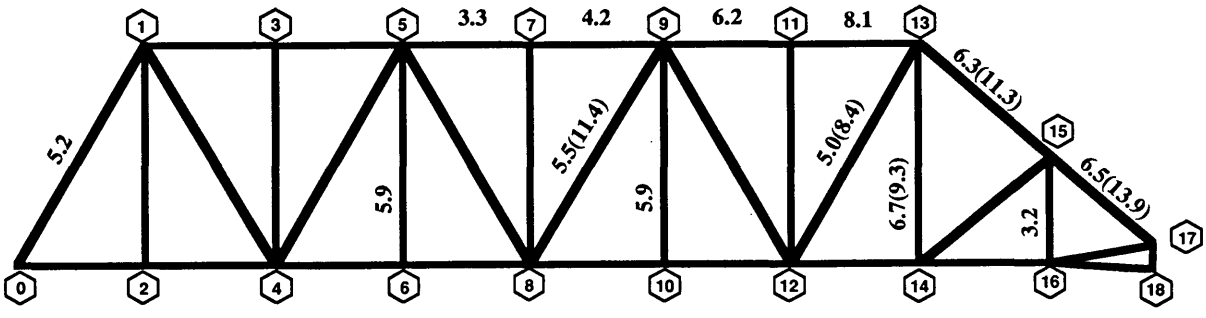

(a) Draw Span Motion, Lift Angle = 60°

Number in parentheses denotes stress range for sequential draw span motion and locomotive movement.

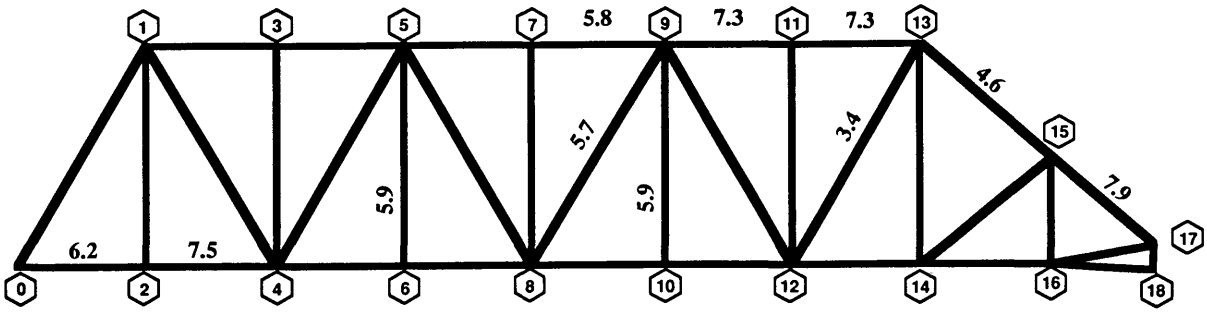

(b) Locomotive Movement

⬢ = Node Number

FIGURE 4 Cyclic stresses greater than 3 ksi (tensile portions only), far truss.

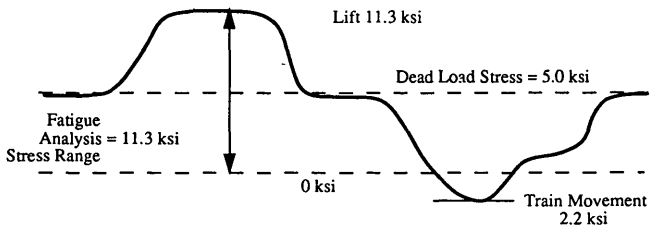

(a) Member 13 - 15

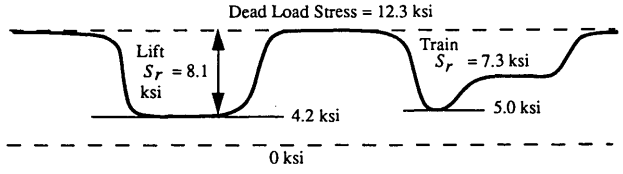

(a) Member 11 -13

FIGURE 5 Sequential draw span movement.

stresses in most truss bridges, this is a tensile stress, because of the influence of the counterweight link. During a lift the stress increases to 11.3 ksi and, during train movement, the member receives a 2.2-ksi compressive stress. Thus the tensile portion of the stress cycle that is used for fatigue analysis is 11.3 ksi. Top chord member 11-13 does not receive such additive stress cycles (Figure 5*b*). The dead load stress is 12.3 ksi. Lifting the bridge reduces the stress to 4.2 ksi. Similarly, train movement reduces the stress to 5.1 ksi. For fatigue analysis, these cycles may be counted as separate cycles of 8.1 and 7.3 ksi, respectively. In cases in which the stress cycles are additive, the full stress range is shown in parentheses (see Figure 4*a*).

One possible strategy for performing the fatigue analysis was to run the entire sample of 72 load strings on the frame model and then to analyze the cyclic stresses for every member of the bridge. Because the frame model included 228 members, the computational effort rendered that strategy impractical. Instead, a model test load of two 6-axle locomotives (33-kip wheel loads) and four 40-ft cars (19-kip wheel loads) was used (geometry shown in Figure 3), and the resulting cyclic stresses were examined to select six critical members for complete analysis: Top chord 11-13 receives relatively large stress ranges because of both draw span movement and rail traffic. End post 13-15 had a large stress range because of draw span movement. Diagonal 8-9 is a representative diagonal for the bridge. Hangers and stringers are members that receive many cycles and often develop fatigue problems. Therefore, Hanger 13-14, a typical hanger, and a typical stringer were selected (the hangers above Nodes 6 and 10 and the stringers between Nodes 2 and 16 are identical). Because they experienced relatively small stress ranges, the floor beams were not selected.

From the frame model, stress influence lines were developed for each critical member and coded into a FORTRAN program. The load strings were advanced over the influence lines to give a time history of the cyclic stress. These stress histories were converted to stress spectra using a rain flow counting method (*11*); an equivalent constant amplitude stress range, S_{re}, was calculated using a derivation of Miner's rule:

$$S_{re} = (f_i S_{ri}^3)^{1/3} \quad (1)$$

where f_i is the fraction of the stress range within interval i and S_{ri} is the midwidth of the stress interval i. The results of this analysis are shown in Table 2. An example calculation is shown in Figure 6. The tons per cycle (TPC) were calculated by dividing the tonnage of the traffic sample by the number of cycles that each member experienced. Top chord 11-13 and the typical stringer have the largest S_{re}; however, considering TPC, it is apparent that the stringer is subjected to more cyclic loading than the top chord. The stringer receives two cycles (one large and one small) per rail car, whereas the top chord receives about three cycles per train (average gross weight of train = 2,249 tons; see Table 1). BN provided historical information on annual gross tonnage and average gross weight per car from which an estimate of the yearly cyclic stresses was developed. Using Equation 1, a lifetime S_{re} was calculated. The calculations were not altered to reflect changes in car geometry, locomotive geometry, or impact factors. Analysis of stress cycles caused by hypothetical historical trains showed that this simplification has little effect on the final results because draw span motion and modern freight traffic has contributed the most to the bridge's fatigue damage.

Further adjustments were made to the cyclic stresses after reviewing the results of the field instrumentation described in the next section.

TABLE 2 Tons per Cycle and Equivalent Stress Ranges

Member	Tons per Cycle[a]	Current Equivalent Stress Ranges[a] (ksi)	Lifetime Equivalent Stress Range[b] (ksi)
Typical hanger	55.2	3.2	2.9
Framed hanger (13–14)	90.5	2.2	2.0
End post (13–15)	813.6	3.7	3.4
Top chord (11–13)	852.1	4.2	3.8
Diagonal (8–9)	71.2	2.6	2.3
Stringer (Panels 2–16)	46.5	4.3	3.8

[a]Calculated from a sample of 72 trains that crossed Bridge No. 4 in August 1988 (see Table 1).
[b]Adjusted for historical loads.

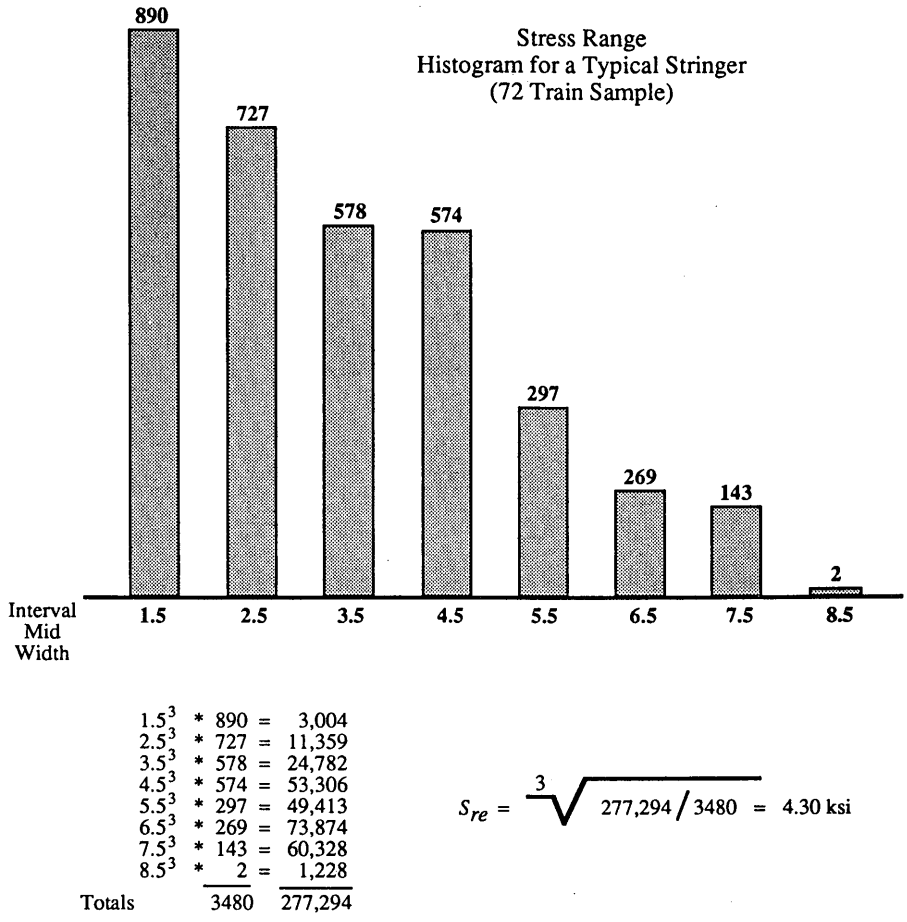

FIGURE 6 Example of effective stress range calculation.

FIELD INSTRUMENTATION

The experimental portion of this study was performed to confirm the calculated stress ranges for the critical members and to check for stress transients during draw span movement. Strain measurements were taken at a typical stringer (midspan Panel 2-4), a typical hanger (9-10, 81 in. above Node 10), and the top chord near the counterweight link (11-13, 107 in. from Node 13). The instruments were located on the near truss because more heavily loaded trains were expected on the near track. Later observations, however, showed that loaded trains used both tracks equally. The strain gauges were read and digitally recorded by a personal computer equipped with a data acquisition board.

A comparison was drawn between the stresses inferred from the strain-time plots of two SD40-2 locomotives (33-kip wheel load; Figure 3*d*) traversing the bridge at crawl speed and the analytical result for the same load. The stress history for the bottom flange of the stringer is shown in Figure 7*a*. The four peaks in stress correspond to the four locomotive trucks, and the stress reversals indicate that there is some fixity in the stringer-to-floor-beam connection. The stress inferred from the instrumentation for the top flange 8.9 to 10.6 ksi (compressive portion of stress range only) and the bottom flange was between 5.0 and 6.8 ksi (tensile portion of stress range only). The analytical comparison for both the compression and tension flanges was 6.9 ksi. The angles of the top flange of the stringers had been replaced, and the replacement may have caused a redistribution of stresses that would account for the higher compressive stresses found in the top flanges.

The hanger is an H-shaped built-up member consisting of a web plate and four flange angles that serve as flanges. The floor beam is riveted to the inside flange angles of the hanger. For the hanger, the strain readings on the flange exceeded those at the neutral axis by as much as 20 percent and indicated the existence of bending stresses, as shown in Figure 8. Fisher and Daniels (*6*) observed similar bending stresses in hangers of railroad bridges. Shear lag in the stringer-to-floor-beam connection may cause a further increase in stress on the inside flange of the hanger because strain in the outside flange is not mobilized.

The top chord is a box-shaped member. Strain gauges were located on the top of one web plate and the bottom of the other web plate, as shown in the legend of Figure 7*b*. The stress range at the top of the member was larger than at the bottom, indicating that the member experiences some bending. The frame analysis predicted the presence of bending at this location but the stress ranges from instrumentation ex-

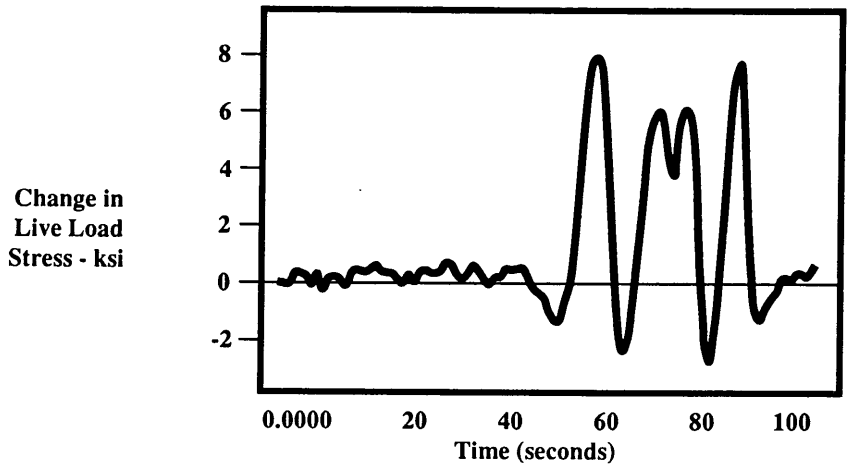

(a) Stringer, Lower Flange, 6 Axle Locomotive

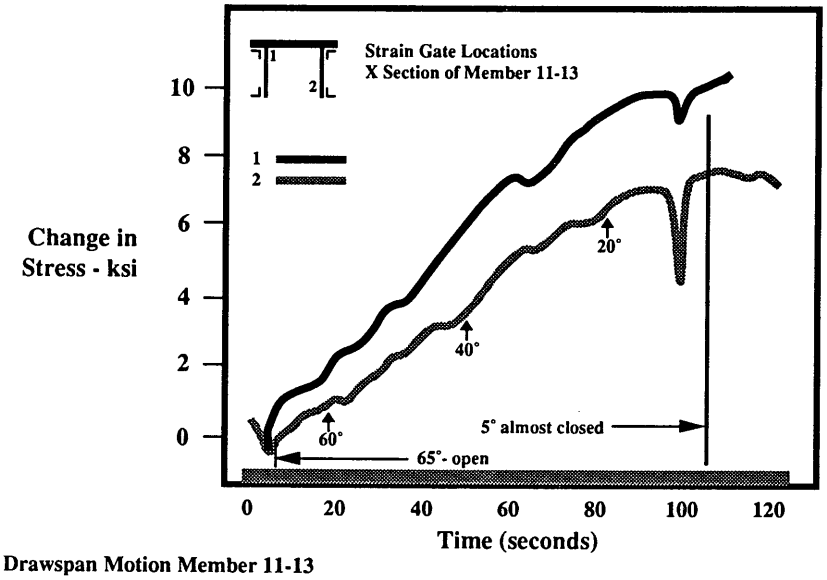

(b) Drawspan Motion Member 11-13

FIGURE 7 Field test results.

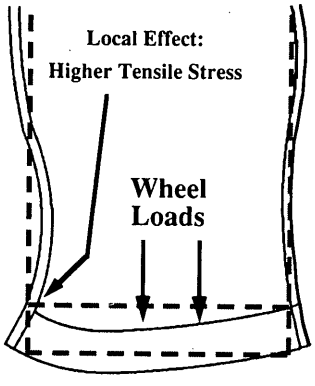

FIGURE 8 Deformed floor beam.

ceeded those from the frame analysis. Time histories of stresses in the top chord members were recorded during the draw span movement. The draw span was brought to a jerking halt several times so that any resulting impact strains could be recorded. The stress history is shown in Figure 7*b*. The measurements indicate that a stress range of 3.8 ksi results from this jerking action.

Results from the frame analysis suggested that the expected vibrational period was 0.5 sec; however, no vibrational stresses of this period were detected by the instrumentation during rail traffic or draw span motion.

The structural model was also checked using optical surveying methods. Using frame analysis, an estimate of the midspan deflection of the truss (0.07 ft) was calculated for the load of two SD 40-2 locomotives. Readings with an engineer's level gave the same result.

FATIGUE EVALUATION

Rivet holes are often the critical details that initiate fatigue cracks in riveted bridges. For built-up members, initial cracking can be expected after the stress exceeds the Category D curve; however, since several components must crack before a built-up section collapses, Category C is an appropriate fatigue life limit (*12*). For all critical members, Table 3 presents estimates of D, the amount of fatigue damage caused by draw span movement or rail traffic (stringers are not affected by drawspan movement). D_i is calculated by

$$D_i = \frac{n_i}{N_i} \tag{2}$$

where n_i is the number of stress cycles in a particular stress range and N_i is the number of cycles allowed by the appropriate S-N relationship. The summation of D_i gives D the total fatigue damage. Fatigue life ends when $D = 1$. Except for a set of stringers in an end span, none of the members that were analyzed have expended more than 50 percent of their Category D fatigue life or 25 percent of their Category C life (Table 3).

Adjustments were made in the stress range to account for local effects detected by field instrumentation, impact, and double track (see notes, Table 3). An impact factor was applied to the stringers and hangers only because it was judged that the longer tributary length of the other components reduced impact effects. The factor of 1.10 is conservative because the speed limit of the trains is 20 mph, and other researchers have obtained lower factors for higher-speed traffic. For example, Kritzler (*7*) obtained an impact factor of 1.08 at 50 mph. An adjustment for double track was necessary because the stress ranges were calculated for one train using the near track. The adjustment accounts for 47.5 percent of the trains using the near track, 47.5 percent of the trains using the far track, and 5 percent of the trains using both tracks concurrently.

Few of the stress cycles for the typical hanger exceed the Category D fatigue limit of 7 ksi; therefore, it is unlikely that these members accumulate fatigue damage. The other truss members have expended between 14 percent and 43 percent of their fatigue life in Category D or between 7 percent and 22 percent of their fatigue life in Category C. The diagonal has suffered the most fatigue damage; its remaining fatigue life is 30 years. This estimate allows for a 5 percent increase in both stress range and cycles per year. In addition, the draw movement stress range is increased to 16 ksi (after 20 percent

TABLE 3 Cumulative Fatigue Damage for Selected Members

Member	S_{re} (ksi)	n_i to 1989 ($\times 10^6$)	N_i, Category D ($\times 10^6$)	D_i, Category D	N_i, Category C ($\times 10^6$)	D_i, Category C
Framed Hanger (13–14)						
Traffic	2.3[a]	28	180	0.16	365	0.08
Draw motion	11.2[b]	0.27	1.55	0.18	3.2	0.09
Total				0.34		0.17
End Post (13–15)						
Traffic	3.5[c]	1.05	51	0.02	103	0.01
Draw motion	13.6[b]	0.27	0.88	0.32	1.78	0.16
Total				0.34		0.17
Top chord (11–13)						
Traffic	3.9[c]	0.99	36	0.03	74	0.01
Draw motion	9.7[b]	0.27	2.4	0.11	5	0.06
Total				0.14		0.07
Diagonal (8–7)						
Traffic	2.4[c]	18.4	164	0.11	334	0.06
Draw motion	13.7[b]	0.27	0.85	0.32	1.74	0.16
Total				0.43		0.22
Stringers (traffic only)						
Panels 0–2 (I = 1.2)	4.2[d]	14	30	0.47	54	0.26
Panels 2–16 (I = 1.1)	3.8[d]	14	40	0.35	80	0.18
Panels 16–18 (I = 1.2)	4.7[d]	14	22	0.64	44	0.32

[a]Hangers: local effects (1.20) × impact (1.10) × double track* (0.86) = 1.15.
[b]Draw span motion only: local effects = 1.20.
[c]Chord member traffic loads: local effects (1.20) × double track* (0.86) = 1.03.

Near track	0.475	(1)	= 0.475
Far track	0.475	(0.4)	= 0.030
Both tracks	0.05	(1.4)	= 0.137
	Result of addition		0.642
	$(0.642)^{1/3}$		= 0.866

[d]Stress range at bolt hole, flange angle to web plate connection.
*Double-track root mean cube adjustment based on Miner's rule and typical S-N curves.

adjustment for local effects) to account for planned modifications that will increase the lift angle to 75 degrees. Draw span movement contributes the most to fatigue damage for end post (Member 13-15), the top chord (Member 11-13), and the diagonal (Member 8-9), whereas draw span movement and freight traffic contribute almost equally to fatigue damage for the framed hanger (Member 13-14).

The bottom end post (Member 15-17) also has substantial stress ranges (Figure 4) but was not analyzed in detail during this study. The large stress ranges are partially due to bending moments near Node 17. The stresses are most likely altered by several large gusset plates that reinforce the end trunnion that were not modeled in the frame analysis. Further field instrumentation or a more refined analysis should be undertaken before the damage index for Member 15-17 is estimated.

The peak stresses for the typical stringers (Panels 2 through 16) is at the fatigue limit of 7 ksi. The peak stresses for stringers in the end span (Panels 16 through 18) are somewhat higher. If the stringers accumulate fatigue damage, they accumulate it faster than other members. Considering the design of the bridge and the location of the stringer, this is a reasonable conclusion. Except for the stringers, all of the members of the bridge were designed to resist the load of two trains; however, most cyclic loads are the result of one train's passage. The stringers receive more cycles because of their short tributary length even though only half of the trains use each stringer.

Impact factors of 1.10 and 1.20 were assigned to the intermediate (Panels 2–16) and end (Panels 0–2, 16–18) stringers, respectively. The higher-impact factor was selected for the end stringers because special rail joints exist near the supports and are likely to increase impact loading. This is consistent with the results of a study about the effect of rail defects on impact loading (*13*). The stress ranges for the nontypical stringers (Panels 0–2 and 16–18) were estimated by calculating an equivalent fatigue load (EFL) from the stress range and section properties of a typical stringer and applying this load to the nontypical stringers. The geometry of the EFL is similar to a rail car's wheel set (Figure 3*a*), and the wheel load is 21 kips. For Stringer Panel 16–18, the remaining Category D and C fatigue life is estimated at 7 and 25 years, respectively. The remaining Category D fatigue life of a typical (Panels 2–16) stringer is estimated at 22 years. These estimates allow for a 5 percent increase in cyclic stresses and the number of cycles per year. At the end of the Category D service life, an abrupt failure of the entire member is not expected. As stated earlier, Category D indicates the lower bound for the fatigue strength of an individual component in a built-up member (*12*). It is likely that cracks may be detected as they occur and the individual components replaced to extend the life of the member.

The service life of the stringer-to-floor-beam connection was also investigated (*10*). The calculations are sensitive to changes in assumptions regarding the joint's fixity, which was not known with certainty; however, the results show that it is possible that these connection angles have reached the end of their design fatigue life. This possibility may be determined by regular inspection. Since the connection is supported by two angles, both would have to crack before the connection would collapse. If cracks were detected, the angles could be replaced at a relatively low cost.

CONCLUSIONS AND RECOMMENDATIONS

It is concluded that most of the components in BN's Bridge 4, except for the stringers, have a remaining fatigue service life of at least 30 years. The service life of many of the components may be much longer. Of the components analyzed, it is expected that the end stringers will be the first major components to reach the end of their service life. It is likely that service life may be extended by replacing individual components of built-up members as cracks occur.

Comparisons with weigh-in-motion data and instrumentation results show that computerized train lists are a valuable source of data that may be used in the development of current load spectrums.

Two possible methods were identified that could be used to generalize site-specific fatigue information. If an estimate exists for the number of TPC for a particular type of member (perhaps a stringer of a certain length), the number of cycles per year can be estimated if the gross annual tonnage is known and the traffic mix is similar. Since railroads routinely collect data on gross annual tonnage, this information is easily available.

If a set of EFLs could be developed by calculating the wheel loads that would cause the equivalent stress range for certain members, these EFLs could be used to estimate the equivalent stress range in similar members. Ultimately, the EFLs could be developed into a fatigue train that would be similar in concept to the fatigue truck that was proposed by Moses et al. (*14*).

ACKNOWLEDGMENT

Funding for this project was provided by Burlington Northern's Research and Development Department and TransNow, U.S. Department of Transportation's Region 10 University Transportation Center. This support is gratefully acknowledged.

REFERENCES

1. Steel Bridges, Chapter 15. In *Manual for Railroad Engineering*, American Railway Engineering Association, 1989.
2. Z. Prucz and W. B. Conway. Extending the Fatigue Life of the US 190 Mississippi River Bridge, Baton Rouge, Louisiana. *Proc., 6th Annual International Bridge Conference*. Pittsburgh, Pa., June 1989, pp. 308–316.
3. R. A. P. Sweeney. The Load Spectrum for the Fraser River Bridge at New Westminster, B. C. *Area Bulletin 658*, 1976.
4. P. Grundy. Fatigue Life of Australian Railway Bridges. *Civil Engineering Transactions*. The Institution of Civil Engineers, Australia, 1982.
5. E. A. Ebrahimpour, E. A. Maragakis, and D. N. O'Connor. On Fatigue Evaluation of Riveted Connections in Railway Bridges. *Proc., Firth of Fourth Bridge Centenary Conference*, Edinburgh, Scotland, Aug. 1990.
6. J. W. Fisher and J. Hartley Daniels. An Investigation of the Estimated Fatigue Damage in Members of the 380-ft. Main Span, Fraser River Bridge. *AREA Bulletin*, No. 658, 1976.
7. R. W. Kritzler. Rating of Railroad Bridges by Field Load Testing. *Proc., 6th Annual International Bridge Conference*, Pittsburgh, Pa., June 1989, pp. 171–178.

8. D. A. Foutch, S. D. Schiff, and J. Choros. Development of Load Spectra for Railway Bridges Under Changing Operating Conditions. *Proc., 6th Annual International Bridge Conference*, Pittsburgh, Pa., June 1989, pp. 179–192.
9. E. L. Wilson and A. Habibullah. *SAP90 Users Manual*. Computers and Structures, Inc., Berkeley, Calif., 1989.
10. J. A. Rooker. Fatigue Life Investigation of Ballard Railway Bridge. M.S. thesis. University of Washington, Seattle, 1989.
11. C. G. Shilling. Stress Cycles for Fatigue Design of Steel Bridges. *Journal of the Structural Division*, ASCE, Vol. 110, No. 6, June 1984, pp. 1222–1234.
12. J. W. Fisher, B. T. Yen, D. Wang, and J. E. Mann. *NCHRP Report 302: Fatigue and Fracture Evaluation for Rating Riveted Bridges*. TRB, National Research Council, Washington, D.C., 1987.
13. J. F. Muller and P. F. Dux. Pre Stressed Concrete Bridge Line Load Stresses Due to Heavy Haul Coal Traffic. *Proc., Fourth International Heavy Haul Railway Conference*, Brisbane, Australia, 1989.
14. F. Moses, C. G. Schilling, and K. S. Raju. *NCHRP Report 299: Fatigue Evaluation Procedures for Steel Bridges*. TRB, National Research Council, Washington, D.C., 1987.

Publication of this paper sponsored by Committee on Steel Bridges.

Testing an Integral Steel Frame Bridge

M. ELGAALY, T. C. SANDFORD, AND C. COLBY

The Forks Bridge in the state of Maine has integral abutments and approach slabs that are connected to the abutments. The main carrying components are five rigid steel frames each in the form of an inverted U; the legs of the frames are embedded in the abutments and the horizontal girders are connected to the reinforced concrete deck by shear connectors. Because the design is unique, it was decided to instrument and monitor the bridge behavior for the duration of 3 years. The equipment and instruments used are described. Measured and calculated strains in the steel frames caused by the weight of the deck are reported. The bridge was tested on completion using three loaded trucks. The results of the tests are given and compared with the corresponding results obtained from a finite element analysis. Finally, the instrument readings taken every 6 hr for a duration of approximately 6 months are presented and discussed.

The new Forks Bridge between the Forks and West Forks is a stiff-legged steel rigid-frame bridge that spans the Kennebec River and replaces an existing steel truss bridge built in 1932 (Figure 1). The old bridge had been damaged a number of times by protruding logs from logging trucks. The new bridge's design, location, and approach layout will reduce the type of accidents that had occurred at the old bridge and will provide a higher live-load capacity to meet current highway needs. Because there is considerable rafting on the Kennebec River at the bridge location, a center pier was not considered. In addition, a center pier raised the possibility of excessive scour.

The new bridge is a 20-degree skewed bridge with a 165-ft span and a 37-ft 8-in. overall width. It consists of five steel frames in the shape of an inverted U resting on shallow foundations. The composite reinforced concrete deck is rigidly connected to the abutments and the approach slabs, and the steel legs of the frames are embedded in the abutments. Because the steel legs were to be covered by concrete, the abutment wall thickness varies from 4.8 ft at the footing to 8.5 ft at the top. The footing, called the seal, is approximately 15 ft wide and 9 ft thick and is resting on the bouldery and cobbley gravel terrain that exists at the site. The legs of the girders are fixed to the foundation block through a height-adjusting distribution slab between the bottom of the legs and the top of the seal. The granular backfill with its good drainage minimizes differential water levels behind the abutment, which can add large forces to the abutment walls. It is also important to have free draining material with low fines so that frost pressures are not generated behind the wall. Construction commenced in the summer of 1989, and the bridge was open to traffic early in December of the same year.

Since the soil pressure as a function of the deck movements is not well known, this was the principal reason for instrumenting, testing, and monitoring the bridge.

Department of Civil Engineering, University of Maine, Orono, Maine 04469.

DATA ACQUISITION SYSTEM

It was desired to monitor the behavior of the new bridge by instrumenting it and taking the readings from the instruments at frequent intervals. The bridge is 110 mi from the University of Maine, and the use of a data acquisition system that can be reached via a telephone line from the university was found to be cost-effective. The system would have to read strain, temperature, and pressure instruments and be reliable while enduring Maine's climate for the 3-year monitoring period. The possibility of data storage in digital form and remote access through the telephone biweekly was another desired feature. Data storage in a digital form would eliminate manual data entry and should facilitate the reduction, interpretation, and presentation of results. Remote access also provides access at critical times for readings and frequent access to check instrument functioning.

INSTRUMENTATION

Strain gauges, temperature sensors, and pressure cells were installed to monitor the behavior of the Forks Bridge. The strain gauges are intended to measure the strains in the steel frames caused by loads and thermal effects. The pressure cells are intended to measure the pressure of the soil on the back of the concrete abutment wall as the bridge abutment moves in response to loading and temperature change. The temperature sensors are intended to measure air and soil temperature behind the abutment.

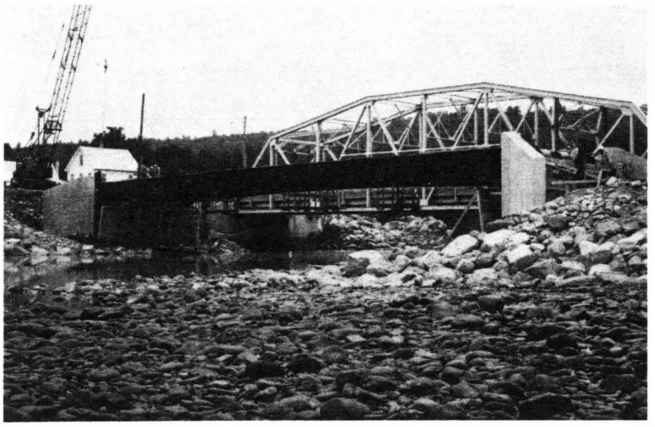

FIGURE 1 Old and new bridges at the Forks.

Strain Gauges

Weldable electrical resistance strain gauges were used. Spot welding is often more convenient than adhesively bonding a gauge, particularly in field testing applications for which bonding conditions are not ideal. After welding wires were soldered to the gauge terminals and the gauges were protected using special coating, the wires were run to the equipment box through polyvinylchloride (PVC) conduits. For each single active gauge welded to the bridge, three resistors are required to complete the circuit. Two precision resistors for each gauge and one common gauge for all the gauges connected to one logger were used for circuit completion.

Pressure Cells

Because it was anticipated that the soil pressure behind the abutment would vary with elevation, with skew side (obtuse or acute), and possibly with the abutment location (north or south), it was decided to use four vertical lines of pressure measuring cells with four cells per line for a total of 16 pressure cells. For each abutment, two lines of pressure cells were installed at 10 ft on each side of the abutment centerline. The top cell was 7 ft below grade, and the remaining three were 6, 12, and 17 ft below the top cell. One of the four bottom cells was covered with a screen to allow water pressure to be measured.

The 9-in.-diameter pressure cell consists of a fluid-filled pressure pad connected by a length of high-pressure tubing to a pressure transducer (Figure 2). The pressure pad is formed by welding two thin disks of stainless steel around the periphery. The narrow gap between the two disks as well as the tubing leading to the pressure-sensing device is filled with deaerated oil. Pressure on the face of the cell is thus reflected directly in oil pressure, which is sensed by the pressure transducer. Because temperature affects the pressure reading for a vibrating wire transducer, each transducer is equipped with a temperature-sensing thermistor. The thermistor output is used to adjust the pressure reading for temperature changes.

To ensure that the cells were mounted to be flush to the back of the concrete abutment wall, they were provided with concrete bedding under the whole cell (Figure 3). A special concrete block with a recess for the cell was prepared in the laboratory. During field installation this concrete block with the recessed cell was placed between the reinforcing and the forms and secured to the inside of the abutment formwork by concrete form bolts. This block protected the cell during concreting operations and isolated the cell from stresses caused by the set of the field-placed concrete.

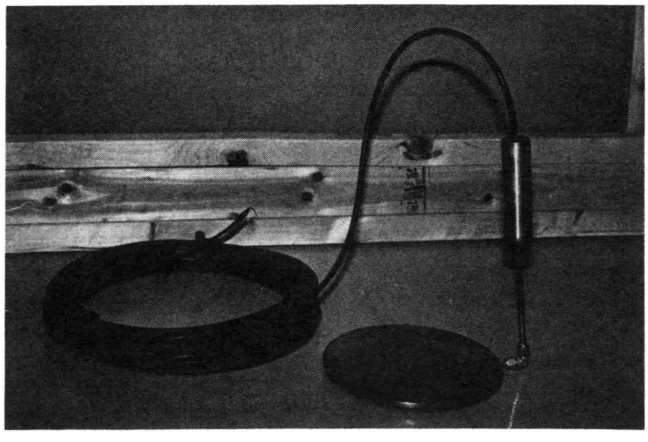

FIGURE 2 Pressure cell and vibratory wire transducer.

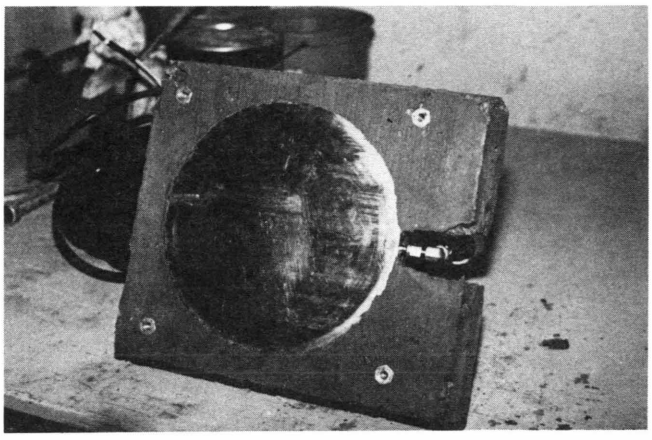

FIGURE 3 Pressure cell and concrete backing pad.

In the laboratory each cell was calibrated in the recess of its own concrete block. The loads measured with a calibrated electronic load cell were raised incrementally to an equivalent of about 20 lb/in.^{2} and then decreased to zero. The calibration factor was obtained using the best-fit line through the points.

Temperature Sensors

Thermistor sensors are provided by the manufacturer in each pressure cell. Calibrations for the thermistor were provided by the manufacturer. Three resistance temperature detectors (RTDs) were used to measure the air temperature in the vicinity of the central steel frame under the bridge: one near the south abutment, one near the center of the span, and one inside the equipment box. The reading from the RTD is resistance; the resistance to temperature conversion was calibrated in the field using the manufacturer's conversion tables.

TEST RESULTS

Two sets of test results are given and discussed. The stresses in the steel frames caused by the wet weight of the concrete deck constitute the first set. When the deck was placed, the fill behind the abutments was not in place; hence, soil pressure readings are not applicable. The second set, obtained during load testing of the bridge with three loaded trucks, includes frame stresses as well as soil pressure behind the abutments.

Stresses from Weight of Concrete

Three of the five bridge frames, adjacent to one another, were instrumented using strain gauges. Initial readings were

TABLE 1 Measured and Calculated Stresses Caused by Weight of Concrete

Gage No.	Measured Stresses (ksi)	Calculated Stresses (ksi)
301	1.83	1.19
303	1.31	1.28
307	-6.06	-9.63
310	-10.73	-14.21
312	4.64	5.35
315	8.24	8.50
316	-5.97	-9.63
405	-11.98	-14.21
406	6.82	5.35
408	-6.35	-9.63
501	1.60	1.28
504	-6.84	-9.63
505	-14.24	-14.21
506	6.06	5.35
508	-7.13	-9.63
509	1.28	1.28

The negative signs indicate compression

taken on October 26, 1989, after the forms and the reinforcing bars were in place. The concrete was placed on October 27, 1989, and another set of readings was taken on October 28. The difference between the initial and final readings represents the strain caused by the weight of the concrete. To determine the corresponding stresses, the measured strains were multiplied by the Young's modulus of elasticity, E = 29,000 kip/in.^{2}. This is a reasonable approximation, because the strains in the perpendicular direction are negligible. The calculated stresses from the measured strains are tabulated in Table 1.

The frame was analyzed with a finite element program under the tributary weight of the concrete. Axial forces and bending moments at the locations of the strain gauges were determined. The stresses were then calculated at the locations of the gauges. As can be noted from Table 1, there is reasonable agreement between the measured and calculated stresses. The differences can be attributed to

1. Differences between the actual locations of the strain gauges and the locations used in the calculations, particularly important at zones of high moment gradients;
2. Differences between actual geometric and material properties of the frame and values used in the analysis;
3. Possible inaccuracies in the measured strains, which can be attributed to thermal output and wire resistance of strain gauges; and
4. Readings that were taken several hours after the concrete was placed, creating the possibility that some concrete slab strength was not accounted for in the analysis (particularly true since, in general, the calculated stresses are higher than those calculated from the measured strains).

Truck Load Testing

Testing of the bridge was conducted on December 2, 1989, by using three loaded trucks at various positions on the bridge and recording the effect on the bridge and the abutments. The three-axle trucks weighed 59,800, 58,700, and 53,725 lb,

TABLE 2 Measured and Calculated Stresses Caused by Truck Loads

Gage No.	Measured Stresses (ksi)	Calculated Stresses (ksi)
301	-.05	.04
303	-.16	.04
307	-1.95	-2.94
310	-.03	-.46
316	-2.23	-2.94
403	.74	.72
404	-1.43	-2.60
406	2.51	3.08
407	1.27	.72
408	-1.44	-2.60
501	1.03	.04
504	-.72	-2.02
506	1.93	2.07
508	-.67	-2.02
509	1.10	.04

The negative signs indicate compression

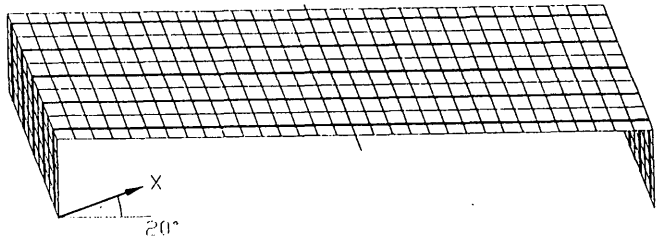

FIGURE 4 Finite element analysis model.

respectively. Two tests were conducted with the trucks on the approach slabs, whereas 10 tests were conducted with the trucks on the bridge deck at various positions. Stresses were calculated using the measured strains as described earlier. These stresses are referred to as the measured stresses and are tabulated for the case in which the trucks were centered on the middle frame at midspan (Table 2).

The bridge was modeled using a three-dimensional finite element model, as shown in Figure 4. Plate elements were used to model the concrete slab and abutments, and beam elements were used to model the steel frames. The bridge was analyzed for the case in which the trucks were centered on the middle frame at midspan. Axial forces and bending moments in the steel frames were determined. The stresses caused by these forces and moments at the gauge locations were then calculated and are tabulated in Table 2 for comparison with the measured values.

Earth Pressure Caused by Truck Loads

When the trucks were on the bridge deck, the soil pressure behind the abutments increased or decreased depending on

the location of the loading and the location of the pressure measurement. In general, at the obtuse side of the abutment, there was an increase, whereas on the acute side there was a decrease in pressure. The pressure readings caused by temperature changes during testing were of the same magnitude or larger than the load response readings. The maximum pressure increase measured at any cell was 35 lb/ft^2, but the maximum decrease was higher at 53 lb/ft^2. These low pressures are indicative of the very little movement of the abutments in response to the loading. The pressures were higher when the trucks were on the approach slabs.

MONITORING BRIDGE BEHAVIOR

Monitoring of the strain in the steel, soil pressure at the back of the abutment, and temperatures of the soil, water, and air was started on a regular basis on December 2, 1989. Continuous readings of all instruments were taken every 6 hr—at midnight, 6 a.m., noon, and 6 p.m.—during the monitoring period beginning December 2, 1989 and ending June 6, 1990. Some small gaps in monitoring caused by minor equipment malfunctions or problems with data transfer occurred during this period. Intermittent monitoring was conducted before December 2, 1989. The days of monitoring are numbered using January 1, 1989, as Day 1.

Air Temperatures

Air temperatures were monitored by the RTDs mounted on the steel below the deck. These gauges are shielded from the direct rays of the sun by the concrete deck, and the temperatures are most likely moderated somewhat by the presence of the steel and the river. Although they may be less extreme than those occurring in the open, these temperatures are believed to be representative of the steel and adjacent air. The

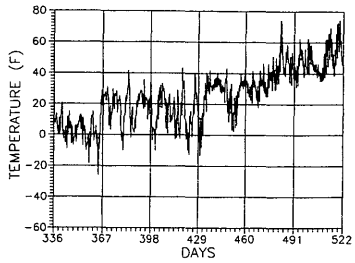

FIGURE 5 Air temperature at the Forks.

average air temperatures plotted in Figure 5 show a relatively cold December 1989 and a relatively warm January 1990. The coldest recorded air temperature at the bridge for this period was −27°F on December 30, 1989 (Day 364), at 6 a.m. The most dramatic change in temperature occurred on December 31, when the temperature changed 55°F in 36 hr to a temperature of 28°F at 6 p.m. Temperature increased steadily from approximately March 6, 1990 (Day 430).

Temperature of Fill Behind Abutments

The Kennebec River does not freeze in the channel beneath the bridge. The bottom cell, which is 24 ft below grade, is always below the river water level and thus is surrounded by water connected through the surrounding gravel to the river. The cell that is 5 ft above the bottom cell is submerged periodically during each day because the river rises following daily water releases at the Harris Dam upstream.

Temperatures measured directly behind the abutment show that freezing occurred in the winter at all elevations above the sustained river water level (Figure 6). Since the shallowest cell was 7 ft below grade and the deepest that froze was 19

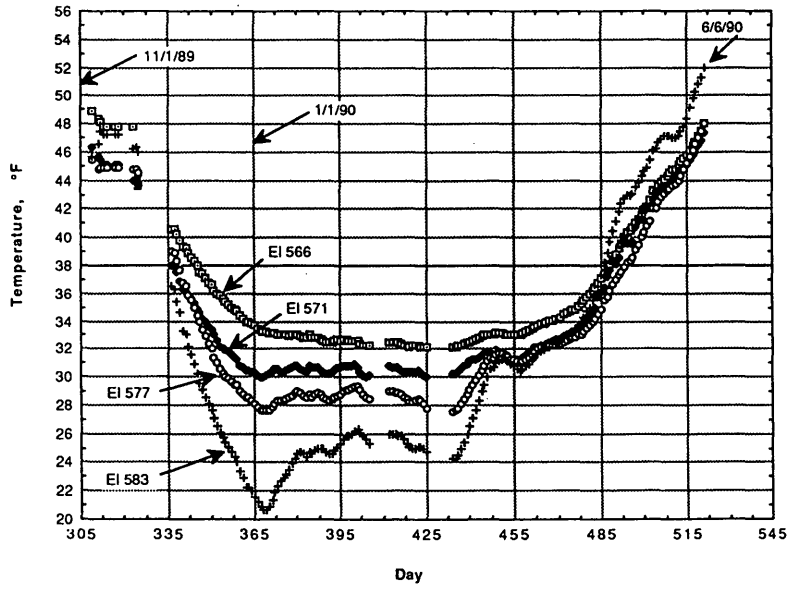

FIGURE 6 Temperature behind abutment.

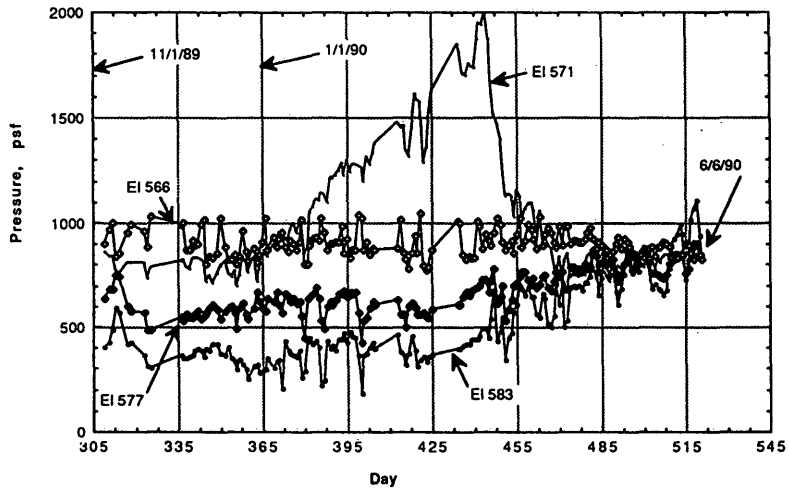

FIGURE 7 Earth pressure.

ft below grade, one can conclude that the freezing front penetrated the thick abutment concrete. The temperature at the bottom cell never went below freezing, which confirmed that the surrounding water was in contact with the Kennebec River, which is not frozen at the bridge location.

As can be noted from Figure 6, the freezing in the soil behind the abutment first occurred at the highest elevation on about Day 340, which is at the end of the first week of December 1989. At that time the river temperature was approximately 39°F. By the third week of December the soil adjacent to the second cell from the bottom, which was inundated with river water, was frozen. December 1989 was much colder than normal; thus, the extent of freezing that occurred probably will not be duplicated for many years.

The warmer weather that occurred in January 1990 was reflected in the temperatures behind the abutment, which climbed several degrees during the first 2 weeks of January, as can be noted from Figure 6. The soil behind the abutments remained frozen until the end of the first week of April 1990, or approximately for 4 months.

No measurements were made between the elevation of the top cell and the surface. It is anticipated, however, that the temperature in this 7 ft may fluctuate more with the daily air temperature than at greater depths. It is also possible that more extreme cold temperatures were experienced in December in this upper region.

Soil Pressure

The average pressure measured at the elevation of each cell is plotted against time in Figure 7. As can be noted from Figure 7, most pressure changes appear to be related to temperature changes and the changes in length of the bridge that these temperature changes cause, fluctuations in the river water levels, and frost buildup.

The fill behind the abutments started on November 2, 1989, and was almost completed in 1 week. For the period from 6 p.m. on November 19, 1989, to 11 a.m. on November 21, pressure measurements taken at ½-hr intervals (Figure 8) clearly show the rise and fall of the water levels at the bottom cells. Cell 7 is the one covered by the screen; it measures only water pressure.

Temperature variation affects soil pressure because of the resulting bridge deck expansion and contraction. The movement of the abutments is greater at the top next to the deck, and thus pressure changes should vary with depth. Although the approach fill was completed late in the fall, there is still a reduction in pressure in response to the cooling from November 8 to November 20, 1989, as can be noted from Figure 7. Frost effects at the elevation of the load cell second from the bottom dominated that level's pressure changes and are discussed separately. Between March 26 and the end of this monitoring period on June 6, the pressure increased, as can be noted from Figure 7; this increase varied with depth. For the lowest elevation, there was little to no seasonal change,

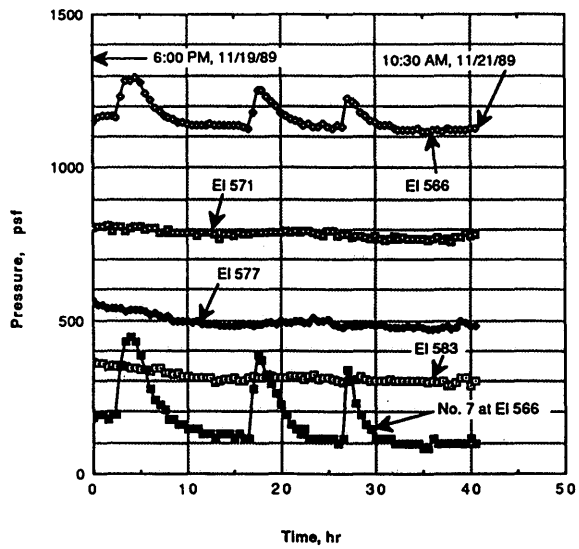

FIGURE 8 Pressure versus time, ½-hr intervals.

since the influence of the deck movement has little effect at this depth. By June 6 pressures at all depths were practically the same because the expansion of the deck at the top increased the upper pressures.

Superimposed on the seasonal changes shown in Figure 7 are pressure changes related to weather periods, typically of 1 day to a week. At the smallest scale are daily fluctuations as the day to night temperature changes. The mean air temperature difference from 6 a.m. to 6 p.m. for this entire period is 15°F.

The most unexpected and significant effect monitored was the frost buildup at the elevation of the second cells from the bottom. This frost buildup was not expected because the soil behind the abutment was free draining and considered a frost-free material; the percentage of fines is less than 1 percent. The mechanism for the frost buildup appears to be related to the change of the river water level, which is typically 7 ft and occurred more than once a day. The frost buildup occurred in this zone, which was alternately saturated and then drained. The pores caused by filling with ice are fine enough so that frost buildup begins and keeps occurring as long as the ground stays frozen. The frost buildup began about January 1, 1990, although freezing temperatures had been at the frost buildup level for almost 2 weeks.

Although freezing occurred at all levels except below the sustained river water level, there was no indication that freezing was deep enough to affect the stress-strain properties of the soil as felt by the abutment. It is possible that there was a change in the soil properties in the upper 5 ft of the approach fill. This depth would be frozen at all points and not just near the abutment wall.

Skew Effects

One of the purposes of installing multiple lines of pressure gauges was to detect pressure differences that may occur because of the bridge skew. There was a higher pressure on the obtuse side relative to the acute side, which indicates that there is more movement of the bridge into the soil on the obtuse side than on the acute side. These lines are at only 10 ft from the bridge centerline, and it is possible that the difference is greater at greater distances from the bridge centerline.

ABUTMENT SOIL PRESSURE COMPARED WITH DESIGN ASSUMPTIONS

For the design of the Forks Bridge, it was anticipated that the expansion of the bridge deck would push the abutment into the approach fill. It was also recognized that this movement would occur primarily near the top. The envelope pressure shown in Figure 9, which was established for design in 1986, was based on this anticipated behavior and on results for rigid frame bridges in Sweden and Britain (*1*). The envelope combined the Rankine passive pressure to one-third of the depth with the at-rest pressure at the bottom of the abutment wall. The passive pressure was used, although it

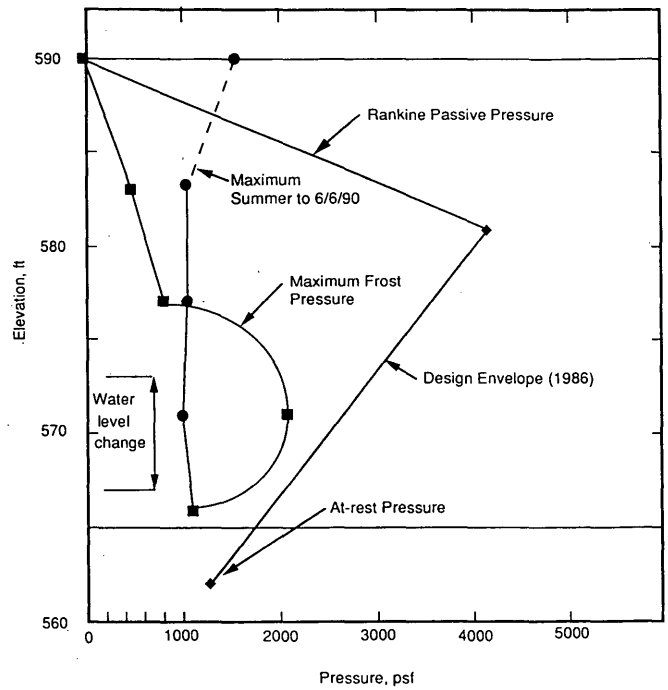

FIGURE 9 Earth pressure versus depth.

was realized that the full passive pressure would probably not be developed for the expected movement associated with the deck expansion. A unit weight of 115 lb/ft^3, an at-rest coefficient of 0.41, and a passive coefficient of 3.85 were used to obtain the design pressure.

Two limiting cases obtained from the monitoring conducted between November 1989 and June 6, 1990, are plotted in Figure 9. One case is the maximum frost pressure and the other case is the maximum pressure found caused by summer heat up to June 6. The frost condition was unanticipated in the original design, but the conservative design envelope did cover the frost pressure for the 1989–1990 winter. All measured pressures up to June 6, 1990, are within the design envelope. However, the measured values based on one winter and on part of a summer do not represent the most severe values that will be encountered at the bridge.

CALCULATED STRESSES IN STEEL FRAMES

Two earth-pressure distributions behind the abutments were recommended based on the readings from the pressure cells during the monitoring period (Figure 10). One of these distributions is for the summer and the other is for the winter.

The three-dimensional finite element model of the bridge, described earlier, was used to calculate the axial forces and bending moments in the steel frames caused by the summer and winter earth pressures. The stresses caused by these forces and moments were calculated at the locations of the gauges. The maximum stress calculated did not exceed 0.8-kip/in^2. The 0.8-kip/in^2 stress corresponds to a strain of 0.000028, which is within the error tolerances of the strain readings.

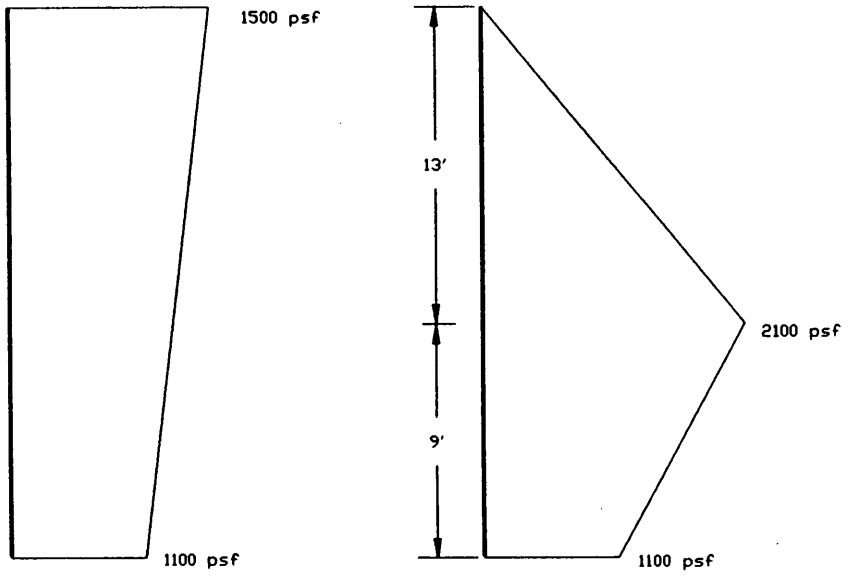

FIGURE 10 Maximum earth pressure for analysis: *left*, summer; *right*, winter.

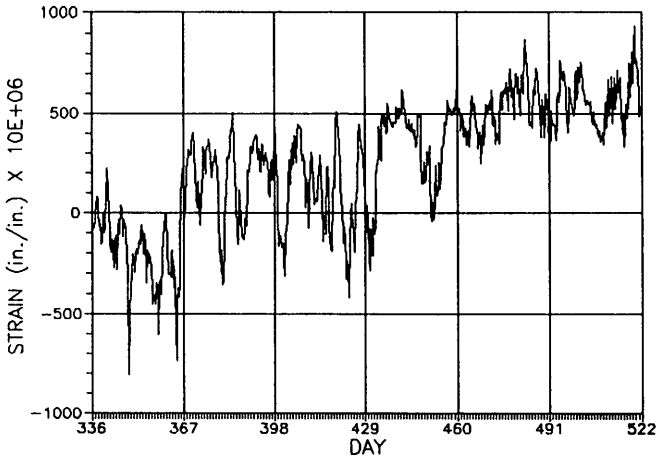

FIGURE 11 Strain readings, Gauge 405.

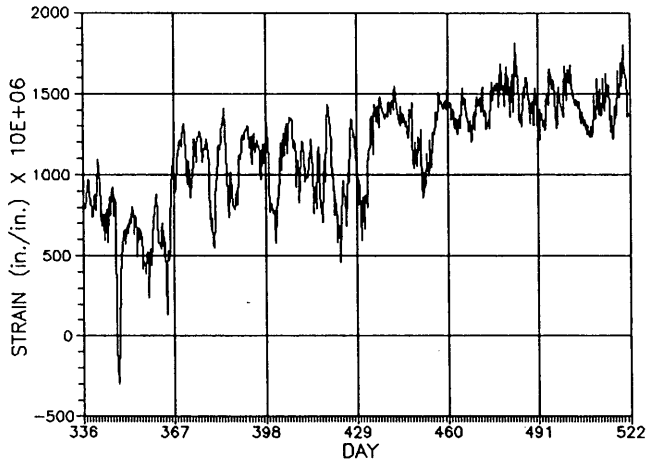

FIGURE 12 Strain readings, Gauge 406.

STRAIN READINGS OF STEEL FRAMES DURING MONITORING

Not all the gauges were functional; however, there is more information than is needed. More strain gauges were installed in anticipation that some of them would not function.

The readings from two strain gauges on one of the two intermediate frames, one on the girder top flange and the other on the bottom flange at midspan (Gauges 405 and 406, respectively), over about 6 months are plotted in Figures 11 and 12. The readings from the two gauges are almost identical, which indicates a more or less uniform expansion and contraction of the bridge. Furthermore, the strain readings follow the temperature variation (Figure 13). In Figure 13 third-degree polynomial curves are fitted to the temperature and strain readings as shown. It is evident that the measured strains are mostly caused by free thermal expansion and contraction of the bridge, thermal output from the gauges, thermal effects on the gauge factor, and resistance of strain gauge wires. In Figure 13, one can note the effect of the compressive strains from the soil pressure during the last month, as indicated by the higher rate of the temperature increase compared with the rate of strain increase during that month. In summary, the strains in the steel frames caused by soil-structure interaction are very small and can hardly be noted.

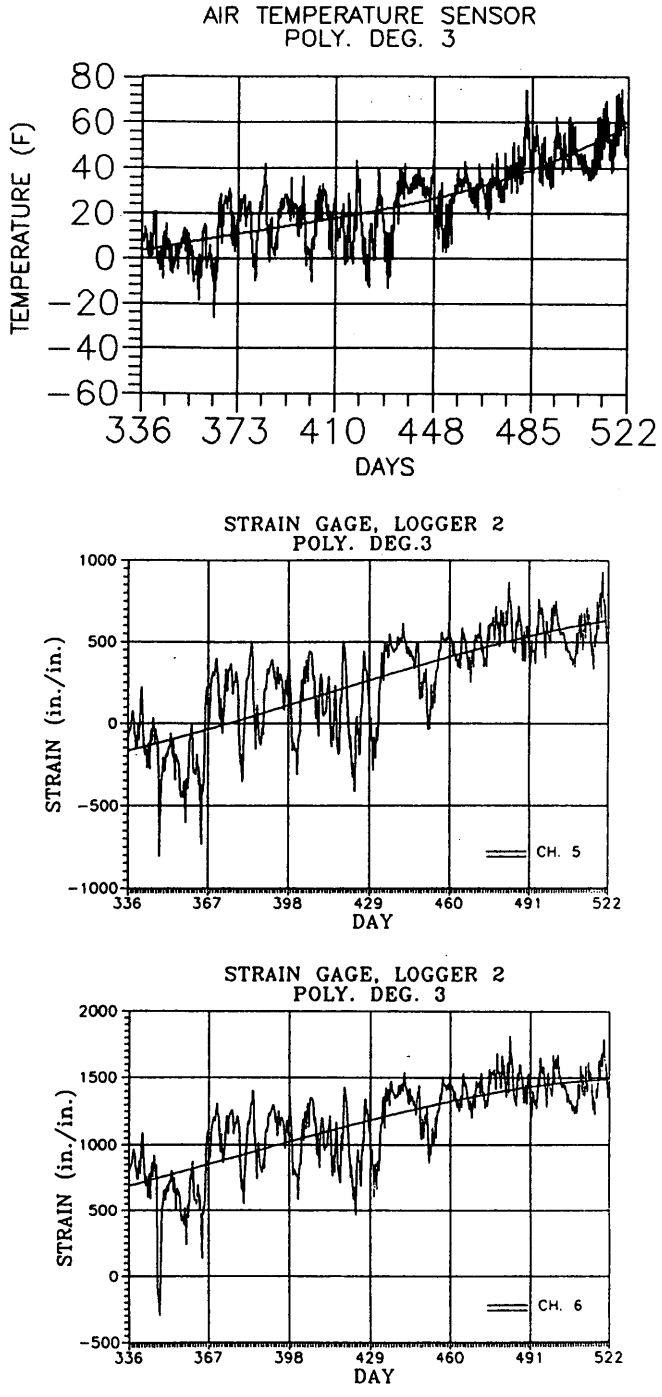

FIGURE 13 Temperature and strain versus time.

CONCLUSIONS

1. To eliminate the center pier for rafting safety and to avoid scour problems, the Forks Bridge has been designed as a rigid frame with integral abutments. Since this design is a first for the state of Maine, performance experience, especially under freezing conditions, is lacking. To improve design for future bridges and to check the present design assumptions, a performance monitoring program was established to be conducted for 3 years.

2. An economical data acquisition system that is able to read, store, and transmit all monitoring signals from the instruments at the Forks Bridge was assembled from off-the-shelf components. Currently, all instruments are read by the data acquisition system every 6 hr, and the data are downloaded at Orono every 2 weeks, although up to 6 weeks of data can be stored at this frequency of readings.

3. Strains in the steel frames caused by the weight of the concrete deck and truck load tests conducted after the bridge completion were measured. Agreement between the measured and calculated strains are reasonable for all practical considerations.

4. The Forks Bridge moves in response to temperature changes, but as the bridge expands, the level of soil resistance behind the abutment gives minor stresses in the steel frames. The movements of the abutments were largest at the top and appeared to be little or none at the level of the footing. Although the concrete deck was connected to the steel girder by shear connectors, there were no indications of any appreciable stresses caused by differential thermal movements of the concrete and the steel.

5. Frost pressures were measured in the non-frost-susceptible fill in the zone of fluctuating river water levels. The frost was not detected outside this approximate 7-ft fluctuation level.

6. Although the concrete abutment was about 8 ft thick, the freezing front penetrated into the backfill behind the abutment by mid-December 1989 and remained until April 9, 1990.

7. The 12-in.-thick approach slab that is keyed into the concrete abutment provides a bridge over gaps that will develop between the abutment and the backfill during shrinkage of the deck in colder weather. It also provides a compression resistance of approximately 1,600 lb/ft^2 for the upper 1-ft of the abutment during deck expansion as it drags on the underlying soil. During deck shrinkage, it should provide a tensile resistance of the same magnitude.

8. The bridge has a 20-degree angle of skew. Although the results are different at the obtuse corners from those at the acute corners (larger forces at the obtuse corners), the differences are not excessive.

ACKNOWLEDGMENTS

This work was sponsored by the Maine Department of Transportation (MDOT) under James Chandler. The bridge was designed by the MDOT Bridge Division under Lawrence L. Roberts.

REFERENCE

1. B. B. Broms and I. Ingleson. Earth Pressures Against the Abutments of a Rigid Frame Bridge. *Geotechnique*, Vol. 21, No. 1, Jan. 1971, pp. 15–28.

Publication of this paper sponsored by Committee on General Structures.

Generalized Approach to Design of Posttensioned Concrete Anchorage Zones

DAVID H. SANDERS AND JOHN E. BREEN

The current provisions for the design of posttensioned concrete anchorage zones in AASHTO's bridge design specification state only that designers should limit the average bearing pressure ahead of the anchorage device to less than 3,000 lb/in.^{2} or $0.9f'_{ci}$ (f'_{ci} is the initial concrete compressive strength), whichever is smaller. The specification does not give any guidance for other forces in the anchorage zone, which in many cases are critical. A research project funded by NCHRP and conducted at the University of Texas at Austin was initiated in 1984 with the primary objective of developing a rational and systematic approach to anchorage zone design that could be implemented in the AASHTO bridge specification. The project is completed, and the process of submitting provisions to AASHTO is under way. The proposed provisions provide guidelines for both ultimate and service limit states. It is proposed to divide the anchorage zone into a local zone and a general zone, to require an acceptance test for anchorage devices with high bearing stresses, and to implement design procedures for the general zone that can use a strut-and-tie model, finite element analysis, or approximate equations, or all of these. An introduction into the project and those provisions that are being proposed to AASHTO are presented.

In the 1950s and 1960s extensive research on anchorage zones for posttensioned concrete members was conducted (*1–6*). Most researchers used theory-of-elasticity–type analysis and small anchor block tests to investigate anchorage zone forces and stresses. These studies gave a basic understanding of the forces in simple anchorage zone configurations. The theories and charts developed by Guyon (*7*) in the 1950s are still often used in the design of concentric, multiple, and eccentric anchorage zones. However, when anchorage zone configurations are more complex, engineers have difficulty extrapolating from these basic results. In the 1970s the situation improved somewhat as the use of finite element analysis (FEA) became more common. Yet, many times, this type of analysis is too time consuming, expensive, or difficult to translate into reinforcement patterns. In the late 1970s and early 1980s, a study by Stone and Breen (*8,9*) provided empirical equations for the design of single anchorages in thin members but did not provide a generalized approach.

In 1987 an article by Schlaich et al. (*10*) helped to focus attention on the importance of a consistent and rational approach to design. The article introduced the concept of D- and B-regions within a structural system and utilized the strut-and-tie model (STM). B-STM regions are zones in which Bernoulli's theory of plane strain is valid. D-regions (discontinuity, disturbed, or detailed) are zones in which the strain distribution is significantly nonlinear. These regions are near concentrated loads (anchorage zones in posttensioned concrete), corners, and openings. Even though the STM can be used in both D- and B-regions, it is especially useful in D-regions where few rational techniques are available. The use of the STM for anchorage zone design was first introduced by Mörsch in the 1920s but has not been used extensively.

A rational and systematic approach to anchorage zone design is critical for maintaining a consistent factor of safety. A survey of design engineers around the world conducted by the Comité Euro-International du Béton (CEB) in 1987 helped to indicate the wide variability that occurs in the factor of safety (*11*). Engineers were asked to design a beam having six anchorages applying a total force of 2700 kN (607 kips), each according to their own national code or handbook. For instance, asked to calculate the bursting force (that is, the force caused by the spreading of the applied concentrated load), engineers provided results ranging from 49.5 kN (11.1 kips) to 440 kN (98.9 kips), with an average of 192 kN (43.3 kips). Calculations of the length of the bursting zone and the cross-sectional area of the reinforcement needed to carry the bursting force showed similar variations. The survey makes it clear that progress in the current state of the art in design of anchorage zones is not a matter of refining 5 or 10 percent, but rather is at the point of reducing differences of as much as 500 percent.

In the United States there are other issues as well. There is not a consistent division of responsibility for the anchorage zone between the anchorage device supplier, the engineer of record, and the contractor. This inconsistency and the confusion that often results increase the potential of having a design that does not provide adequate section size or reinforcement to ensure a safe force path for the posttensioning force when the final approval is given by the engineer of record.

The current anchorage zone design provisions of AASHTO's bridge design specification (*12*) state only that designers should limit the average bearing pressure ahead of the anchorage device to 3,000 lb/in.^{2} or $0.9f'_{ci}$, whichever is smaller. (The symbol f'_{ci} is the concrete compressive strength at stressing). It gives no guidance for other forces in the anchorage zone, which in many cases are critical. A research project was initiated and funded in 1984 by NCHRP and conducted at the University of Texas at Austin with the primary objective of developing a rational and systematic approach to anchorage zone design that could be implemented in the AASHTO bridge specification. In seeking to properly define responsibilities, both the legal traditions of engineering responsibility and the physical behavior of the anchorage zones were examined. An

D. H. Sanders, Department of Civil Engineering, University of Nevada, Reno, Nev. 89557. J. E. Breen, Ferguson Structural Engineering Laboratory, 10100 Burnet Road, Room 24, University of Texas, Austin, Tex. 78758.

approach was found that closely relates these two seemingly different considerations. The purpose of this paper is to provide a brief review of the findings from that project and an introduction to the provisions that are being proposed to AASHTO.

DESIGN APPROACH

A concept central to the design approach developed is the division of the anchorage zone into a local zone and a general zone (see Figure 1). This concept came from the results of the elastic FEA done by Burdet (*13*), which indicated that stresses in the zone immediately ahead for the posttensioning bearing surface and within the lateral dimension of the anchorage device were essentially the same regardless of the type of anchorage configuration (concentric, eccentric, inclined, multiple, etc.).

The local zone is defined as the volume of concrete surrounding and immediately ahead of the anchorage device, throughout which the force applied to the anchorage device is transferred to the general zone. The local zone includes any confining reinforcement required by the specific anchorage device. The local zone must resist the very high local pressures introduced by the anchorage device. Its behavior is strongly influenced by the specific characteristics of the anchorage device and its confining reinforcement, and considerably less influenced by the geometry and loading of the overall structure.

The general zone is defined as the volume of concrete through which the lateral spreading of posttensioning forces occurs from the highly concentrated load at the anchorage device to a more linear force distribution across the entire cross section at some distance from the anchorage device (D-region) (the so-called Saint Vénant Region). In the general zone, the spreading of forces and the induced tensile stresses are the major design considerations. The sections in Figure 1 are two-dimensional representations of the anchorage zone. The anchorage zone is analyzed by analyzing each of the principal planes.

By defining the local zone and the general zone, it is possible to attribute the various responsibilities for the proper performance of the anchorage zone to the engineer of record, the anchorage device supplier, and the constructor. The engineer of record is responsible for (a) the overall design for both the service and ultimate limit states, (b) the approval of the local zone details usually based on test data submitted by the anchorage device supplier, and (c) the design or approval of working drawings for the general anchorage zone, including the specific locations of the tendons, anchorage devices, and general zone reinforcement and for the specific stressing sequence.

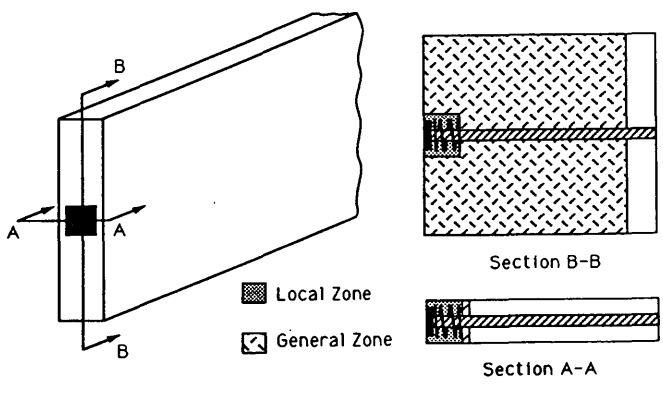

FIGURE 1 Local and general zones, Sections A-A and B-B.

The anchorage device supplier is responsible for (a) furnishing adequate hardware devices; (b) specifying the required auxiliary and confining reinforcement, minimum-edge, and center-to-center distances; and (c) specifying the minimum concrete strength for stressing to ensure the proper performance of the local zone.

The constructor is responsible for (a) the proper placement of all materials and (b) the correct performance of all stressing operations according to the design documents of the engineer of record and the requirements stipulated by the anchorage device supplier.

The posttensioned anchorage zone design provisions proposed for the AASHTO bridge specification incorporate a limit states approach by using the load and resistance factor technique for strength calculations in conjunction with service and detailing checks. A load factor of 1.2 was selected for use with the maximum tendon jacking force ($0.8f'_sA^*_s$) (f'_s is the ultimate strength of the prestressing steel and A^*_s is the area of the prestressing steel). This results in a design force 0.96 times the nominal ultimate strength of the tendon, which is essentially the maximum force that can be applied to a tendon before the grips fail. A ϕ-factor of 0.85 was selected for anchorage zones when normal weight concrete is used and 0.70 for lightweight concrete. The factor reflects the importance of the anchorage zone, the brittle compression failures that can occur, and the relatively wide scatter of the experimental results. The overall factor of safety (load factor/ϕ = 1.2/0.85 = 1.41) is essentially the same as that recommended by the International Federation of Prestressed Concrete (FIP) (*14*).

Local Zone

In the project, to assist in the development of the proposed specification, the large preexisting data base was examined by Roberts (*15*). In addition, 31 tests were performed that investigated the effects of spiral and tie size, spacing and length, anchorage size and type, and concrete strength.

Roberts concluded that to satisfy service and safety requirements, anchorage devices must be divided into two groups: (a) those with reasonable stiffness and an average bearing stress at ultimate of less than $0.7\phi f'_{ci}\sqrt{A/A_g}$ (A is the maximum area of the supporting surface that is similar to and concentric with the loaded area, and A_g is the gross area of the bearing plate) and $2.25\phi f'_{ci}$; and (b) those with higher bearing stresses. Anchorage devices in the first group are called basic anchorage devices. They are limited to a level of bearing stresses that provide good service and ultimate load performance without auxiliary confining reinforcement, and they can be used without further testing. Anchorage devices in the second group are called special anchorage devices, and they must pass an acceptance test. (Most anchorage devices

are in this category.) For an anchorage device system to pass the acceptance test proposed, the crack widths must remain below certain limits at several load stages and the anchorage must be able to reach either (a) 1.2 times the ultimate load of the tendons when tested with a long-term (48-hr) testing procedure or a cyclic testing procedure; or (b) 1.3 times the ultimate load of the tendons with a monotonic testing procedure.

General Zone

The design procedure for the general zone must also satisfy service and ultimate limit states. Unlike the local zone—in which generally there are a limited number of practical configurations—the general zone has a wide range of acceptable configurations. Therefore, it is impossible to use an acceptance test. Design procedures must ensure proper performance. Basing the service limit state on a crack-free performance is unrealistic because of the complex stress state, the effects of shrinkage and restraints, and the reticence of relying on tensile concrete strength. Therefore, in the proposed specification, the service limit state has been addressed by providing guidelines for reinforcement to control cracking to within acceptable limits.

Recommended Design Methods

The proposed provisions describe three methods for determining ultimate capacity of the anchorage zone: (a) FEA, (b) STM, and (c) approximate equations. In each of these procedures, all possible failure modes must be checked, that is, compressive failure of the concrete and tensile or development failure of the reinforcement. The compression failure in the general zone will in most cases occur immediately outside the confined local zone or at a change in thickness within the section.

Finite Element Analysis

FEA allows the calculation of the elastic flow of forces [see Figure 2 (*left*) and paper by Burdet (*13*)], compatibility stresses, and the compression stresses from stress trajectories. The compressive stresses determined are compared with the maximum permissible stress of $0.7\phi f'_{ci}$. The location and magnitude of the bursting force may be obtained by integrating the bursting stresses along the tendon path. However, the time required to input data and the overall cost can make FEA expensive.

Strut-and-Tie Model

STM is a lower-bound plasticity model that has the advantage of showing clearly the design forces necessary for tension reinforcement as well as indicating a plausible force path for the prestress force from the anchorage device into the member. The STM consists of compression struts, tension ties, and nodes (intersection points). Figure 2 (middle) shows a simple STM that crudely represents the force flow, whereas Figure 2 (*right*) shows an STM that more closely models the pattern of the compressive force and tension force distribution. The centroids of tie T in Figure 2 (middle) and group of ties T_1, T_2, and T_3 in Figure 2 (*right*) are approximately at 0.5h. The ties represent the location of the reinforcing bars. Tests showed that either model is acceptable (*16*).

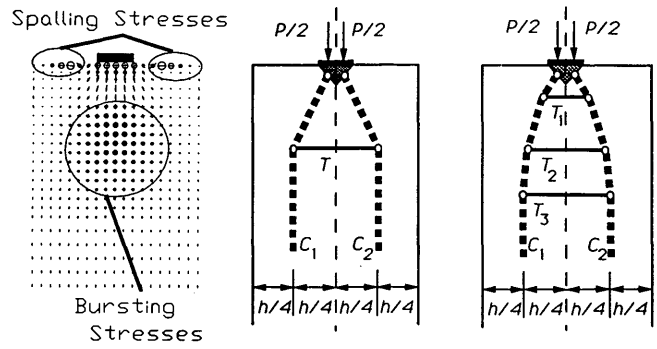

FIGURE 2 Concentric anchorage analysis comparison: *left*, elastic stress; *middle*, single-tie STM; *right*, multiple STM trajectories (*12*).

An STM is sketched by following the compression force paths and satisfying equilibrium. The model can be developed by intuition or in complex cases by following the results of an FEA. The model uses the elastic stress distribution at the end of the general zone to determine the location and magnitude of the compression struts. It is not critical that the tension ties be located exactly at the elastic centroid of the tension stresses. The STM allows flexibility in the placement of the tension reinforcement. The STM has the adaptability to be used for the design of many different geometries and loading configurations.

The potentially complex aspect of the STM is the checking of the compression capacity of the struts and nodes. The size of the compression struts and nodes must be estimated. The special anchorage device local zone is assumed to be an acceptable node, if sufficient capacity exists at the local zone-general zone interface. Tension ties must be developed at the other nodes. In addition, since the STM is an equilibrium-based model, it does not accurately model the forces that are needed only to satisfy compatibility conditions [see Figure 2 (*left* and *middle*), spalling stresses]. Rules are given in the proposed specification for estimating the magnitudes of these compatibility forces, which are typically small.

Approximate Methods

The use of approximate equations can be a quick and easy way to design an anchorage zone as long as the assumptions of the equations are met. The extrapolation of an approximate equation to a more complex anchorage zone can produce unconservative designs. The proposed approximate equations are limited to members with (a) a rectangular cross section, (b) an anchorage zone length equal to at least the largest dimension of the cross section, (c) no discontinuities within or ahead of the anchorage zone, (d) only one anchorage device or one group of closely spaced anchorages, (e) straight tendons within the anchorage zone, and (f) a minimum-edge

distance for the anchorage in the main plane of the member of at least 1.5 times the corresponding lateral dimension of the anchorage device.

The approximations for the compressive stresses at the interface between the local zone and the general zone are calculated using Equations 1 and 2, whereas the approximations for the bursting tension force needed are calculated using Equations 3 and 4.

$$f_{ca} = \kappa \frac{0.6P_u}{A_{\text{eff}}} \frac{1}{1 + l_c\left(\frac{1}{b_{\text{eff}}} - \frac{1}{t}\right)} \tag{1}$$

$$\kappa = 1 + \left(2 - \frac{s}{a_{\text{eff}}}\right)\left(0.3 + \frac{n}{15}\right) \qquad \text{for } a_{\text{eff}} \le s < 2a_{\text{eff}}$$

$$\kappa = 1 \qquad \text{for } s \ge 2a_{\text{eff}} \tag{2}$$

$$T_{\text{burst}} = 0.25 \sum P_u \left(1 - \frac{a}{h}\right) + 0.5\, V_a \tag{3}$$

$$d_{\text{burst}} = 0.5(h - 2e) + 5e \sin\alpha \tag{4}$$

where

$\sum P_u$ = sum of factored tendon loads,
V_a = shear force in anchorage zone at time of stressing,
a = lateral dimension of anchorage device or closely spaced group of anchorages,
e = eccentricity of the anchorage device or group from section centroid (always positive),
h = lateral dimension of cross section being considered, and
α = angle of inclination of resultant of tendon force with respect to the centerline of the member, positive for concentric tendons or if anchor force points toward the centroid of section (must be between −5 and 20 degrees).

VERIFICATION OF GENERAL ZONE DESIGN PROCEDURES

A physical testing program was developed to verify the design procedures that use the STM, FEA, and approximate equations. Using tests to verify procedures instead of to develop empirical expressions enabled the researchers to test a wide variety of specimens with few replicates. This seemed to be the best use of limited resources.

Testing Procedures

The program was divided into two phases. Phase A focused on end-type anchorages and consisted of 36 general zone physical specimens reported by Sanders (*16*). Anchorage location and reinforcing patterns were varied (concentric anchorage with both prestressed and nonprestressed reinforcement, eccentric anchorage, multiple anchorages, and anchorages with inclination and tendon curvature). In Phase B, a total of 14 general zone specimens (specimens with intermediate anchorages, anchorages in beams with support conditions perpendicular to the posttensioning force, and anchorages in blisters, ribs, and diaphragms) were reported by Wollmann (*17*) and 6 slab specimens (each with multiple anchorage tests) were reported by Falconer (*18*). The test specimens were designed using the STM to proportion the general zone reinforcement after using FEA (*13,17*) to indicate the stress fields. The critical reinforcement in each test specimen was instrumented. Crack development and ultimate loads were recorded. The specimen results were compared with the design models.

Basic STM

Examples of STM appear in Figures 3 and 4. These were constructed assuming an elastic stress distribution at the end of the general zone. For eccentric anchorages with the resultant force outside the kern [see Figure 3 (*left*)], a tension force occurs on the outer longitudinal edge fibers farthest from the anchorage device (tension tie T_2). To keep crack sizes small, the spalling force (T_3) is located very close to the exterior surface, a distance from the loading surface approximately equal to the width of the anchorage plate divided by four. The use of tendons with curvature adds radial forces along the tendon path. These forces act as a distributed load perpendicular to the tendon path with a value equal to the tendon load divided by the radius of curvature of the tendon. The radial forces can be modeled as forces being applied to the compression struts [see Figure 3 (*right*)]. Tie-back reinforcement used to carry the radial forces back across the tendon path are modeled as tensile forces applied to the compression strut [see left compression strut in Figure 3 (*right*)]. An example of an STM when multiple anchorages are close together is shown in Figure 4 (*left*), and Figure 4 (*right*) shows two anchorages that are far enough apart to cause a major spalling tension force (T_3) to develop along the loaded surface in the concrete. As with the spalling force in Figure 3 (*left*), the forces C_7 and T_3 are very close to the loading surface.

Once the designer determines the basic shape of the STM, which implicitly assumes a particular reinforcement distribution, the equally important task of defining the size and capacity of the compression struts and nodes must be done. The local zone surrounding the anchorage device contains the node that transfers the tendon force onto the concrete. In this and several previous studies, a pyramid or cone was observed under the loading plate when a bearing failure occurred; therefore, a pyramid was assumed for the shape of the local zone node. The idealization of the pyramid shape in a principal direction for a concentric anchorage zone appears in Figure 5. The compression struts initiate from the local zone node.

In most anchorage zone configurations, the struts will widen and the stresses will decrease with distance from the anchorage device. The spreading of the struts is why Schlaich et al. (*10*) describe some nodes as discrete and others as smeared. The two nodes [see Figure 2 (*middle*)] near the bearing surface are discrete nodes; they are confined to a small area and have high concentrated forces. The two nodes shown further away from the anchorage device are shown as two dots but are actually smeared nodes spread over a much larger area. Proper reinforcement detailing is necessary for both node types to ensure that reinforcement can be fully developed at the node.

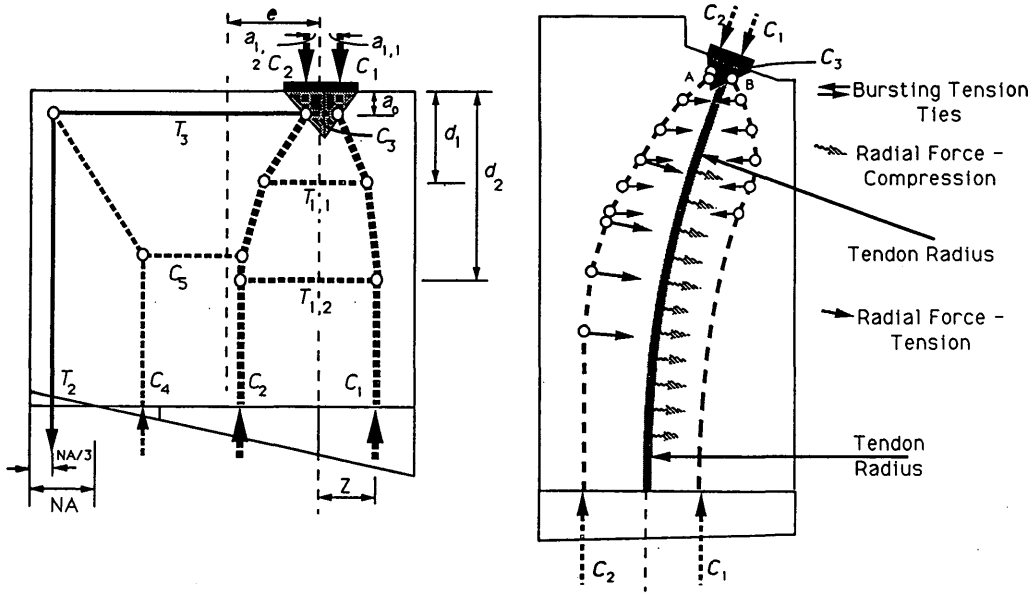

FIGURE 3 Eccentric anchorage STM: *left*, straight tendon outside kern; *right*, curved tendon with anchorage inclination.

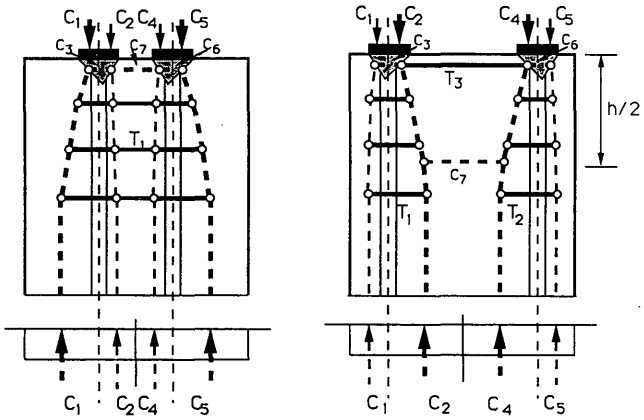

FIGURE 4 Multiple anchorage STM: *left*, closely spaced anchors; *right*, widely spaced anchors.

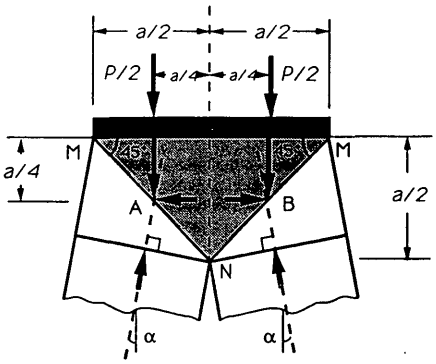

FIGURE 5 Idealized concentric node.

However, discrete nodes must also be checked for concentrated compressive stresses, whereas smeared nodes have distributed compressive stresses and do not need to be checked.

The width of the compression strut is assumed to be equal to twice the distance from the tendon axis to the centerline of the strut as measured normal to the strut axis (see Figure 5). This is assumed because (a) the two struts cannot overlap at the tendon axis; and (b) a uniform stress distribution is assumed for the strut, which defines the exterior boundary since the centroid of the strut is known. Three locations are critical for verifying the strut capacity: (a) the interface between the node and the strut where a portion of the strut is typically unconfined; (b) the interface between the local zone and the general zone where the strut leaves the local zone and enters the general zone (the strut is assumed fully unconfined); and (c) at sections where thickness changes and increases in the strut stresses can occur. For design purposes, the certification of the special anchorage device provided by the anchorage device supplier is used to check the adequacy of the interface between the node and the strut. The engineer of record must check the compressive stresses at the local zone-general zone interface. The location of the local zone-general zone interface can be assumed to be at a distance equal to one times the lateral dimension of the anchorage device away from the bearing surface or the end of the confining reinforcement, whichever is closer. This assumption provides the best correlation with the experimental results when using a concrete compressive stress limit of $0.7f'_{ci}$.

The STM is a lower-bound model based on the theory of plasticity and was found to be a conservative way of estimating the ultimate strength of the specimens. The average of the test ultimate strength divided by the STM prediction for the specimens in Phase A (end-type anchorage zones) was 1.50 (see Table 1) with a coefficient of variation of 0.32 (*16*) when assuming the critical depth for the local zone-general zone interface at the end of the local zone confining spiral. Setting

aside Specimen B5, which had no general zone reinforcement and hence is really outside the scope of the STM, only one specimen was unconservatively predicted. This was Specimen B2, where the prediction was one percent unconservative, possibly because its bursting reinforcement was very deep within the section. (The distance from the loaded surface to the centroid of the bursting reinforcement divided by the section width was equal to 0.84.) If the critical depth for the local zone–general zone interface is placed at a depth equal to the lateral dimension of the anchorage device, then the average of the test ultimate divided by the STM prediction for the specimens only changes slightly to 1.52 with a coefficient of variation of 0.31. More details on reasons for this assumption are given in the next section.

Care should be taken not to place reinforcement, which is depended on to carry bursting tension, too far from the anchorage device. If reinforcement is placed too deep within the section, additional cracking must occur for this reinforcement to become active. This increased cracking could cause serviceability problems or reduce compressive strength, or both.

Modified STM

The strength of several specimens exceeded the basic STM prediction, in one case by a factor of 3.3. The cause was sought by examining cracking patterns from the physical tests and using a step-by-step elastic analysis. It was determined that as the anchorage zone cracked along the tendon axis, the anchorage zone extended further into the section and the compression struts began to shift closer to the tendon axis (see Figure 6). In the physical specimens, this created a more plastic stress distribution at the base of the specimens. As the struts shift in toward the tendon axis, the posttensioning axial capacity (as governed by the tension ties) increases because the moment arm of the compression force C_1 about Point A decreases. The shift of the strut reduces the width of the strut at the local zone-general zone interface [Plane a-a in Figure

TABLE 1 Phase A: Basic STM Results (*16*)

		LZ-GZ Interface at End of Spiral			LZ-GZ Interface at Plate Width from Bearing Surface		
Test Name	Ultimate	STM Prediction Mode	Load	Test/ STM	STM Prediction Mode	Load	Test/ STM
A1	298	N-S	195	1.52	N-S	195	1.49
A2	275	N-S	190	1.45	N-S	190	1.45
A3	265	N-S	204	1.30	N-S	204	1.30
A4	437	N-S	306	1.43	N-S	306	1.43
B1	366	T-Tie	299	1.22	T-Tie	299	1.22
B2	290	T-Tie	292	0.99	T-Tie	292	0.99
B3	331	T-Tie	296	1.12	T-Tie	296	1.12
B4	337	T-Tie	277	1.22	T-Tie	277	1.22
B5[a]	212	LZ-GZ	218	0.97	LZ-GZ	201	1.05
B6	297	Bearing	218	1.36	Bearing	218	1.36
B7	296	T-Tie	269	1.10	T-Tie	269	1.10
B8	276	T-Tie	252	1.09	T-Tie	252	1.10
C1	370	T-Tie	192	1.93	T-Tie	192	1.93
TPT1	310	T-Tie	180	1.72	T-Tie	180	1.72
TPT2	300	T-Tie	253	1.19	T-Tie	253	1.19
TPT3	370	T-Tie	247	1.50	T-Tie	247	1.50
TPT4	332	T-Tie	235	1.41	T-Tie	235	1.41
E1	475	Bearing	404	1.17	Bearing	404	1.18
E2	500	Bearing	445	1.12	LZ-GZ	425	1.18
E3[b]	522	Bearing	453	1.15	LZ-GZ	438	1.19
E4	500	Bearing	434	1.15	LZ-GZ	407	1.23
E5	332	T-Tie	238	1.39	T-Tie	238	1.39
E6	348	T-Tie	259	1.34	T-Tie	259	1.34
M1	304	T-Tie	189	1.61	T-Tie	189	1.61
M2	401	LZ-GZ	322	1.25	LZ-GZ	245	1.64
M3	364	T-Tie	290	1.26	LZ-GZ	244	1.49
M4	411	T-Tie	180	2.28	T-Tie	180	2.28
M5	339	T-Tie	202	1.68	T-Tie	202	1.68
M6	300	T-Tie	104	2.88	T-Tie	104	2.88
ME1	350	T-Tie	226	1.55	T-Tie	226	1.55
ME2	370	T-Tie	261	1.42	T-Tie	261	1.42
F1	248	T-Tie	133	1.86	T-Tie	133	1.86
I1	423	T-Tie	281	1.51	T-Tie	281	1.51
I2	437	T-Tie	223	1.96	T-Tie	223	1.96
I3	375	T-Tie	262	1.43	T-Tie	262	1.43
I4	420	T-Tie	126	3.33	T-Tie	126	3.33
Average				1.50			1.52
Standard Deviation				0.49			0.48
Coef. of Variation				0.32			0.31

T-Tie = Tension Tie Capacity Governs
N-S = Node-Strut Interface Capacity Governs
LZ-GZ = Local Zone-General Zone Interface Capacity Governs
Bearing = Bearing Capacity Under Anchorage Device Governs
All Units in kips

[a] *no bursting steel, zero tension capacity ignored*
[b] *longitudinal edge tension and spalling tension capacity*

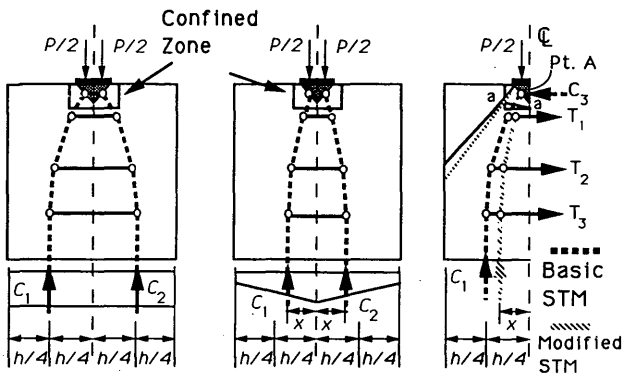

FIGURE 6 Basic STM (*left*), modified STM (*middle*), and comparison (*right*).

6 (*right*)], reducing the posttensioning axial capacity (as governed by the compression struts).

The configuration of the modified STM (*16*) is determined by locating the strut C_1 [distance x in Figure 6 (*right*)] at a position where the STM-predicted ultimate load, assuming that the bursting tension ties control, is the same as the STM-predicted ultimate load, assuming that the compression struts control. The location is determined by shifting the assumed centroid of the compression strut toward the tendon axis until the two loads match.

Even though the modified STM was much more accurate for modeling behavior, it predicted unconservatively the ultimate strength for 14 out of the 35 specimens (setting aside Specimen B5). The average of the ratio between the ultimate test load and the predicted load for all the specimens was 1.05 with a coefficient of variation of 0.20 (see Table 2) (*16*) when

TABLE 2 Phase A: Modified STM Results (*16*)

		LZ-GZ Interface at End of Spiral			LZ-GZ Interface at Plate Width from Bearing Surface		
Test Name	Ultimate	STM Prediction Mode	Load	Test/ STM	STM Prediction Mode	Load	Test/ STM
A1	298	N-S	199	1.49	N-S	199	1.49
A2	275	N-S	204	1.35	N-S	204	1.35
A3	265	N-S	200	1.33	N-S	200	1.33
A4	437	LZ-GZ	335	1.30	LZ-GZ	335	1.30
B1	366	LZ-GZ	440	0.83	LZ-GZ	343	1.07
B2	290	LZ-GZ	381	0.76	LZ-GZ	305	0.95
B3	331	LZ-GZ	416	0.80	LZ-GZ	326	1.02
B4 [a]	337	LZ-GZ	429	0.79	LZ-GZ	330	1.02
B5	212	LZ-GZ	218	0.97	LZ-GZ	201	1.05
B6	297	Bearing	218	1.36	Bearing	218	1.36
B7	296	LZ-GZ	421	0.70	LZ-GZ	327	0.91
B8	276	LZ-GZ	405	0.68	LZ-GZ	303	0.91
C1	370	LZ-GZ	419	0.88	LZ-GZ	328	1.13
TPT1	310	LZ-GZ	346	0.90	LZ-GZ	290	1.07
TPT2	300	LZ-GZ	376	0.80	LZ-GZ	311	0.96
TPT3	370	LZ-GZ	432	0.86	LZ-GZ	351	1.05
TPT4	332	LZ-GZ	401	0.83	LZ-GZ	328	1.01
E1	475	Bearing	404	1.18	Bearing	404	1.18
E2	500	Bearing	445	1.12	Bearing	445	1.12
E3 [b]	522	Bearing	453	1.15	Bearing	453	1.15
E4	500	Bearing	434	1.15	Bearing	434	1.15
E5	332	Bearing	343	0.97	LZ-GZ	315	1.05
E6	348	LZ-GZ	339	1.03	LZ-GZ	333	1.05
M1	304	LZ-GZ	293	1.04	LZ-GZ	231	1.32
M2	401	LZ-GZ	336	1.19	LZ-GZ	256	1.57
M3	364	LZ-GZ	355	1.03	LZ-GZ	236	1.54
M4	411	LZ-GZ	345	1.19	LZ-GZ	280	1.47
M5	339	LZ-GZ	280	1.21	LZ-GZ	245	1.38
M6	300	LZ-GZ	206	1.46	LZ-GZ	206	1.46
ME1	350	LZ-GZ	410	0.85	LZ-GZ	328	1.07
ME2	370	LZ-GZ	374	0.99	LZ-GZ	330	1.12
F1	248	LZ-GZ	227	1.09	LZ-GZ	205	1.21
I1	423	LZ-GZ	349	1.21	LZ-GZ	302	1.40
I2	437	LZ-GZ	381	1.15	LZ-GZ	335	1.30
I3	375	LZ-GZ	350	1.07	LZ-GZ	277	1.35
I4	420	LZ-GZ	343	1.22	LZ-GZ	288	1.46
Average				1.05			1.20
Standard Deviation				0.21			0.19
Coef. of Variation				0.20			0.16

N-S = Node-Strut Interface Capacity Governs
LZ-GZ = Local Zone-General Zone Interface Capacity Governs
Bearing = Bearing Capacity Under Anchorage Device Governs
All Units in kips

[a] *no bursting steel, zero tension capacity ignored*
[b] *longitudinal edge tension and spalling tension capacity*

the local zone-general zone interface was assumed to be at the end of the confining spiral. This coefficient of variation is similar to that found when estimating the bearing capacity of anchorage device systems using compression capacity equations developed by Roberts (*15*). Possible reasons for the unconservative prediction are (a) a reduction in the concrete compression capacity because of the excessive and large cracking, (b) inaccuracies in the strut width approximation, or (c) inaccuracies in the assumed location of the critical local zone-general zone interface, or all of these.

When the basic STM was used to predict the capacities of the specimens, only 6 of the 36 specimens were controlled by compression strut failure. It was difficult to refine the compression model using the basic STM. Initially, the location of the local zone-general zone interface was assumed to be at the end of the local zone-confining spiral, which varied between one and two times the anchorage width in the specimens tested. When the depth of the interface was limited to the width of the anchorage, the average of the modified STM comparison ratio increased to 1.20 and the coefficient of variation dropped to 0.16 (see Table 2). The ultimate strength was unconservatively predicted for only four specimens. Those that were unconservatively estimated had predicted to actual strength ratio values greater than 0.9. Therefore, in the proposed specification, the location of the local zone-general zone interface was assumed to be at a distance from the bearing surface equal to one times the lateral dimension of the anchorage device or at the end of the confining reinforcement, whichever was closer.

The design of the anchorage zone must provide some degree of ductility and plenty of warning before failure. In this regard, an analogy between the modified STM and the basic STM can be seen with reinforced concrete beam design. To provide ductility and warning before failure, reinforced concrete beam design has an upper limit on the amount of flexural reinforcement; the design load is based on the yielding of the tensile reinforcement occurring before the compression failure of the concrete. In the anchorage zone tests, extensive cracking was typically observed between the failure load predicted by the basic STM and the actual failure load when the bursting reinforcement controlled the design. Thus the basic STM provides a warning of failure by predicting the ultimate capacity before the extension of the anchorage zone occurs and additional redistribution of forces. The modified STM predicts the final failure state. At this stage of design procedure development, the basic STM is desirable for safety.

CONCLUSIONS

The major characteristics of the proposed design procedure for anchorage zones are

1. Clear division of criteria into those associated with the anchorage device (local zone) and those having to do with the overall spread of the anchor forces (general zone);
2. Flexibility for the engineer of record in choosing an analysis based on the STM, FEA, or, for certain simpler cases, approximate equations;
3. A rational and systematic approach that examines the flow of forces from the anchorage device until the forces have spread over the entire cross section;
4. A lower-bound plasticity method (basic STM) that is highly transparent and provides reasonably accurate results while being conservative; and
5. A clear and logical division of responsibility among the anchorage device supplier, engineer of record, and the constructor.

The current research has established the ground rules for a generalized approach to the design of posttensioned concrete anchorage zones. The design method an engineer selects will depend on the designer's preference as well as the characteristics of the anchorage zone being designed. Each method can yield slightly different results, but all will be conservative when applied properly and when used with proper reinforcement detailing techniques.

Detailed reports (*12*,*15*–*18*) are available that document the experimental study and the various methods used. A series of shorter articles is being developed that will discuss in more detail the topics examined in this paper. Several examples were presented by the authors at the American Segmental Bridge Institute (ASBI) Meeting in Miami, Florida, in December 1990. Handouts from this meeting are available through ASBI (*19*). Although some small changes have been made in the code since they were published, these examples should provide a good reference.

ACKNOWLEDGMENTS

This work was conducted at the Phil M. Ferguson Structural Engineering Laboratory, the University of Texas at Austin. Funding was provided by NCHRP. The authors would like to acknowledge the contributions of Olivier Burdet and Carin Roberts, whose work is cited in this paper.

REFERENCES

1. J. L. Zielinski and R. E. Rowe. *Research Report 9: An Investigation of the Stress Distribution in the Anchorage Zones of Post-Tensioned Concrete Members*. Cement and Concrete Association, London, England, Sept. 1960.
2. J. L. Zielinski and R. E. Rowe. *Research Report 13: The Stress Distribution Associated with Groups of Anchorages in Post-Tensioned Concrete Members*. Cement and Concrete Association, London, England, Oct. 1962.
3. D. J. Douglas and N. S. Trahair. An Examination of the Stresses in the Anchorage Zone of a Post-Tensioned Prestressed Concrete Beam. *Magazine of Concrete Research*, Vol. 12, No. 34, March 1960, pp. 9–18.
4. S. Ban, H. Mugurama, and Z. Ogaki. Anchorage Zone Stress Distribution in Post-Tensioned Concrete Members. *Proc., World Conference on Prestressed Concrete*, Vol. 16, University of California, San Francisco, 1957, pp. 1–14.
5. T. Huang. Stresses in End Blocks of a Post-Tensioned Prestressed Beam. *ACI Journal*, Vol. 61, No. 5, May 1964, pp. 589–601.
6. F. Leonhardt. *Prestressed Concrete—Design and Construction*. Wilhelm Ernest and Son, Berlin, Germany, 1964.
7. Y. Guyon. *Prestressed Concrete*. John Wiley and Sons, Inc., New York, N.Y., 1953.
8. W. C. Stone and J. E. Breen. Behavior of Post-Tensioned Girder Anchorage Zones. *PCI Journal*, Vol. 29, No. 1, Jan.–Feb. 1984.
9. W. C. Stone and J. E. Breen. Design of Post-Tensioned Girder Anchorage Zones. *PCI Journal*, Vol. 29, No. 2, March–April 1984.

10. J. Schlaich, K. Schafer, and M. Jennewein. Towards a Consistent Design of Reinforced and Prestress Concrete Structures. *PCI Journal*, Vol. 32, No. 3, May–June 1987, pp. 563–715.
11. *Anchorage Zones of Prestressed Concrete Members*. No. 181. Comité Euro-International du Béton, April 1987.
12. *Standard Specification for Highway Bridges*, 14th ed. AASHTO, Washington, D.C., 1989.
13. O. Burdet. *Analysis and Design of Post-Tensioned Anchorage Zones of Concrete Bridges*. Ph.D. dissertation. University of Texas, Austin, May 1990.
14. *FIP Recommendations for Acceptance of Post-Tensioning Systems* (Revision of FIP Document 5/9). May 17, 1991.
15. C. Roberts. *Behavior and Design of the Local Anchorage Zone in Post-Tensioned Concrete*. M.S. thesis. University of Texas, Austin, May 1990.
16. D. H. Sanders. *Design and Behavior of Anchorage Zones in Post-Tensioned Concrete Members*. Ph.D. dissertation. University of Texas, Austin, Aug. 1990.
17. G. P. Wollmann. *Anchorage Zones in Post-Tensioned Concrete Structures*. Ph.D. dissertation. University of Texas, Austin, May 1992.
18. B. Falconer. *Post-Tensioning Anchorage Zones in Bridge Decks*. M.S. thesis. University of Texas, Austin, May 1990.
19. *Proposed Post-Tensioned Anchorage Zone Provisions for Inclusion in the AASHTO Segmental Bridge Specification*. Handout at Annual Meeting of the American Segmental Bridge Institute, Miami, Fla., Dec. 1991.

The opinions of the authors do not necessarily reflect those of the sponsor.

Publication of this paper sponsored by Committee on Concrete Bridges.

Lateral-Load Tests of Reinforced Concrete Bridge

MARC O. EBERHARD, M. LEE MARSH, TOM O'DONOVAN, AND GAUKUR HJARTARSON

Static and dynamic tests were performed on a three-span reinforced concrete highway bridge in eastern Washington. The objectives of these tests was to improve the ability of bridge engineers to assess the vulnerability of similar bridges to earthquakes. During a first series of tests, a University of Washington team measured the stiffness and strength of the bridge in its unaltered state. Large, slowly varying, cyclic loads were applied in the transverse direction of the bridge with hydraulic rams; small-displacement dynamic response was induced with an eccentric-mass shaker. The bridge was then isolated from the abutments and a second series of static tests was performed to measure the stiffness, strength, and toughness of the intermediate piers. Preliminary inspection of the measured data indicated that the tests provided good data with which to calibrate analytical models of bridge response. At a drift ratio (ratio of horizontal deflection to clear height of column) of less than 0.15 percent, the bridge resisted a transverse force equal to two-thirds the weight of the bridge. This large stiffness and strength were attributed to the contribution to resistance of the soil at the abutments and to the soil surrounding the columns at the intermediate piers. Tests of the piers demonstrated that, despite their deficiencies, the piers were able to resist forces up to approximately 40 percent of the weight of the bridge at a drift ratio of 3 percent.

Static and dynamic tests performed on a three-span reinforced concrete highway bridge in eastern Washington were part of a Washington State Department of Transportation (WSDOT) research program to assess the seismic vulnerability of multiple-span state highway bridges built before 1983 and to develop economical retrofit strategies. The WSDOT has identified 250 bridges in seismically active areas with superstructure deficiencies. A total of 85 of these bridges have in-span hinges and 165 bridges have inadequate support lengths at piers or abutments. Recognizing the vulnerability of bridges with these deficiencies, the WSDOT has begun to install restrainers and seat extensions in these bridges. An additional 127 bridges supported on single-column piers are scheduled to be retrofitted within the next 20 years (*1*).

The WSDOT has identified an additional 431 bridges with deficient multicolumn piers, similar to those of the test bridge (Figures 1 and 2). Common deficiencies in piers include (a) bridge columns that have little confinement reinforcement, (b) reinforcing splices between column reinforcement and footing dowels that are too short and are unconfined, and (c) lack of top reinforcement in footings. The California Department of Transportation is committed to expeditiously improving the seismic response of bridges with multicolumn piers (*2*). Facing a different seismic threat (*3*) and political situation, the WSDOT has deferred retrofit of multicolumn bents until further research has been performed to assess the need to retrofit these structures (*1*). Research now focuses on identifying critical deficiencies in substructures.

The vulnerability of a pier to transverse components of ground motion depends on the stiffness and strength of the entire bridge, including the effect of abutments, and on the stiffness, strength, and toughness of the pier itself. Despite its deficiencies, a pier may not require costly modifications if

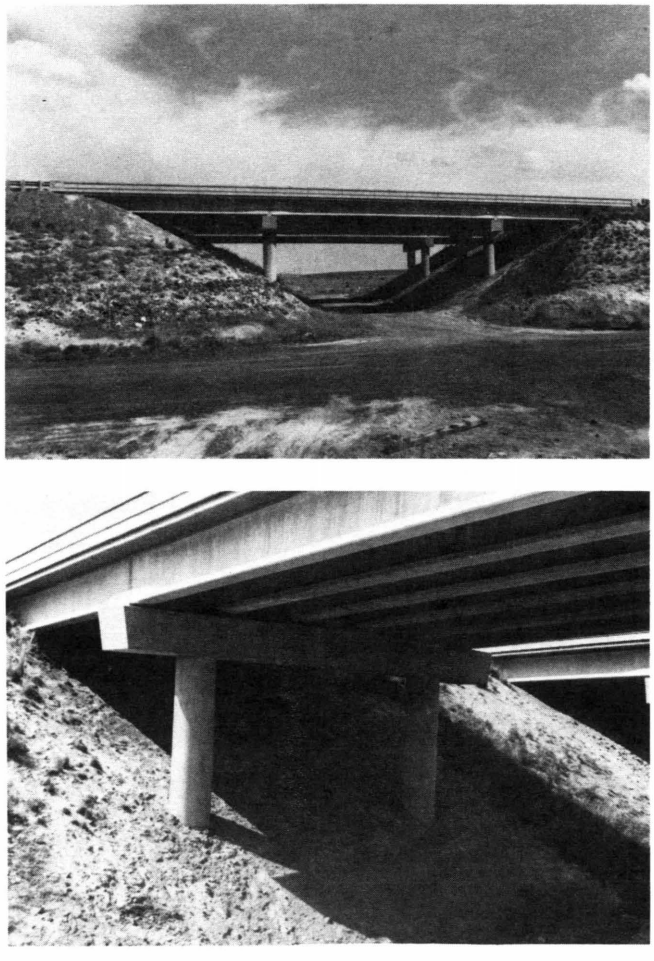

FIGURE 1 Test bridge: *top*, south view; *bottom*, west bent.

M. O. Eberhard and G. Hjartarson, Department of Civil Engineering, University of Washington, Seattle, Wash. 98195. M. L. Marsh, Department of Civil and Environmental Engineering, Washington State University, Pullman, Wash. 99164. T. O'Donovan, U.S. Army Corps of Engineers, Seattle, Wash. 98195.

transverse displacements of the pier are small and if the pier is relatively flexible. In contrast, a pier is likely to be damaged during an earthquake if it undergoes large displacements, particularly if the pier is stiff and brittle. Data from destructive tests of a bridge and of piers provide the opportunity to calibrate analytical models of bridge response and to improve estimates of pier toughness. Both the selection of an analytical model and the ductility capacity assumed for piers are critical to the decision to retrofit a pier.

DESCRIPTION OF BRIDGE

The test bridge was one of a pair of bridges (Figure 2) constructed in 1966 to carry I-90 traffic across a railroad line located 188 mi east of Seattle near Moses Lake, Wash. After the railroad line was abandoned, the WSDOT decided to eliminate these obsolete bridges. During testing and demolition, traffic on the south bridge was diverted to the north bridge. To minimize traffic disruption, testing was limited to 30 days.

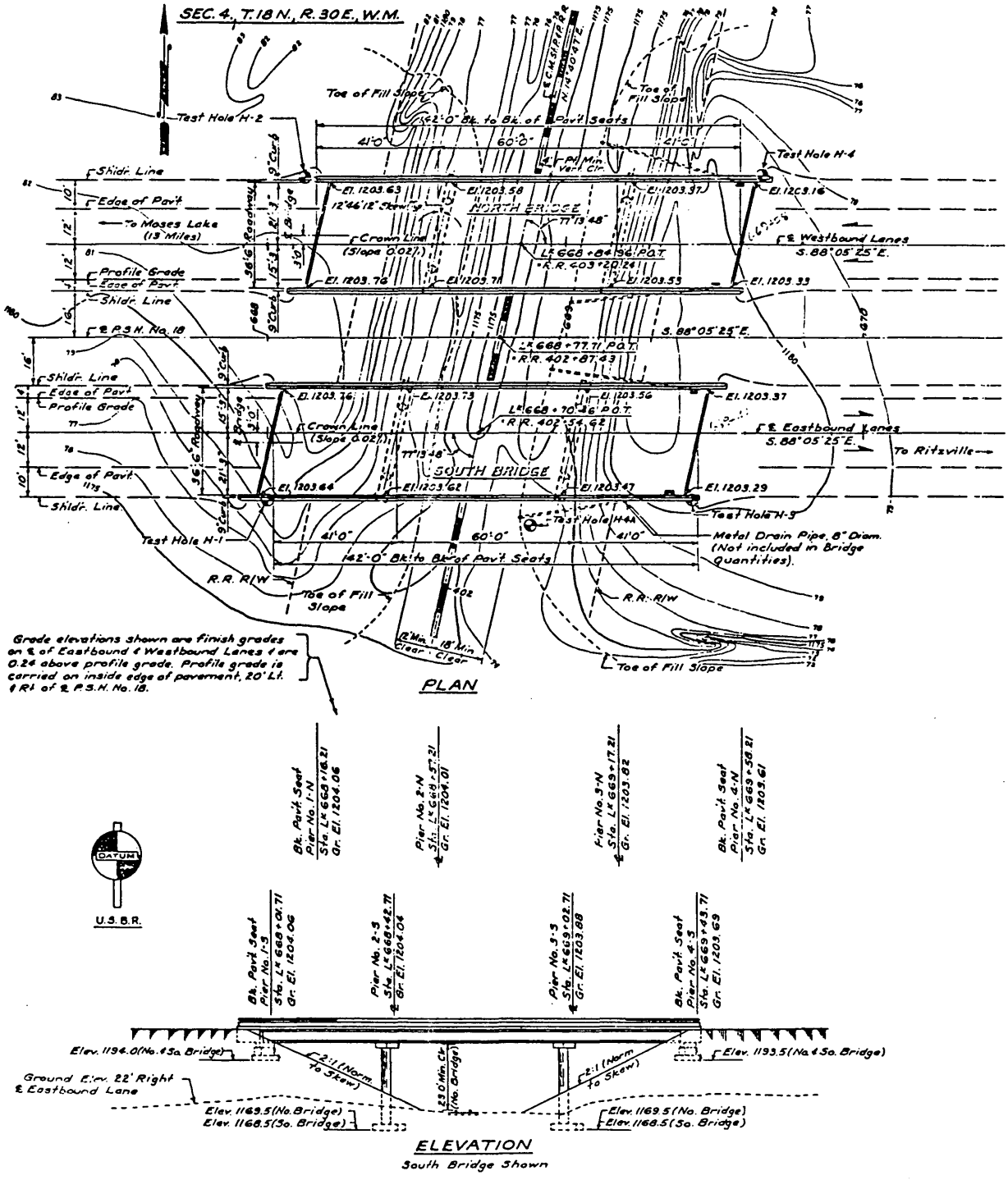

FIGURE 2 Structural plan and elevation.

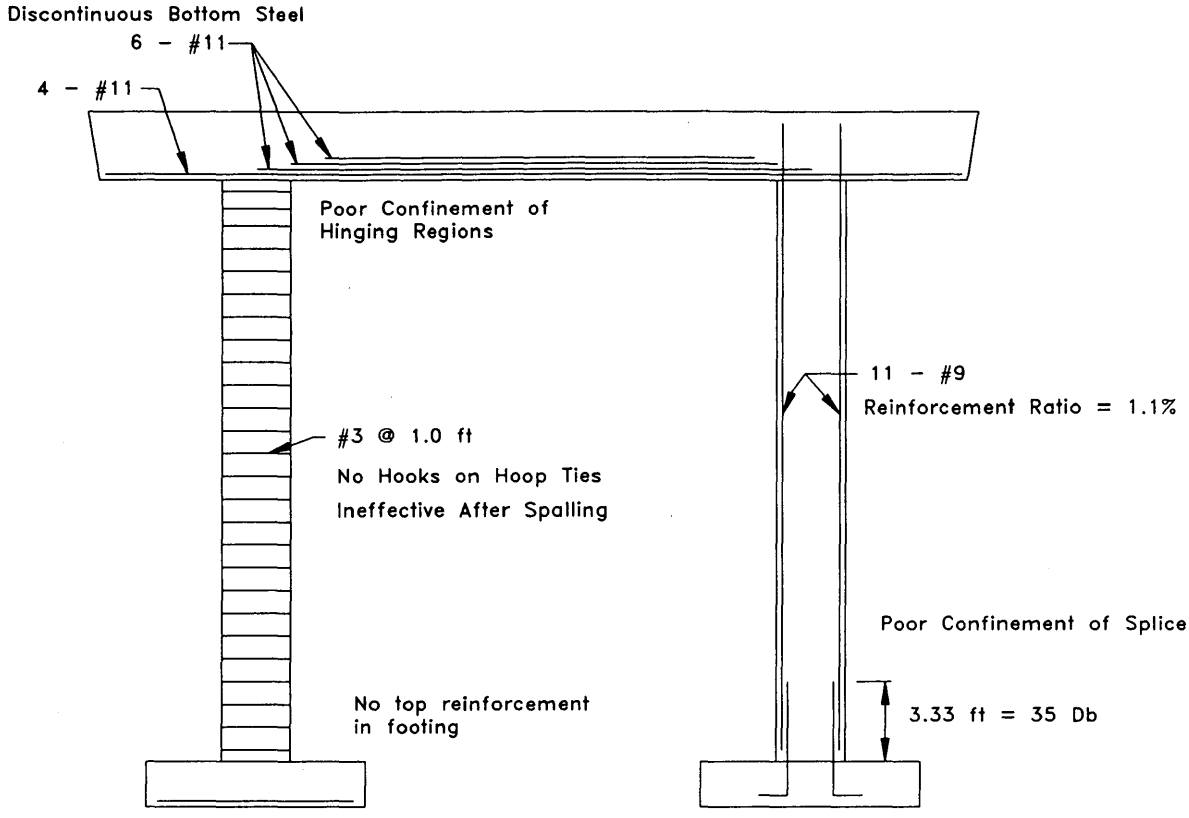

FIGURE 3 Potential deficiencies in bents.

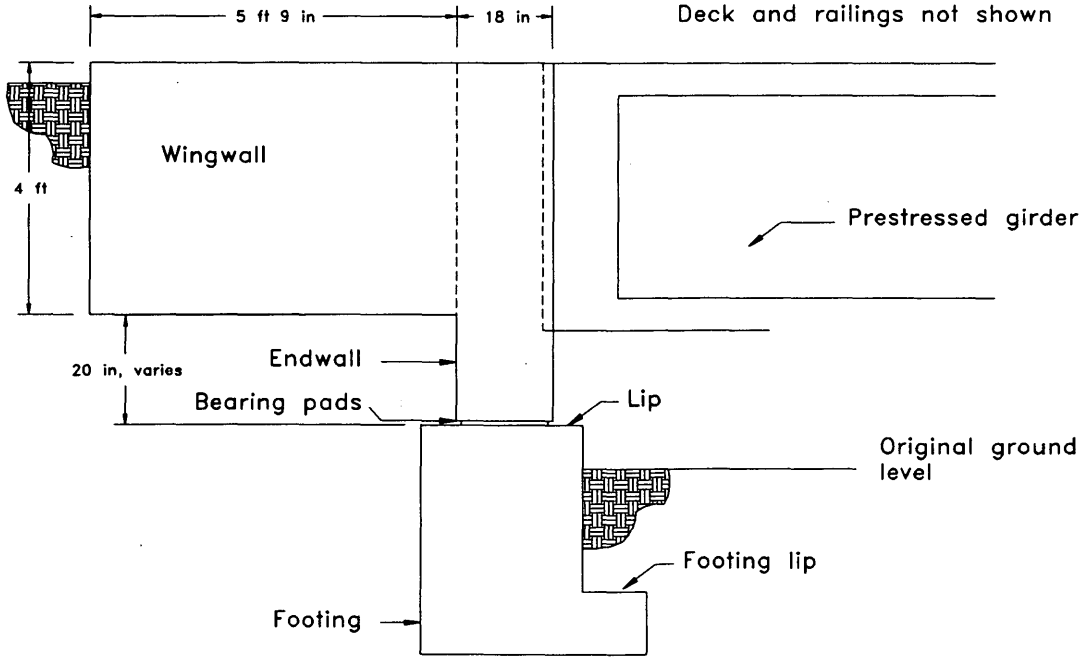

FIGURE 4 Elevation of abutment.

An inspection of the design calculations verified that, consistent with WSDOT practice for earthquake-resistant design at that time, the bridge was designed to resist transverse and longitudinal forces equal to 3 percent of the dead load of the bridge. In making this check, the stiffness of the abutments was neglected, and allowable stresses were permitted to exceed those permitted for gravity loading by 33 percent. A result of the relatively small design forces and the increase in allowable stresses was that earthquake loading did not affect the final design. The structural design was governed by gravity load considerations.

The test bridge included three spans of 41 ft, 60 ft, and 41 ft (Figure 1 and 2). Gravity loads from the 6.5-in. deck were carried to the piers and abutments by six prestressed girders measuring 3 ft 6 in. deep. At each pier, the deck was continuous and the ends of the girders were embedded into a heavily reinforced, cast-in-place diaphragm. Dowels connected this diaphragm to a supporting cast-in-place cross beam, which, in turn, was supported by 3-ft-diameter columns with a clear height of approximately 25 ft (Figure 3). Longitudinal reinforcement for columns consisted of 11 No. 9 bars, providing a reinforcement ratio of 1.1 percent. Transverse reinforcement consisted of No. 3 hoops at 12-in. spacings.

Columns were supported on spread footings that were embedded in approximately 10 ft of soil at the centerline of the column (Figure 2). At the base of each column, a 3 ft 4 in. splice connected longitudinal reinforcement to footing dowels. The footings had no top reinforcement. Though the transverse stiffness of the abutments was neglected in designing the bridge, its abutments were exceptionally stiff in the transverse direction. At each abutment, the prestressed girders were embedded 2 in. into a diaphragm/endwall which, in turn, was cast monolithically with the wingwalls (Figure 4). Loads that were applied to the bents would be resisted by passive earth pressures developed along the wingwalls and by friction developed behind the endwall. Additional resistance was provided by elastomeric bearing pads on which the diaphragm/endwall was supported. The elastomeric bearing pads rested on the pedestal of a spread footing.

TEST PROGRAM

The test program consisted of two phases, which are shown schematically in Figure 5. In Phase 1, large static loads were applied to the bridge in its unaltered condition. Resistance to

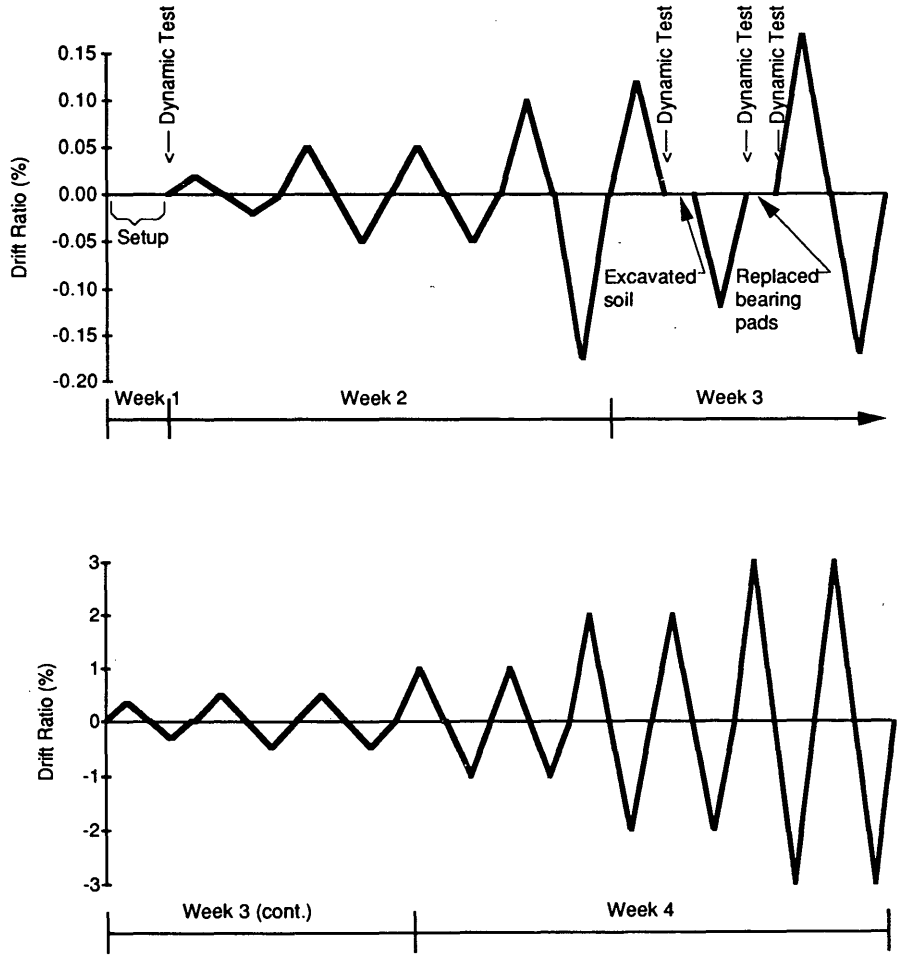

FIGURE 5 Imposed displacement history: *top*, Phase 1; *bottom*, Phase 2.

the loads was provided by both the intermediate piers and the abutments. The purpose of this phase was to measure the lateral stiffness and strength of the full bridge, thus providing data with which to calibrate analytical models.

After the stiffness and strength of the entire bridge had been measured, all soil behind the wingwalls and along the end diaphragms was removed. Transverse loads were then applied to the bridge to measure its stiffness without the contribution of the soil to resistance. The influence of the abutments was further reduced by lifting the bridge at the abutments and replacing the elastomeric bearing pads with a sandwich of hard nylon, grease, and polished stainless steel. Then another static test was performed to measure the stiffness of the bridge without the contribution of the bearing pads to resistance.

During Phase 1, the static tests were complemented by small-displacement dynamic tests in which the structure was excited with an eccentric-mass shaker. These small-displacement dynamic tests were performed (a) before the structure was damaged, (b) after slowly varying loads had damaged the bridge, (c) after the soil had been excavated, and (d) after replacement of the bearing pads. In addition, ambient vibration measurements and vertical impact transient vibration tests were performed intermittently. The dynamic tests provided further data with which to calibrate analytical models (*4*) and provided the opportunity to compare large-displacement static response with small-displacement dynamic response.

In Phase 2, the stiffness, strength, and toughness of the bents (i.e., intermediate piers) were measured. The structural properties of the intermediate piers are particularly important for bridges in which the abutments do not contribute significant lateral-force resistance. Such bridges would rely heavily on the piers for stiffness and energy dissipation during an earthquake.

After the test bridge had been isolated from the abutments, the bents were subjected to cycles of displacement of ± 1.5, 3, 6, and 9 in., corresponding to drift ratios of 0.5, 1, 2, and 3 percent. The tests were finally stopped when damage to the columns threatened to collapse the structure.

After testing had been completed, concrete cores and samples of longitudinal reinforcement were obtained from the structure to permit the measurement of material properties in the laboratory. Additional laboratory tests were performed to measure the friction properties of the bearing pads and of the isolation system. These tests indicated that the coefficient of friction of the sandwich of hard nylon, grease, and stainless steel was less than 8 percent.

LOADING SYSTEM

The short length of time, 30 days, during which traffic would be rerouted, was the critical constraint in designing and conducting these tests. The loading system (Figure 6) needed to be able to apply slowly varying, cyclic loads of up to 800 kips and yet be installed before traffic was diverted. Thus, although most of the mass of the bridge was located in the deck, lateral loads were applied directly to the piers because workers could obtain access to them without disrupting traffic above.

Loads were applied to the ends of pier cross beams by 64 prestressing cables (32 per side in groups of eight). A harness, composed of two C10 × 30-channel sections, welded back to back—a system of gusset plates and two heavy bearing plates—distributed the concentrated loads from the cables across the face of the cross beam. The rural location of the site allowed the cables to be extended at a 1:4 slope beyond the end of the I-90 right-of-way into an adjacent field. Reaction forces were provided by deadmen anchors, consisting of four steel beams, each encased in 9 to 12 yd^3 of concrete, buried 15 to 20 ft below ground level. At the location at which the cables emerged from the ground, jacking frames enabled eight 100-ton hydraulic jacks (four per side) to pull the cables attached to the bridge with respect to cables attached to the deadmen (Figure 7).

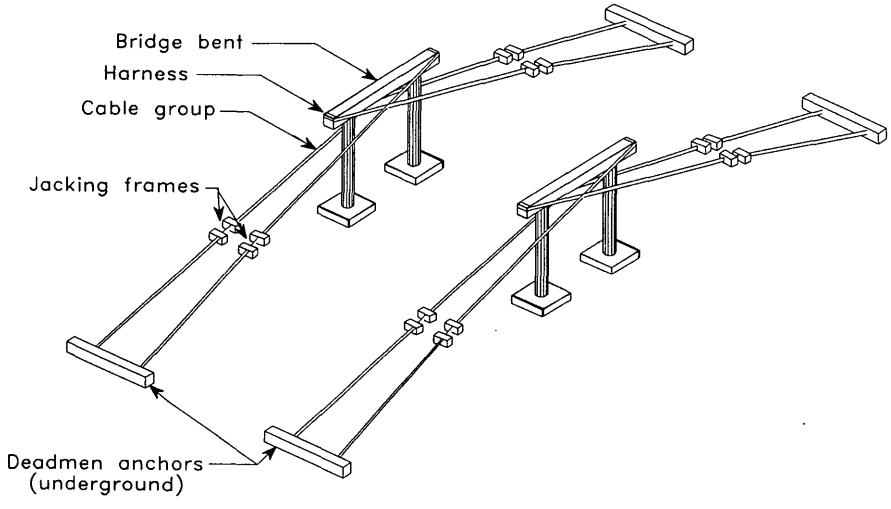

FIGURE 6 Loading system schematic. Deck is not shown for clarity.

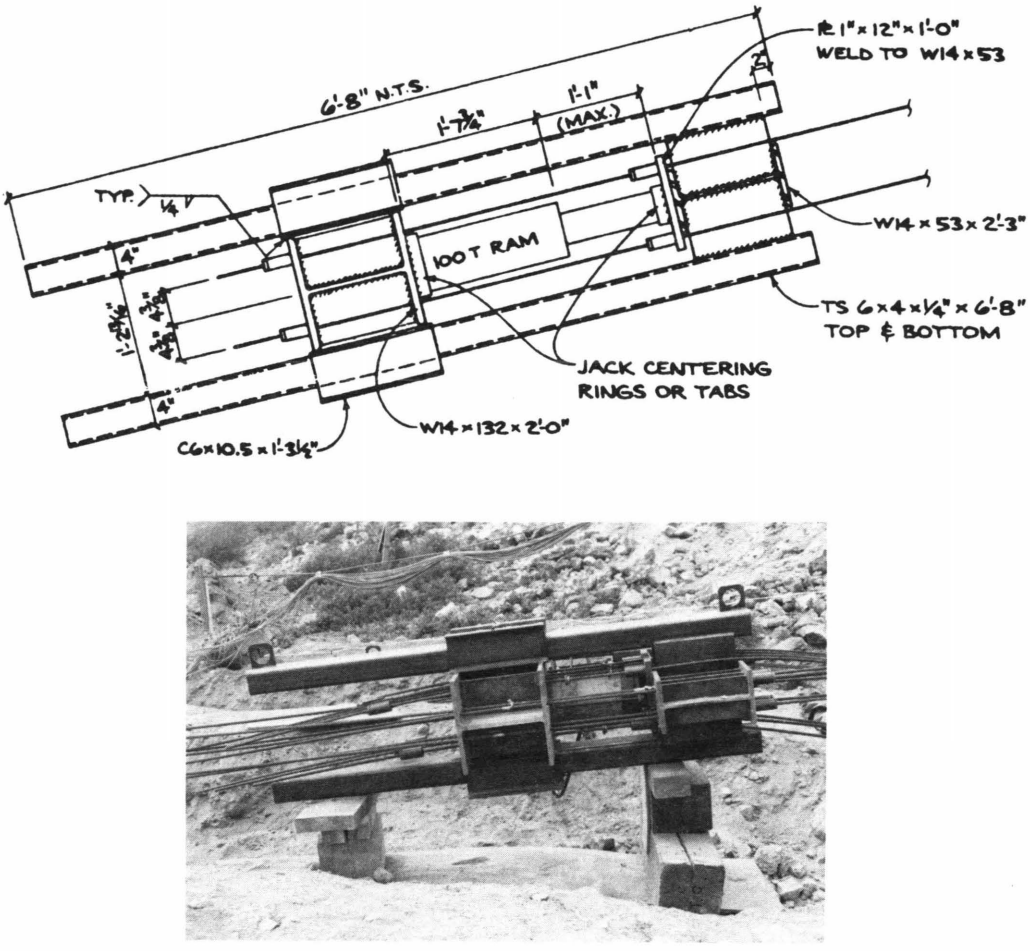

FIGURE 7 Jacking frame: *top*, elevation; *bottom*, photograph.

INSTRUMENTATION

During the static tests, absolute displacements of the bridge at the piers and the abutments were measured with respect to reference posts that were located in soil that was undisturbed by bridge movements (Figure 8). In this arrangement, displacement transducers measured vertical movements of weights that were suspended on 1/16-in. cables that ran over pulleys back to the bridge. The reliability of these measurements was verified using an electronic distance meter to monitor displacement of the structure and to verify that the reference posts did not move.

Relative rotations of cross sections of the columns and cross beams were recorded at 22 locations, including the tops of all four columns. A trench was excavated down to the footings to permit installation of similar instrumentation at the bottom of the columns of the west bent. To minimize disturbance of the soil resistance, the trench was oriented transverse to the direction of movement of the piers. In these locations, relative rotations of column cross sections and absolute rotations of the footings were measured. At the abutments, deformation of the bearing pads at each abutment was measured. Applied forces were determined from measurements of ram hydraulic pressure. The reliability of these measured loads was confirmed by measurements from a linear variable differential transducer (LVDT) placed to measure strand elongation.

The harsh environment posed complications. The temperature varied from 60°F on some mornings and evenings to above 100°F during some afternoons. Fortunately, the variation of temperature during one test rarely exceeded 10°F. The effect of these temperature variations during static tests on electronic components was minimized by forgoing the use of signal amplifiers or filters, both of which can be sensitive to temperature. For two cable systems that were exposed to the wind, protective plywood shelters were installed. Dust was also of great concern because the site was covered with ash from the 1980 eruption of Mount Saint Helens. Ongoing construction near the site and the windy conditions compounded this problem. To minimize the effect of dust on instrumentation, all instruments were carefully protected from the elements. The eight instruments that depended on pulley systems were placed in sealed wooden shelters along with their pulleys.

An IBM AT computer was used to record the nearly 70 channels of data measured during the static tests. All of the nearly 4 mi of instrument cabling was shielded and grounded to minimize disruptive effects of stray electrical fields. During dynamic tests, an accelerometer and several velocity trans-

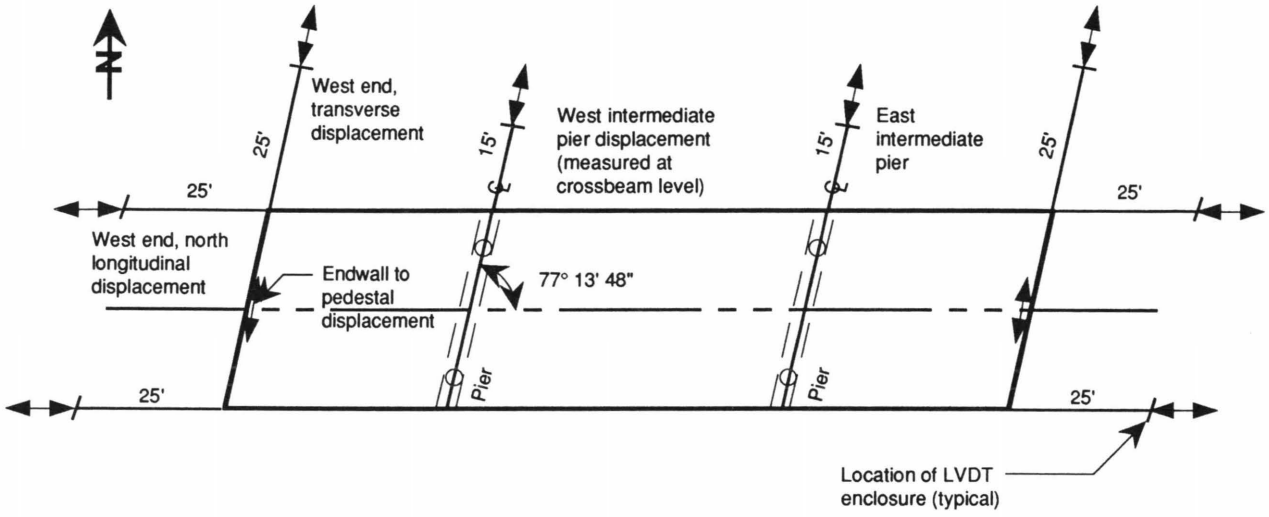

FIGURE 8 Plan of deck instrumentation.

ducers measured the vertical and transverse response of the deck, abutments, and column footings. Signals were recorded on a Compaq 386/20 personal computer.

OBSERVED BEHAVIOR

The tests were completed in mid-July of 1991. Descriptions of observed behavior are preliminary and may be revised after the data have been studied further. Data from the dynamic tests have not yet been converted to a presentable form.

The bridge was stronger and stiffer in Phase 1 than had been predicted by analysis before testing began. As indicated in Figure 9, the maximum lateral load resisted by the bridge was approximately 800 kips, corresponding to two-thirds its weight. The maximum load was measured at a displacement of approximately 0.4 in., corresponding to a drift ratio of 0.13 percent. Despite being subjected to large forces, damage during the first series of tests was limited mainly to cracks in the wingwalls, which resulted from large passive pressures (Figure 10). These cracks abruptly opened to approximately 0.10 in. wide at an applied load of approximately 800 kips. The abutments were exceptionally stiff because the wingwalls were cast monolithically with the end diaphragm. In comparison, piers were relatively flexible and sustained only minimal damage during the first phase of testing. During Phase 1, the columns sustained only minor cracking, with all cracks less than 0.01 in. wide.

The load-deflection response of the bridge during Phase 2 is shown in Figure 11. In this phase, the contribution of the abutments to lateral-force resistance was small. The drift ratio shown in the figure corresponds to the average displacement of the intermediate piers normalized by the clear height of the columns. Since, in all but the simplest structures, there exists no unique yield point, the displacement ductility factor shown in the figure is approximate. It resulted from an inspection of the force-deformation curve for the structure. Despite the small contribution of the abutments to resistance, the piers resisted transverse forces equal to approximately 40 percent of the weight of the structure. The structure continued to dissipate energy, with little pinching of the load-displace-

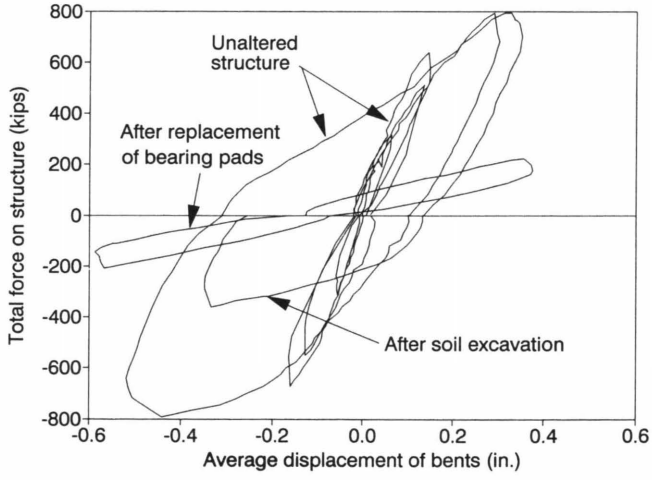

FIGURE 9 Hysteretic response during Phase 1.

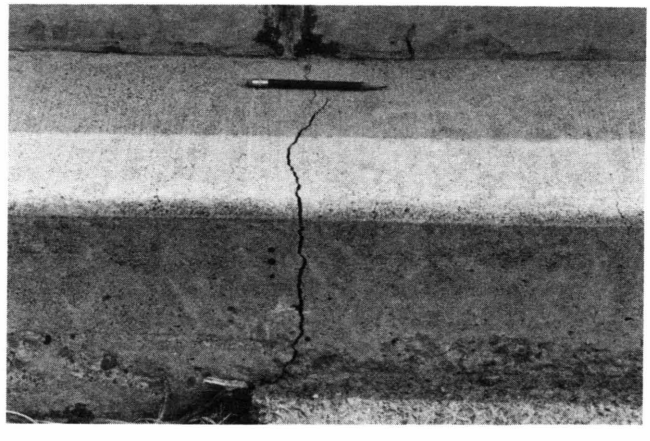

FIGURE 10 Damage to southeast wingwall at end of Phase 1.

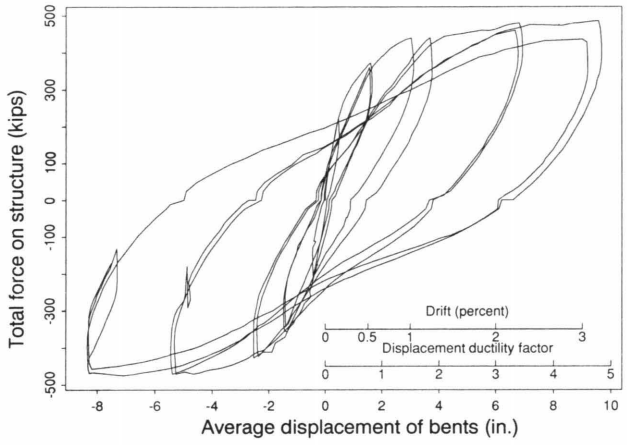

FIGURE 11 Hysteretic response during Phase 2.

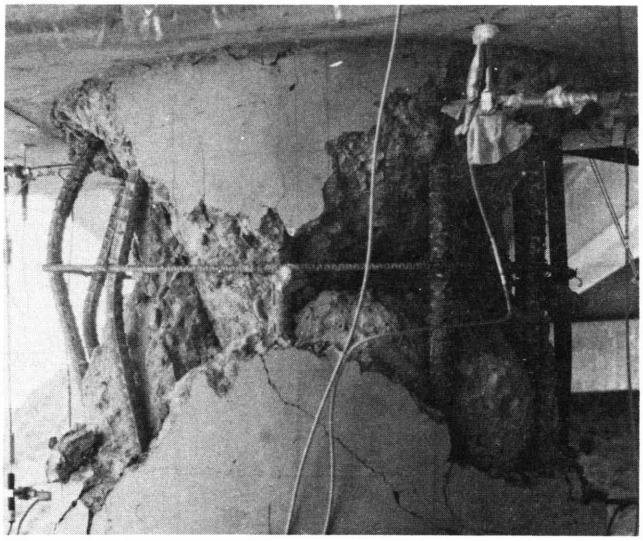

FIGURE 12 Damage to top of southeast column at end of Phase 2: Cycle B352; load, 3,600 psi; displacement, 9 in. (absolute); July 13, 1991.

ment curves, up to displacements of 9 in., corresponding to a drift ratio of 3 percent.

During Phase 2, most of the damage was concentrated at the tops of the columns. The cross beams remained nearly undamaged, except for hairline cracking. At the bottom of the columns damage was limited to cracking; no spalling was observed. Most of the cracking at the bottom of the columns occurred above the splice regions, suggesting that the soil surrounding the column may have greatly affected its stiffness and reduced the effective column height. The footings showed no signs of distress.

Column damage increased with imposed drift. At a drift ratio of 0.5 percent, damage consisted of 0.02- to 0.05-in. flexural cracks at the top of the columns. At a drift ratio of 1 percent, maximum crack sizes at the tops of the columns increased to 0.10 in. and minor flaking of the concrete in compression was observed. Spalling and the onset of bar buckling was clearly visible at a drift ratio of 2 percent. After the structure was pulled to two cycles at a drift ratio of 3 percent, spalling was widespread and many of the longitudinal bars had buckled (Figure 12). Whereas the cracks had been primarily flexural for smaller displacements, the cracks at larger displacements had a more noticeable shear component. At this point, the tests were stopped out of concern for safety.

CONCLUSIONS

Full-scale testing of a bridge was shown to be a feasible means of obtaining data on the large-displacement behavior of a bridge and of a pair of piers. Full-scale testing is attractive because it avoids scaling limitations and permits study of the effect of soil on structural response. However, the results of these tests must be interpreted in light of the fact that full-scale tests do not duplicate the effects of earthquakes. Earthquake motions include dynamic longitudinal, vertical, and torsional components that were not duplicated in the tests. The rates of loading during the destructive tests were much smaller than those that would occur during an earthquake.

Despite the limitations of these tests, several preliminary observations were made. In itself, the observation that the bridge resisted a force equal to two-thirds its weight at a drift ratio of less than 0.15 percent is not trivial. The tests demonstrated the importance of the contribution of the soil to the stiffness and strength of a bridge. In this bridge, the abutments were stiff enough that damage would be expected to be minimal during earthquakes of the magnitude that are commonly considered in design. The soil also affected the damage at the base of the columns. Unfortunately, from the point of view of the designer, estimates of soil stiffness are accompanied by great uncertainty.

Although the piers were heavily damaged, they were able to continue to carry gravity loads while resisting transverse loads of 40 percent of the weight of the structure at a drift ratio of 3 percent. Despite their deficiencies, the columns had sufficient flexural ductility to prevent collapse in these tests. This ductility may be critical in ensuring the survivability of many other bridges. Many other bridges do not have abutments that are as strong or as stiff as the test bridge or the number of spans is large enough that the abutments have little effect on intermediate pier response.

In the remaining year of the study, the measured static and dynamic response will be used to calibrate analytical models and to better understand the sources of stiffness and strength. The large amount of data that describe local behavior will be reduced and compared with laboratory results from previous investigators (*5*,*6*). The role of the soil will be studied further (*7*), as will the relationship between the measured static and dynamic response.

ACKNOWLEDGMENTS

This unusual project required the cooperation and efforts of many persons and organizations. S. Clark, R. Mah, and C. Wang, undergraduates at the University of Washington, helped prepare for and conduct the static tests. The dynamic tests were performed by B. Hushmand and R. Relles from the

California Institute of Technology, in consultation with C. B. Crouse from Dames and Moore, Consulting Engineers.

The project was funded primarily by WSDOT and FHWA. The support of A. Walley, of the Office of Bridges and Structures, and E. Henley, of WSDOT, is appreciated. Additional support was provided by the National Science Foundation through the Research Experience for Undergraduates Program. T. O'Donovan was supported by the U.S. Army Corps of Engineers and G. Hjartarson was supported by the Valle Foundation at the University of Washington. The loading system was fabricated by Concrete Technology Corporation under the direction of S. Moustafa.

REFERENCES

1. O. George and E. H. Henley, Jr. *Bridge Seismic Retrofit Program Recommendations*. Bridge and Structures Office Report. Washington State Department of Transportation, Olympia, 1991.
2. J. E. Roberts. Recent Advances in Seismic Design and Retrofit of Bridges. In *Transportation Research Record 1290*, TRB, National Research Council, Washington, D.C., 1991, pp. 75–79.
3. L. L. Noson, A. Qamar, and G. W. Thorsen. *Washington State Earthquake Hazards*. Washington Division of Geology and Earth Resources Information Circular 85. Washington State Department of Natural Resources, Olympia, 1988.
4. C. B. Crouse, B. Hushmand, and G. R. Martin. Dynamic Soil-Structure Interaction of a Single-Span Bridge. *Earthquake Engineering and Structural Dynamics*, Vol. 15, pp. 711–729, 1987.
5. Y. H. Chai, M. J. N. Priestley, and Fr. Seible. Seismic Retrofit of Bridge Columns by Steel Jacketing. In *Transportation Research Record 1290*, TRB, National Research Council, Washington, D.C., 1991, pp. 95–103.
6. H. Coffman. Seismic Retrofit of R.C. Columns. M.S.C.E. thesis, University of Washington, Seattle, 1990.
7. I. P. Lam, G. R. Martin, and R. Imbsen. Modeling Bridge Foundations for Seismic Design and Retrofitting. In *Transportation Research Record 1290*, TRB, National Research Council, Washington, D.C., 1991, pp. 113–126.

Publication of this paper sponsored by Committee on Concrete Bridges.

Lessons Learned from Diagnostic Load Testing of 100-Year-Old Elevated Mass Transit Structures

R. W. KRITZLER, S. G. PINJARKAR, R. A. ROLSING, AND P. O. MCCARTHY

A comprehensive study has been undertaken by the Chicago Transit Authority and its consultants for condition assessment of the rapid-transit system's elevated steel structures. This study included a series of full-scale diagnostic load tests performed to evaluate actual behavior of these structures under train loading. Static and dynamic load tests, using an empty four-car test train, were performed on four different line segments, representing different structural systems. Dynamic monitoring of tensile bending stresses was also conducted for normal rush-hour traffic, providing actual variable stress and average response data to be used for fatigue life assessment. Strain gauge response data for the test structures showed that stringer midspan bending stresses were 36 to 93 percent of nominal calculated stresses, assuming simply supported spans. The measured negative moments at the supports, caused by partial end continuity, were 25 to 86 percent of the fully continuous end moments for three of the test structures. The continuity at the stringer supports is provided by typical riveted full-depth web-shear framing angles. Dynamic test results showed the average measured impact loading for each stringer span to vary from 7 to 34 percent of the respective maximum static test response stresses, compared with American Railway Engineering Association-required design effects of 53 to 59 percent. The measured impact varied inversely with the span length. Train braking test results indicated that longitudinal braking forces are nonuniformly distributed along a length of the track structure exceeding the train length, and the rails are effective in distributing those braking forces across longitudinal structural expansion joints.

Previous load tests of older and apparently deteriorated railroad and highway structures (*1*) indicate that these structures can carry substantially higher loads than are computed by analytical design methods. The factors that contribute to this increase in strength include unintended continuity, unintended composite action, better lateral load distribution, much smaller impact than is required by design codes, and smaller magnitude of live load stresses used in fatigue rating calculations. Results of a pilot load testing program of a Chicago Transit Authority (CTA) mass transit structure (*2*) indicated that diagnostic load tests can be successfully conducted for rating and evaluation of older mass transit structures.

The Chicago Rapid Transit System includes approximately 40 mi of elevated steel structures and bridges. As part of a comprehensive Engineering Condition Assessment of the entire system, a series of full-scale diagnostic load tests were performed to evaluate actual behavior of these structures under train loading. Load tests were performed on four different line segments of the elevated system built from 1891 through 1905.

The test locations were selected to represent variations in structural system and details between each line segment. A test program was specifically designed for each location to evaluate end connection continuity, load distribution, critical stresses, impact loading, fatigue, and longitudinal forces caused by train braking. Both static and dynamic load tests were performed to determine the response characteristics of the track structures. The dynamic tests included both empty four-car test trains and actual rush-hour commuter trains. The results of this diagnostic load testing are currently being used to supplement the engineering analyses and rating calculations for these structures.

R. W. Kritzler, Raths, Raths & Johnson, Inc., 835 Midway Drive, Willowbrook, Ill. 60521. S. G. Pinjarkar, Desman Associates, 300 West Washington, Suite 1010, Chicago, Ill. 60606. R. A. Rolsing, McDonough Associates, Inc., 224 South Michigan, Chicago, Ill. 60604. P. O. McCarthy, H. W. Lochner, Inc., 20 North Wacker Drive, Suite 1200, Chicago, Ill. 60606.

DESCRIPTION OF STRUCTURES

The elevated structures at the four test locations are generally constructed of steel or wrought-iron longitudinal stringers spanning 40 to 60 ft to transverse support bents. Two stringers support each open-deck standard-gauge track on timber ties. The ties also support the electric "third" rail to power the train cars. The support bents carry two active tracks and sometimes a third inactive track (Figures 1 through 4). The two stringers supporting each track are laterally braced between their top flanges and contain either vertical cross bracing at span third points (Figure 3) or lateral bracing between the bottom flanges. The stringer pairs supporting each track are generally connected with a top and bottom flange horizontal strut at the span third points (Figure 3).

Each of the four line segments was constructed under a separate contract between 1891 and 1905. Although the various line segments are of a similar type of structural system, there were significant variations in design and construction details among the segments.

The South Mainline structure was built in two phases. The present southbound structure was built in 1891 using wrought iron. The present northbound structure was added in 1905 and constructed of steel (Figure 1). The stringers are riveted built-up plate-and-angle I-sections connected to the support bents with full-depth web angles (Figure 5). A stringer expansion seat bearing connection ("pocket") is typically lo-

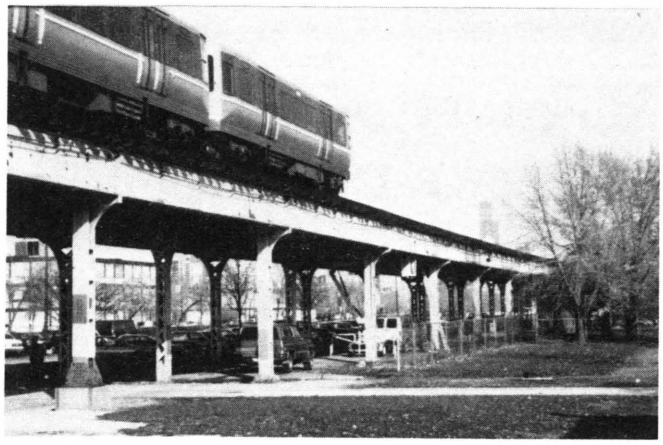

FIGURE 1 South Mainline elevated structure.

FIGURE 3 View from below Englewood test structure.

FIGURE 2 South Loop elevated structure.

FIGURE 4 Jackson Park elevated structure.

cated on one side of every third bent. The support bent columns are located below the centerline of each track (similar to Figure 3). Longitudinal forces on the elevated structure are resisted by bending of the columns.

The Englewood Line structure was built in 1905 using "railway bridge steel." The construction is very similar to that of the northbound South Mainline structure, except for the addition of longitudinal vertical x-bracing at every fourth bay (Figures 3, 5, and 6). The x-bracing, or "traction bracing," resists longitudinal forces applied to the elevated structure. A stringer expansion seat-bearing connection typically is located on one side of every fourth support bent.

The South Loop Line structure in the test area was built in 1891 using wrought iron (Figure 2). The stringers and end connections are similar to those of the South Mainline structure. The support bent columns are located outboard of the two supported tracks, forming a rigid frame for supporting the track stringer gravity loads. The transverse ("cross") girders are single-web riveted built-up I-sections. Longitudinal forces applied to the track by train braking and accelerating are resisted by cross-girder horizontal bending and longitudinal column bending.

The Jackson Park Line was constructed in 1892 using "soft steel" (Figure 4). The stringers were replaced in 1940, and the stringer end connections were modified in 1964. The stringers are riveted open-web trusses with chords and web members composed of wide-flange tee sections. The stringers are connected to the support bents with a combination of a top chord bearing connection and full-depth web angles (Figure 5). There are no stringer-end longitudinal expansion joints in the structure. The support bent columns are located outboard of the tracks and support the cross girders that span across 63rd Street from curb to curb. The support bent cross girders are double trusses tied with top horizontal batten plates and vertical diaphragms. Again, longitudinal forces applied to the track by train braking and accelerating are resisted by cross-girder horizontal bending and longitudinal column bending.

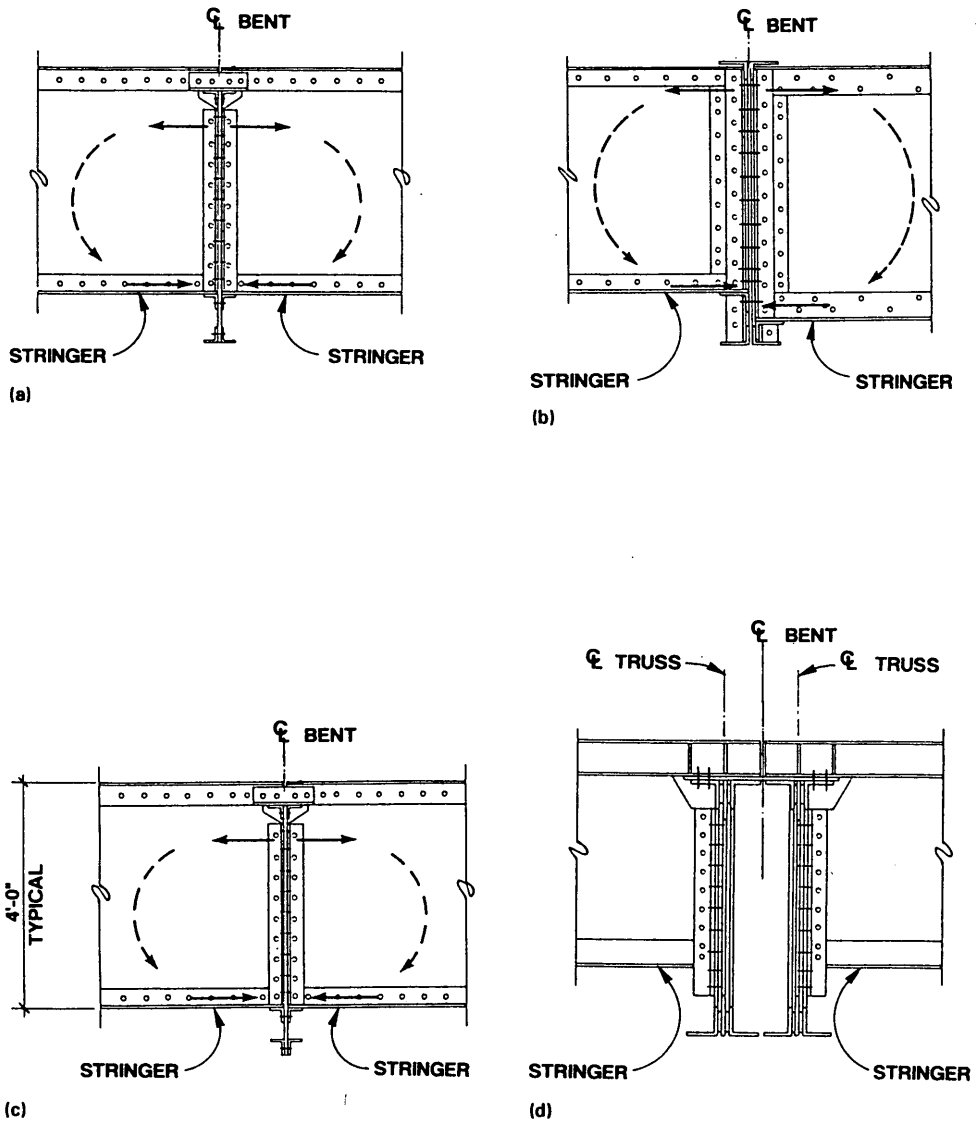

FIGURE 5 Typical details at fixed connections between stringers and support bent: *a*, South Mainline; *b*, South Loop Line; *c*, Englewood Line; *d*, Jackson Park Line.

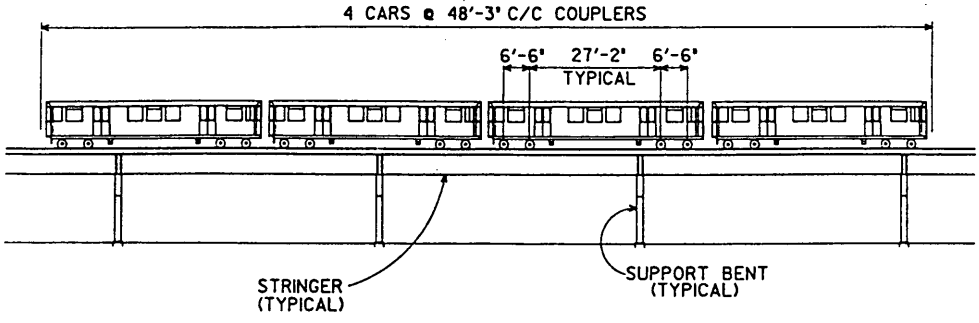

FIGURE 6 Elevation of four-car test train.

DESCRIPTION OF TESTING PROGRAM

Test Type and Loading

For each line segment test structure, the following types of load tests were performed: (a) static tests, (b) dynamic tests at controlled speeds, (c) train braking tests, and (d) rush-hour tests.

Test Trains

An empty four-car test train was furnished by CTA for each test location (Figure 7). Controlled static and dynamic tests were conducted using the test train on four Sundays during low passenger travel periods. A single-track outage, for ¼ to ½ mi in each direction from the test location, was provided by CTA for test train movement during the testing.

Empty train car weights are approximately 54,000 lb each, or approximately 14 kips per axle for the Series 2601-3200 cars used on the test structures. Passenger loading used by CTA for fatigue rating is 5.5 kips per axle for a total of 19.5 kips per axle.

Static load tests were conducted by stopping the test train at specific locations along the test spans to measure the response at each location. Dynamic tests were performed by moving the test train across the test spans at a crawl speed

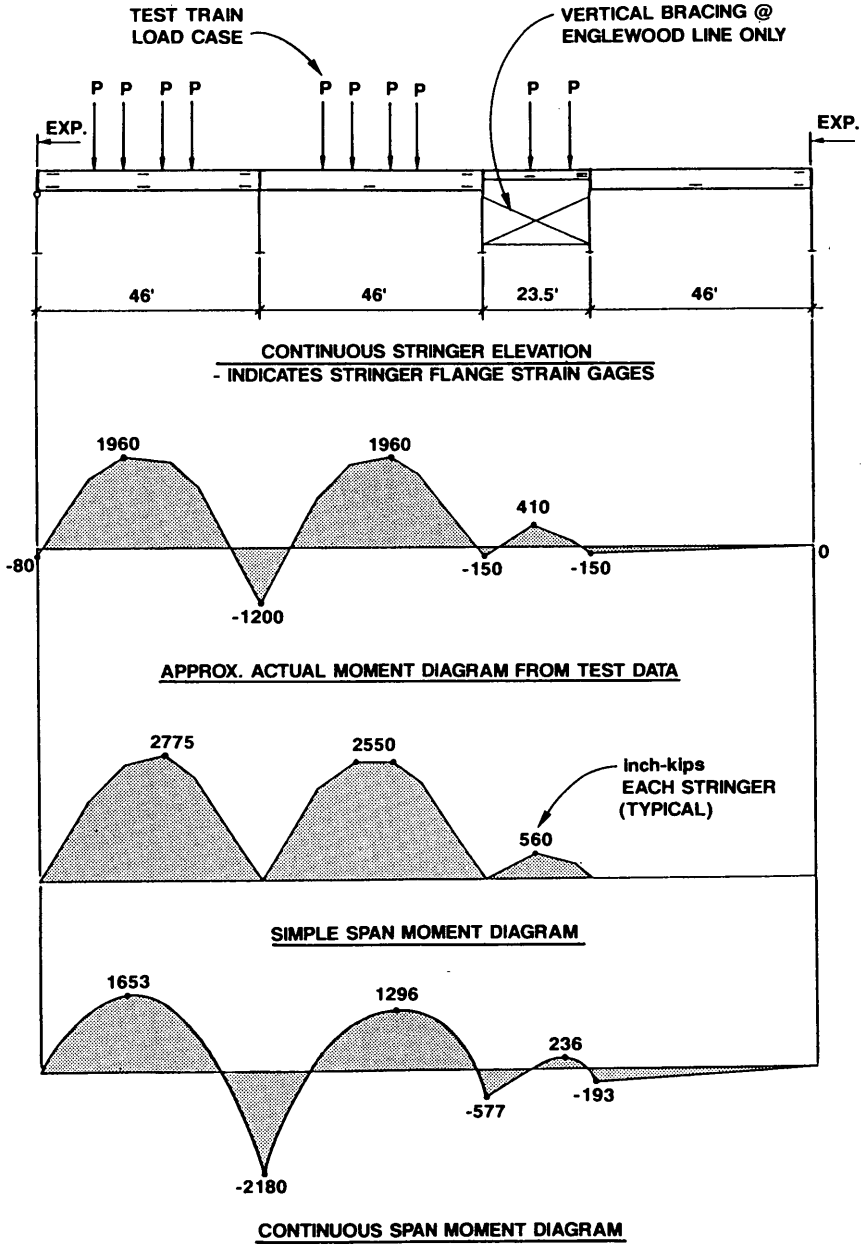

FIGURE 7 Example of comparison of measured and calculated stringer bending moments.

and at various operating speeds up to a maximum speed of 55 mph to measure the effects of impact loading. Dynamic train braking tests were performed to determine the magnitude of longitudinal force caused by the application of emergency brakes (includes track brake). At each test location, braking tests were carried out by stopping the train directly over the test bent and also by stopping the train at various distances from the test bent along the track in each direction.

Rush-Hour Trains

Rush-hour dynamic load tests were conducted to monitor strains and to evaluate the effect of passenger loading. The measured strain responses included the combined dynamic effects of the eight-car trains moving at normal speeds with passenger loading. Strains in the stringer bottom flanges at midspan were measured for both the inbound and outbound tracks. Since the passengers predominantly travel in one direction during each rush hour, both tracks were monitored to record responses to both the loaded car trains and near-empty car trains.

Instrumentation

A total of 32 to 42 weldable electric-resistance strain gauges were installed on each test structure.

The gauges were located at the top and bottom flanges of the stringers at midspan and near each end to measure positive and negative bending and axial stresses. The gauges near the stringer ends were positioned to avoid discontinuities adjacent to the end connections and also shear lag in transferring flexural stress to the stringer flange angles from any longitudinal continuity through the end connection components. Strain gauges were installed on the bottom flanges at midspan of some stringers to monitor positive bending tensile stresses only at these locations.

The support bent cross girders were instrumented with four strain gauges at the point of maximum positive moment to measure vertical and horizontal bending stresses. Strain gauges were installed on support bent columns to measure transverse and longitudinal bending along with axial stresses. The longitudinal vertical x-bracing of the Englewood Line structure was instrumented with strain gauges to measure longitudinal forces caused by the train braking.

The data acquisition system, used to record and process the test data, was composed of a digital scanner, strain gauge completion boards, DC power supply, amplifier, and a portable computer. A digital sampling rate of 500 samples per second per channel was typically used for most of the dynamic tests. A sampling rate of 100 samples per second per channel was used for the dynamic train braking tests and for all of the dynamic tests conducted on the South Loop Line. Severe radio interference, probably caused by the nearby Chicago Central Police headquarters, precluded the use of the more sensitive equipment capable of higher data sampling rates at the South Loop location.

The data obtained from each test were reviewed in the field for accuracy and correctness, using computer analysis and screen plots, before proceeding with the next test.

ANALYSIS OF TEST RESULTS

Stringer End Continuity

The results of the static tests are compared to calculated stringer midspan bending stresses, assuming each stringer span is simply supported (Table 1). The comparison, by test structure and span, indicates that midspan bending stresses were 36 to 93 percent of the calculated stresses, assuming simply sup-

TABLE 1 Static Tests (Using Empty Four-Car Test Train): Stringer Bottom Flange Stress at Center of Span

			STATIC LIVE LOAD STRESS (KSI)		
LOCATION	SPAN (FT.)	END SUPPORT CONDITION [a]	Maximum Measured	Calculated Simple Span [b]	MEAS. CALC. RATIO
Jackson Park	50	Fix-Fix	4.2	4.5	0.93
Englewood	46	Exp-Fix	2.5	3.6	0.70
	46	Fix-Fix	2.5	3.6	0.70
	23.5	Fix-Fix	2.1	3.4	0.62
	46	Fix-Exp	3.0	3.6	0.83
South Loop	40	Exp-Fix	2.3	4.0	0.57
	39.8	Fix-Fix	1.4	4.0	0.36
	60	Fix-Exp	3.1	4.1	0.77
South Mainline	46	Exp-Fix	2.9	3.5	0.85
	46	Fix-Fix	2.8	3.6	0.80
	46.8	Fix-Exp	3.1	3.6	0.85

[a] Fix = Full-Depth Shear Angle Connection
Exp = Expansion Seat Connection
[b] Bending Stress Assuming Span Simply-Supported

ported spans. Additional data analysis will show that, except for the Jackson Park structure, the reduced midspan stresses were the result of partial continuity at the stringer-end support connections.

The stringer-end support connections consist of full-depth web connection angles (Figure 5) except at the expansion seat bearing connections, typically located at every third or fourth bent support. The partial continuity, provided by the full-depth web connections on both sides of a support bent, transfers stringer negative bending moment across the support bent and into the adjacent stringer span. This continuity, or stringer end rotation restraint, causes tension through the connection angle top rivets and compression or thrusting through the bottom portion of the connection angles or bottom flange ends. The rotational stiffness of these particular connections is enhanced by the near full-depth length of the connection angles, the short outstanding legs and rivet gauges of the connection angles, and the opposing stringer end rotations caused by the train axle loads acting simultaneously on both spans.

The degree of stringer end continuity is determined for these test structures by comparing measured static load end moments with calculated end moments, assuming the stringers are continuous over, and fixed to, the columns or cross girder. Bending moment diagrams for one Englewood test structure static load case are shown in Figure 7. This figure shows the approximate measured bending moments calculated from the test data. The measured axial stresses, sometimes caused by higher compressive forces across the bottom of the end connections than the top tensile forces, or by frozen expansion seat connections, are separated from the measured bending stresses. The bending moments calculated at the strain gauge locations from the bending stresses are extrapolated to the support bent centerlines using calculated simple span or continuous span shears.

Comparisons between measured end moments and calculated continuous span end moments are summarized in Table 2. The continuity, expressed as a percent ratio of measured moment to calculated continuous span moment, varied from 25 to 86 percent. The percent degree of continuity compared very well to the measured reduction in midspan stresses shown in Table 1.

The maximum continuity (72 to 86 percent) was found in the South Loop Line, which has the longest vertical end connection angles relative to the depth of the stringer (Figure 5). The Englewood and South Mainline structures indicated less continuity (25 to 84 percent) because of the web coped below the top flange angles (Figure 5). The top flange tie angles are deteriorated and too small to increase the degree of stringer continuity at these structures. The static tests on the Jackson Park structure indicated very little or no measured end continuity. The double truss cross-bent support at this structure (Figure 5) allowed nearly free end rotations of the stringers through twisting of each cross truss between vertical diaphragm spacers.

Cross Bent Twist

The results of the static tests for the cross-girder bottom flange stresses were compared with calculated stresses using rigid frame analysis. The measured vertical bending stress for the Jackson Park structure compared very well with the calculated stress. Lower calculated vertical bending stresses than measured stresses for the South Loop structure indicated a lack of full fixity at the cross girder to column connections.

Horizontal bending stresses in the cross-girder bottom flanges were measured for both the Jackson Park and South Loop structures. This increased the total measured stress in the girder flange outstanding legs by 60 and 47 percent, respectively, over the measured vertical stresses. The horizontal flange bending is a twisting behavior of the cross girders caused by end rotation of the stringers. The twisting of the South Loop cross girder appears to be caused by the rotation of the near fully continuous stringers at a support between unequal adjacent spans (39.8 ft and 60 ft).

Impact (Dynamic Amplification)

Dynamic tests, using the empty four-car test train, were conducted to measure the effects of trains moving along the elevated structures at various speeds. The results of the stringer dynamic tests are summarized in Table 3. The dynamic amplification of stress caused by moving live loads, or "impact,"

TABLE 2 Static Tests (Using Empty Four-Car Test Train): Stringer Bending Moment Continuity at Supports

LOCATION	ADJACENT SPANS (FT.)	MEAS. MOMENT [a] / CALC. CONTINUOUS [b] RATIO
Jackson Park	50 - 50	0
Englewood	46 - 46	0.45 - 0.62
	46 - 23.5	0.26 - 0.84
	23.5 - 46	0.35 - 0.46
South Loop	40 - 39.8	0.86
	39.8 - 60	0.72 - 0.81
South Mainline	46 - 46	0.25 - 0.34

[a] Average measured moment in both stringers with each adjacent span loaded.
[b] Calculated continuous span moments are the theoretical calculated moments assuming the stringer is continuous over, and fixed to, the columns or cross-girder, as determined by computer frame analysis.

TABLE 3 Dynamic Tests (Using Empty Four-Car Test Train): Stringer Bending Vertical Impact

LOCATION	SPAN (FT.)	SPEED (MPH)	PERCENT IMPACT [a] Average [b] Measured	Maximum [b] Measured	AREA Design
Jackson Park	50	23 - 33	14	18	55
		46 - 55	19	23	55
Englewood	46	31	26	34	56
		41 - 48	27	39	56
	23.5	31	33	34	59
		41-48	34	46	59
South Loop	60	24 - 33	7	15	53
		44	11	16	53
South Mainline	46	31 - 38	22	30	56
		44 - 51	27	40	56

[a] Impact = Percent increase in peak stringer bending stress, at mid-span, from the moving test train loading across a given stringer, compared to the peak measured static load stress for that stringer.
[b] One impact event = maximum recorded impact under one passage of entire test train.

is herein defined as the percent increase in peak measured stress from the moving test train loading compared with the peak *measured* stress at the same location from the static test train loading.

The passage of a moving train across a stringer span produces a stress-time history record of a variable amplitude complex stress cycle. An example of a measured dynamic stress record is shown in Figure 8. The stringer midspan bottom flange stress cycle indicates the passage of an eight-car rush-hour train (Figure 8). Each group of car axles crossing the span produces a variation (subcycle) in stress as shown by the nine peaks. The dynamic effects of the moving train load are shown by the higher-frequency oscillations in the stresses, or vibrations, with frequencies typically in the range of 70 to 100 Hz for these elevated structures.

The measured impact loading for these structures is compared with the AREA manual (*3*) design impact values in Table 3. The average measured impact loading for the stringers varied from 7 to 34 percent. Although the magnitude of impact varied between test locations, the average measured impact values varied inversely with the stringer span length

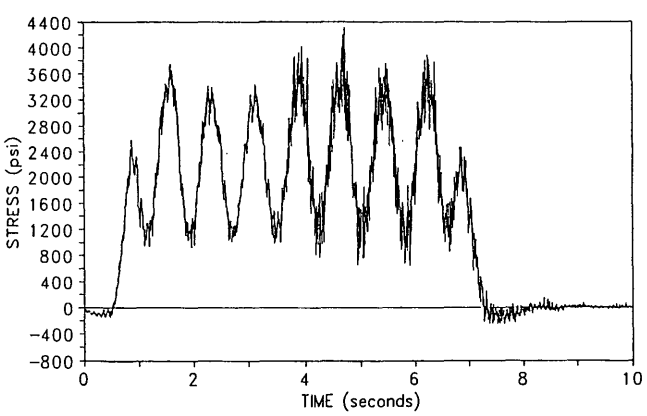

FIGURE 8 South mainline stringer dynamic response at midspan of bottom flange for eight-car rush-hour train (speed, 44 mph).

(Table 3). There was some general increase in the measured impact values at higher train speeds. However, in some cases, the effect of increased train speed was negligible. The maximum measured impact of 46 percent was recorded for a short 23.5-ft span.

Fatigue Assessment Data

The results of the rush-hour dynamic tests conducted on the stringers of each of the four test structures are summarized in Table 4, presenting the average and maximum measured stresses in the stringer bottom flanges at midspan for rush-hour trains traveling in each direction. These measured stresses include the combined effects of the eight-car trains moving at normal speeds with typical passenger loading.

A comparison of the measured stringer stresses for the eight-car rush-hour trains with the dynamic stresses for the empty four-car test trains indicates approximately the same stresses occurring in the Jackson Park and Englewood test structures. The rush-hour trains were almost empty of passengers when they passed these test locations.

A comparison of the average measured peak stress for the South Loop and South Mainline rush-hour tests with the dynamic empty train tests indicates a 14 and 11 percent average stress increase primarily caused by the weight of passengers. The maximum recorded increase in stress over the average empty train tests was 25 and 26 percent, respectively.

The rush-hour average response data (Table 4) and the actual variable stress cycle plots (Figure 8) can be used for fatigue life assessment of the stringer bottom flanges at midspan. These data verify that the train loads of 19.5 kips per axle (plus impact), used by the CTA for fatigue evaluation, are conservative for these test structures. The average weight of passengers during the rush-hour tests was approximately 1.5 to 2 kips per axle at the South Loop and South Mainline test locations and was negligible at the Jackson Park and Englewood test locations.

The dynamic test results indicate that the partially continuous stringer end connections undergo variable stresses with

TABLE 4 Rush-Hour Dynamic Monitoring (Using Eight-Car Trains with Passengers): Stringer Bottom Flange Stress at Center of Span

			LIVE LOAD PEAK STRESS (KSI)		
			Prevailing Commuter Travel Direction		Opposite Direction
LOCATION	SPAN (FT.)	SPEED (MPH)	Ave. Meas. [a]	Max. Meas. [a]	Ave. Meas. [a]
Jackson Park	50	20 - 48	4.7	5.4	4.1
Englewood	46	38 - 44	2.9	3.5	2.7
	23.5	38 - 44	2.9	3.6	2.6
South Loop	40	15*	2.8	2.9	-
	39.8	13 - 15*	-	-	1.6
	60	13 - 15*	3.5	3.9	2.8
South Mainline	46	42 - 44	4.0	4.5	3.7

* Train speed restriction at time of test monitoring.
[a] One peak stress event = maximum recorded stress under one passage of entire train.

the passage of each train car. The associated tension forces through the top portion of the connections reduces fatigue life of the web connection angles and top rivets. The design and behavior of the stringer web-angle end connections are currently under evaluation at each structure using the degree of continuity measured by this test program, as summarized in Table 2.

Train Braking Effects

The results of the train braking tests on the four structures are summarized in Figure 9. Longitudinal forces were computed on the basis of measured bending stresses near the test column bases or axial stresses in vertical bracing. The Figure 9 graph, showing the maximum test column bending stress relative to the distance of the braking train from the test column, indicates that the longitudinal braking forces are nonuniformly distributed along the track structure, and the rails are effective in distributing those braking forces across longitudinal structural expansion joints. Longitudinal structural expansion joints are typically located 140 to 160 ft center to center.

The Jackson Park and South Loop test locations recorded a reduction of column bending stress 300 ft away from the train braking location to about one-third of the maximum value directly below the braking train. The measured maximum longitudinal forces in the column directly below the test train were approximately 2.4 and 1.6 kips, respectively, for the Jackson Park and South Loop braking tests. The AREA manual longitudinal design load for both structures is approximately 3.8 kips in each column, distributed uniformly along a 200-ft length of elevated structure directly below the 200-ft-long test train. The AREA load is calculated as 15 percent of the test train load (weight) multiplied by a standard factor of 0.80 to account for continuous rail along the elevated structure exceeding 1,200 ft in length.

The Englewood Line segment was built with vertical longitudinal x-bracing at every fourth bay, as shown in Figure 7.

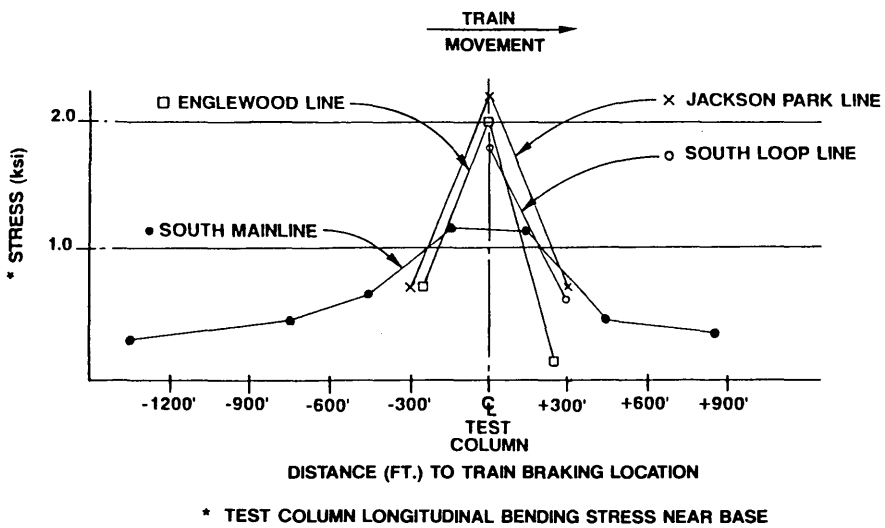

FIGURE 9 Measured effects of longitudinal force (braking) tests using four-car test train.

For the test train stopping 250 ft away from the x-bracing, the reduction in x-bracing forces and column bending stresses was approximately one-half, or less, of the maximum recorded braking force. The maximum horizontal force resisted by the vertical bracing was 22.6 kips, and by column bending 0.9 kips, when the train was stopped directly over the test spans. The AREA longitudinal design load for the entire test train is 25.9 kips distributed to 200 ft of elevated structure, consisting of one bay of vertical x-bracing and five columns in bending.

The dynamic braking tests conducted for the South Mainline structure included stopping the test train using the emergency brakes at seven locations along the elevated structure up to a distance of 1,350 ft away from the test column. Test records indicated that the longitudinal braking forces were nonuniformly resisted up to a distance of at least 850 ft away from the braking test train, resulting in a distribution of horizontal load over a length of elevated structure exceeding 1,700 ft. Structural rebound and longitudinal oscillation (rocking) were shown by the stress record at 1,350 ft from the just-stopped test train. The record indicated very little column bending during train braking, but that significant column stresses, equal to 25 percent of the maximum recorded column stress, occurred at this distance immediately after the train had stopped. The maximum longitudinal force in one column introduced by braking was measured to be approximately 3.6 kips. This value is compared with the AREA design load of approximately 5.3 kips per column, distributed along 200 ft of the elevated structure directly below the 200-ft-long test train.

CONCLUSIONS

Diagnostic load tests have provided knowledge about the actual response of the elevated steel transit structures to operating loads. This knowledge, currently being used to supplement the engineering analysis and rating calculations and to design rehabilitations for these structures, is summarized as follows:

1. Measured stringer midspan bending moments were 25 to 86 percent of those calculated, assuming simply supported spans, because of partial continuity through the stringer end support connections. The full-depth web-shear framing angle connections exhibited a wide variation in degree of continuity depending on the particular connection configuration. One test structure developed up to 86 percent of the theoretical end moment determined from a fully continuous analysis.
2. Stringer end rotations can impose out-of-plane stresses in cross-girder supports. Cross-girder horizontal bending stresses increased the total measured stress at one test location by 60 percent more than the vertical bending stresses. The total measured stresses were well within design allowable stress values.
3. Vertical impact testing was carried out using empty test trains. Measured vertical impact loading on the stringers, expressed as a percent of measured static stresses, averaged 7 to 34 percent for the test spans of 23.5 ft through 60 ft. The average measured impact varied inversely with the span length. A maximum vertical impact of 46 percent was recorded for the short 23.5-ft span. There was no appreciable correlation between impact and train speed.
4. Stringer midspan bending stresses were monitored during rush-hour commuter travel periods. The measured stresses indicated that the standard CTA fatigue design load of 19.5 kips (plus impact) per axle is conservative for the current trains in service and may therefore be safely used to estimate the remaining fatigue life. The actual variable amplitude stress plots, recorded during rush hour, can be used for a more accurate assessment of stringer fatigue life.
5. The measured partial continuity provided by the stringer web-shear framing angle connections is beneficial in reducing the stringer midspan stresses. This continuity reduces the fatigue life of the end connections by subjecting the top portion of the connections to variable tensile stresses with the passage of each train car. Retrofitted end connections are being considered to either reduce the continuity or provide improved fatigue resistance for the degree of continuity measured by this test program.
6. The timber open-deck track structure and steel rails were effective in distributing longitudinal forces caused by train braking across longitudinal expansion joints in the elevated structures.
7. Braking tests indicated that the longitudinal forces are nonuniformly distributed along the elevated structure. The typical elevated structure resists the train braking forces through column bending. The measured individual column longitudinal forces were less than AREA design loads uniformly distributed to columns directly below the 200-ft-long braking test train. The measured longitudinal forces significantly decreased in magnitude at a distance of 300 ft from the train. Longitudinal braking forces were nonuniformly distributed over a length of elevated structure exceeding 1,700 ft at one test location.

ACKNOWLEDGMENT

The authors appreciate the cooperation and assistance provided by the Chicago Transit Authority in conducting the load tests. Also, the authors wish to thank K. R. Hoigard, C. J. Malfitano, and B. J. Smith for their valuable contribution during the instrumentation and data acquisition phases of the test program.

REFERENCES

1. S. G. Pinjarkar, O. C. Guedelhoefer, B. J. Smith, and R. W. Kritzler. *NCHRP Research Project 12-28(13): Nondestructive Load Testing for Bridge Evaluation and Rating*. TRB, National Research Council, Washington, D.C., Feb. 1990.
2. S. G. Pinjarkar, R. W. Kritzler, R. A. Rolsing, and P. O. McCarthy. Evaluation and Load Testing of a 100-Year-Old Elevated Steel Transit Structure. Presented at 3rd Bridge Engineering Conference of the Transportation Research Board and FHWA, Denver, Colo., March 10–13, 1991.
3. *Manual for Railway Engineering, 1990–1991*. American Railway Engineering Association, Washington, D.C.

The opinions and conclusions expressed or implied in the paper are those of the authors only and are not approved or endorsed by the Chicago Transit Authority.

Publication of this paper sponsored by Committee on Dynamics and Field Testing of Bridges.

Retrofitting of Reinforced Concrete Bridge Columns

HARVEY L. COFFMAN

The seismic performances of one control and three retrofitted half-scale circular reinforced concrete columns were studied. The columns were 10 ft high, 18 in. in diameter, fixed at the base, and free at the top. An axial, vertical load of 158 kips was applied at the top, which was translated horizontally in a plane symmetrically about the vertical in such a way as to produce a maximum of four times the yield strain in the longitudinal reinforcing steel at the extremes of the first cycle. The columns were then oscillated between these extreme displacements of the first cycle until the lateral forces required to produce these translations approached zero. The measure of seismic durability used was the number of such cycles that a column sustained before losing structural integrity. The four columns were all made at the same time with 3,200-lb/in.^{2} concrete and the same reinforcing and ties. The arrangement was intended to model that of bridge columns of the 1960s. Three columns were retrofitted with prestressed, externally located circular ties at intervals along the lower 3 ft. The spacing and size of these ties varied from column to column. The control column sustained less than one cycle before losing structural integrity; the retrofitted columns sustained a minimum of 13 cycles.

Seismic design criteria for bridge columns have been changed considerably by the Applied Technology Council (ATC). Many bridges designed before the inception of the ATC-6 criteria are seismically deficient. Column inadequacies are usually evidenced by insufficient ties.

Inelastic response of these bridges under seismic loading could involve plastic hinging of the columns. Confinement of column reinforcing steel is essential for plastic hinging to dissipate energy under seismic loading without resulting in catastrophic column failure. Various details have been suggested for column retrofitting to increase confinement. Currently, there is no consensus as to which confinement detail is best.

The purpose of this research project was to determine the effectiveness of retrofitting circular concrete columns by adding external hoops made from standard Grade 60 steel reinforcing bars. To reduce parameters, columns were selected so that the predominant failure would be in flexure, which would satisfy two concerns: to fit the size and configuration of the existing loading frame, and to produce the predominant damage in the column itself. A cantilever column was selected so the retrofit hoops could be specifically located in the damaged region.

PROTOTYPE COLUMN DESIGN

AASHO first included earthquake design guidance in the 1958 interim (*1*). Column confinement was not officially incorporated for ductility purposes until 1983 when AASHTO published its *Guide Specifications for Seismic Design* (*2*). Soon after the 1971 San Fernando earthquake, bridge designers began to detail columns with additional confinement reinforcement. With the majority of Washington State's bridges built in the mid-1960s, during the interstate program, confinement reinforcement was not utilized for column ductility. A recent program by the Washington State Department of Transportation (WSDOT) (*3*) found 897 bridges in seismic WSDOT performance category C to be potentially vulnerable to a seismic event. Circular columns with deficient details exist in 65 percent of these bridges. The predominant details evolved from AASHO's specifications for highway bridges in the 1950s and 1960s. AASHO made three stipulations affecting the design of column confinement reinforcement. These three criteria are based on (a) compression reinforcing in flexure, (b) shear reinforcement, and (c) confinement for axial load. Buckling of flexural compression reinforcement required tie spacings not to exceed 16 longitudinal bar diameters. Shear reinforcement was required for concrete stresses exceeding an allowable of $0.03f'_c$ or a maximum of 90 lb/in.^{2}. Axial load requirements specified a minimum spiral volumetric ratio of

$$p_s = 0.45\,(A_g/A_c - 1)f'_c/f_{yh} \quad (1)$$

with a limiting size of a No. 2 spiral at 3-in. maximum spacing. Minimum tied confinement was more lenient with No. 3 hoops at 12-in. maximum spacing. These columns were allowed to carry only 80 percent of the axial load of the spirally reinforced columns.

WSDOT's typical circular column design consisted of a 3-ft-diameter column with 4-kip/in.^{2} concrete strength, a maximum aggregate size of 1.5 in., and 1 to 2 percent longitudinal reinforcement. All longitudinal reinforcement was lapspliced at the footing, with lengths ranging from 20 to 35 bar diameters. Most column designs were governed by flexure with an axial load range of 5 to 20 percent $A_g f'_c$. This concept resulted in the frequent utilization of No. 3 hoops at 12-in. spacing in lieu of the alternate No. 2 spiral at 3-in. spacing. These No. 3 hoops were constructed with a 2-ft 4-in. lapsplice without anchoring the splice tails into the column core. These columns were generally supported on footings that often had no top mat of reinforcement, leaving the footing vulnerable to failure. Although footing failure is a major concern, the main emphasis of this project is on the isolated capacity of the column. To determine the effectiveness of the column retrofit method, these details were incorporated into the modeled column.

Washington State Department of Transportation, Transportation Building, Olympia, Wash. 98504.

MODELED COLUMN DESIGN

The four modeled columns (Figures 1 and 2) are identified as Columns 1 through 4. Columns were 18-in. in diameter with 1.5 percent longitudinal reinforcement (nine No. 6 grade 40). The concrete mix was designed for a strength of 4 ksi at 28 days with a maximum aggregate size of ¾ in. Internal hoops were No. 3 grade 40 reinforcing bars spaced at 1 ft with a 1-ft 2-in. lapsplice without anchoring the splice tails into the column core. Dowel bars utilized at the base were lapspliced with 35 bar diameters to the longitudinal column reinforcement.

To match the bolt pattern of the existing test slab, the column footing was simulated by a steel base plate. The base plate was roughened by grinding gouges into the surface to simulate the construction joint. Footing dowels were threaded 2 in. into the base plate, welded with ⅜-in. fillet welds and normalized to relieve crystallization of the welded area.

Column 1 was the control specimen tested without additional external confinement. The full column elevation in Figure 1 shows Column 1 as tested. The partial elevations in Figure 1 combine with the control column to make up the three retrofitted columns. The external reinforcement was varied to determine its effectiveness. Ratios were selected above and below the requirements of AASHTO (2, p. 28).

External confinement reinforcement ratios are listed in Table 1. The percentage of volumetric ratio, p_s, is based on the gross section (2, p. 28) and is

$$p_s = 0.12 f'_c/f_{yh} \quad (2)$$

The percentages in Table 1 are based on f'_c = 4,000 lb/in.^{2} and f_{yh} = 60,000 lb/in.^{2}.

Swaged couplers, designed to 150 percent of the specified yield strength of the Grade 60 ASTM A615 reinforcing bar, were utilized to attach the half circumferential external hoops. These hoops were prestressed to the column by swaging opposing threaded couplers to each end of the hoop. As shown in Figure 3, a machined stud was threaded into the couplers to pull the two half hoops tight. A tension test showed that tightening with an open-end wrench produced a stress in the hoops to an average of 50 kip/in.^{2}.

Retrofit hoops would require some type of protection. This could be accomplished by painting the hoops or placing an additional cover concrete by slip forming. Nominal reinforcement may be required for crack control. Neither of these schemes was included in this project.

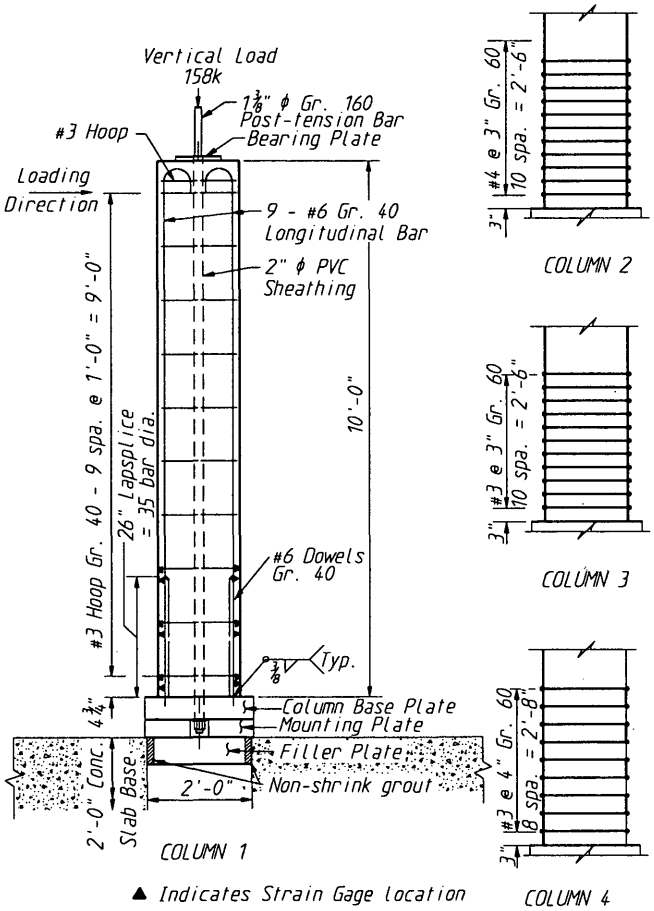

FIGURE 1 Column details and retrofit schemes.

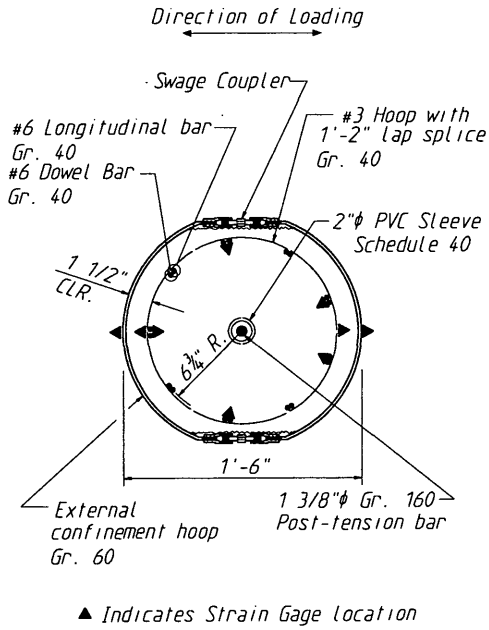

FIGURE 2 Column cross section.

TABLE 1 External Confinement Ratio

Column	Reinf. Ratio	Size/Spacing	% AASHTO
1	0.0	No Retrofit	
2	0.0152	#4 @ 3"	191%p_s
3	0.0083	#3 @ 3"	104%p_s
4	0.0062	#3 @ 4"	77%p_s

$p_s = 0.12 f'_c/f_{yh}$ (volumetric ratio)
All retrofit reinforcement ASTM A615 GR. 60

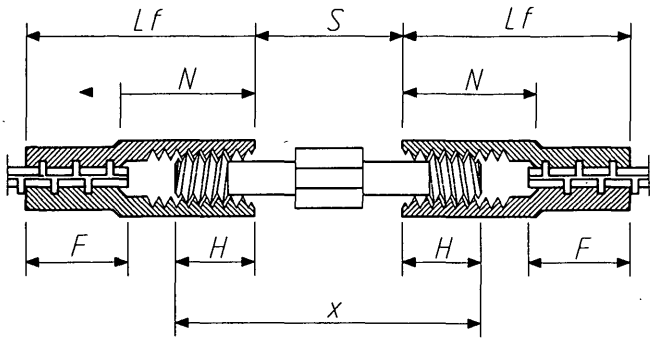

Dimension

Size	Lf	F	N	H	S	X	Weight coupler	Weight stud
#3	3"	1½"	1⅝"	⅝" min 1⅜" max	⅝" min 1⅞" max	3"	.23 lb	.13 lb
#4	3¾"	1⅞"	1⅞"	1⅛" min 1⅝" max	⅝" min 1⅞" max	3¼"	.41 lb	.29 lb

FIGURE 3 Swaged coupler detail and dimensions.

COLUMN CONSTRUCTION

All columns were constructed simultaneously. Reinforcement was tied in cages and supported from the forms utilizing 1½ in. steel wire chairs. Concrete was placed in the vertical forms by concrete bucket and consolidated with probe vibrators. After curing for 10 days, the forms were removed and the columns were open-air cured (approximately 84 days) until tested. During curing, columns were freestanding with no axial load applied.

MATERIAL

The concrete mix design was based on WSDOT standard specifications for Class AX (4,000 lb/in.^{2}) concrete. Ready-mix concrete was purchased from a batch plant and delivered by truck. Concrete was designed as a four-sack mix with a ¾-in. maximum aggregate size. Slump was 3 in. at the time of delivery. Concrete properties were established by ASTM C469-87. Concrete test cylinders were taken throughout the placement of columns. Sample concrete was removed from cylinder forms after 10 days and air cured in situ with the columns. Average compressive strength was 3,200 lb/in.^{2} at 84 days and modulus of elasticity (E_c) was 3,176,000 lb/in.^{2}. The standard deviation of the concrete strength was 87.5 lb/in.^{2}.

ASTM A615 deformed bars were used for column reinforcement. Table 2 shows the size and average material properties. The modulus of elasticity was 29 million lb/in.^{2}. Couplers were swaged to reinforcement for tensile test. Coupler strengths equaled or exceeded 150 percent of the specified yield strength for the Grade 60 reinforcing bars. Table 3 lists a summary of the values from coupler test.

Strength and pretensioning of the couplers can be improved by using a higher-strength material for the stud. The extra strength will prevent the wrench from stripping the hex-head when tightened, allowing more tension to be exerted to the hoop.

TEST APPARATUS AND LOADING

Axial Loading

A total force of 158 kips was applied by a concentric rod and a centerhole hydraulic jack. The loading was monitored continuously by a load cell at the column top. The external hoops were placed before testing and before the axial load was ap-

TABLE 2 Reinforcement Properties

Size	Grade	Yield f_y (ksi)	Strength f_u (ksi)	Type of Reinforcement
#4	60	70.0*	94.0	Exterior Hoop
#3	60	81.0*	99.0	Exterior Hoop
#6	40	55.0	90.0	Longitudinal Reinf.
#3	40	63.0*	80.6	Interior Hoop

* Estimated yield. Actual yield was not determined due to pre-bending of reinforcement hoop bars.

TABLE 3 Coupler Data

COUPLER SIZE	INITIAL TIGHTENING (KIPS)	MAXIMUM TENSILE (KIPS)	FAILURE MODE
#4	9.35	20.0*	STUD
#4	10.5	20.7	BAR
#3	4.8	11.0	STUD
#3	4.7	11.0	STUD

* Ultimate specified force for a #4 is 18.0 kips, and #3 is 9.9 kips.

plied. The axial load produced hoop strains of approximately 4 percent of the total maximum strain during testing.

Horizontal Loading

The horizontal load was applied by a 110-kip MTS actuator. Each end of the load train was attached to MTS swivels. The swivels allowed rotation in both vertical and horizontal directions. The actuators were displacement controlled by computer analog converter at a maximum loading rate of approximately 0.4 in./min.

The actuator's total displacement stroke length was 10 in. Take-up in the load train limited cycling displacement to ±4.33 in. The first cycle had a maximum displacement of three-quarters of the yield displacement, followed by two cycles with maximum displacements of yield and twice yield, respectively. Loading continued with cycles of four times the yield displacement until forces required to maintain four times the yield displacement dropped significantly.

INSTRUMENTATION

Strain gauges were placed on dowels and longitudinal reinforcing bars at 3, 12¾, and 20¼ in. above the base plate on longitudinal reinforcing bars at five plan locations. Additional gauges were placed diametrically opposite on the bottom three internal hoops in the plane of loading. The external hoops were gauged in a manner similar to that for the internal hoops. Figures 1 and 2 show the strain gauge locations.

Lateral force was measured with a 110-kip MTS load cell placed integral with the load train. Lateral displacements were measured with a Temposonic displacement transducer. An isolated reference bridge was used to support the Temposonic. Absolute displacements were measured directly from the column at the same elevation as the load train.

DATA ACQUISITION

All data were recorded by an HP 3497A data acquisition/control unit. This unit interfaced with an HP 9216 computer that reduced data and stored values on 3½-in. HP 9121 disk drives. All voltage readings were normalized and zeroed. Data were collected under static conditions as the column completed each incremental step.

TEST RESULTS

For the purpose of testing, a yield displacement was defined as D_y = 1.07 in. (*4,5*). This is the displacement required to cause yielding of the extreme longitudinal reinforcement. The maximum ductility factor, $\mu = D/D_y$, for the test was 4.0.

Results of the testing are illustrated as hysteresis graphs in Figures 4 through 7 and as photographs in Figures 8 through 10. The hysteresis graphs are plotted as horizontal force versus horizontal displacement. A comparison of Figures 4 through 7 illustrates the significance of the retrofit method. Note that the initial cycles of the four hysteresis graphs show similar stiffness. This aspect is crucial to bridges because the retrofit method does not increase loading to the foundation.

The hysteresis curve for Column 1 (Figure 4) is unstable at 4μ. Evidence of a sudden drop in load-carrying capability is observed. The column failed to form a plastic hinge. Energy dissipation was poor in subsequent cycles.

The hysteresis curves for all three retrofitted columns (Figures 5 through 7) are very stable at 4μ. No evidence of sudden drop in load-carrying capability was observed, and the plastic

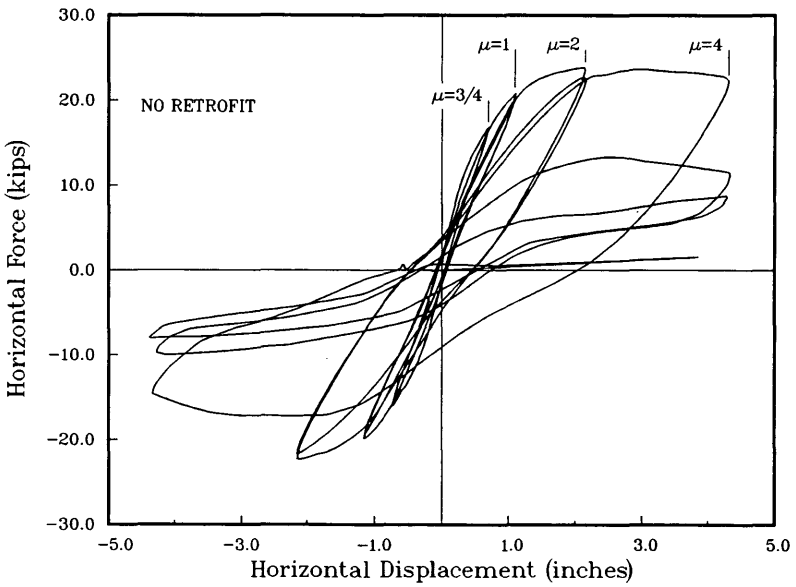

FIGURE 4 Hysteresis Column 1: less than one cycle at 4μ.

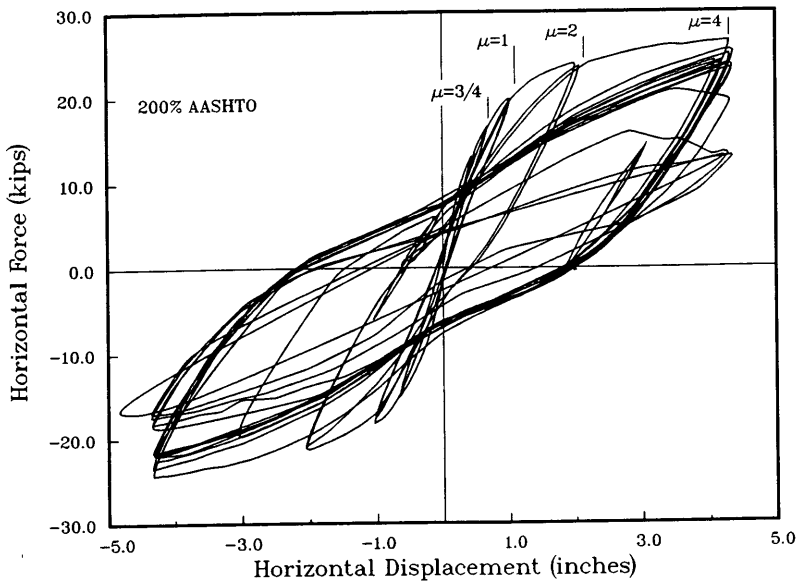

FIGURE 5 Hysteresis Column 2: 13 cycles at 4μ.

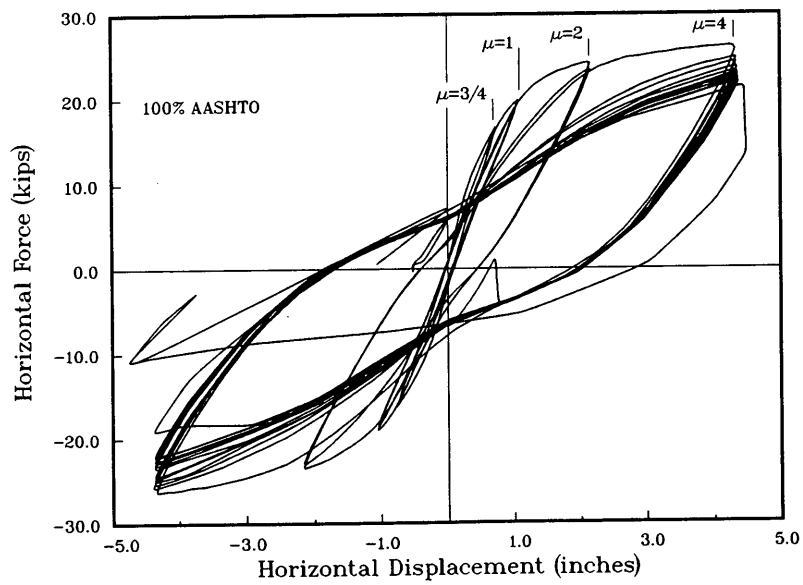

FIGURE 6 Hysteresis Column 3: 14 cycles at 4μ.

hinge continued to dissipate energy throughout the test. A large drop in load was evidenced near the end of testing when dowel reinforcement bars fractured at the weld to the base plate. The failure of the dowel at the weld is believed to be caused by embrittlement due to welding and was not a true characteristic of the prototype column.

FAILURE MODES

Two types of failures were encountered. The first type was in the lapsplice of the longitudinal reinforcement of Column 1. Figure 8 is a photograph of Column 1 at the completion of testing, illustrating the nature of the lapsplice failure. Notice that the concrete spalled over the entire length of the lapsplice. Failure began at 2μ with the development of a large flexure crack at the top of the lapsplice and concrete crushing at the base. The flexure crack increased in size, progressing into a diagonal shear crack as cycling proceeded to 4μ. A lateral translation kept the crack from closing, causing the concrete cover to spall, the lapsplice to slip, and the horizontal force required to attain 4μ to drop significantly. Completion of the second half-cycle resulted in the complete failure of the lapsplice. The hysteresis curve shows a force on subsequent cycles, which is attributed to the action of the posttensioning rod. In the final half-cycle, the axial load was removed

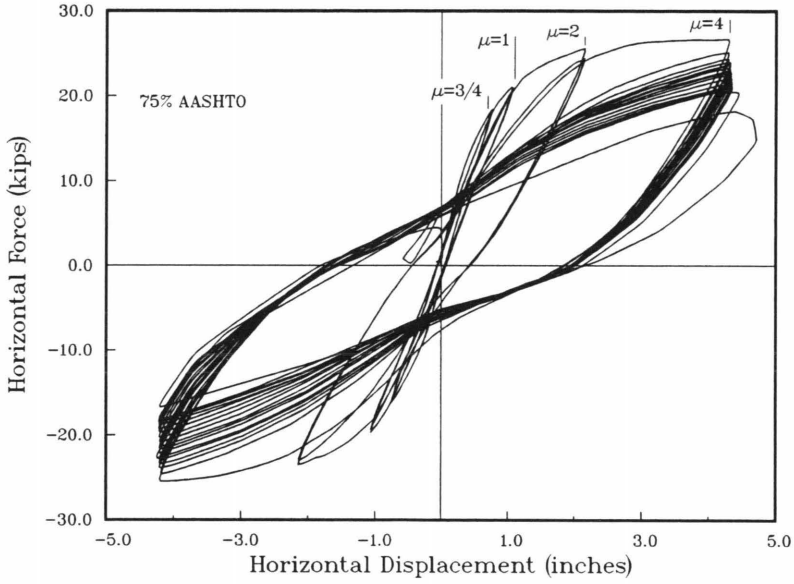

FIGURE 7 Hysteresis Column 4: 17 cycles at 4μ.

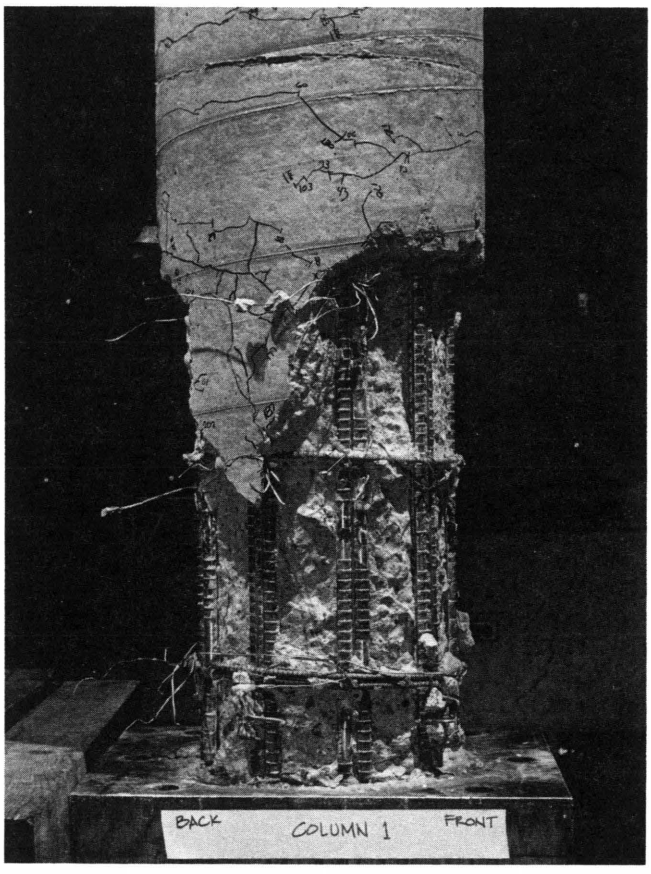

FIGURE 8 Column 1 elevation at completion of test: cover spalled but did not fall off and was easily removed manually for visual inspection.

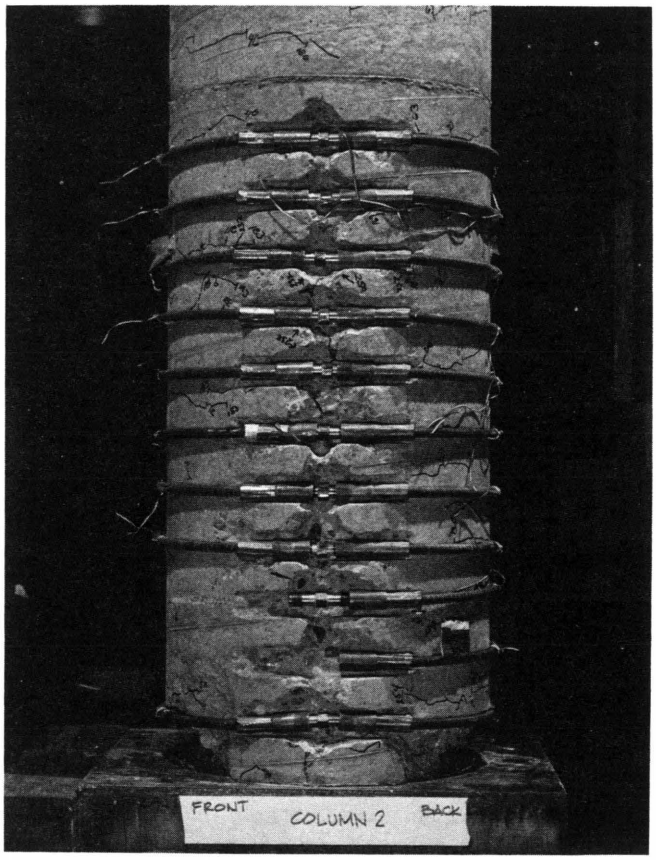

FIGURE 9 Column 2 elevation at completion of test: notice that damage is all located below bottom exterior hoop; hoops were undamaged; bottom hoops were removed at completion of testing.

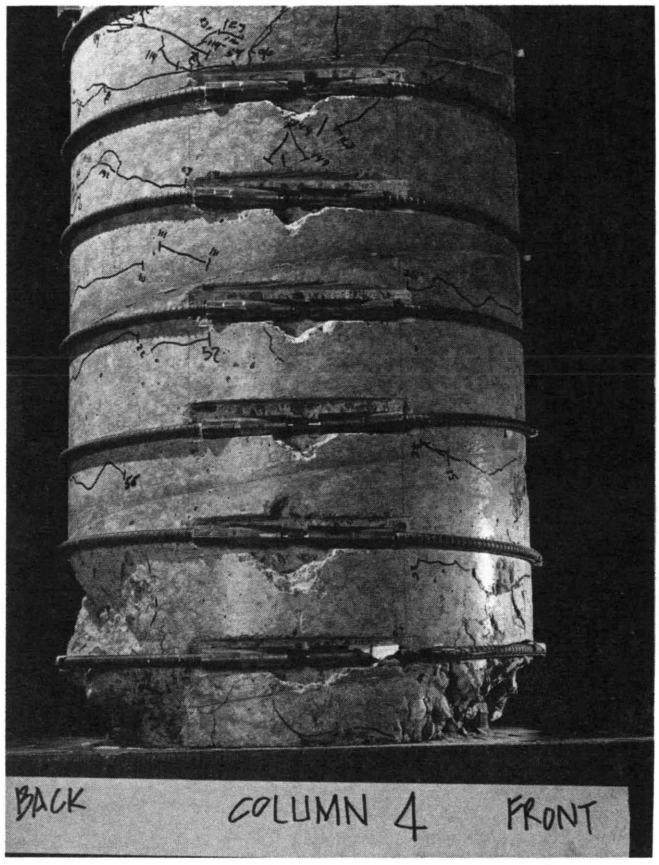

FIGURE 10 Column 4 elevation at completion of test: this column had minimum external confinement; concrete crushing developed above bottom hoop.

and Column 1 was displaced to 4μ. The horizontal force required to attain 4μ was 500 lb compared with the ultimate of 23,870 lb. The core concrete was unspalled at the end of testing and capable of carrying the axial load, although the section would be vulnerable to failure in shear or uplift with further loadings because the internal hoops were no longer effectively confining the lapsplice.

The second mode of failure was predominant in the three retrofitted columns and consisted of concrete crushing below the bottom external hoop. Figures 9 and 10 are photographs of Columns 2 and 4 after testing. These figures illustrate the second failure type. Notice that the majority of the damage is now located in the bottom 3 in. Concrete crushing at the base continued to propagate toward the column core until the dowel reinforcement fractured at the weld to the base plate. Dowel reinforcement fractured just above the fillet weld. Failure was restricted at the base because of the steel plate. A concrete foundation would allow crushing of concrete and a longer hinging length, which would be beneficial to performance under these testing conditions. Increasing the length of plastic hinging in turn increases the energy dissipation.

This method of retrofitting columns is successful in improving the column performance, but it does nothing for improvement of the footing. Potentially the failure will be located in the footing with the retrofit that has not increased the durability of the structure on the global scale. If it is impractical to retrofit the foundation, the alternative to do nothing at the column base may be plausible. The failure of Column 1 was essentially a hinge. If the column could then carry the loads at the top, no retrofit would be necessary at the bottom, which simplifies the entire retrofit to just the top of the column and cross beam.

Column 1 failed in slippage of the lapsplice after the concrete cover spalled. Spalling was largely caused by the wedging action of the deformations of the longitudinal reinforcement. Samples of longitudinal reinforcement had a small sheared wedge embedded on the compression side of the bar deformation. This wedging created a perimeter crack at the center of the longitudinal reinforcement where the concrete cover spalled away from the inner column core.

Columns 2 and 3 failed by concrete crushing due to flexural compression. Further damage was not evident until the displacement was increased. This pattern continued up to 4μ, where the dowel reinforcement fractured after a minimum of 13 cycles. Columns 2 and 3 retrofit hoops prevented the formation of a flexure crack at the top of the lapsplice. Column 4 failure varied from that of Columns 2 and 3, developing instead a flexural crack at the top of the lapsplice. The crack did not propagate into a significant size. Column 4 also had concrete crushing at the base propagate above the bottom external hoop during the initial cycles of 4μ. Figure 10 shows the damage above the bottom external hoop. No further damage above the bottom bar was observed in later cycles of 4μ. As testing continued, Column 4 settled into the same failure mode as the first two retrofitted columns. This damage is an indication that Column 4 was failing in the same manner as Column 1. Reflecting the retrofit reinforcement was close to the minimum required to prevent the lapsplice failure.

EXTERNAL HOOP REINFORCEMENT

The external confinement reinforcement showed no signs of distress. Strains in the bottom retrofit bars did reach 1.5 to 2 times yield strain. Strains in the retrofit hoops varied along the length of the main reinforcement lapsplice, decreasing as you move up the column vertically to mid-lapsplice and then increasing again to the top of the lapsplice. Retrofit bars above the lapsplice showed little variation in strain.

Figure 11 indicates strain profiles of the bottom internal hoops for columns 1, 2, and 4. Also shown in Figure 11 (*middle* and *bottom*) are strains of corresponding external hoops from Columns 2 and 4. The relative magnitudes show the force distribution between the internal and external confinement hoops.

Note the unstable nature of strain in the internal hoop of column 1. This instability follows the first displacement to 4μ when the cover concrete spalled. The interior hoop lapsplice begins to slip, causing chaotic strain readings. The internal hoop strains of the retrofitted columns indicate no evidence of instability because the external hoops carry a majority of the load. The strain in the interior hoops of the retrofitted column is a function of the exterior hoop confinement. Without the additional exterior hoops, interior hoops do not contribute to confinement and should be excluded in designing the confinement reinforcement.

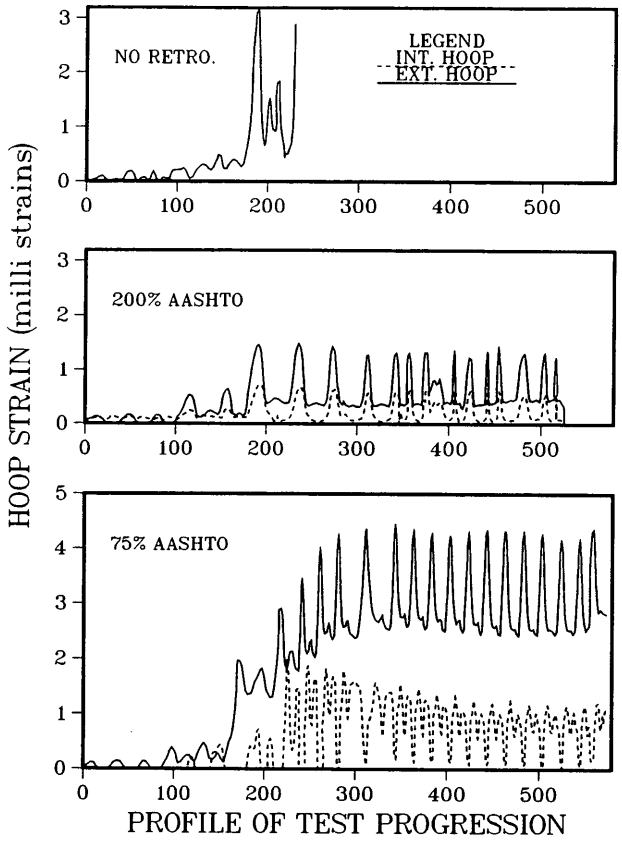

FIGURE 11 Strain profile of bottom hoops: *top*, Column 1; *middle*, Column 2; and *bottom*, Column 4.

INCREASED DUCTILITY

Ductility is a measure to withstand cyclic loading. Although it is not clear how much ductility a column should be designed for, ductility can be used to weigh the effectiveness of the retrofit method. The ductility of the retrofitted columns improved markedly over that of the control column. Energy dissipation was 269, 1,459, 1,565, and 1,842 kip-in. for Columns 1 through 4, respectively. Thus the energy dissipation as percentages of Column 1 are as follows: Column 2, 541 percent; Column 3, 581 percent; and Column 4, 684 percent.

Figure 12 relates the stability of the four columns as energy dissipation per cycle. Column 1 was unable to dissipate energy after the first cycle of 4μ. Retrofitted columns continued to dissipate a large proportion of energy after the first cycle of 4μ. Figure 12 also shows the duration of cycling at 4μ. The drop in Column 2 is caused by the continuation of testing after the dowel bars fractured at the weld.

The increase in energy dissipation with the reduction of confinement reinforcement can be attributed to the pinching of the longitudinal bar. As the confinement reinforcement decreases, the length to transfer force from longitudinal to dowel reinforcement increases. As the confinement reinforcement is decreased, strains increase when wedging separate cover and core concrete. This allows the longitudinal reinforcement to yield over a longer length, thus permitting an increase in strain energy of the longitudinal reinforcement and, thus, the amount of energy dissipated. With the larger confinement reinforcement, the strain energy of the longitudinal reinforcement is distributed over the bottom 3 in. of the column because of lower confinement reinforcement strains. This can be seen in Figure 9, where all the damage to Column

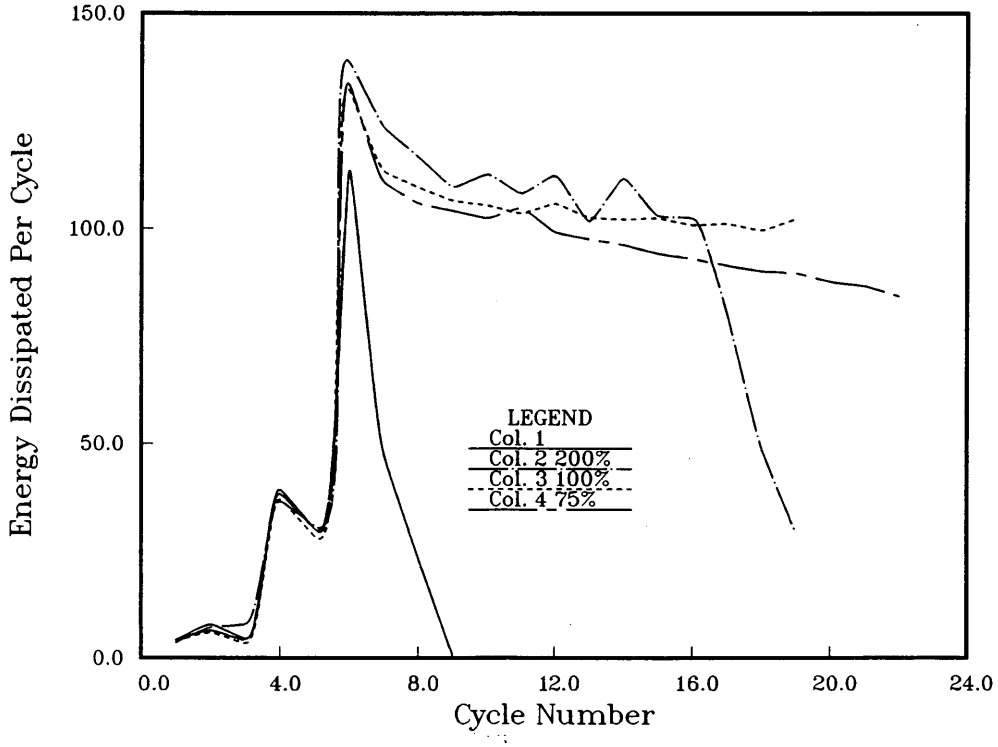

FIGURE 12 Energy dissipation per cycle.

2 is at the base plate. Column 4 in Figure 10 had damage above the bottom hoop, allowing about twice the length of longitudinal reinforcing to yield.

This increase in length was also evident in the strain profiles of Figure 11. Column 2 strains in Figure 11 (*middle*) are much smaller than those in Column 4 in Figure 11 (*bottom*). The No. 4 external hoops of Column 2 are large enough to confine the forces in the longitudinal reinforcement at the bottom hoop. It was apparent from the confinement hoop strains going up the column that the lapsplice was fully developed in half of its specified length; that is, the confinement hoops exhibited the greatest strains at the base of the column and just below the top of the lapsplice. The strain decreased toward the midpoint of the lapsplice.

SUMMARY

1. Installing hoops around the exterior as confinement improved the performance of the reinforced concrete columns by preventing lapsplice failure and thus increasing the ductility. Confinement is provided by exterior reinforcement, as indicated in Figure 11. Interior confinement had smaller strains than did exterior confinement and was unstable without exterior hoops such as those in Column 1 [Figure 11 (*top*)]. Design should exclude the contribution of internal hoops. Confinement should be provided as specified in the AASHTO guide specifications for plastic hinging (*2*). When retrofitting confinement is placed around the existing column, the gross area becomes equal to the core area, and the reinforcement ratio is limited by Equation 2.

2. Tensioning the exterior hoop is essential to performance. Confinement hoops should be tightened snug against the concrete. Although active confinement was not studied as a parameter in this project, previous studies (*6,7*) show that passive confinement reinforcement does not restrain the core until the column core fractures. This action generates a tension reaction in the confining reinforcement as the lateral strains increase markedly. Active confinement can increase strength by reducing core fracturing. The active confinement prevented the spalling of concrete cover, thus maintaining the lapsplice strength. Although no external hoops failed during column testing, hoop strengths were limited by the strength of the stud. Performance of hoops could be improved to provide additional strength and pretensioning by making the stud from a higher-strength material.

3. External hoops should be placed as close as possible to the supporting element to prevent concrete spalling. Column connections to footings and cross beams are regions of high stress during seismic loading. These connections are where the concrete is most likely to spall. To prevent large spalling in this locality, hoops should be as close as possible to the connecting part. Although shear failure was not investigated in this project, this retrofit method can be utilized in strengthening columns with insufficient shear capacity by standard design practice.

4. This retrofit technique is recommended for use at potential plastic hinge locations or in regions in which existing ties are insufficient to handle shear.

5. Foundation retrofitting is very difficult and expensive. Loads created in a seismic event are proportional to the column stiffness. Increasing loads to the foundation can generate expensive retrofits. To reduce costs, column retrofitting should thus minimize the effects to the foundation. The advantage of this retrofit is improved ductility without changing column stiffness. Although it is not clear whether it necessarily would be needed at the bottom of these columns, the retrofit could be used at the top. The reason to doubt the effectiveness at the bottom of the column is because of the need to retrofit the footing. It may be possible to eliminate footing retrofit by only retrofitting the top portion of the column.

ACKNOWLEDGMENTS

This research project was funded by WSDOT through the Transportation Research Center. The National Science Foundation funded the design and construction of the testing apparatus.

REFERENCES

1. *Standard Specifications for Highway Bridges, 1957–1973*. AASHO, Washington, D.C.
2. *Guide Specifications for Seismic Design of Highway Bridges*. AASHTO, Washington, D.C., 1983.
3. *Seismic Retrofit Program Recommendations*. Washington State Department of Transportation, Olympia, 1991.
4. R. Park and T. Paulay. *Reinforced Concrete Structures*. Wiley-Inter-Science, New York, N.Y., 1975.
5. R. Park and P. D. Leslie. Curvature Ductility of Circular Reinforced Concrete Columns Confined by the ACI Spiral. Presented at 6th Australias Conference on the Mechanics of Structures and Material, University of Canterbury, Christchurch, New Zealand, Aug. 22–24, 1977.
6. W. E. Armstrong and S. H. Perry. Spirally Bound Concrete Columns. *Proc., Royal Society of London, Series A: Mathematical and Physical Sciences*, Vol. 400, No. 1818, July 1985, pp. 127–144.
7. V. V. Mikhailov. *Proc., 6th International Congress of the International Federation of Prestressed Concrete*, Prague Cement and Concrete Association, 1970.

Publication of this paper sponsored by Committee on Dynamics and Field Testing of Bridges.

Seismic Retrofitting of Rectangular Bridge Columns for Shear

LAURA L. BERNARDS, DAVID I. MCLEAN, AND EDWARD H. HENLEY, JR.

Retrofitting measures applied to 2/5-scale shear-deficient columns representative of existing rectangular bridge columns in the Puget Sound area of Washington state were investigated. The retrofit methods studied included external hoops applied over the height of the column and full-height rectangular steel jacketing. Test specimens consisted of a single column connected at the base to a rectangular footing. The specimens were subjected to increasing levels of cycled inelastic displacements under constant axial load. Performance of the specimens was evaluated in terms of load capacity and ductility. Tests on the column representing as-built conditions resulted in a brittle shear failure at the calculated yield displacement, that is, at a displacement ductility level of $\mu = 1$. Both retrofit methods investigated improved the behavior of the deficient column. With the external hoop retrofit, performance of the retrofitted columns was only moderately improved over that of the as-built column. Brittle fracture of the retrofit hoops limited the load-carrying capability and ductility enhancement, with displacement ductility levels of $\mu = 2$ and 4 being achieved. With the use of the rectangular steel jacket retrofit, performance was significantly improved over that of the as-built column. The jacket retrofit resulted in a ductile column response with good load-carrying capability through $\mu = 8$. Application of this retrofit over the full height of the column enabled the steel jacket to increase the column shear strength so that a flexural failure mode resulted. Although buckling of the steel jacket and longitudinal reinforcement occurred near the maximum moment section, sufficient confinement to the hinging region was provided by the buckled steel jacket to maintain load-carrying capability.

The extensive damage to bridge structures in the 1971 San Fernando earthquake caused a significant reevaluation of the seismic design approach for bridges. Since then, improvements have been incorporated into current design criteria. However, many bridges were built before the introduction of these new standards. Bridge failures in California and Alaska under relatively moderate earthquake loadings and, most notably, the collapse of the I-880 freeway in the Loma Prieta earthquake clearly indicate the vulnerability of older bridges and the need to develop methods for strengthening these bridges to meet current safety requirements.

In the United States, much of the work on seismic retrofitting of bridges has been done in California. Significant retrofit efforts began there in the late 1970s, with the focus of the retrofit program being to improve the performance of superstructures in an earthquake. Only relatively recently did the California Department of Transportation (Caltrans) begin retrofitting bridge substructures. It is notable that many of the bridges that experienced substructure damage during the Loma Prieta earthquake had movement restrainers installed in the superstructures. Clearly, retrofit efforts must address the entire structure before adequate structural safety can be achieved.

L. L. Bernards and E. H. Henley, Jr., Washington State Department of Transportation, Olympia, Wash. 98504. D. I. McLean, Department of Civil and Environmental Engineering, Washington State University, Pullman, Wash. 99164.

A common problem in pre-1971 bridges is an insufficient amount of transverse reinforcement in the columns. Typically, No. 3 or No. 4 transverse hoops spaced at 12 in. on center were used in rectangular columns, regardless of column cross-section dimensions, and the hoops had short hook extensions and anchorage only by lapping the ends in the cover concrete. Further, intermediate ties were rarely used. This detail results in many older columns being susceptible to shear failures, and it provides little confinement for developing full flexural capacity or preventing buckling of the longitudinal reinforcement.

The objective of the research presented in this paper was to identify retrofit techniques for increasing the shear strength and ductility capacity of rectangular reinforced concrete bridge columns. A detailed account of the research program can be found elsewhere (*1*). This paper presents an overview of the study and discussion of the test results and conclusions.

BRIDGE COLUMN RETROFITTING

Previous Retrofit Research

Chai et al. (*2,3*) examined the effectiveness of retrofitting circular and rectangular bridge columns with circular and elliptical steel jackets, respectively, in which the gap between the jacket and column was filled with high-strength grout. Initially, the jacket was used only in the plastic hinge region and terminated just above the footing. As-built circular columns with lapped starter bars did not reach their theoretical strength because of bond failure in the early stages, after which the stiffness and strength degraded quickly. A comparable column retrofitted with a 3/16-in.-thick circular steel jacket showed tremendously improved results. In tests of as-built rectangular columns with lapped starter bars, there was bond failure at the splice leading to rapid strength and stiffness degradation. When retrofitted with a 3/16-in.-thick elliptical jacket, excellent hysteretic response was achieved. A later phase of testing showed that the same circular and elliptical steel jackets, extended over the full height of the columns, were effective in enhancing the shear strength and ductility in circular and rectangular columns, respectively.

Coffman et al. (*4*) studied a retrofit method for improving bridge column ductility that used external hoops, prestressed with turnbuckles, around the lower portion of circular columns. This scheme resulted in a dramatic increase in the total

energy dissipation of the section and an increase in seismic durability by an order of magnitude over the as-built column. This method appears to improve the force transfer between the dowels and longitudinal steel in the splice region, even under repeated inelastic displacements.

Bett et al. (*5,6*) improved the performance of rectangular columns by adding external longitudinal reinforcement and closely spaced ties. This retrofit method was varied by adding cross ties through the column that were anchored by hooking around the longitudinal reinforcement. The cross ties improved the confinement, resulting in decreased strength and stiffness degradation under reversed cyclic loading.

Fyfe and Priestley (*7*) studied a retrofit method that used a high-strength fiber-reinforced fabric that was posttensioned around the plastic hinging region of a column. This retrofit method enhanced the flexural ductility and prevented the bond failures that were observed in the as-built columns tested by Priestly et al. (*2,3*).

Current Retrofit Practice

Currently, very little information exists on standard procedures for retrofitting bridge substructures. In the United States, only Caltrans has implemented any standardized procedures for selection of critical substructure elements and specifications for retrofitting once a bridge substructure has been identified as critical (*8*).

In bridges with columns identified as being unsatisfactory, Caltrans has standardized two column retrofit methods, the Class P retrofit and the Class F retrofit, which consist of ⅜-in.-thick steel jackets around the columns. For shear-deficient columns, a full-height jacket is used. Circular or elliptical jackets are used, depending on whether the column is circular or rectangular. The Class P retrofit provides partial confinement in the plastic hinging regions and only modifies the column, whereas the Class F retrofit modifies both the column and the footing, resulting in higher costs with the Class F retrofit. For this reason, a common starting point in Caltrans retrofit strategy is to use a Class F retrofit on one column per frame and Class P retrofits on the other columns in the frame.

EXPERIMENTAL TESTING PROGRAM

A representative bridge column from the Puget Sound area of Washington state was identified and used as the deficient specimen to which retrofit measures were applied and evaluated. The prototype column was formulated by compiling design information from existing Washington state bridges and identifying common dimensions, reinforcement arrangements, and deficient details in the columns. The column chosen was a 20- × 30-in. section with reinforcement concentrated on the 20-in. faces and with a total reinforcing ratio of 2.6 percent. The column contained No. 3 transverse hoops at 12 in. on center with 4-in. hook extensions that were lapped in the cover concrete for anchorage. All reinforcement in the column was Grade 40, which was used almost exclusively in the older bridges being studied.

The experimental tests were conducted on ⅖-scale specimens that modeled the dimensions, reinforcement content and arrangement, deficient detailing, and material properties of the chosen prototype column. A cross section of the scaled specimen is shown in Figure 1, which represents the control specimen to which all retrofitted column results were referenced. The test specimens consisted of a single column connected at the base to a rectangular footing. To prevent a footing failure that would introduce another variable into the testing program, the footing was designed to be stronger than those commonly found in pre-1971 designs. Continuous longitudinal bars extended into the footing using 90-degree hooks for resistance to pullout (see Figure 1). Tests were performed on parallel sets of specimens: one specimen incorporated deficient as-built detailing (the control specimen), and the other incorporated the same detailing but was retrofitted so that the benefit of the retrofit could be clearly seen.

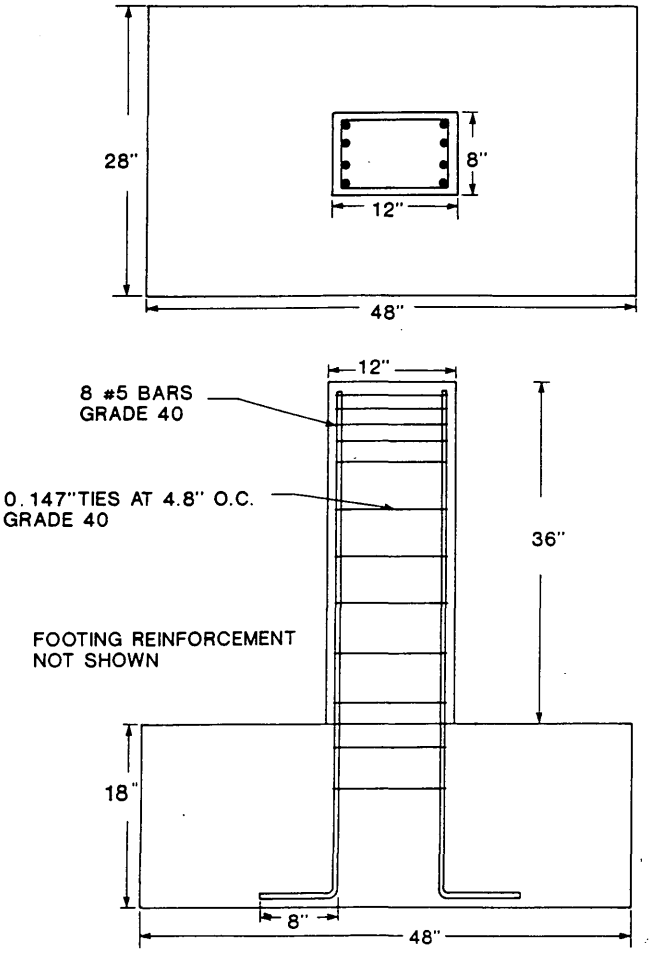

FIGURE 1 Column control specimen: *top*, plan view; *bottom*, elevation view.

Retrofit Methods Studied

Two basic retrofit methods were selected for study, each with a set of parameter variations. The first was a technique using steel plates welded up four longitudinal seams to form a rectangular jacket to encase the full height of the column. It was made slightly oversized for ease in construction, and the gap

between this jacket and the specimen was then filled with high-strength, nonshrink cement grout. A ½-in. space was left between the top of the footing and bottom of the jacket to eliminate bearing of the jacket on the footing that would increase the flexural capacity and transfer excessive force to the footing. This retrofit scheme is shown in Figure 2.

The effects of various plate thicknesses in the jacket retrofit method were studied by testing specimens retrofitted with 12- and 16-gauge steel plates, corresponding to approximately 1/10- and 1/16-in. thicknesses, respectively. A second variation was to use an epoxy mixture rather than cement grout to fill the gap between the jacket and column. This epoxy mixture is used commercially in anchor bolt applications and consisted of a 1:1 ratio of epoxy to sand in which a rounded sand was used to produce a fairly fluid mixture. A third variation was investigated in which steel dowels were anchored into the column core near the footing to improve confinement of the jacket under cyclic loading and delay longitudinal bar buckling. The dowels used were 0.25-in.-diameter bars set in 4-in.-deep predrilled holes and were anchored with epoxy. They were located at 1 in. and 4 in. from the top of the footing on each 8-in. face.

The second retrofit technique that was investigated used steel angle configurations at each corner of the specimen that were connected by threaded 0.25-in.-diameter rods acting as hoops spaced along the specimen (see Figure 3). These angle/rod configurations, hereafter referred to as retrofit hoops, were expected to act as confinement for the specimen under cyclic loading and to provide shear reinforcement, much like tie reinforcement would in new construction. Expected advantages with this method were the minimal increase in flexural capacity and the ease of applying the retrofit in the field. Various spacings between the hoops were studied.

A summary of the test specimens is given in Table 1.

Test Setup and Procedures

Figure 4 shows the test setup for the column specimens. The specimens were tested using reversed cyclic lateral loading about the strong axis of the section under a constant axial load. Anchor bolts were used to secure the footing to the strong floor, and sliding of the specimen was prevented by horizontal stays. An axial load level of $0.09f'_cA_g$ was applied to all columns, equivalent to a stress level of 360 lb/in.^{2} on the 8- by 12-in. cross section. The axial load varied by at most ±12 percent during testing.

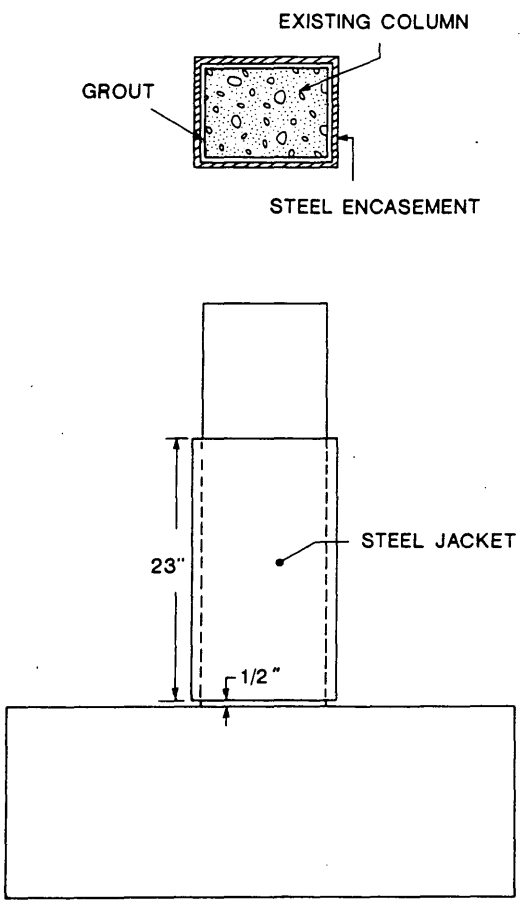

FIGURE 2 Steel jacket retrofit: *top*, plan view; *bottom*, elevation view.

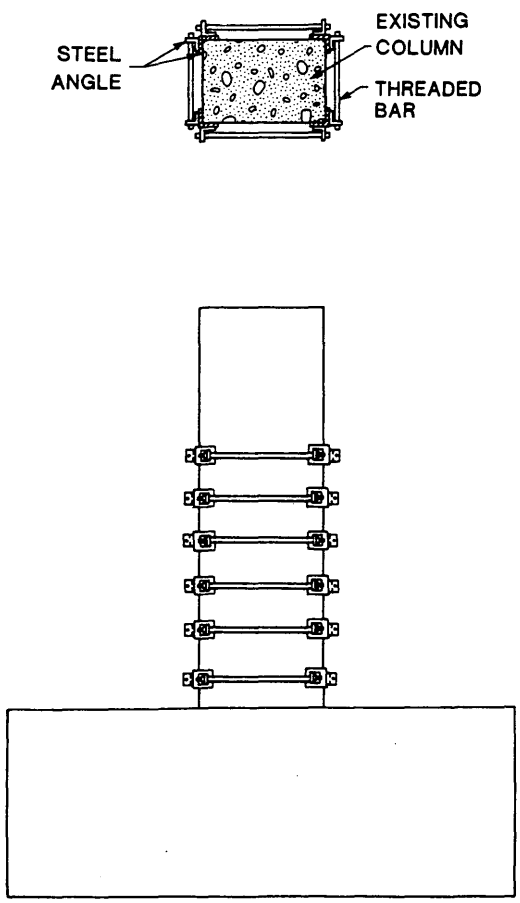

FIGURE 3 Angle and rod retrofit: *top*, plan view; *bottom*, elevation view.

TABLE 1 Column Specimens

SPECIMEN NO.	COLUMN SPECIMEN DESCRIPTION
1	Control
2	Control
3	Angle/rod retrofit, 6 in. o.c.
4	Steel jacket retrofit, 16 gage
5	Angle/rod retrofit, 4 in. o.c.
6	Steel jacket retrofit, 12 gage
7	Steel jacket retrofit, 16 gage with dowels
8	Steel jacket retrofit, 16 gage with epoxy

The cyclic lateral load was applied at 30 in. above the top of the footing by a 55-kip capacity actuator operated under displacement control using a closed-loop servohydraulic system. The sequence used was chosen to display the general hysteretic characteristics and ductility of each specimen and consisted of an increasing displacement pattern to various multiples of the yield displacement of the column. Two cycles were used at each displacement to displacement ductility levels of μ = 1, 2, 4, 6, and 8, unless premature failure of the column occurred.

Determination of the yield displacement, Δ_y, of the column specimens was altered from typical methods [e.g., Priestly and Park (*9*)] because of restrictions associated with the particular columns under study. Use of the conventional method for the shear deficient columns in this research program was not considered feasible because of the probability of a shear failure occurring before ¾ of the flexural capacity was reached. Therefore, an alternate method using an approximate cracked section analysis was used; this method produced a yield displacement of 0.11 in. For the first column test, this value was used; however, it significantly underpredicted the actual yield displacement evident in the experimental data from Column 1. On the basis of this first test, the actual yield displacement was determined to be 0.26 in. This value was used as the Δ_y for all subsequent column tests to subject the control and retrofitted columns to the same displacement history.

Strain gauges were used to monitor the strains of the flexural and transverse reinforcement as well as the external retrofit rods and steel jackets. All data were recorded intermittently throughout the testing sequence.

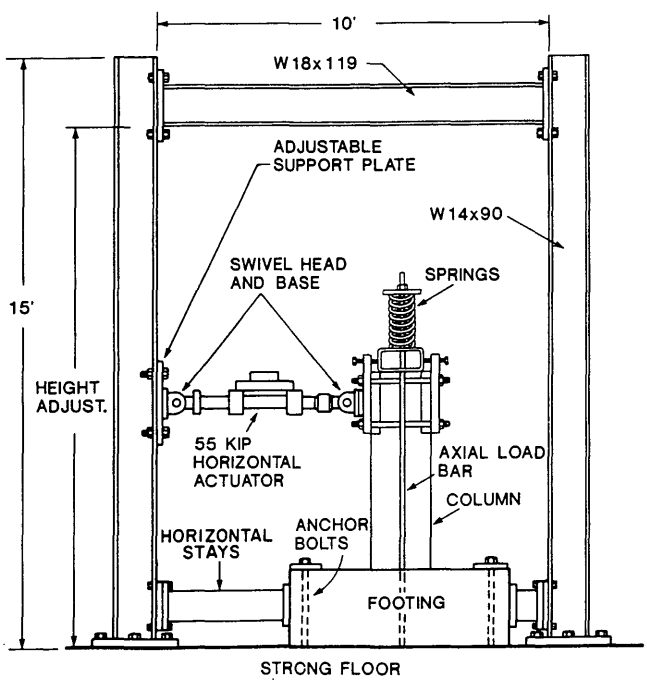

FIGURE 4 Test setup.

TEST RESULTS AND DISCUSSION

In this section, experimental results for the column studies are presented. Results from each specimen are discussed separately to begin with, followed by a discussion of various groups of specimens to facilitate comparisons. Performance of the specimens was mainly evaluated in terms of moment capacity and ductility enhancement along with general hysteretic behavior.

Control Column Test

Column 2, which represented existing field conditions, displayed a classic shear failure with an x-pattern of cracking developing as the testing progressed. The failed control specimen is shown in Figure 5. Results from this column served as the reference for all retrofitted columns. In this specimen, shear cracking and yielding of the ties occurred early on in testing, beginning in the first cycle to 1 Δ_y. Referring to the load-displacement hysteresis shown in Figure 6, there was a sharp degradation in load-carrying capability during the second cycle to 2 Δ_y, after which the load continued to drop until almost no load was carried. This column was evaluated as having a displacement ductility level of μ = 1.

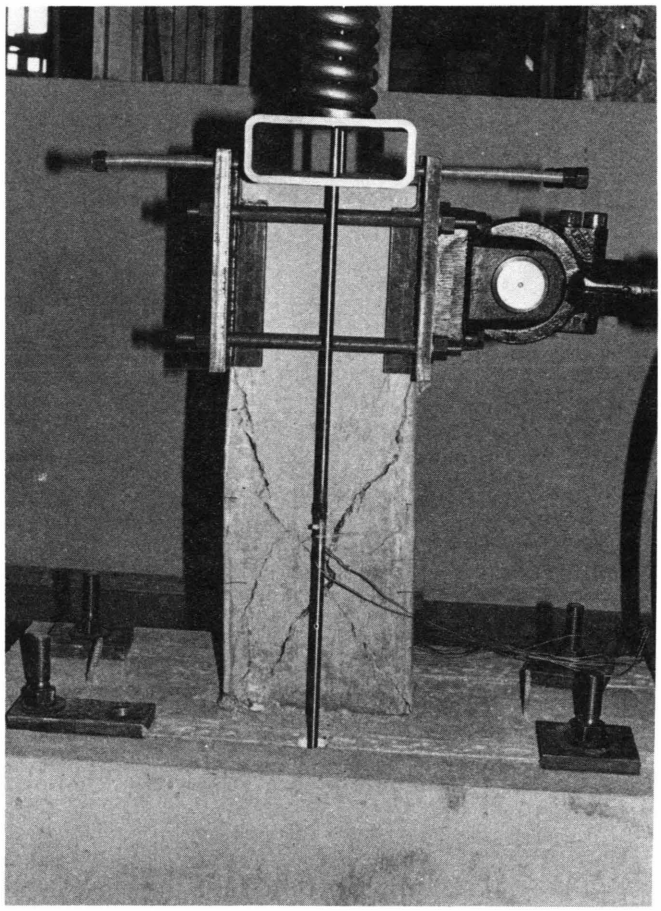

FIGURE 5 Shear cracking in control column specimen.

Angle and Rod Retrofit

Columns 3 and 5 were tested using the angle and rod technique, each with a different spacing between retrofit hoops. For both columns, all bars in the retrofit hoops were uniformly prestressed to 50 percent of the bar's yield stress.

In Column 3, retrofit hoops were used at a spacing of 6 in. on center. During testing, internal tie yielding was observed during the first cycle to 2 Δ_y. At this time displacement level, cracks developed between the corner angles at an inclination of approximately 45 degrees. The load capacity dropped sharply in the first cycle to 4 Δ_y because of brittle fracturing in the threads of the external bars, with failure of the bars beginning at the bottom of the column and working upward. Although a mild steel (A36) was used as the material for the external rods, this was not reflected in the mode of failure. When the retrofit hoops were lost, shear cracks progressively opened up, similar to those observed in the control column. After formation of these large shear cracks, the load capacity continued to drop until almost no load was carried. The lateral load capacity of Column 3 showed an increase of 7 percent over that of the control column because of the addition of the retrofit hoops. A load-displacement hysteresis plot for Column 3 is shown in Figure 7. This column was evaluated as having a ductility of $\mu = 2$.

In Column 5, retrofit hoops were used at a spacing of 4 in. on center. Before this test was conducted, the bars to be used in the retrofit hoops were annealed to produce a material that would respond in a more ductile manner than those used in Column 3. Internal tie yielding did not occur in the testing of Column 5 until the first cycle to 4 Δ_y. Again, shear cracks formed between the corner angles at an inclination of approximately 45 degrees. Column 5, using a smaller spacing

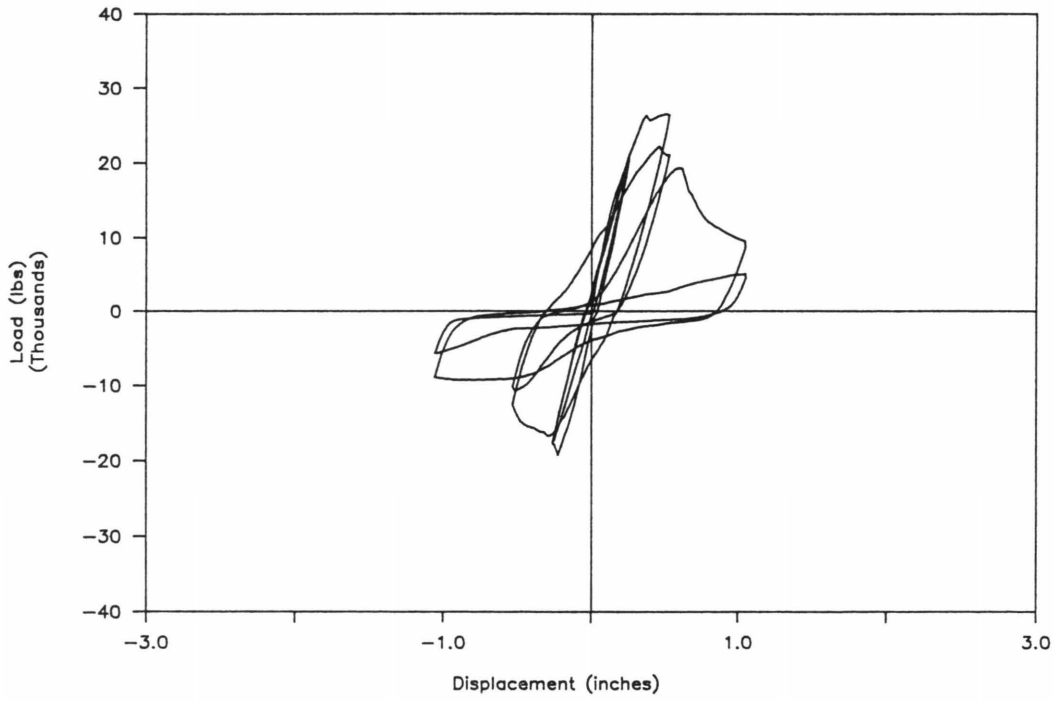

FIGURE 6 Lateral load displacement curves for Specimen 2.

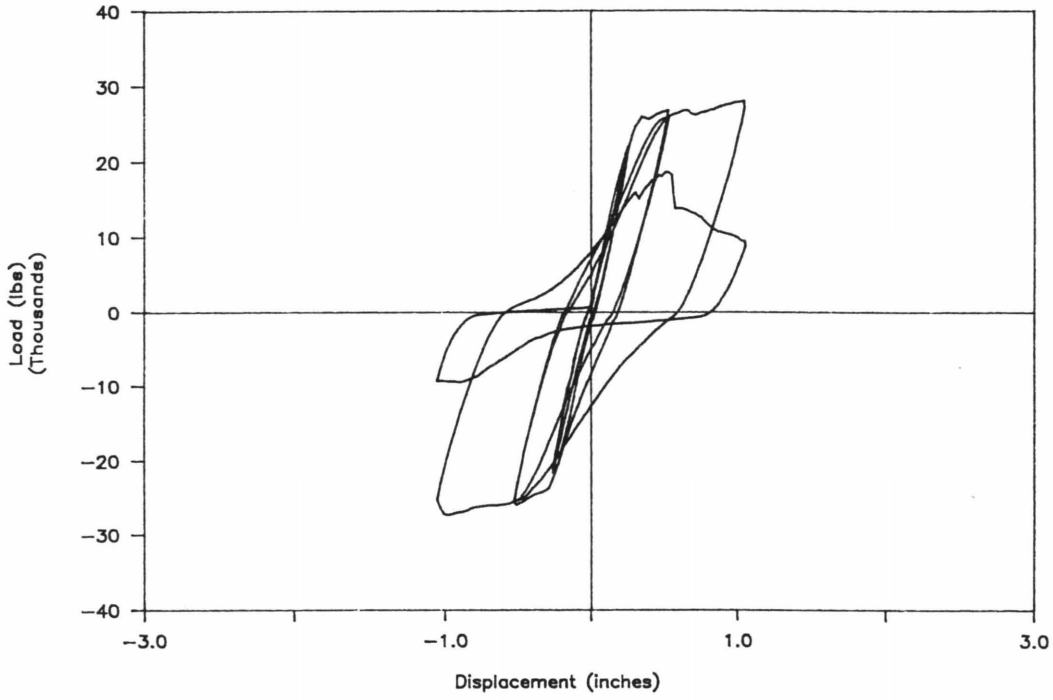

FIGURE 7 Lateral load displacement curves for Specimen 3.

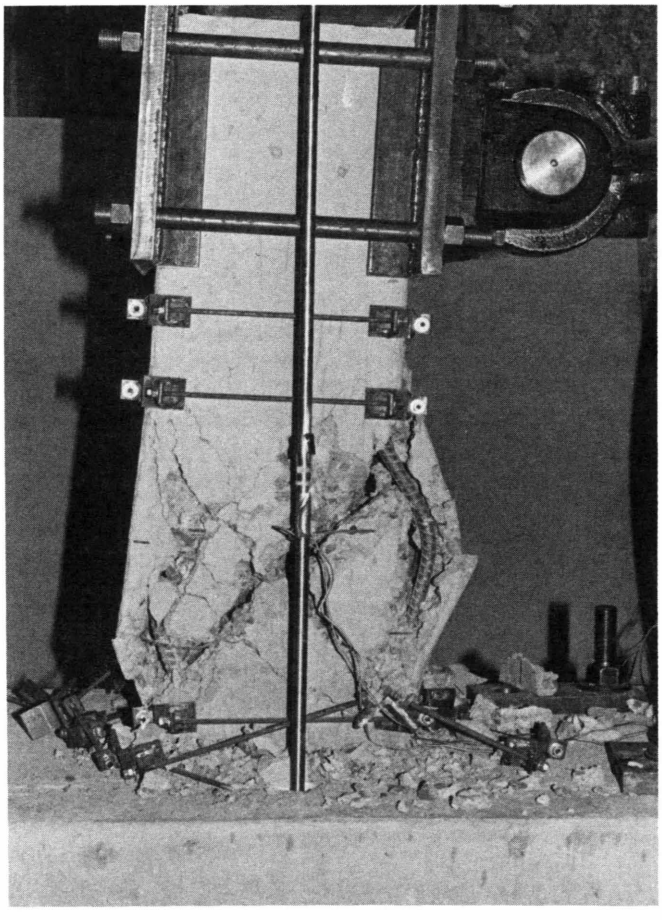

FIGURE 8 Specimen 5 after testing.

between retrofit hoops than in Column 3, held its load into the first cycle to 6 Δ_y, when the external bars began to fail in the threads. However, in this specimen, the bars necked down in a ductile manner before fracturing, with failure of the bars beginning at the middle of the column and working downward. When the retrofit hoops fractured, shear cracks began to open up, as in the control column, followed by a substantial buckling of the longitudinal reinforcement and destruction of the column core (see Figure 8). As with Column 3, the lateral load capacity showed an increase of 7 percent over that of the control column. Column 5 displayed an increase in ductility capacity over that of Column 3, with good performance through $\mu = 4$. A load-displacement hysteresis plot for Column 5 is shown in Figure 9.

This discussion indicates that both columns utilizing the angle and rod retrofit displayed only a moderate amount of improvement in strength and ductility over that of the control column. Column 5, with a smaller spacing between retrofit hoops, resulted in increased ductility capacity and delayed internal tie yielding when compared with Column 3. Both columns showed an increase in lateral load capacity of 7 percent. Of note is the fact that shear cracks developed before fracture of the external hoops, indicating that the mode of failure was not changed from shear to flexure.

With use of this retrofit technique it was expected that the number of retrofit hoops added would increase the shear capacity of the column so that a flexural failure mode would occur. However, the contributions to shear strength from the as-built specimen and the retrofit hoops were not directly additive. This behavior possibly can be explained by limitations in the ductility or elongation of the retrofit bars. As a result, the bars were not able to sufficiently stretch to accommodate the load without fracturing. The use of upset threads

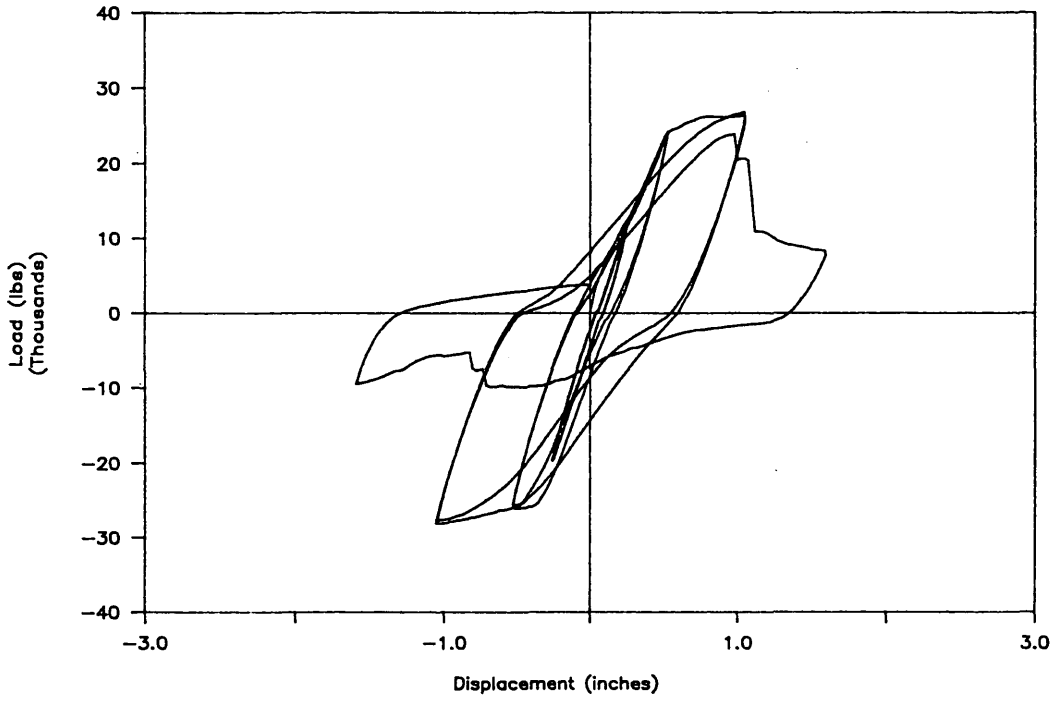

FIGURE 9 Lateral load displacement curves for Specimen 5.

could improve the performance but would significantly increase the cost of the retrofit.

Steel Jacket Retrofit

In the steel jacket retrofit, four columns were tested with variations in the thickness of the steel plate, material in the gap between the existing column and jacket, and confinement near the base of the column.

Column 4, which used a 16-gauge steel jacket with nonshrink cement grout between the existing column and jacket, performed very well under the imposed cyclic loading, with good load-carrying capability through a displacement ductility of $\mu = 8$. A lateral load capacity enhancement of 16 percent was seen in this column when compared with the as-built specimen. From the load-displacement hysteresis plot of Column 4 (Figure 10), it can be seen that the retrofitted column displayed good energy dissipation, and its performance was vastly improved over that of the unretrofitted column. Beginning during cycles to 4 Δ_y, the column longitudinal bars and steel jacket buckled near the base of the column at the maximum moment section. During testing to larger displacement levels, buckling increased, but the jacket continued to provide some confinement to the hinging region. As a result of this confinement, cracks penetrated into the footing because the plastic hinging region was forced downward into the footing. Throughout the testing sequence, there was no evidence of internal tie yielding. After the jacket had been removed, no evidence of any shear cracks was visible in the column.

Column 6, which was retrofitted using a 12-gauge steel jacket and cement grout between the jacket and existing column, also performed well with good load-carrying capability through a ductility of $\mu = 8$. Even though the steel jacket in Column 6 was 75 percent thicker than that in Column 4, the lateral load capacities were the same. From the load-displacement hysteresis plot of Column 6 shown in Figure 11, the width of the loops, which are slightly wider than those in Column 4, indicates good energy dissipation throughout the test sequence. As in Column 4, buckling of the longitudinal bars and steel jacket occurred near the base of the column beginning during the cycles to 4 Δ_y. However, the extent of buckling was slightly reduced by the use of a thicker jacket. Cracking was again seen in the footing around the base of the column because of the downward shifting of the plastic hinge zone. Internal tie yielding was prevented using this retrofit scheme, and no shear cracks were seen in the column after the jacket had been removed.

Column 7, which used a 16-gauge steel jacket, cement grout, and four steel dowels into the column core, showed excellent performance through a ductility of $\mu = 8$. This specimen had a lateral load capacity increase of 19 percent over that of the control column, which was the largest of all columns tested, possibly because of the increased confinement at the plastic hinge. In addition, the use of dowels through the column core near the maximum moment section resulted in an increase in energy dissipation, as seen by the width of the loops in the load-displacement hysteresis plot in Figure 12. These hysteresis loops were the widest of all columns tested. By using dowels through the column core, buckling on one side of the column was essentially eliminated. However, buckling was seen on the other side of Column 7, possibly because of the severing of an internal tie while drilling into the core on this side of the column. As with the other jacketed columns, no shear cracks were seen after removal of the steel jacket, and

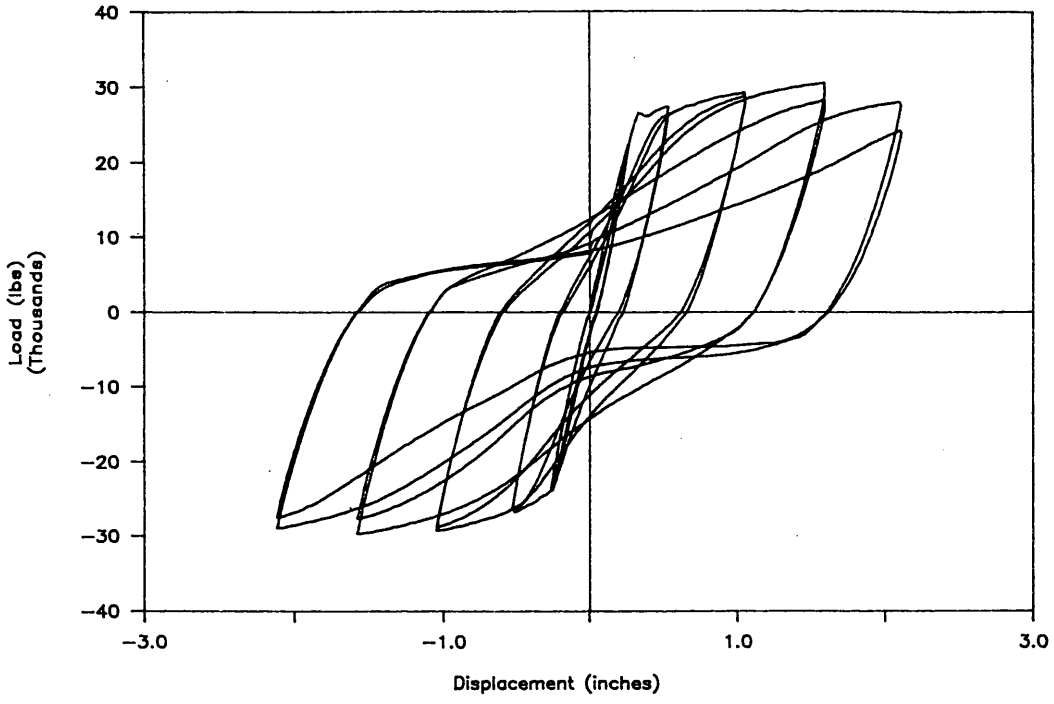

FIGURE 10 Lateral load displacement curves for Specimen 4.

cracking in the footing was seen because of the downward migration of the zone associated with plastic hinging.

In Column 8, which used a 16-gauge steel jacket with epoxy between the jacket and column, very good load-carrying capability was seen though $\mu = 8$. This retrofit resulted in a lateral load capacity increase of 18 percent over that of the control column. In this specimen, tie yielding was prevented throughout the testing sequence, and no shear cracks were seen after the steel jacket had been removed. The load-displacement hysteresis curves of Column 8 (Figure 13) are almost identical to those of Column 6 with the thicker jacket. With the epoxy filler, performance is slightly improved over that in Column 4, which used the cement grout, but not enough to justify the substantially higher cost of the epoxy. The use

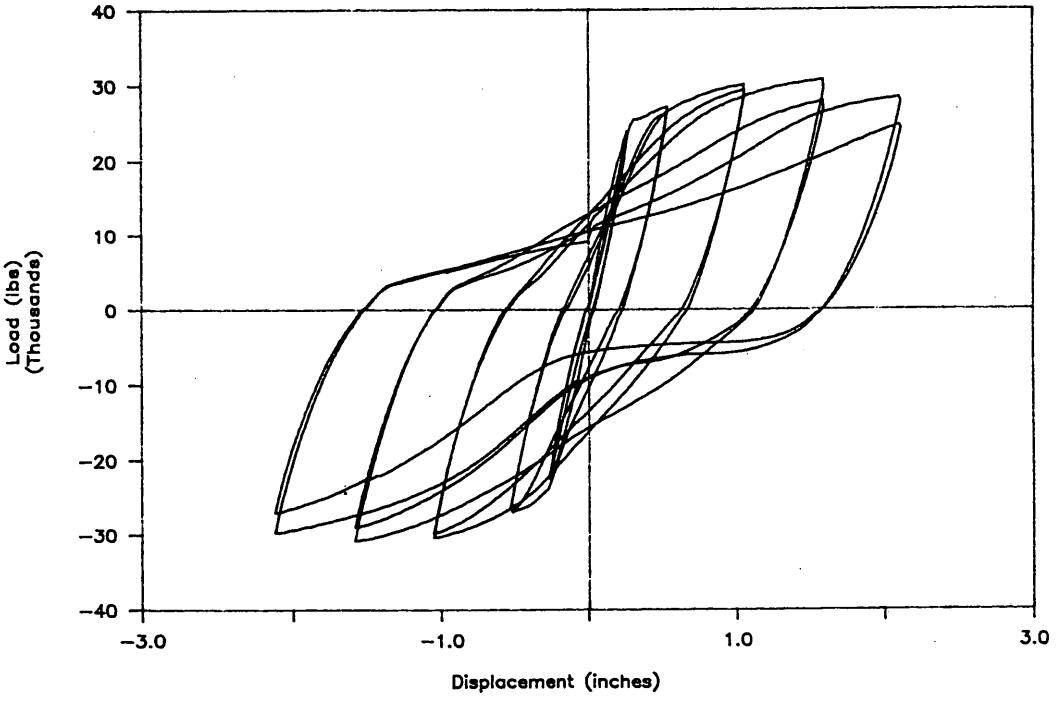

FIGURE 11 Lateral load displacement curves for Specimen 6.

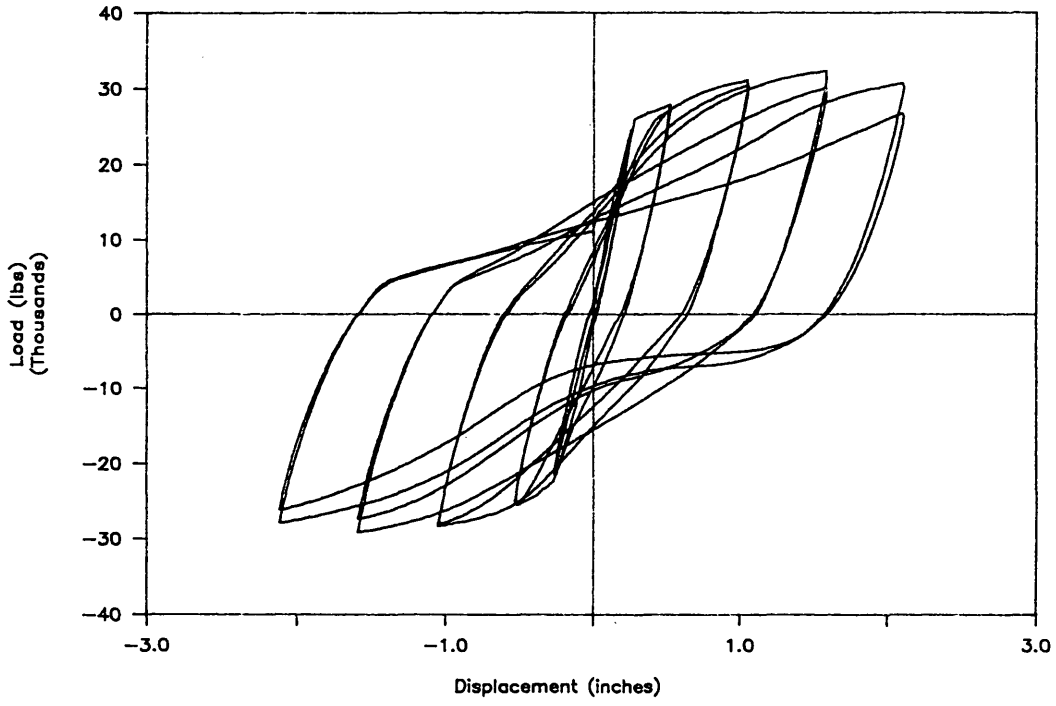

FIGURE 12 Lateral load displacement curves for Specimen 7.

of epoxy between the existing column and jacket significantly delayed buckling of the longitudinal reinforcement and steel jacket, but buckling ultimately reached the same extent as that in Column 6. Cracking of the footing due to shifting of the plastic hinge zone also occurred.

From this discussion it can be seen that all steel-jacketed specimens performed well in improving the strength and ductility capacity of the deficient section. In each column, a ductility of $\mu = 8$ was achieved with good load-carrying capability, after which testing was stopped. Load capacity increases were nearly uniform for all jacketed specimens, ranging from 16 to 19 percent, with the highest value in the specimen incorporating dowels through the column core. In all jacketed columns, initial stiffnesses were only slightly larger than that

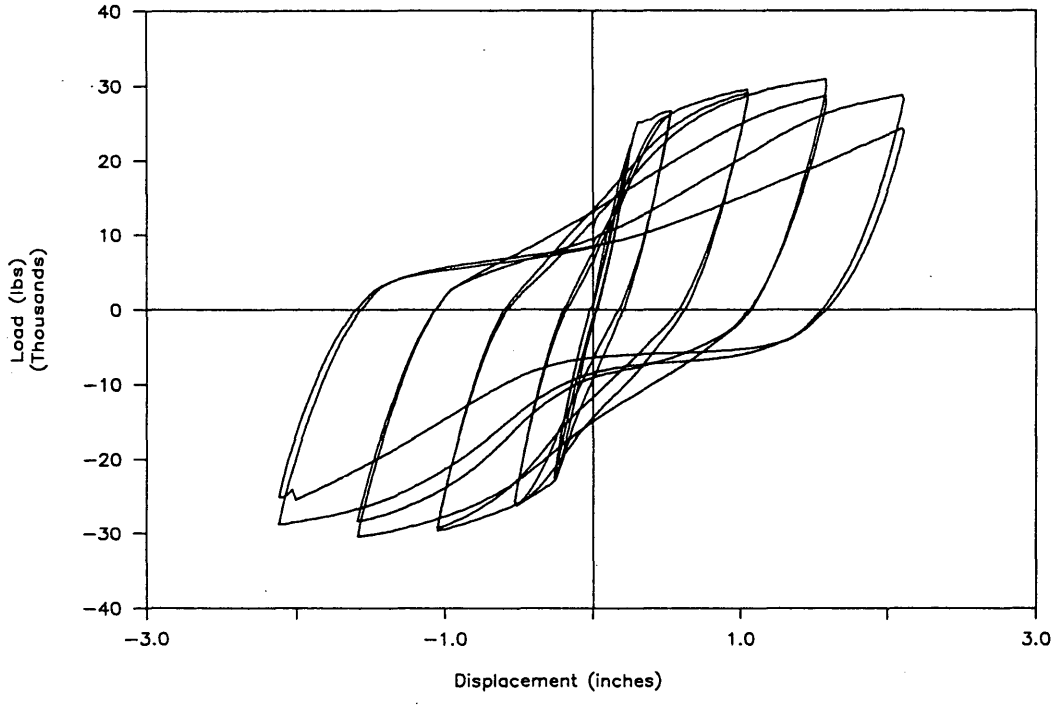

FIGURE 13 Lateral load displacement curves for Specimen 8.

for the control column. Yielding of the internal ties was prevented using this retrofit method. After the steel jackets had been removed at the completion of testing, no shear cracks were seen in any of the columns, indicating that the mode of failure was changed from shear to flexure. The energy absorption characteristics of the jacketed specimens were improved substantially when compared with those seen in Column 2. The use of dowels through the column core at the maximum moment section resulted in the most energy dissipation of all specimens. Increasing the thickness of the steel jacket slightly improved the energy dissipation, as did using the epoxy mixture instead of a nonshrink grout between the column and steel jacket.

Throughout the testing sequence, each steel-jacketed specimen showed some buckling of the longitudinal reinforcement and jacket at the base of the column under the imposed cyclic loading. By using dowels through the column core, buckling was reduced and on one side was essentially eliminated. Although the jackets yielded because of buckling of the longitudinal bars, all jacketed columns maintained some confinement in the hinging region. However, tests by Chai et al. (*3*) have shown that this level of confinement provided by the buckled rectangular steel jacket would be insufficient to prevent strength degradation if an inadequate longitudinal reinforcement splice was present in the plastic hinging region.

CONCLUSIONS

On the basis of the results of this experimental investigation, both the angle and rod retrofits and the steel jacket retrofit were beneficial in improving the seismic performance of shear-deficient rectangular bridge columns. Only moderate improvements in ductility resulted from the application of the angle and rod retrofit. The full-height rectangular steel jacket retrofit provided significant enhancement in lateral load capacity and ductility of the deficient section. Although buckling of the steel jacket at the maximum moment section occurred, sufficient confinement was provided to maintain stable hinging behavior. This buckling was reduced, and specimen performance was improved, by providing dowels through the column core in the maximum moment region. An elliptical or circular shaped jacket used locally in the hinging regions would improve confinement and should be investigated in future research.

ACKNOWLEDGMENTS

The research presented in this paper was funded by the Washington State Transportation Center. The authors acknowledge the valuable contributions of Harvey Coffman and Raymond Shaefer of the Washington State Department of Transportation.

REFERENCES

1. L. L. Bernards. Seismic Retrofitting of Rectangular Reinforced Concrete Bridge Columns For Shear. M.S. thesis. Washington State University, Pullman, 1991.
2. M. J. N. Priestley and F. Seible. Seismic Bridge Damage and Retrofit to Date. *Seismic Assessment and Retrofit of Bridges, SSRP 91/03*, pp. 13–26.
3. Y. H. Chai, M. J. N. Priestley, and F. Seible. Retrofit of Bridge Columns for Enhanced Seismic Performance. *Seismic Assessment and Retrofit of Bridges, SSRP 91/03*, pp. 177–196.
4. H. L. Coffman, M. L. Marsh, and C. B. Brown. Seismic Durability of Retrofitted RC Columns. *Journal of the Structural Division*, ASCE (in press).
5. B. J. Bett, R. E. Klingner, and J. O. Jirsa. Lateral Load Response of Strengthened and Repaired Reinforced Concrete Columns. *ACI Structural Journal*, Vol. 85, No. 5, Sept.–Oct. 1988, pp. 499–508.
6. B. J. Bett, R. E. Klingner, and J. O. Jirsa. Behavior of Strengthened and/or Repaired Reinforced Concrete Columns Under Reversed Cyclic Deformations. Department of Civil Engineering, University of Texas, Austin, 1984.
7. M. J. N. Priestley. Flexural Test of a High Strength Fiber Retrofitted Column. Preliminary Report No. 1. Fyfe Associates, Inc.; Seqad Consulting Engineers, Nov. 1990.
8. *CALTRANS Seismic Design References*. California Department of Transportation, June 1990.
9. M. J. N. Priestley and R. Park. Strength and Ductility of Concrete Bridge Columns Under Seismic Loading. *ACI Structural Journal*, Vol. 84, No. 1, Jan.–Feb. 1987, pp. 61–76.

Publication of this paper sponsored by Committee on Dynamics and Field Testing of Bridges.

Proof Load Formula for Highway Bridge Rating

GONGKANG FU AND JIANGUO TANG

A proof load formula is proposed for highway bridge evaluation through proof load testing to determine target proof load and load rating. This formula is based on a target structural safety index β of 2.3, which is consistent with current bridge evaluation practice and also with an evaluation method of load and resistance factors under development. It is demonstrated that the proposed formula will ensure a relatively uniform level of bridge structural safety and that possible changes in input data and probability distribution assumptions in the reliability models will not affect the results obtained. This formula can be applied to highway bridge evaluation by proof load testing, and the resulting rating can be directly input to the current national bridge rating inventory. The formula may be included in specifications for highway bridge evaluation by proof testing.

According to FHWA, about 40 percent of this country's highway bridges are considered either structurally deficient or functionally obsolete. Some 68 percent of New York State's bridges fall into these categories, representing the highest percentage among the states. Funds necessary to replace and rehabilitate them will not be available in the foreseeable future. Major factors contributing to this serious situation are age of the infrastructure, increases in both volume and weight of vehicular loads, environmental contamination, and inadequate maintenance (*1*).

These statistics are based on current evaluation technology. For existing bridge structures, AASHTO's *Manual for Maintenance Inspection of Bridges* (*2*), referred to here as "the AASHTO manual," provides technical guidelines for routine analytical evaluation on the basis of data supplemented by field inspection. However, such an analytical evaluation often is not applicable because of inaccessibility of bridge structural components due to their locations or protection methods or lack of detailed information such as design plans of bridges, or both. When a bridge is evaluated by physical testing, many assumptions critical to analytical evaluation methods may be unnecessary. In addition, in many cases, physical testing may be the only way to obtain a reliable rating; it has proved effective in many parts of the world (*3–5*). The results have also demonstrated higher load-carrying capacity than predicted by conventional analytical methods. This is often attributed to (a) generally conservative analytical methods and (b) structural system effects not covered by simplified analytical methods that usually address only behavior of structural components. Despite these advantages of physical testing in bridge evaluation, the current AASHTO Manual does not include provisions for field testing to evaluate highway bridges.

Engineering Research and Development Bureau, New York State Department of Transportation, State Campus, Albany, N.Y. 12232.

This paper presents partial results of a study sponsored by FHWA to develop and evaluate a proof load testing program for bridge evaluation. This study was undertaken based on recognition that proof load testing is one of the most effective approaches to examine structural load-carrying capacity. Development of a consistent method for determining both target proof load and load rating is a major focus here, based on a criterion of target structural reliability. The theory of structural reliability has been employed elsewhere to develop codes of structural design and evaluation (*6–9*). This theory has been recognized as an effective and realistic means to address unavoidable random variations of physical quantities used in structural engineering decision making. Recently, a load and resistance factor methodology for bridge evaluation, based on the same theory, has been adopted by AASHTO in guide specifications (*8*). This study attempts to be consistent with the concept used there in prescribing target proof load levels. The proposed proof load levels are intended to apply to evaluation of short- and medium-span highway bridges whose response is governed by vehicular loading.

PROOF LOAD FORMULA FOR BRIDGE RATING

A proof load formula is proposed as follows, in the load and resistance factor format,

$$\phi\, Y_p = \alpha_L L_n g_n I_n \tag{1}$$

where

Y_p = target proof load effect,
L_n = nominal static live load effect,
g_n = nominal load distribution factor,
I_n = impact factor accounting for dynamic effects of vehicular loading, and
ϕ, α_L = resistance reduction and live-load factors, respectively.

L_n, g_n, and I_n are specified by AASHTO (*8*) and are respectively based on the current AASHTO rating vehicles with a lane load, empirical estimations, and road surface roughness. Load and resistance factors are to be determined in this study based on a structural reliability criterion. In addition to determining target proof load, the proposed formula is also intended to be used for rating through proof load testing:

$$\text{rating factor} = \phi R_p/\alpha_L L_n g_n I_n = R_p/Y_p \tag{2}$$

where R_p is proved capacity for live load equaling or lower than the target value Y_p. This rating methodology is consistent

with the current rating method given by AASHTO in both concept and format (*2*). Only bending moment as load effect is considered in this paper, although Equations 1 and 2 are in general forms.

STRUCTURAL RELIABILITY MODELS FOR BRIDGE PROOF TESTING

Safety Index and Target Level

Consider a limit state function Z for a typical primary bridge member (e.g., a girder):

$$Z = R - D - L = R' - L \tag{3}$$

where R, D, and L are true values of resistance, dead load, and live load effects, respectively, and $R' = R - D$ is a resistance margin for live load. Considering uncertainties and random variation associated with these quantities, R' and L are modeled by independent random variables that are assumed to be of lognormal distribution. The uncertainties are attributed to such factors as fluctuation of vehicular load, variation of material properties and construction quality, and scatter caused by simplified analysis methods. The mean and standard deviation of R', $M_{R'}$, and $\sigma_{R'}$, are given by means and standard deviations of R and D:

$$M_{R'} = M_R - M_D$$

$$\sigma_{R'}^2 = \sigma_R^2 + \sigma_D^2 \tag{4}$$

on the basis of an assumption that R and D are independent of one another. Z equaling or lower than 0 indicates failure of the member, and a value higher than 0 means survival. The live-load effect is further modeled by a combination of the following factors (*7*):

$$L = a\, HW_{.95} m g I \tag{5}$$

where all variables are modeled by independent lognormal random variables except a, which is a deterministic coefficient correlating truck weight to bending moment as load effect based on AASHTO rating vehicles (*2*). H is a factor accounting for multiple presence of vehicles on the bridge, and $W_{.95}$ is a characteristic value of the vehicle weight spectrum; their product is treated here as a single variable. m covers effect of vehicle configuration variation on the load effect, g is a lateral distribution factor, and I is an impact factor for dynamic effect. $HW_{.95}$ and m refer to characteristics of traffic load, and I addresses interaction of traffic and bridge structure. They may not be determined in a proof test with acceptable accuracy. On the other hand, g may be obtained by a proof test since it is largely a function of the structure. However, its accuracy depends very much on test procedures used and efforts affordable, which may vary considerably in practice. To be conservative, g is also modeled here by a random variable.

Structural reliability is often measured by its complement, failure probability P_f, of the component:

$$P_f = \text{probability}\,[Z \leq 0] \tag{6}$$

If Z were a normal random variable, which can be a linear combination of normal variables, then

$$P_f = 1 - \Phi(\beta) = 1 - \Phi(M_Z/\sigma_Z) \tag{7}$$

where $\Phi(\ )$ is the cumulative probability function of the standard normal variable, and β is called safety index. In this study Z defined in Equation 3 is not a linear combination of normal variables. However, it can be linearized (by a polynomial series expansion of first order) and variables R', m, $HW_{.95}$, g, and I transformed (equivalently in failure probability) to normal variables at a point known as the design point in the variable space. Equation 6 can then be used to calculate the safety index after linearization and transformation, about which the reader is referred to Ang and Tang (*10*) for more computation details.

It has been estimated that current bridge evaluation practice by the AASHTO Manual assures a reliability level of the safety index of about 2.3 for primary components (*6,7*). $\beta = 2.3$ is thus used here as the target safety level for this study to prescribe the target proof load level, because only redundant structures are addressed here. This criterion is consistent with that used in development of the AASHTO *Guide Specifications for Strength Evaluation of Existing Steel and Concrete Bridges* (*8*). The same target safety index also has been used for development of a permit overload checking method (*11*). The target value will not be hit exactly for every case of application, and thus certain variation in resulted β is expected.

Proof Load Testing with Analytical Rating

Proof load testing has an important application in verifying or enhancing an existing rating obtained by analytical methods. This need emerges when the existing rating factor RF is not satisfactory—namely, lower than the required 1.0. For this case, it is advantageous to use the existing rating for modeling resistance. Nominal resistance R_n related to the existing rating factor RF is obtained by an analytical evaluation

$$\phi\, R_n = \gamma_D\, D_n + \gamma_L\, L_n\, g_n\, I_n\, RF \tag{8}$$

where D_n is nominal dead load effect, and ϕ, γ_D, and γ_L, respectively, are resistance-reduction, dead-load, and live-load factors given by AASHTO (*8*). Resistance R is thus assumed to have a mean M_R related to its nominal value R_n by a bias B_R, as follows:

$$M_R = B_R R_n \tag{9}$$

A proof load test eliminates possibilities that the true resistance margin R' is lower than the applied proof load Y_p. This is shown in Figure 1 by truncating and then normalizing the probability density function of R' at Y_p. Thus the limit state function takes the following form:

$$Z = R' - a\, m\, HW_{.95}\, g\, I \tag{10}$$

where R' has a truncated lognormal distribution. A method developed by Fujino and Lind (*12*) is used here to calculate the safety index for this case. This method transforms R' to

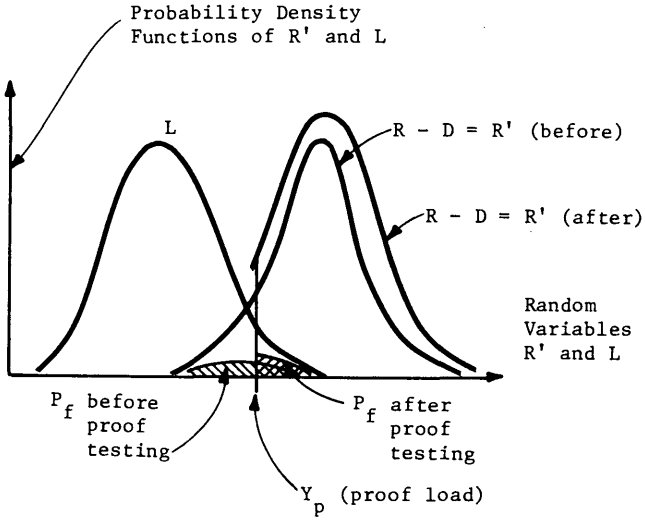

FIGURE 1 Structural reliability model for proof load testing with information on resistance *R*.

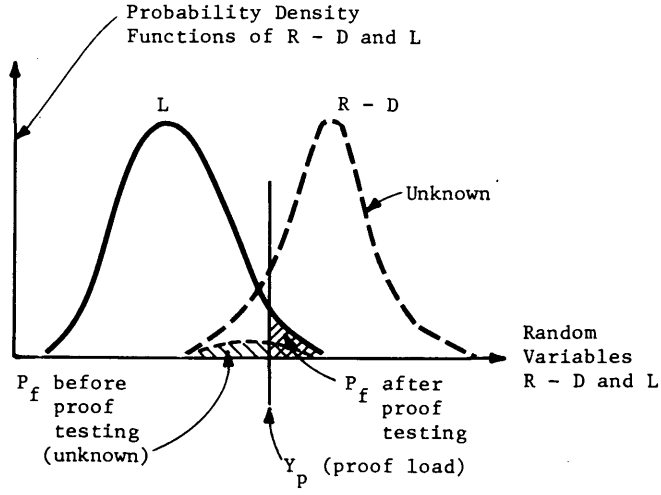

FIGURE 2 Structural reliability model for proof load testing without information on resistance *R*.

a standard normal variable by equivalence in probability. The limit function is transformed accordingly, providing a basis for calculating the safety index. This method has been compared with a direct integration method over a wide range of parameter variation for practical applications. Consistency has been observed in results obtained by the two methods (*13*).

Proof Load Testing Without Analytical Rating

Proof load testing is often desired also for bridge evaluation when a bridge is not suitable for rating by analytical methods. This occurs when necessary information on the bridge or reliable analysis methods are not available. R' is thus assumed to be equal to the applied proof load effect Y_p if the bridge survives the proof test, since no further information on R' is available. Therefore

$$Z = Y_p - L = Y_p - a\,m\,HW_{.95}\,g\,I \tag{11}$$

is used to calculate the safety index β for this case. The assumption $R' = Y_p$ underestimates the resistance conservatively, because it certainly can be higher than Y_p. A graphic demonstration of the proof testing effect on structural reliability for this case is shown in Figure 2. One can find a Y_p by satisfying a target structural reliability.

Statistical Data Base for Bridge Structural Reliability Models

Substantial statistical data collection has occurred for bridge structural reliability assessment (*7,14–18*). Table 1 contains a comprehensive data base used in this study as input to these reliability models, with information sources identified. It includes mean or bias (ratio of mean to nominal value), and coefficient of variation (COV, as ratio of standard deviation to mean). Three types of construction material are considered here: steel, reinforced concrete (RC), and prestressed concrete (PC), which covers a reasonably wide range of highway bridges in this country. The live-load parameters cover traffic load variation for a period of 2 years, to be consistent with the current maximal inspection interval. The four traffic conditions characterizing the live (vehicular) load are defined by AASHTO (*8*). This classification permits evaluation engineers to take site-specific loading conditions into account in rating bridges. The nominal dead load effect D_n used in Equation 8 is estimated by its empirical relations to live load effect L_{HS20} based on the HS-20 loading. These relations are also listed in Table 1 with sources identified. Note that the mean and COV of R in Table 1 are intended to cover minor deterioration of structural components caused by factors such as steel corrosion, concrete spalling, and prestress loss. They are used in β-calculation for the application case of proof testing only with the analytical rating, where it is usually desired to take deterioration into account for a more reliable rating by proof testing. They differ from those for components in good condition (*7,17*), to represent average strength decrease (by lower bias values) and uncertainty increase (by higher COV values) caused by deterioration. These values are selected here on the basis of subjective estimates, since no data are available. Implications of their use are examined in a sensitivity analysis presented later.

The data base in Table 1 is a summary of data collected by a variety of techniques, including field measurement for member dimensions, weigh-truck-in-motion for the real load spectrum, and empirical regression for a ratio of live to dead load. This data base is considered typical in covering the statistical variation of current practice and traffic loadings in the United States.

TABLE 1 Statistical Data Base for Structural Reliability Assessment

Random Variable[a]	Span Length (ft)	Mean	COV (%)
m	30	1.0	11.0
	40	1.0	11.0
	50	0.95	11.0
	60	0.92	11.0
	70	0.90	11.0
	80	0.91	8.2
	90	0.92	7.5
	100	0.93	5.7
	120	0.95	5.4
	140	0.95	4.6
	160	0.96	3.4
	180	0.97	3.9
	200	0.97	3.2

Random Variable[a]	Traffic Condition	Combinations, Singles	Combinations, Singles
$HW_{0.95}$	1	170 kips, 92 kips	5.0, 8.0
	2	180 kips, 100 kips	6.0, 8.0
	3	210 kips, 120 kips	10.0, 10.0
	4	225 kips, 125 kips	10.0, 10.0

Random Variable[a]	Surface Roughness	Mean	COV (%)
I	Smooth	1.1	10.0
	Medium	1.2	10.0
	Rough	1.3	10.0

	Bias			COV (%)		
Random Variable[a]	Steel	Reinforced Concrete	Prestressed Concrete	Steel	Reinforced Concrete	Prestressed Concrete
R	1.05[a]	1.05	1.0	16[a]	14[a]	11
D	1.0[a]	1.0	1.0[a]	10[a]	10[c]	10[a]
g	0.9[a]	0.97[b]	0.96[a]	13[a]	11[b]	8[a]

Notes: COV = standard deviation/mean, Bias = mean/nominal, SL = span length (ft)

$$D_n/(L_{HS20}\ I_n) = \begin{cases} 0.0132 \times SL \text{ (for steel, from Ref. 19)} \\ 0.6967 - 0.00762 \times SL + 0.0001554 \times SL \times SL \text{ (for reinforced concrete, from Ref. 17)} \\ 0.014 \times SL \text{ (for prestressed concrete, from Ref. 20)} \end{cases}$$

[a]From Ref. 7.
[b]From Ref. 18.
[c]From Ref. 17.

PROOF LOAD FACTORS BASED ON TARGET STRUCTURAL RELIABILITY

To be consistent with bridge evaluation practice by current analytical methods (*2*) and the recently developed method of load and resistance factors (*8*), the resistance reduction factor ϕ is proposed to be 0.95, 0.9, and 0.95, respectively, for steel, reinforced concrete, and prestressed concrete materials. Thus α_L is the only factor in the proof load formula (Equation 1), to be determined to reach the target safety index of 2.3. Given an α_L, Y_p determined by Equation 1 is used in limit state functions for Equations 10 and 11, respectively, for the two application cases of proof load testing. Their safety indexes are then calculated to be compared with the target value of 2.3. This mechanism allows selection of α_L to satisfy the requirement for structural reliability. For a given α_L, β varies with traffic loading condition, span length, and material type. Thus for each traffic loading condition, α_L is selected by minimizing β's variation as a result of other factors.

For application of proof load testing when an analytical rating exists, Figure 3 shows the relation of required α_L to reach uniformly the target safety index 2.3 and existing rating factor RF. The lower the original rating, the higher the proof load would have to be to reach the same target safety level. This is expected, since the higher proof load is needed to reduce the greater failure risk characterized by a lower rating factor. It is also seen in Figure 3 that when rating factor RF equals or is lower than 0.7, variation of α_L with the RF be-

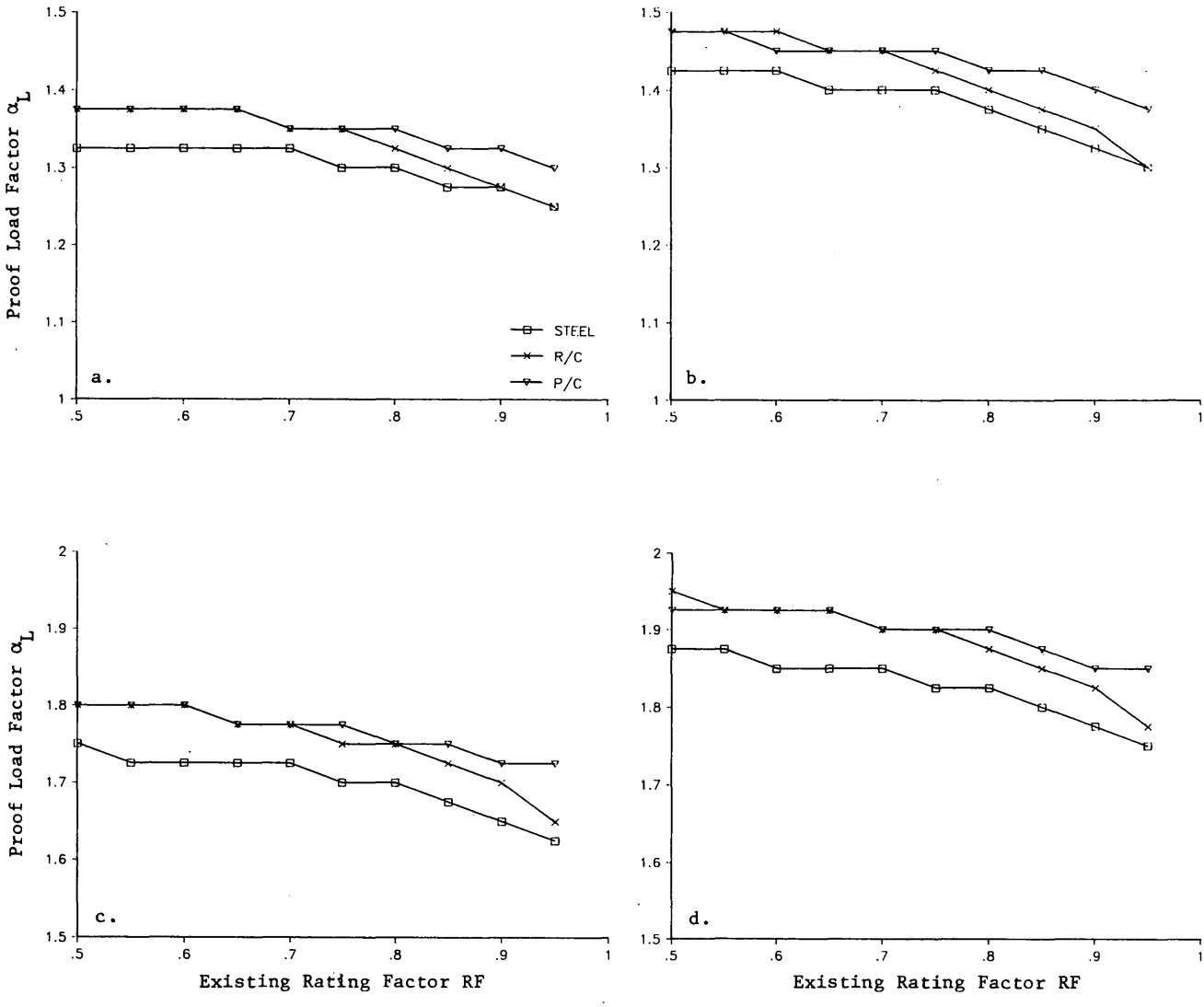

FIGURE 3 Required proof load factors α_L for existing rating factor RF: Traffic Conditions 1 (*a*), 2 (*b*), 3 (*c*), and 4 (*d*).

comes less significant, regardless of traffic loading conditions. Thus, RF equal to 0.7 is selected as a threshold whether to take into account the existing rating in determining target proof load. In other words, when an existing rating factor is higher than 0.7, it is considered an important piece of information to be included in selecting the target proof load level, but lower than 0.7, it is not worth being considered. By this criterion, the proof load factor α_L is proposed in Table 2 for the case of proof load testing with an analytical rating factor equaling or exceeding 0.7. Figure 4 shows safety index β using the proposed load and resistance factors for this case. As shown, they produce a relatively uniform reliability level of safety index equal to 2.3. Note that reinforced concrete bridges have significantly different ratios of live to dead loads than steel and prestressed concrete bridges. This is a major factor, causing safety indexes to be higher for reinforced concrete bridges than for the other two types of bridge, especially for longer spans. Its reliability assessment is not performed for spans longer than 100 ft, because the available empirical ratio of dead to live load is considered valid only up to this span length, and few RC highway bridges in the United States exceed this span length.

For the application case when a rating factor is not available, Table 3 contains a proposed proof load factor α_L for the four categories of live-load traffic. These factors are higher than those for the previous application case, because less information is required to reach the same target safety level. Figure 5 shows the safety index assured by the proposed proof load factor for this case. It is seen that a relatively uniform safety level 2.3 is realized with respect to span length. In this application case, differences in β for various materials are lower than those in the previous case. This is because the dead-load influence on β is eliminated, as it no longer appears in the limit function (Equation 11).

When an existing rating factor is lower than 0.7, the live-load factors in Table 3 can be used to determine required

TABLE 2 Proposed Live Load Factor α_L for Proof Testing with Existing Analytical Rating Factor RF $\geq$ 0.7

Traffic Condition	Live Load Category	Proposed α_L
1	Low volume roadways (ADTT less than 1000), reasonable enforcement and apparent control of overloads	1.35
2	Heavy volume roadways (ADTT greater than 1000), reasonable enforcement and apparent control of overloads	1.45
3	Low volume roadways (ADTT less than 1000), significant sources of overloads without effective enforcement	1.80
4	Heavy volume roadways (ADTT greater than 1000), significant sources of overloads without effective enforcement	1.90

Note: ADTT = Average Daily Truck Traffic

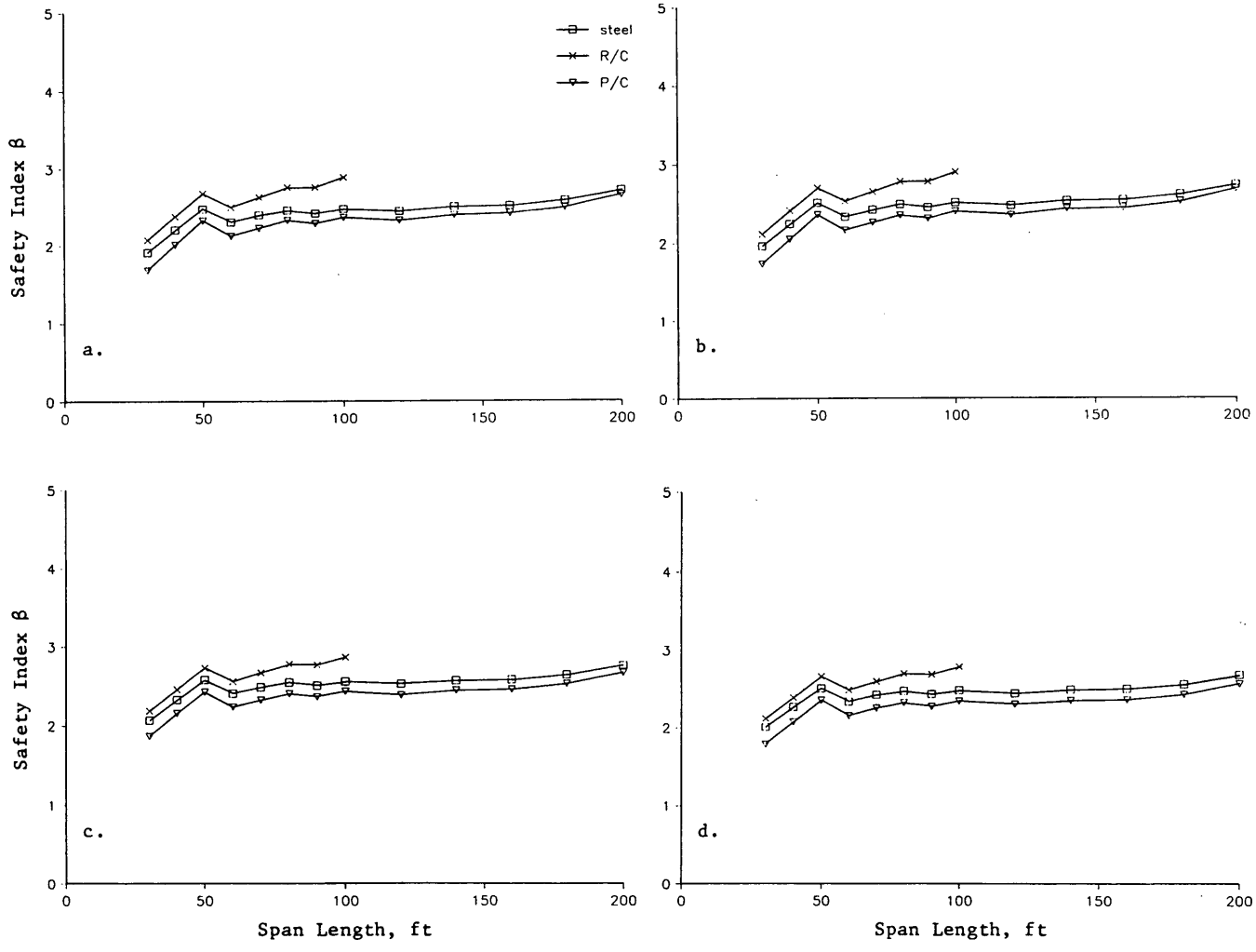

FIGURE 4 Structural reliability based on proposed proof load formula, with analytical rating: *a*, Traffic Condition 1, α_L = 1.35; *b*, Traffic Condition 2, α_L = 1.45; *c*, Traffic Condition 3, α_L = 1.80; *d*, Traffic Condition 4, α_L = 1.90.

TABLE 3 Proposed Live Load Factor α_L for Proof Testing Without Analytical Rating or Existing Rating Factor RF < 0.7

Traffic Condition	Live Load Category	Proposed α_L
1	Low volume roadways (ADTT less than 1000), reasonable enforcement and apparent control of overloads	1.45
2	Heavy volume roadways (ADTT greater than 1000), reasonable enforcement and apparent control of overloads	1.55
3	Low volume roadways (ADTT less than 1000), significant sources of overloads without effective enforcement	1.90
4	Heavy volume roadways (ADTT greater than 1000), significant sources of overloads without effective enforcement	2.00

Note: ADTT = Average Daily Truck Traffic

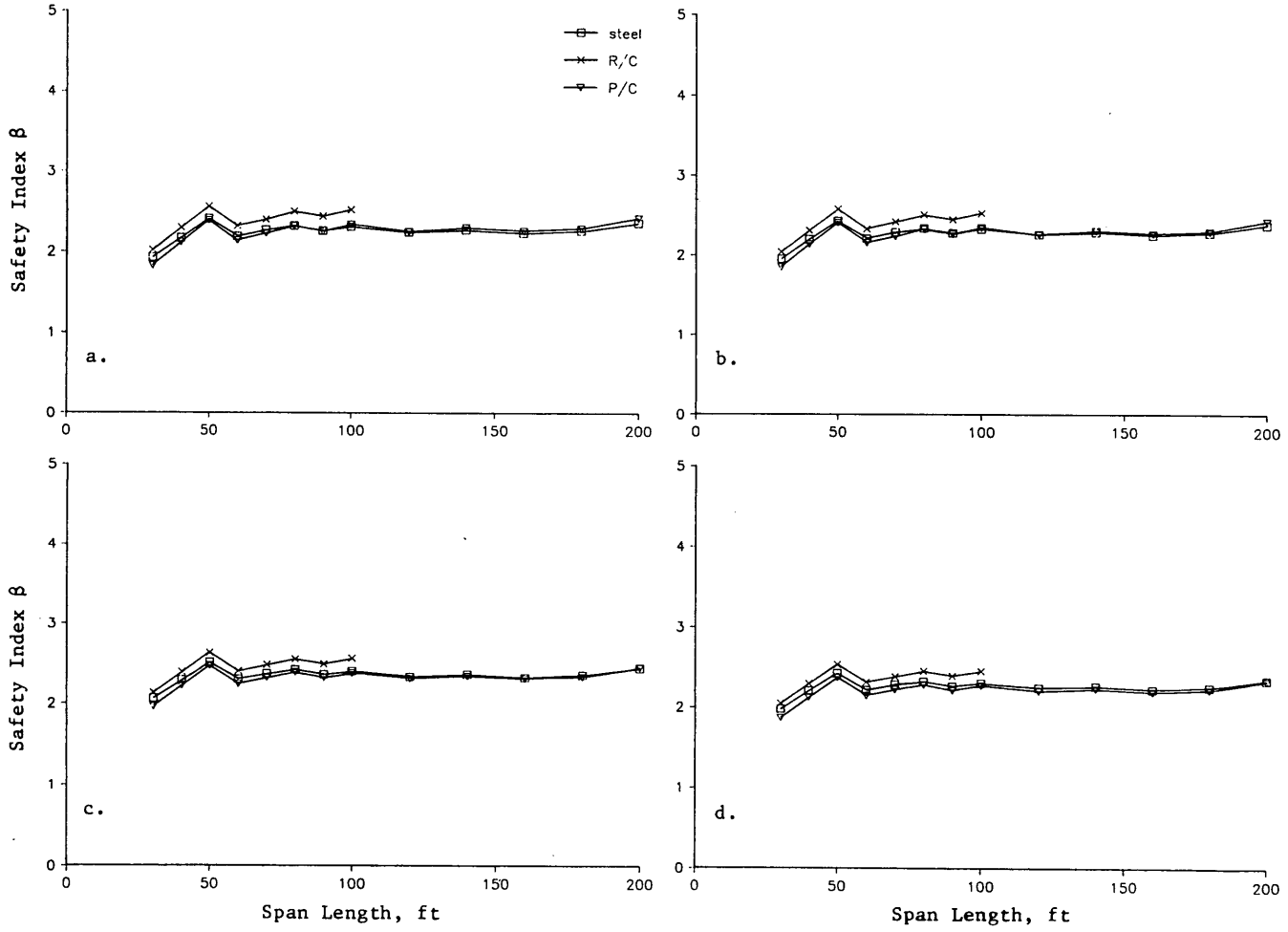

FIGURE 5 Structural reliability based on proposed proof load formula, without analytical rating: *a*, Traffic Condition 1, α_L = 1.45; *b*, Traffic Condition 2, α_L = 1.55; *c*, Traffic Condition 3, α_L = 1.90; *d*, Traffic Condition 4, α_L = 2.00.

target proof load and load rating by proof load testing. They are the maximum proof load levels needed for bridge rating to ensure the target reliability level and do not depend on any a priori information about the bridge's capacity. Other cases have also been checked to ensure the required safety level by the proposed proof load factors, such as nonredundant structures, continuous spans, and posting practice.

SENSITIVITY ANALYSIS

The input data and certain assumptions in modeling and calculation just described may influence the obtained safety index and, in turn, affect the proposed proof load factors. A sensitivity analysis thus is warranted in this exercise of code calibration based on structural reliability. Its purpose is to ensure that reasonable changes in input data and assumptions will not affect uniformity in reliability level and will satisfy appropriate target safety levels reached by the proposed proof load formula.

The assumption of random variable lognormal distribution is examined first. Figure 6 displays the safety index β for cases in which one of the random variables is modeled by a normal, instead of lognormal, variable for the case of steel bridges under Traffic Condition 1. It shows that a different probability distribution assumption has little influence on the safety index, and thus the assumption of lognormal distribution is not critical to the results obtained.

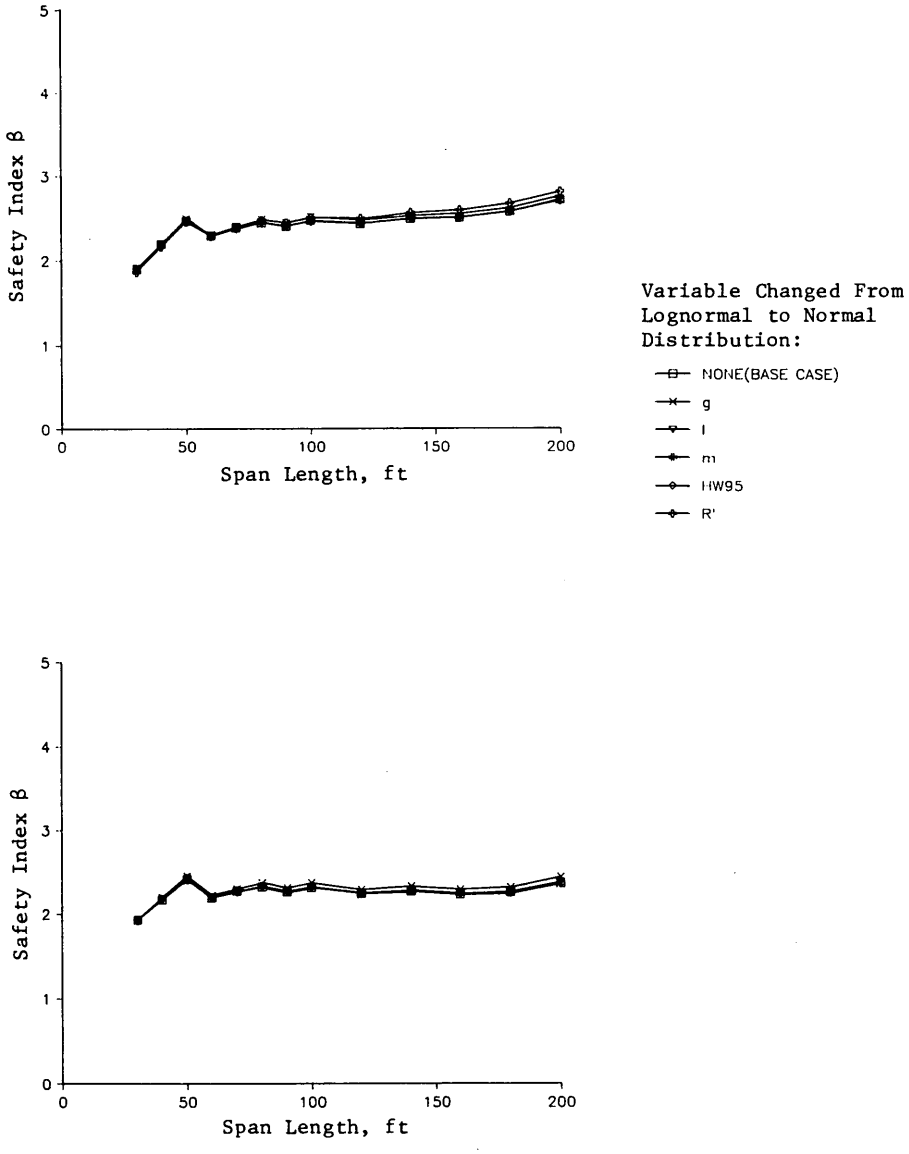

FIGURE 6 Sensitivity of β to probability distribution assumption (steel, Traffic Condition 1): *top*, with analytical rating; *bottom*, without analytical rating.

Figure 7 demonstrates sensitivity of the safety index to bias and COV of R (B_R and V_R) for the application case with analytical rating factor equaling or exceeding 0.7. It is seen in Figure 7 (*bottom*) that higher V_R leads to higher β, especially for shorter spans. This is because the higher scatter in R increases scatter of $R' = R - D$ for shorter spans where the dead-load effect is insignificant, and truncating the distribution of R' by proof testing is more effective to reduce failure risk. For longer spans, the dead-load effect is more dominant and thus higher scatter of R does not significantly increase scatter of R'. Figure 7 also shows that neither B_R nor V_R significantly affects the safety level. Figure 8 shows that the same conclusion applies to the bias and COV of dead-load effect D (B_D and V_D), since they have even lower influence on β than B_R and V_R, respectively. Note that parameters of R and D do not affect β at all in the second application case without analytical rating because information on them is not needed for β calculation using Equation 11.

The lateral distribution factor g has the highest influence on reliability index β among the factors in live-load effect L, because it has the highest COV for most of the cases considered. Thus sensitivity of β to g is discussed here. Figure 9 (*top* and *middle*) shows safety index for the two application cases of proof testing with bias of g (B_g) perturbed. As indicated in the figure, the change of B_g has little influence on the uniformity assured by the proposed proof load formula. On the other hand, this change does affect the level of absolute reliability. Figure 9 (*bottom*) exhibits β produced by

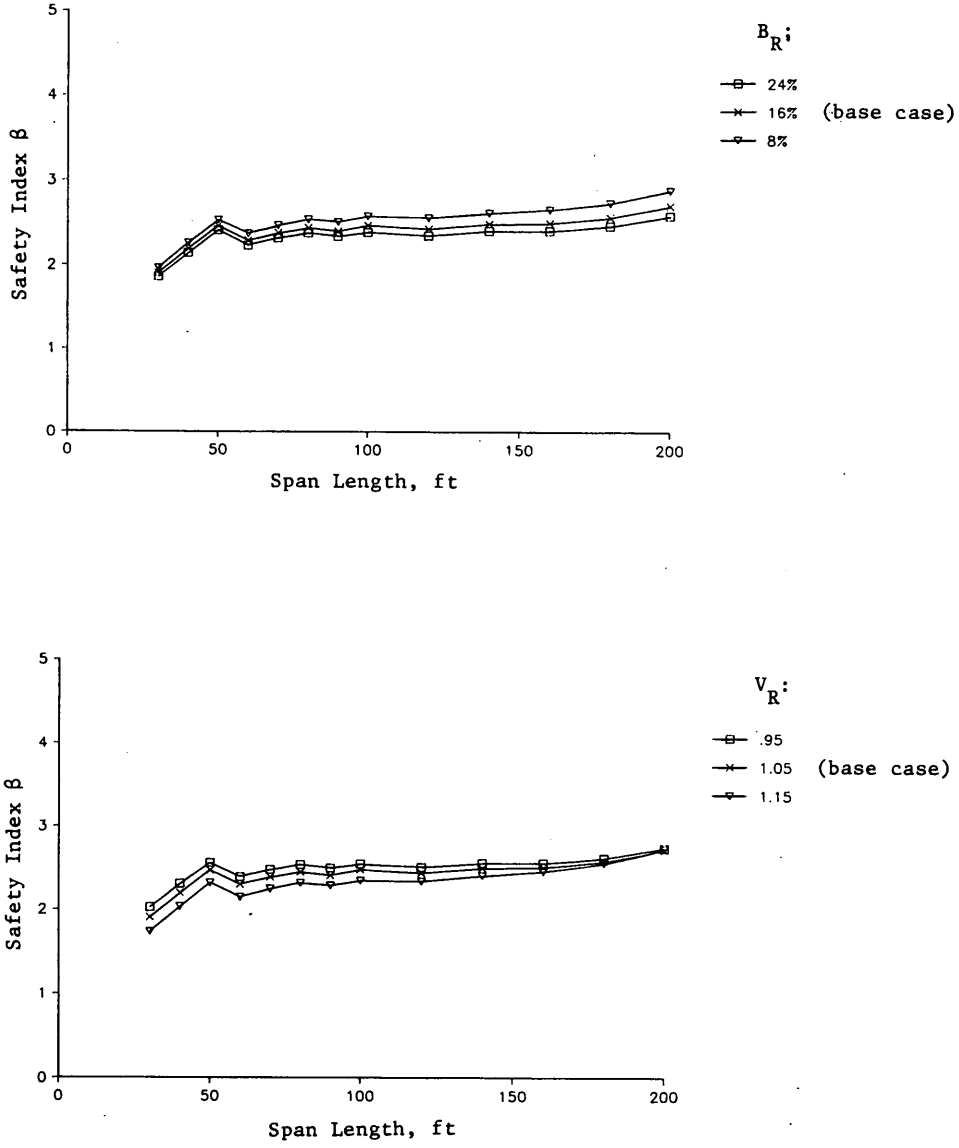

FIGURE 7 Sensitivity of β to bias of R (*top*) and COV of R (*bottom*) (steel, Traffic Condition 1).

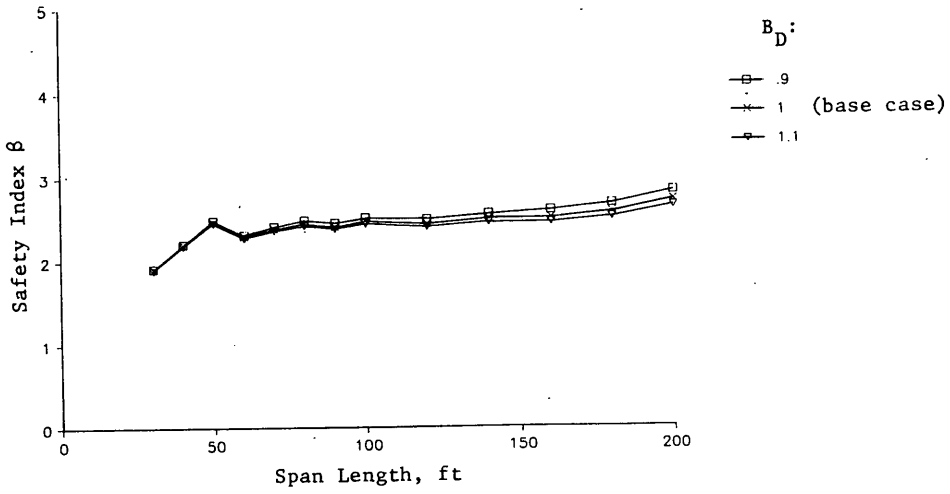

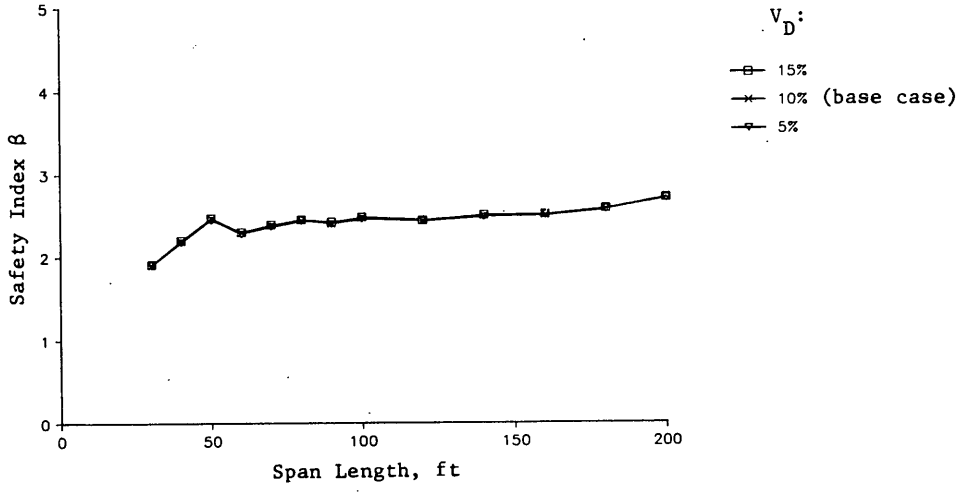

FIGURE 8 Sensitivity of β to bias of *D* (*top*) and COV of *D* (*bottom*) (steel, Traffic Condition 1).

the current working stress evaluation method at the operating level according to AASHTO (*2*). From Figure 9 (*bottom*) target β of 2.3, 2.0, and 1.7 can be recognized for cases of B_g equal to 0.8, 0.9, and 1.0, respectively. Figure 9 (*top* and *middle*) shows that these targets are correspondingly either reached or exceeded by the proposed formula. A similar sensitivity examination for COV of g (V_g) can be undertaken for the results shown in Figure 10. Uniformity of β still remains if V_g is changed for both application cases of proof testing, respectively shown in Figure 10 (*top* and *middle*). Reliability levels reached by the proposed formula are higher than those reached by the current working stress evaluation method at the operating level under the changed parameter. The current evaluation method produces lower reliability levels than those shown in Figures 9 (*bottom*) and 10 (*bottom*) for a more severe loading case (Traffic Condition 4). However, the proposed proof load formula will ensure a uniform target safety index, regardless of traffic conditions.

More cases of input data change have been examined in this sensitivity analysis but are not exhaustively presented here. However, the most predominant parameters and their typical cases have been discussed. It is concluded that possible

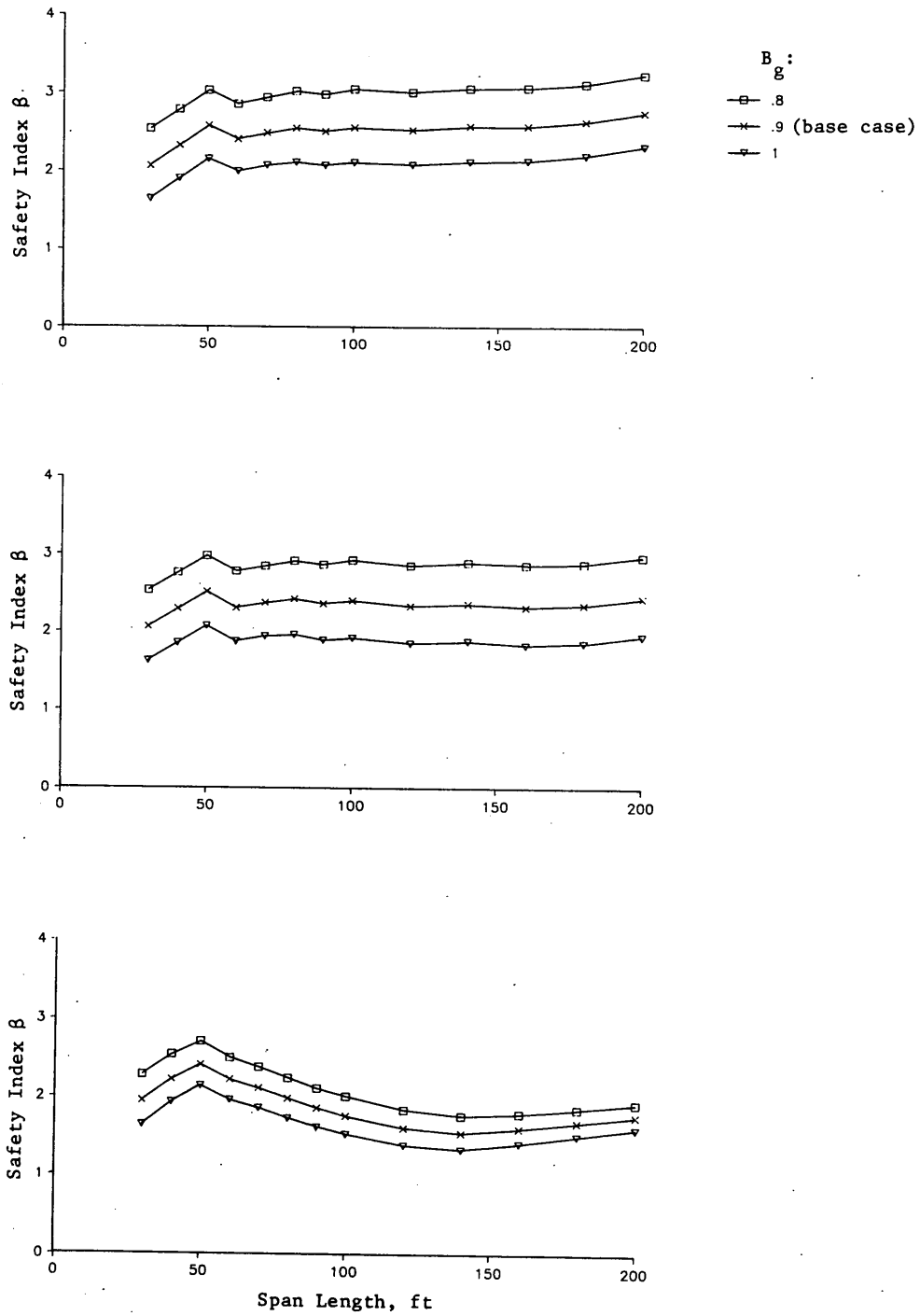

FIGURE 9 Sensitivity of β to bias of *g* (steel, Traffic Condition 3): *top*, with analytical rating; *middle*, without analytical rating; *bottom*, current working stress method at operating level.

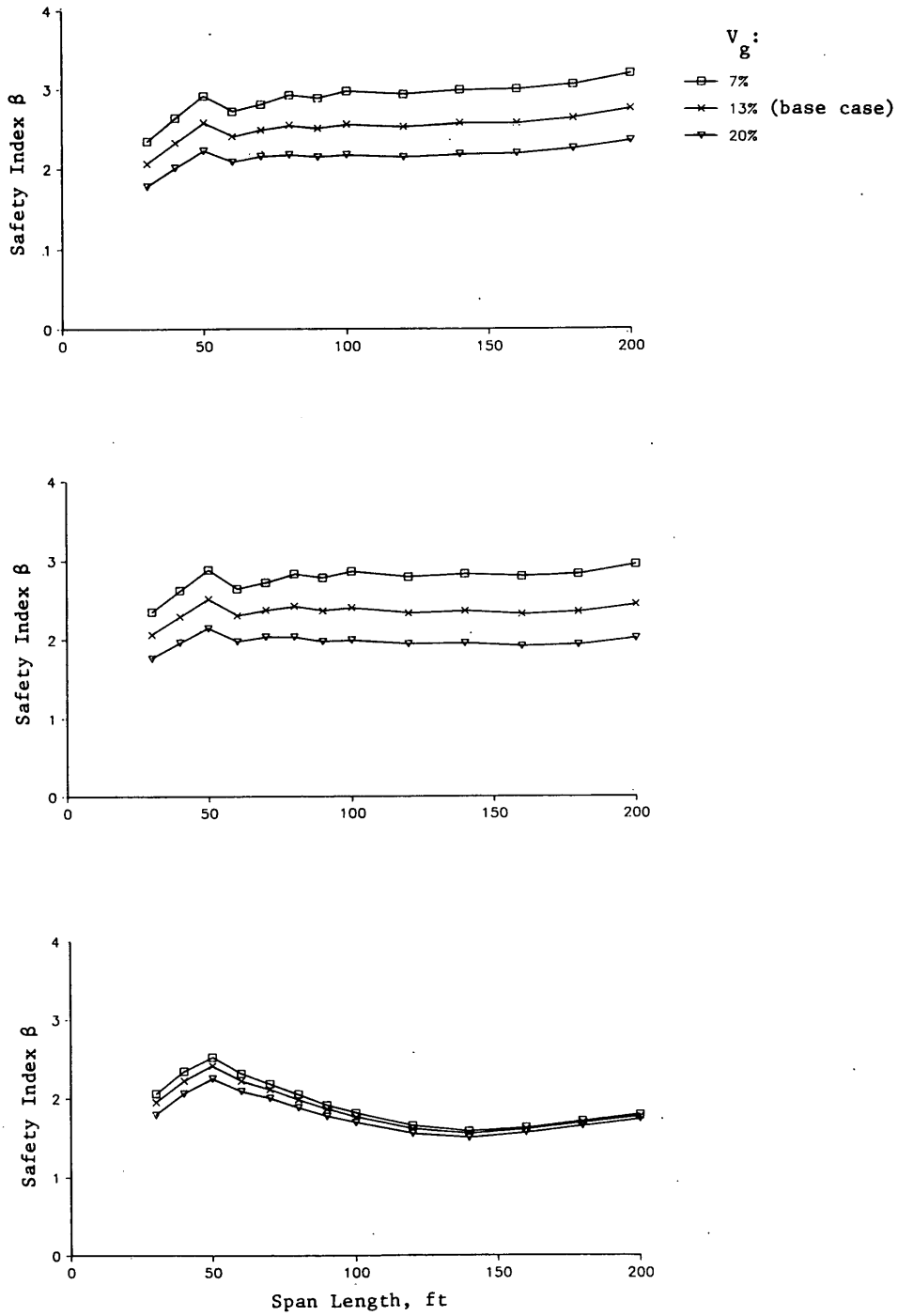

FIGURE 10 Sensitivity of β to COV of *g* (steel, Traffic Condition 3): *top*, with analytical rating; *middle*, without analytical rating; *bottom*, current working stress method at operating level.

changes of input data will not affect the proposed proof load formula, with respect to uniformity of β and satisfaction of target levels.

IMPLEMENTATION CONSIDERATIONS

Typical proof load testing of highway bridges for structural evaluation consists of three steps: planning, test execution, and rating based on analysis of test results. To apply the proposed proof load formula for successful results, factors other than those addressed here may have to be considered to make decisions in various stages of testing. In general, decisions should be made to minimize costs (such as possible bridge damage or failure by test loading, test operation, and penalties caused by improper test procedures) and maximize benefits (such as those resulting from potential reduction or removal of load restriction, deferral of bridge replacement, and savings on evaluating bridges by an alternative means). A thorough investigation of these factors is beyond the scope of this paper, because they often must be examined in consideration of local conditions, specifically site-specific bridge conditions, regional requirements on bridge capacity, and other factors. A procedure manual for proof load testing of highway bridges is under development in New York State to address the particular issues within that jurisdiction.

CONCLUSIONS

A proof load formula is proposed for bridge rating by proof testing. This formula can be used to determine target proof load and bridge load rating. The factors of the proposed formula are prescribed on the basis of a target safety index of 2.3, which is consistent with the current practice. Two cases of proof load testing application are covered: (a) an analytical rating is available but unsatisfactory and (b) no analytical rating can be obtained. A relatively uniform reliability level is produced by the proposed proof load formula for these cases over a practical range of span length, material type, and traffic conditions. A comprehensive sensitivity analysis has been performed to examine implications of the input data. Its results show that the proposed proof load formula is not sensitive to the input statistical parameters and probability distribution assumptions.

ACKNOWLEDGMENTS

This study is partially supported by FHWA. Discussions with D. Verma of Altair Engineering and F. Moses of the University of Pittsburgh are acknowledged. The authors also thank D. B. Beal and G. A. Christian of the New York State Department of Transportation for their valuable comments and suggestions during the course of this study.

REFERENCES

1. A. S. Nowak. System Reliability Model for Bridges. In *New Directions in Structural System Reliability* (D. M. Frangopol, ed.). 1988, pp. 211–222.
2. *Manual for Maintenance Inspection of Bridges*. AASHTO, Washington, D.C., 1983.
3. M. H. Phillips and J. H. Wood. Proof Loading of Highway Bridges. *Proc., New Zealand Roading Symposium*, Vol. 4, National Roads Board, 1987, pp. 803–807.
4. B. Bakht and P. F. Csagoly. *Bridge Testing*. Structural Research Report SRR-79-10. Ontario Ministry of Transportation and Communications, Downsview, Ontario, Canada 1979.
5. D. B. Beal and M. J. Loftus. *Load Test on Five Bridges*. Client Report 30. Engineering Research and Development Bureau, New York State Department of Transportation, Albany, July 1988.
6. F. Moses and D. Verma. *Load Capacity Evaluation of Existing Bridges: Phase II*. Draft Final Report. NCHRP Project 12-28(1). TRB, National Research Council, Washington, D.C., July 1989.
7. F. Moses and D. Verma. *NCHRP Report 301: Load Capacity Evaluation of Existing Bridges*. TRB, National Research Council, Washington, D.C., 1987.
8. *Guide Specifications for Strength Evaluation of Existing Steel and Concrete Bridges*. AASHTO, Washington, D.C., 1989.
9. *Ontario Highway Bridge Design Code*. Ontario Ministry of Transportation and Communications, Downsview, Ontario, Canada, 1983.
10. A. H-S. Ang and W. L. Tang. *Probability Concepts in Engineering Planning and Design, Vol. 2: Decision, Risk, and Reliability*. John Wiley and Sons, New York, N.Y. 1984.
11. G. Fu and F. Moses. Overload Permit Checking Based on Structural Reliability. In *Transportation Research Record 1290*, TRB, National Research Council, Washington, D.C., 1991, pp. 279–289.
12. Y. Fujino and N. C. Lind. Proof-Load Factors and Reliability. *Journal of the Structural Division*, ASCE, Vol. 103, No. ST4, April 1977, pp. 853–870.
13. G. Fu, P. Saridis, and J. Tang. *Proof Load Testing for Highway Bridges*. Report FHWA/NY/RR-92/153. Research Report 153. Engineering Research and Development Bureau, New York State Department of Transportation, Albany, Jan. 1992.
14. B. Ellingwood, T. V. Galambos, J. G. MacGregor, and C. A. Cornell. *Development of a Probability Based Load Criterion for ANSI A58*. Report NBS 577. National Bureau of Standards, June 1980.
15. A. S. Nowak and J. Zhou. *Reliability Models for Bridge Analysis*. Department of Civil Engineering, University of Michigan, Ann Arbor, March 1985.
16. F. Moses and M. Ghosn. *A Comprehensive Study of Bridge Loads and Reliability*. Report FHWA/OH-85/005. Department of Civil Engineering, Case Western Reserve University, Cleveland, Ohio, Jan. 1985.
17. R. A. Imbsen, W. D. Liu, R. A. Schamber, and R. V. Nutt. *NCHRP Report 292: Strength of Existing Reinforced Concrete Bridges*. TRB, National Research Council, Washington, D.C., June 1987.
18. R. V. Nutt, R. A. Schamber, and T. Zokaie. *Distribution of Wheel Loads on Highway Bridges*. Final Report on NCHRP Project 12-26. Imbsen and Associates, Inc., April 1988.
19. W. C. Hansell and I. M. Viest. Load Factor Design for Steel Highway Bridges. *AISC Engineering Journal*, Vol. 8, No. 4, Oct. 1971, pp. 113–123.
20. M. Ghosn. *Bridge Overstress Criteria*. Draft Final Report to FHWA. Project DTFH61-88-R-0096. Civil Engineering Department, City College of New York, New York, 1990.

Publication of this paper sponsored by Committee on Dynamics and Field Testing of Bridges.

Nondestructive and Destructive Testing of Decommissioned Reinforced Concrete Slab Highway Bridge and Associated Analytical Studies

A. E. AKTAN, M. ZWICK, R. MILLER, AND B. SHAHROOZ

Recently there have been many examples of undesirable bridge performance under service loads and scour and after floods and earthquakes. There is also evidence that, according to present inspection and rating procedures, a large number of bridges may be deemed structurally deficient without justification. Many reinforced concrete (RC) slab bridges are now being replaced without taking full advantage of their inherent capacities because of a lack of understanding and knowledge of the effects of deterioration and aging on these bridges. To establish procedures to allow for the full utilization of RC slab bridge capacity, a 38-year-old sample was loaded to failure. The bridge, which was decommissioned because of its age and deteriorated state, endured the equivalent loading of 22 rating trucks before failure.

A legislatively mandated program to inventory, inspect, and improve the nation's bridges was initiated in 1977 after the collapse of the Silver Bridge over the Ohio River at Point Pleasant, W.Va. (*1*). This program has not been able to eliminate bridge collapses and failures completely: over only a 5-year window from 1977 through 1981, 14 cases of bridge collapse and an additional 19 cases of bridge failure short of collapse under service loads were documented (*2*). More recently, the vulnerability of bridges against natural hazards has been realized in the well-publicized collapses of the Schoharie Creek and Hatachie River bridges caused by scour (*3*) and the collapse of segments of the Nimitz freeway and the Bay Bridge in 1989 because of the Loma Prieta earthquake (*4*). Therefore, a more effective means of inspection and diagnosis is needed to evaluate bridge condition and vulnerability against collapse as a result of both traffic and natural hazards.

Certain bridge types, such as reinforced concrete (RC) slab bridges with sound piers and abutments, are inherently more resistant to collapse than others. Not a single RC slab bridge collapse was reported among the 33 cases studied by Hadipriono (*2*). An NCHRP review of field tests also has indicated that redundant bridges may have far greater strength than may be anticipated by the current rating methods (*5*). Other studies confirm this view (*6*). Many of these bridges have been, or are being, decommissioned without fully utilizing their available capacities. The financial implications can be staggering if one considers that the national bridge inventory as of 1987 listed 98,777 RC slab and T-beam bridges, of which 15,519 had an SR of less than 50, and 57,331 had an SR between 50 and 80. By recognizing and using all of the inherent capacities of these bridges, highway funds may be prioritized more effectively.

Department of Civil and Environmental Engineering, University of Cincinnati, Mail Location 71, Cincinnati, Ohio 45221.

OBJECTIVES OF RESEARCH

The first goal of this research is a rigorous study of the technical aspects of inspection, rating, maintenance, and decommissioning of RC slab bridges. The second goal is to assess the state of the art in some of the experimental and analytical tools needed for more effective infrastructure preservation. These included a modal test–based quantitative nondestructive evaluation (NDE) technique that has been developed by University of Cincinnati (UC) researchers for Ohio Department of Transportation (ODOT)/FHWA (*7*).

In this study researchers explore whether the modal test–based NDE technique can accurately diagnose the condition of a concrete bridge deck from over an asphalt overlay, and whether the technique would reveal if a bridge has been overloaded. Further objectives in the area of NDE include exploring the feasibility of using truck-load tests as an effective NDE procedure and calibrating the currently used visual rating procedures for identifying distress in slab bridges.

The analytical tools explored included linearized identification of three-dimensional (3D) finite element models for bridge rating and 3D nonlinear finite element analysis (NLFEA) of complete, aged bridges that may have properties affected by damage and deterioration.

TEST SPECIMEN

Description of Test Specimen

The test specimen (Figure 1) is a three-span, RC skewed slab bridge that was constructed in 1953. The piers are set on footings placed on the bedrock, whereas the abutments are placed on steel piles driven to the bedrock. The piers and abutments are all skewed at a 30-degree angle (Figure 1).

Material Properties

Design drawings indicate Class C concrete, whereas no reference was made to the reinforcing steel grade. Core samples

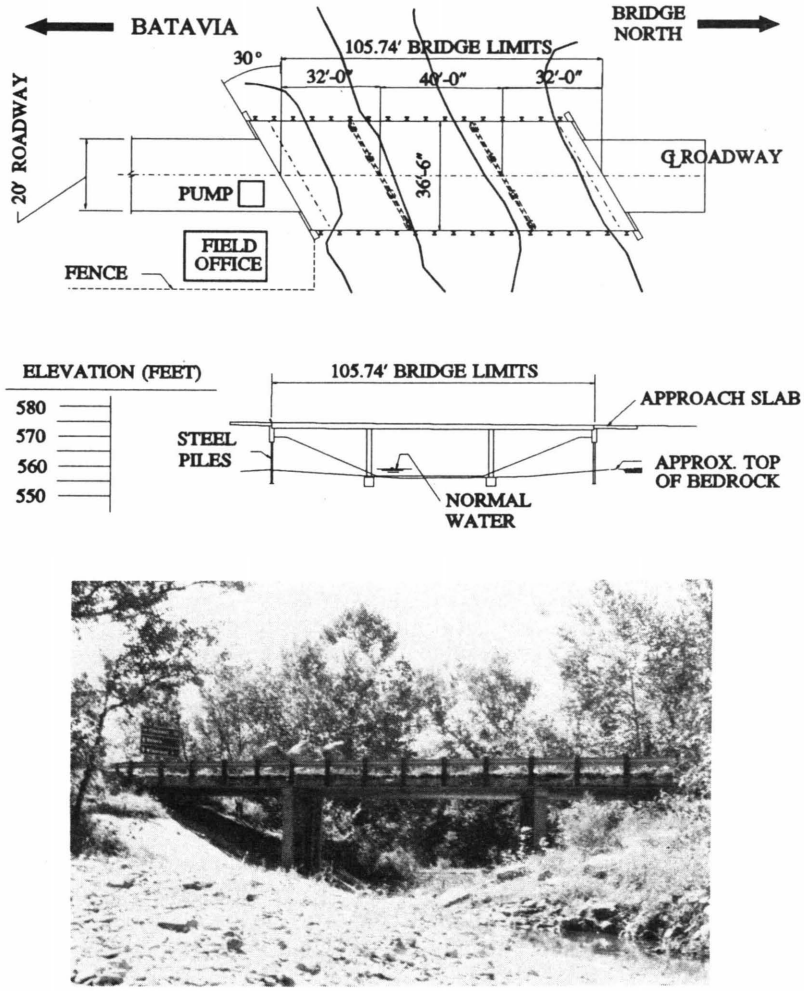

FIGURE 1 Description of test bridge: *top*, site plan; *middle*, site elevation; *bottom*, photograph.

4 in. in diameter through the asphalt overlay and the concrete deck were taken to study the material properties and their variation.

Concrete coring revealed that concrete in the shoulder regions was severely deteriorated. It was not possible to obtain sound cores from the shoulders since the concrete under the asphalt would crumble during coring, which jammed the coring bit. Throughout the driving lanes, full-depth, solid cores could be obtained.

Bridge Condition with Asphalt Overlay

Data for the initial damage surveys could not be collected from the top surface because of the presence of the asphalt overlay. An extensive effort was made toward searching for damage through the overlay by use of NDE techniques, because an overlay is common, especially over older bridge decks. These studies are described in the NDE section of the paper.

Although the bottom of the bridge did not exhibit any signs of extensive deterioration, the exposed sides of the bridge slab were heavily deteriorated. This damage was attributed to run-off mixed with salt used in deicing the bridge during winter months. Other than the heavily deteriorated sides, the survey revealed little other damage that was mostly limited to some light spalling and cracking on the bottom of the slab.

Bridge Condition After Removal of Asphalt Overlay

When the asphalt overlay was removed, the shoulder regions were found to be in an extremely deteriorated state, having completely lost the cover over a large number of bars. The concrete in the traffic lanes appeared reasonably solid. Extensive study and petrographic analyses of the concrete samples indicated that the primary agent in the deterioration was D-cracking of the porous coarse aggregate, which may have initiated during the freeze-thaw cycles of the first winter. The D-cracking left pathways in the concrete through which water and salt could pass. This cracking led to the secondary deterioration mechanism of alkali-silica reaction between some of the aggregates and the cement paste. The overlay was identified as a further facilitator of the deterioration by trap-

ping water between the overlay and concrete deck for long periods. After the cover concrete deteriorated, some of the reinforcing bars rusted, whereas others in the vicinity were observed to be in excellent shape.

The D-cracking near the top rebars opened up pathways for the water to enter and freeze, which induced spalling of the top layer of concrete. This primary deterioration mechanism is attributed to poor selection of materials and poorly implemented concrete construction. The deterioration was not triggered by corrosion of the reinforcing steel. Therefore, the deterioration of the bridge, within a short life span of only 38 years, could not have been avoided only by utilizing epoxy-coated rebars or cathodic protection. Instead, a possible deficiency with concrete material design specifications and the use of asphalt overlay are indicated.

NDE AND SUMMARY OF PRELIMINARY FINDINGS

Two methods of NDE were explored. The first is based on modal testing by impact and structural-identification developed at UC (*7*). The second procedure is based on monitoring bridge responses under static truck loads. Both of these procedures were performed on the bridge before removal of the asphalt overlay; this allowed the researchers to determine the effectiveness of NDE in diagnosing hidden damage and quantifying its effects on the mechanical characteristics of the structure. Modal tests were repeated after various stages of loading and damage during the destructive test program to explore if the modal test–based NDE technique would recognize damage caused by overloading. A complete reporting and evaluation of these tests is forthcoming; meanwhile the preliminary results of NDE conducted above the overlay are presented.

Modal Test–Based NDE Procedure and Preliminary Results

The NDE methodology is summarized in Figure 2. The methodology uses multireference modal testing to measure a sufficient number of mass-normalized mode shapes, frequencies, and damping coefficients that permit quantifying flexibility coefficients with respect to a fine discretization (*7*). Flexibility coefficients of even highly redundant structures may serve as a meaningful structural signature, as well as indexes sensitive to localized damage.

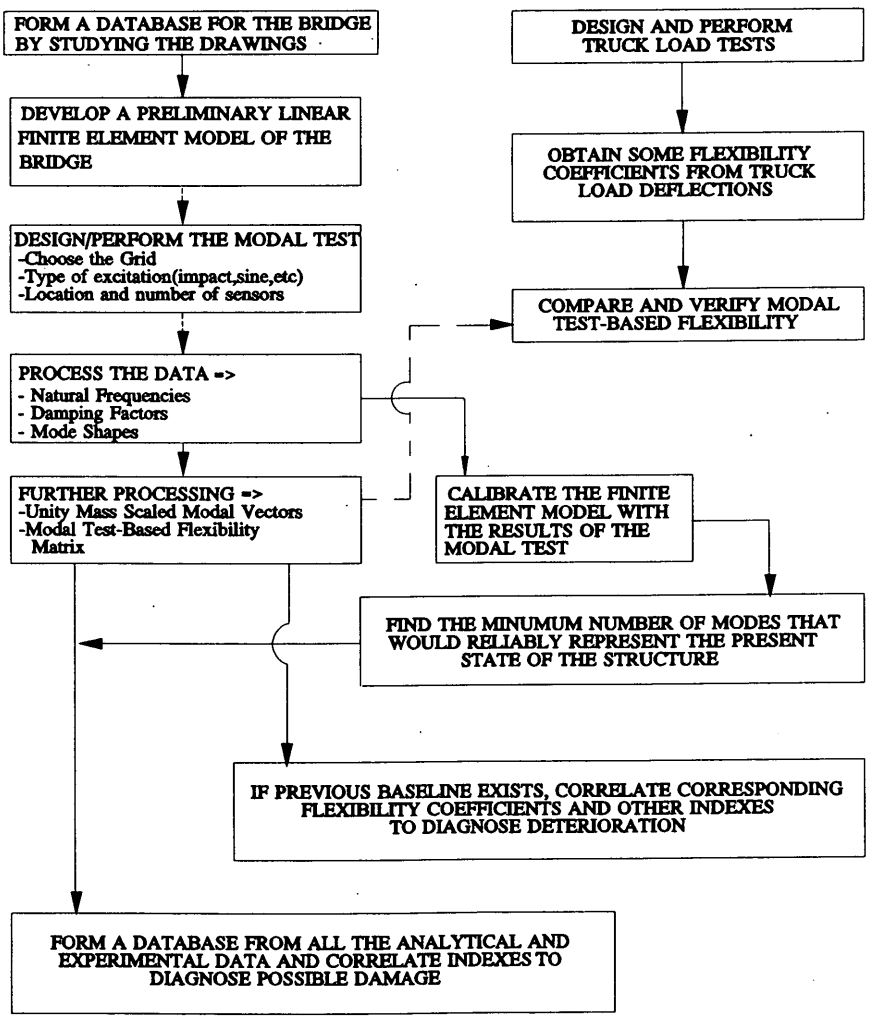

FIGURE 2 Summary of nondestructive evaluation.

Meanwhile, the measured dynamic characteristics are used to develop and numerically calibrate a linearized finite element (FE) model of the bridge in the absence of an experimental baseline. The calibrated FE model may serve as a basis for evaluating the dynamic test–based flexibility coefficients to diagnose damage. Research for establishing derivative indexes from flexibility to diagnose the influence of various forms of damage and deterioration of the capacities of a slab bridge is in progress. Naturally, if a reference flexibility is available from previous tests of the same bridge or tests of another benchmark bridge, damage diagnosis is facilitated.

Since the stress level arising from the modal test is typically much smaller than the stress level under truck traffic, a truck load test may help to validate the dynamic test–based flexibility. Truck load tests of typical slab or beam-slab bridges are generally impractical because measuring small displacements in the field is a difficult problem. Local strain measurement is not revealing, and in general it is possible to measure only a few displacements under truck loads. As a result, truck load tests do not lead to a finely discretized flexibility, as may be obtained from modal testing but serve to validate the reliability of results obtained from modal testing as well as a proof test if several multiples of legal loads may be safely applied.

Figure 3 compares some of the mode shapes and frequencies obtained from modal testing of the test bridge and the cor-

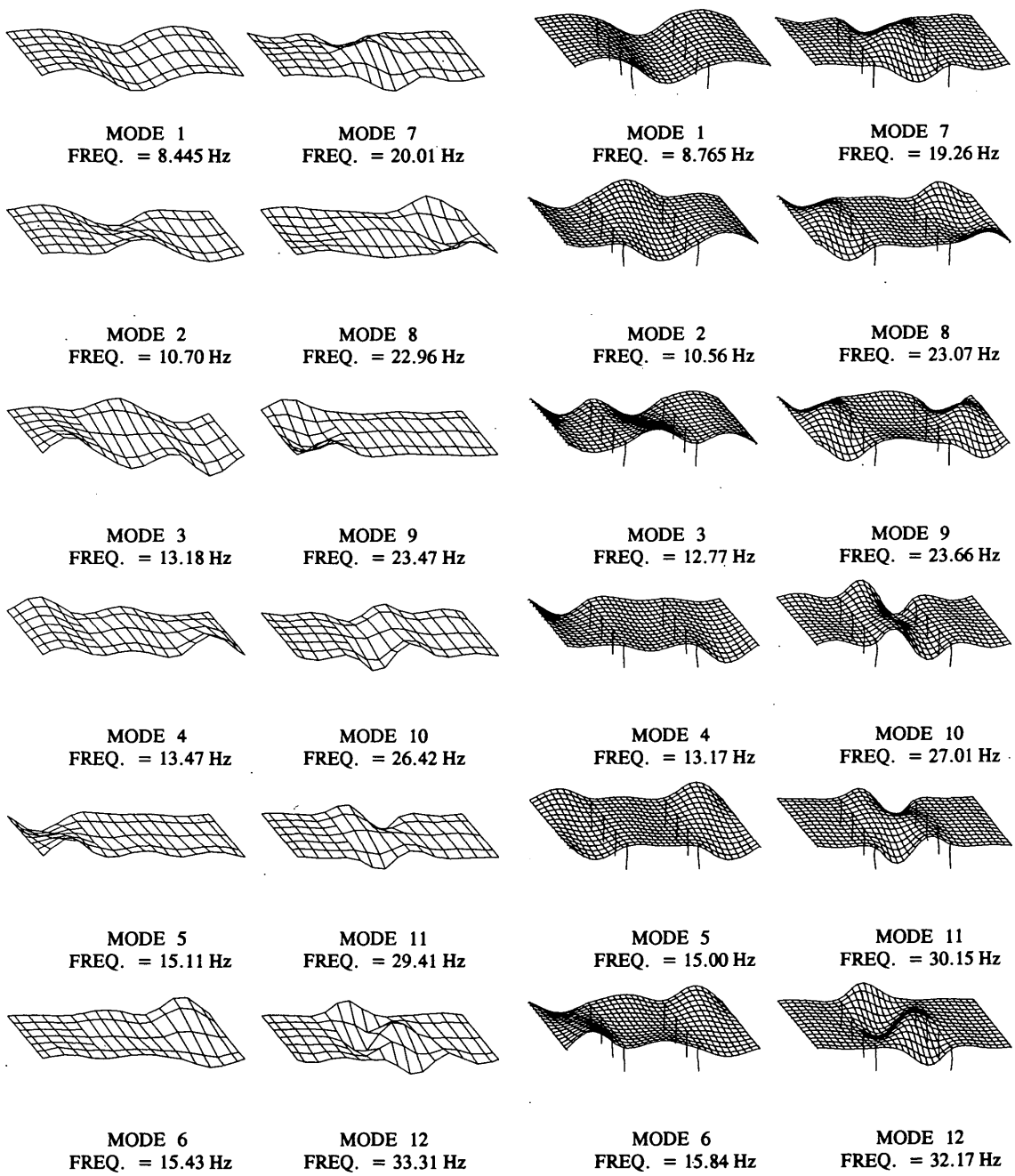

FIGURE 3 Comparison of experimental (*left*) and analytical (*right*) mode shapes.

responding dynamic characteristics of a calibrated FE model. Figure 4 compares some of the dynamic test–based flexibility coefficients with the corresponding coefficients of the calibrated analytical model. The coefficients correspond to bridge deflections along the transverse lines labeled D and I on the modal test grid shown in Figure 4, as a unit load is respectively placed at the midpoint of Lines D and I. The correlations reveal that the bridge is considerably more flexible than the "rational" analytical model along both Lines D and I. The difference between analytical and experimental deflections increases especially toward the east shoulder. These observations reveal that the structural properties of the slab are affected considerably by damage, particularly along the east shoulder. Research is in progress to extrapolate from the influence of damage on flexibility to the influence of damage on strength capacity.

Results of Truck Load Tests

Truck load tests were used to verify the flexibility from the modal test. Three single-axle dump trucks loaded with gravel were used. The tire weights were measured with portable scales, whereas the bridge deflections were measured at 21 points with sufficiently sensitive and specially calibrated and mounted electronic transducers. Bridge deflections measured along Line D under one and three trucks are compared with the corresponding deflections predicted from the calibrated analytical model and modal test–based flexibility in Figure 5. There are magnitude differences in deflections measured under truck loads and those predicted from the modal test-based flexibility, although the deflection patterns are similar. The differences are attributed to the difference in stress level at the impact and truck load tests in conjunction with non-

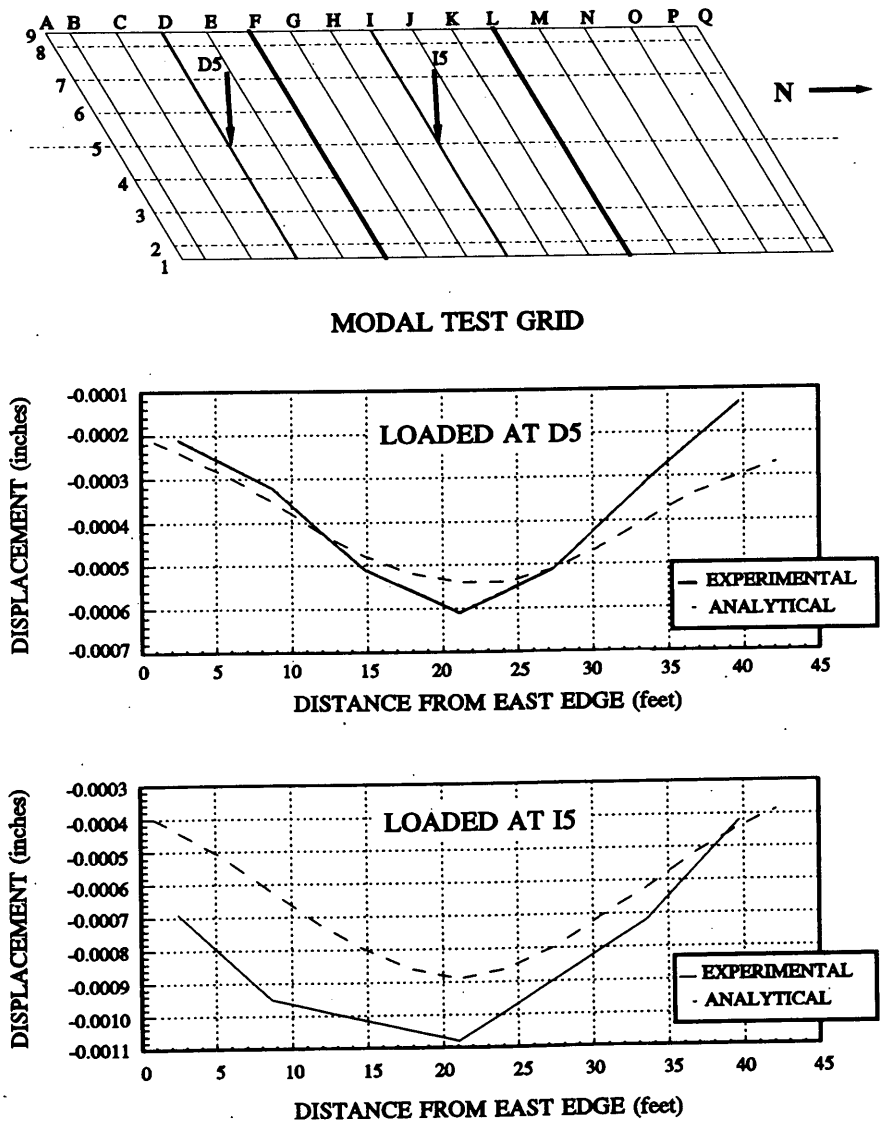

FIGURE 4 Comparison of experimental and analytical flexibility.

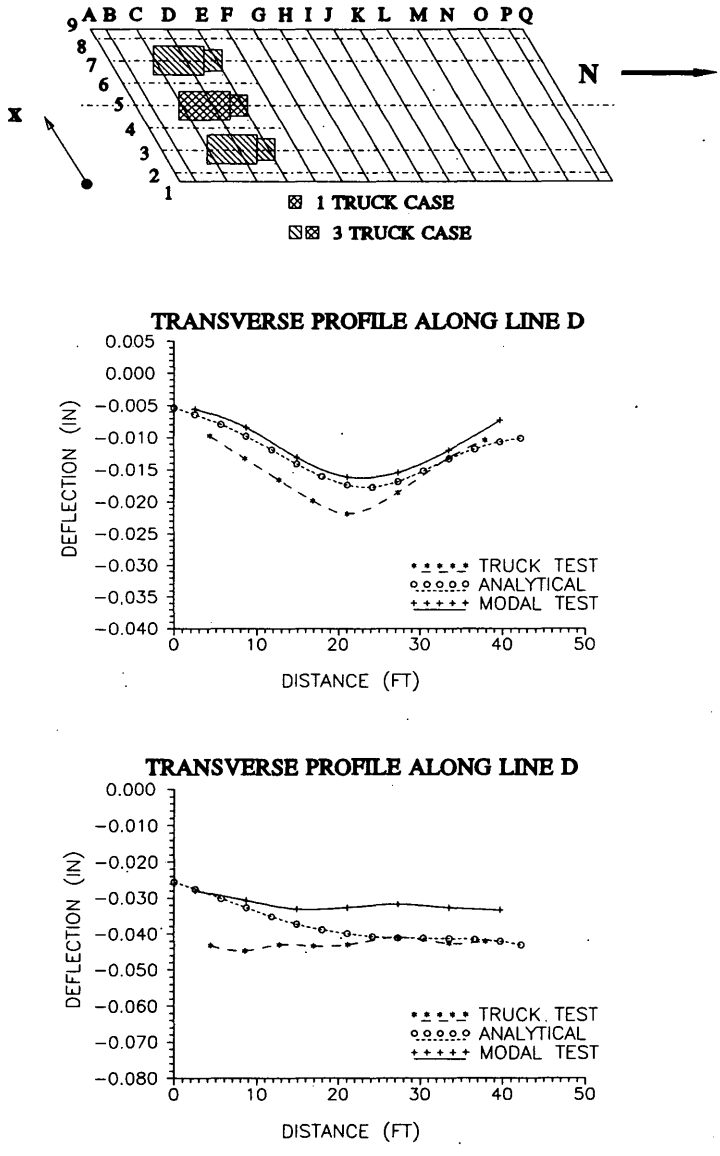

FIGURE 5 Comparison of truck load test flexibility: *top*, truck load configurations; *middle*, one-truck case; *bottom*, three-truck case.

linearity. Although the "rational" analytical model indicates that the flexibility of the east shoulder should be considerably less than the flexibility along the west shoulder because of skew, in reality both the truck load measurements and modal test–based flexibility are contrary, indicating that there should be relatively higher damage along the east shoulder.

PREDICTIVE ANALYSES

Predictive analyses were performed to design the loading setup and to establish the loading program. Another objective was to evaluate the state of the art in NLFEA for predicting behavior of reinforced concrete bridges. Linear finite element analyses and yield line analyses were also performed to support NLFEA.

Researchers from the Delft Technological University (the Netherlands) collaborated with UC researchers at this step of the research. The analyses performed by Delft were helpful in assessing the state of the art since the software (DIANA) developed by the Delft group, as well as the NLFEA expertise represented by this group, is considered some of the best in the world (*8*).

Figure 6 (*top*) shows the geometric characteristics of the analytical model used by UC for the NLFEA. The initial boundary stiffness at the abutments of this model was established through structural identification, incorporating the dynamic characteristics of the bridge measured by modal testing. Although concrete cracking, concrete plasticity, and yielding

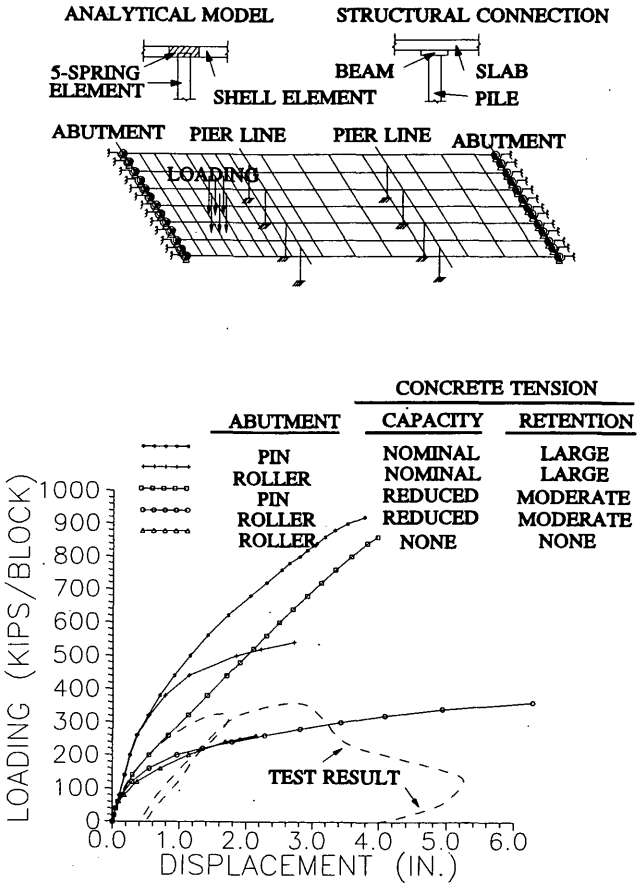

FIGURE 6 NLFEA model (*top*) and results of NLFEA analyses (*bottom*).

of reinforcing bars were accounted for during the NLFEA, the boundary conditions were not. However, subsequent to the tests, it became apparent that the boundary conditions at the abutment comprised the most critical parameter.

Figure 6 (*bottom*) shows some of the predicted global responses of the bridge conducted by UC compared with the corresponding measured response during the test. Analytical responses demonstrate the significance of parameters that define the boundary conditions at the abutment and the stress-strain response of concrete under uniaxial tension. These parameters are associated with the greatest uncertainty in analyzing the bridge, although the modal test results and standard material test responses were available.

The sensitivity of analytical responses to the described boundary and material parameters indicates that it is not yet possible to rely on NLFEA to predict available capacities and failure modes of slab bridges. This analytical tool may serve to understand the critical parameters for optimizing the design of new bridges or the upgrade of existing ones.

DESIGN OF LOADING AND DATA ACQUISITION

Loading Position

A decision was made to simulate a one-lane, one-trailer loading during the test, although a multilane loading of the bridge would have been more critical for rating. One-lane loading permitted the observation of more complex modes of slab-bridge behavior, and made it possible to extend the findings to estimate with reasonable reliability the bridge capacity under multilane loading. Figure 7 shows the position and manner of the loading applied to the bridge during the tests, along with the truck it is simulating. The load simulated the front tandem of a trailer as it is entering the bridge in the northbound lane. Analyses indicate the southbound lane of the loaded end span to be stiffer than the northbound lane, as discussed earlier, in relation to the truck load test responses (see Figure 7). However, NDE also revealed that the loss of stiffness caused by damage at the northbound lane and shoulder at this end span was more critical than at the southbound lane. Therefore, the decision was made for loading the southeast quadrant of the bridge to reveal the extent of the influence of damage and deterioration on bridge behavior.

The destructive test loading simulated loading of the bridge as envisioned in the rating process based on the *AASHTO Manual of Maintenance Inspection* (*9,10*), as opposed to the actual dynamic manner in which the traffic load is imposed on the bridge. The rationale behind loading the bridge statically is clear: it permits one to test the reliability of the rating process, especially as it applies to the computing of capacity and demand for RC slab bridges.

Design of Loading and Loading Control Systems

Predictive analyses indicated that the upper bound of the bridge load capacity may be as high as 1,400 kips (about 40 rating trucks) for the loading position that was selected. The loading system was designed for this upper bound. It is not feasible to apply this level of load without hydraulic cylinders. Moreover, applying the load to the bridge while simulating tire loads and without creating local crushing was a challenge. An even greater challenge was the manner in which reaction could be developed in applying this type of load.

On the basis of lengthy research and feasibility analyses, it was decided to use rock anchors to develop the reaction and to pour two concrete blocks directly on the bridge to simulate the footprints of a tandem trailer (Figure 7). The blocks were designed to accommodate the four hydraulic cylinders (actuators), each with 350-kip capacity and 12-in. stroke. Double-acting actuators were acquired with a 4-in.-diameter hole through their length to accommodate eight-strand rock anchor cables.

To fabricate the loading setup, four cores were drilled in the bridge deck to allow for the drilling of the rock anchors and to allow the cables from the rock anchors to pass through the bridge deck. The rock-anchors were then installed and the concrete loading blocks were fabricated. The cables passed through the bridge deck, the concrete load blocks, and each actuator. The strands were then locked by wedges at the top of the actuator, so that as the actuator extended, the rock-anchors provided the reaction needed to load the bridge (Figure 7).

A state-of-the-art servocontrolled electrohydraulic loading system that consisted of a pump, the four actuators, two servovalves, a two-channel digital servocontroller, pressure feedbacks for load control, and stroke feedbacks for displacement

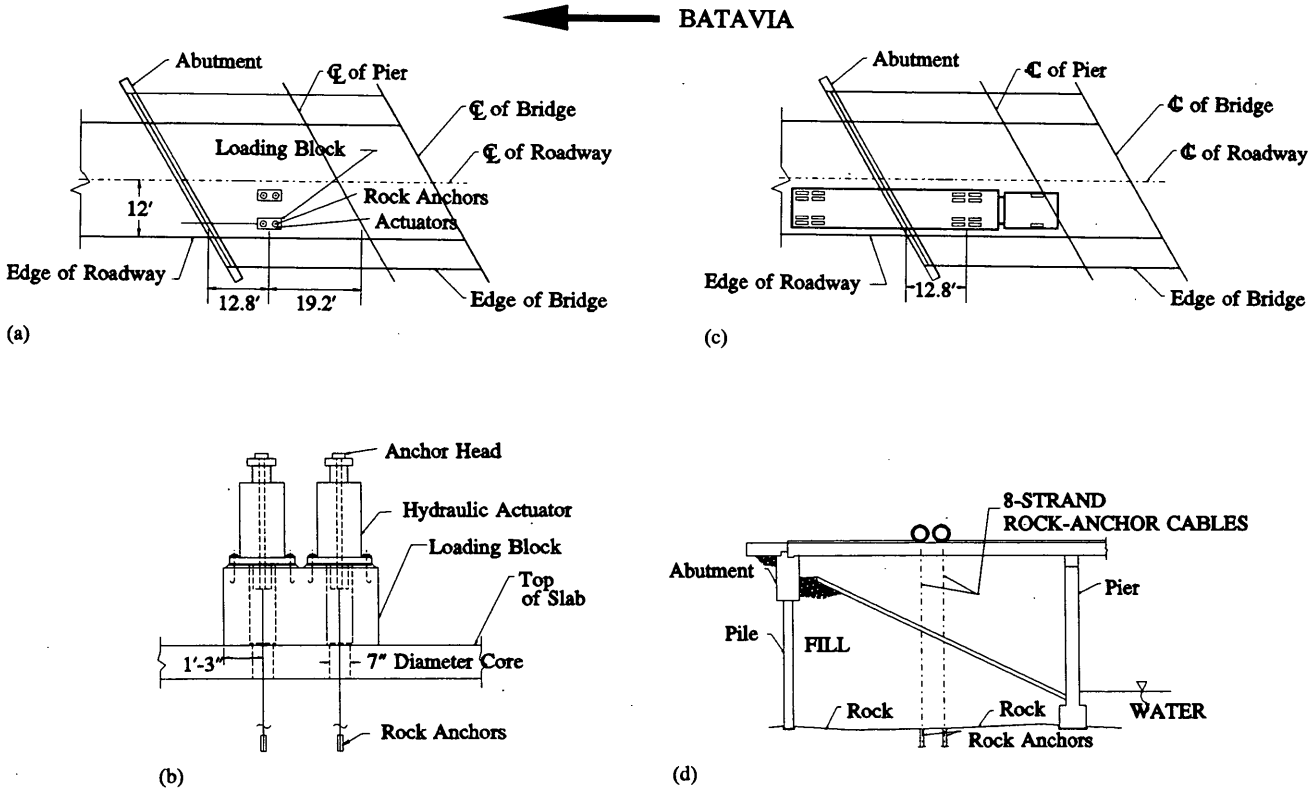

FIGURE 7 Plan view (*a*) and elevation view (*b*) of loading system; plan view (*c*) and elevation view (*d*) of simulated loading.

control was developed for loading. Together with the servocontrol system, real-time digital plotting was used for instantaneous feedback of actuator loads, strokes, and critical specimen responses. This real-time system provided the information needed to make decisions for commanding the servocontrol system. The test control and data acquisition systems were located and controlled at a field office adjacent to the bridge.

Instrumentation and Data Acquisition Systems

A principal objective of the experiment was to evaluate the state of the art in NLFEA. Therefore, extensive global and local instrumentation that would permit comprehensive correlations between analytically predicted (and subsequently simulated) and measured responses of the bridge was required. Such instrumentation was designed on the basis of the results of preliminary analyses conducted by UC and Delft; more than 160 transducers were placed on the bridge. These electronic transducers measured the forces and strokes of the four actuators, vertical and lateral displacements of the slab, slab rotations at the abutment and pier, concrete distortions, and steel strains through the critical regions of the slab.

Global instrumentation consisted of wire potentiometers used to measure the vertical displacements of the bridge deck, and DC-linear variable differential transducers (DC-LVDTs) used to measure the horizontal movements of the bridge deck. For the local instrumentation, DC-LVDTs and clip gauges were used to measure concrete distortions, and pier and abutment rotations. Foil strain gauges were placed on several rebars. All the wire potentiometers, DC-LVDTs, and clip gauges were calibrated in the laboratory through their expected operating spans. The transducer readings were recorded by data acquisition systems supplied by UC and WJE.

Design of Loading Program

Design of the loading program was aided by the upper-bound load-displacement response predicted by the NLFEA, and adjustments were made as the actual responses of the bridge were observed. First the bridge was rated based on the 1989 AASHTO guide specifications (*1*) to establish a rating factor corresponding to an impact factor of unity and to the single-lane load simulation developed for the test. The calibrated 3D finite element model discussed earlier in reference to NDE was used to estimate the demands. This procedure indicated a rating factor of 4.95. Therefore, a test load corresponding to the weight of five rating trucks was considered to signify the upper limit of the serviceability limit state for the bridge. Throughout the test, loading was applied in increments of rating trucks, where one rating truck corresponded to a total of 32 kips (one tandem weight) on the two loading blocks.

Figure 8 shows the load versus vertical displacement response measured next to the loading block near the shoulder (Point C3 shown in the inset). The first stage of the test was composed of numerous loading and unloading cycles that corresponded to shakedown at the serviceability limit state. These cycles also permitted debugging the test control, loading, and

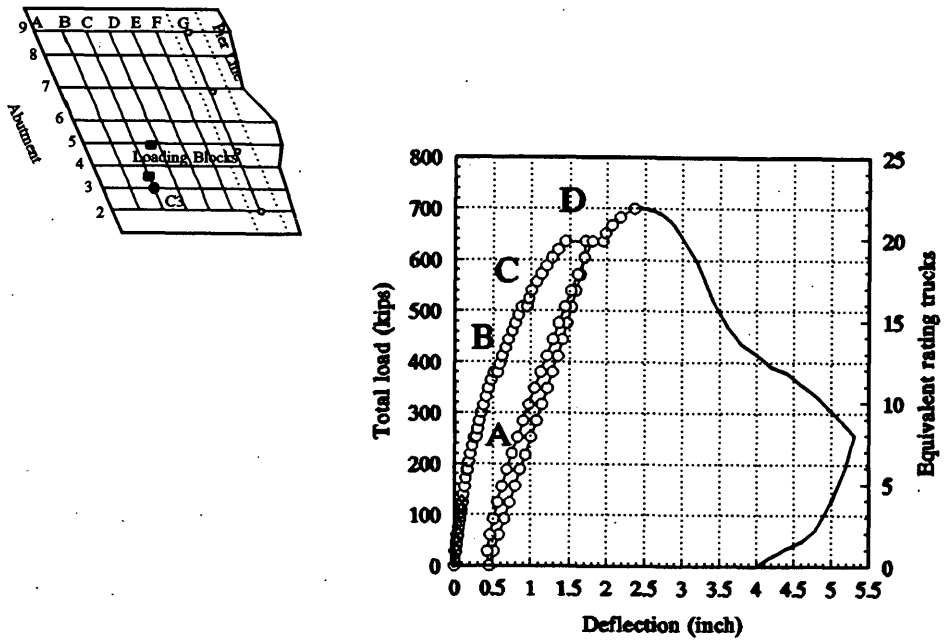

FIGURE 8 Load displacement response at Point C3.

operation of the data acquisition systems. The service-level load cycles were followed by a large inelastic excursion that revealed the damageability limit state characteristics of the bridge and left a permanent vertical deformation of about 0.5 in. after unloading. The final leg of loading led to the failure of the bridge and left a permanent deformation exceeding 4 in. (Figure 8).

Preliminary Results

The limit states indicated by the load versus load-point deflection response of the bridge are marked on Figure 8, corresponding to 7, 13, 17, and 21 truckloads. Each limit state corresponds to a change of stiffness at the load point. These limit states were attributed to progressive cracking of the slab and were also strongly influenced by the slab rotations at the abutment.

To monitor rebar strains at the critical regions, 19 strain gauges were installed on the top and bottom bridge reinforcement in the vicinity of the loading points and near the abutment and pierline. It is significant that none of these gauges indicated yielding before the load level reached 20 truckloads. At a load of 20 truckloads, several of the gauges in the vicinity of the loading blocks indicated initiation of yielding. It follows that the nonlinearity observed in the global load-deflection response in Figure 8 up to a level of 20 truckloads is not caused by yielding.

Figure 9 shows the three points along the abutment where slab rotations relative to the abutment were measured as well as the corresponding load-versus-rotation envelopes. At many limit states marked on the global load-deflection response in Figure 8, the rotational stiffness provided to the slab by the abutment at locations corresponding to Gridlines 3 and 6 experienced a marked change. It follows that changes in the boundary conditions of the slab at the abutment, with increasing load level, played a significant role in the behavior of the bridge up to its failure.

Behavior at Failure Limit State

The damageability limit state behavior (between 7 and 21 truckloads, Figure 8) of the bridge did not reveal any alarming signs of distress although 20 truckloads corresponded to over four times the load the bridge was rated for. Even under sustained 20 truckloads, experienced ODOT bridge engineers did not have any reservations about inspecting the underside of the loaded bridge. Although there was extensive cracking, no distinct yield lines had emerged.

When the load was increased to the equivalent of 22 rating trucks, the bridge failed in a brittle manner. The topside view of the failure plane is shown in Figure 10. The failure was apparently triggered by a diagonal tension failure at the edge of the pier-slab interface in the damaged shoulder region. The failure front then progressed along the pierline until, at about the midpoint of the bridge, it followed a circular path arching back toward the abutment. This failure front followed top-bar cutoff points along most of its circular path. The servo-control system maintained a considerable portion of the failure load until it was turned off, as reflected in the postfailure response in Figure 8. In spite of the brittle nature of the failure, a considerable postfailure strength reserve is implicated. Dowel action of the bottom longitudinal bars that were continuous from the abutment and through the pier was particularly effective in preventing the total collapse of the end span and providing the postfailure strength.

Although a more detailed study of the failure mechanism is in progress, it is relevant that the average shear stress within the failure plane was less than $1.0\sqrt{f'_c}$. A photograph of the topside view of failure is shown in Figure 10 (*bottom*).

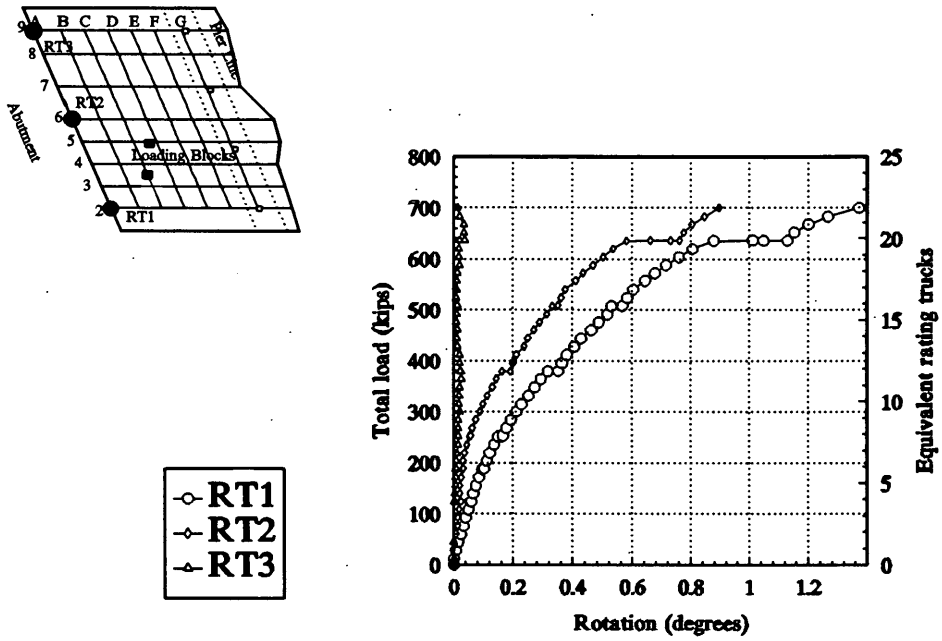

FIGURE 9 Rotational response at abutment.

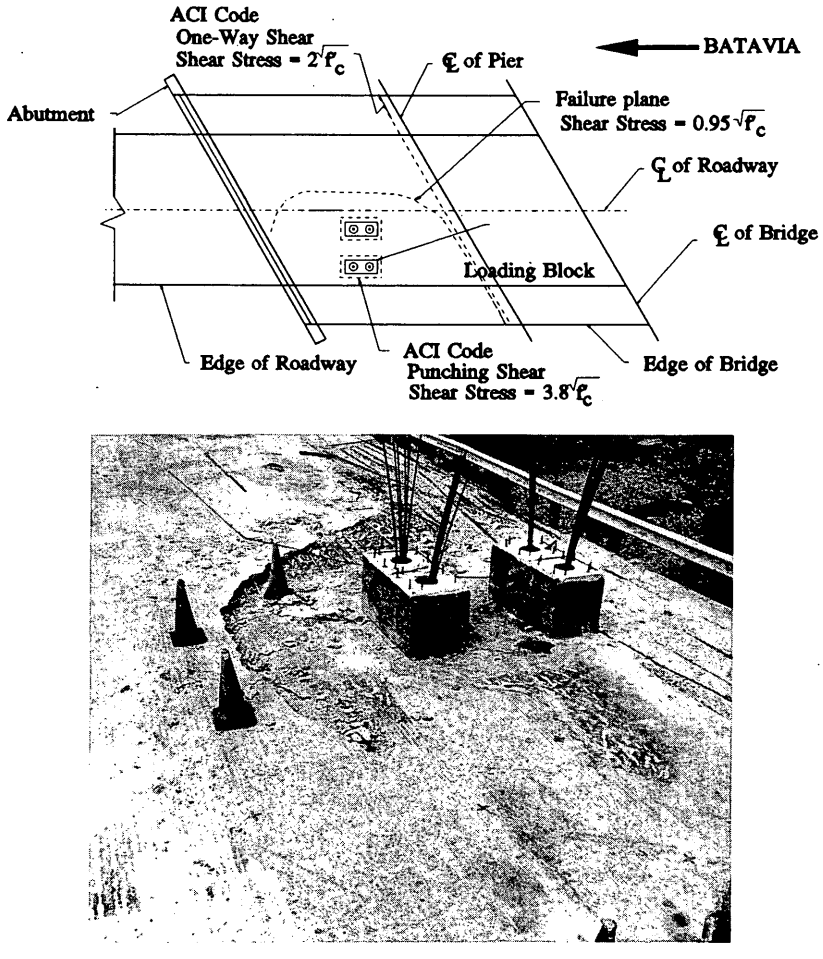

FIGURE 10 Description of failure plane: *top*, plan view; *bottom*, photograph.

PRELIMINARY CONCLUSIONS

The modal test-based NDE procedure holds great promise in diagnosing concrete deterioration and damage hidden under asphalt overlay. The procedure also leads to a calibrated linearized FE model of the bridge that is the key for reliably rating a bridge per the 1989 AASHTO specifications. The capability of the modal test–based NDE procedure to diagnose overload-related damage is promising, as will be reported subsequently.

The truck load tests may serve as an NDE tool as well although instrumentation is difficult and the results do not lead to the comprehensive information that is revealed by a rigorous modal test. The stress level at a truck load test is much higher than the stress level during the impact-modal test. However, considering that the service level stiffness of the bridge did not decrease appreciably until the bridge was loaded by more than five trucks, the differences in the stress levels of the impact test and the truck load tests do not seem very important in bridge diagnostics unless the conditions warrant a proof test.

Bridge engineers should start recognizing the inherent capacities in RC slab bridges that have sound abutments and piers. Even with the extensive deterioration of shoulder concrete, the test bridge safely carried more than 20 rating trucks, a load exceeding four times the bridge rating based on a calibrated FE model. It follows that bridge rating and decommissioning based on only visual inspection may greatly underestimate the actual capacity of slab bridges. Considering that the average replacement cost of a two-lane, three-span, approximately 100-ft-long slab bridge is in the order of $250,000, the financial implications of using these bridges over longer life spans with some maintenance is significant.

The mechanics of the deterioration involved environmental attack directly on the concrete, indicating that measures such as using epoxy-coated rebars or cathodic protection would not avoid all kinds of bridge deterioration. Instead, concrete materials and additives should be specified to eliminate possible alkali attacks or other chemical reactions that may cause deterioration. Concrete should be designed for maximum resistance against cracking and surface deterioration. The mechanical and microchemical characteristics of coarse aggregate are most important parameters and should be adequately specified.

The inability to predict bounds of nonlinear responses of the bridge within a narrow band even by using state-of-the-art software and expertise point to the difficulty in analytically estimating RC bridge capacity. In particular, the failure mode could not be predicted, and it is doubtful that it is possible to properly simulate the failure that was observed in an analytical model. The much simpler limit analyses that were carried out could reveal the possible bounds of the strength capacity with as much error or accuracy as the NLFEA; however, they could not have been used for estimating stiffness characteristics. The assumed concrete tension response and modeling the boundary conditions of the slab at the abutment were found as the most critical parameters influencing significantly the predicted structural response.

Obviously, predicting bridge capacity by NLFEA within a narrow band is not possible since response is very sensitive to a considerable number of parameters that cannot be established with confidence even if the boundary conditions of the bridge are established at the service limit states and the materials are sampled and tested. The sensitivity of RC slab bridges to parameters such as the tension response of concrete is unlike RC beams or bare frames, the strength of which are less sensitive to similar parameters.

The mode of failure of the skew slab was not anticipated as it was not previously experienced in laboratory tests of slabs. In fact, there are no code provisions that would guide a designer to check against this type of shear failure in slab design. The failure initiated as diagonal tension failure at the interface of the slab and pier and was apparently triggered because of the damage to slab concrete at the edge of the pier.

The average shear stress within the failure plane was less than $1.0\sqrt{f'_c}$, which is much less than what is generally expected as the shear capacity of concrete, even in one-way flexural shear. Because of the delamination in the shoulder concrete, no shear resistance may have been provided by the concrete along a certain percentage of the failure plane. This may explain the low level of average shear stress at failure within the failure plane. Obviously, the capacities and failure modes of aged constructed facilities may be profoundly influenced by any existing damage and deterioration. Therefore, an attempt to evaluate the capacities of an aged constructed facility without understanding and incorporating its existing conditions will not be realistic. The existing conditions of a constructed facility cannot be established without nondestructive experimentation coupled with sampling and testing of the materials.

ACKNOWLEDGMENTS

The authors wish to acknowledge the project sponsors, FHWA/ODOT and the National Science Foundation (NSF). The authors acknowledge K. Chong, of NSF, and W. Edwards, V. Dalal, D. Hanhilammi, R. Eltzroth, and W. Fair, of ODOT, as well as many ODOT personnel who provided crucial support and advice throughout the research. At the University of Cincinnati, the authors wish to acknowledge graduate students Ho, Hrinko, Heckenmueller, and Toksoy; research engineer C. Young; and technician D. Strunk for their valuable contributions. M. Carlier of the Manta Corporation designed and operated the electrohydraulic servocontrolled loading system. Invaluable consultation and collaboration were provided by R. Iding and D. Meinheit and D. Heidbrink from Wiss, Janney, Elstner, Associates of Chicago. The authors further recognize the collaboration of the Delft Technological University of the Netherlands. Goettle Corporation provided invaluable support by installing the rock anchors, and the Sheffer Corporation provided the loading actuators at a subsidized cost.

REFERENCES

1. R. A. Imbsen, W. D. Liu, R. A. Schamber, and R. V. Nutt. *NCHRP Report 292: Strength Evaluation of Existing Reinforced Concrete Bridges*. TRB, National Research Council, Washington, D.C., 1987.

2. F. C. Hadipriono. Analysis of Events in Recent Structural Failures. *Journal of Structural Engineering*, ASCE, Vol. 111, No. 7, July 1985, pp. 1468–1481.
3. F. Huber. Update: Bridge Scour. *Civil Engineering*, ASCE, New York, N.Y., Sept. 1991.
4. Loma Prieta Earthquake Reconnaissance Report. In *Earthquake Spectra*, Supplement to Vol. 6, Earthquake Engineering Research Institute, May 1990.
5. E. G. Burdette and D. W. Goodpasture. *NCHRP Report 306: Correlation of Bridge Load Capacity Estimates With Test Data*. TRB, National Research Council, Washington, D.C., 1988.
6. B. Bakht and L. G. Jaeger. Bridge Testing—A Surprise Every Time. *Journal of Structural Engineering*, ASCE, Vol. 116, No. 5, pp. 1370–1383.
7. A. E. Aktan and M. Raghavendrachar. *Nondestructive Testing and Identification For Bridge Rating: Pilot Project*. Report FHWA/ODOT-90/005, May 1990.
8. J. G. M. Van Mier. Examples of Non-Linear Analysis of Reinforced Concrete Structures with DIANA. *HERON*, Vol. 32, No. 3, 1987.
9. *Manual of Maintenance Inspection*. AASHTO, Washington, D.C., 1983.
10. *Manual of Maintenance Inspection*. AASHTO, Washington, D.C., 1989.

The conclusions presented are the opinions of the authors only.

Publication of this paper sponsored by Committee on Dynamics and Field Testing of Bridges.

Feasibility of Applying Cathodic Protection to Underground Corrugated Steel Pipe

J. D. GARBER, J. H. LIN, AND LARRY G. SMITH

The Louisiana Department of Transportation and Development uses corrugated steel pipes in various parts of the state. A study was undertaken to assess the feasibility of applying cathodic protection both externally and internally to corrugated steel pipes to prevent corrosion. The methodology employed ranged from a laboratory test to an actual field study. The laboratory test was conducted to prove that internal cathodic protection would work inside 24-in. corrugated steel pipes using zinc anodes. The field work consisted of installing 10-ft sections of eight different types of corrugated steel pipes with and without cathodic protection. Current and potential measurements have been made during the 2 years of field exposure. The results of the field study have proved that corrugated steel pipes can be protected from corrosion economically using cathodic protection. The outside of the corrugated steel pipe has been found to require significantly more current for protection than does the inside. The corrugated steel pipe requiring the least amount of current is the polymer precoated galvanized steel. All of the unprotected corrugated steel pipes are experiencing corrosion. The polymer coatings used are a film ethylene acrylic acid type.

Field studies conducted previously by the Louisiana Department of Transportation verified that most corrugated steel pipes installed underground experience severe attack in low-resistivity soils after exposure times of 10 years or less (*1*). The nature of the corrosion attack is caused primarily by oxygen in the soil and water. At the same time, the highway department is being asked to install corrugated steel pipes that can provide a life expectancy of 50 to 70 years. From the previously referenced study, it is obvious that coatings alone will never provide the required life expectancy, and, therefore, an alternative system must be considered. Using coated corrugated steel pipes in conjunction with cathodic protection appears to be a viable alternative.

The application of cathodic protection to the outside of pipes has been extensively studied and standards have been established (*2*). One company in California, Farwest Corrosion Control Co., actually presents the design by which one can apply external cathodic protection to corrugated steel pipes. However, to protect the buried pipe completely from corrosion, cathodic protection must be installed internally as well as externally. The primary interest in this study is to determine the current required to completely cathodically protect corrugated steel pipes having various types of coatings. Another consideration is the practical aspect of providing internal cathodic protection to corrugated steel pipes with 24-in. or larger diameters.

A careful study of the available literature on the application of cathodic protection to corrugated steel pipes has revealed that only external anodes have been applied. There has not been any previous work reported that determined the effectiveness of various coatings on corrugated steel pipes when internal cathodic protection is being used. Researchers at Mobil have applied internal cathodic protection in cement-lined piping and have found that the larger-diameter pipes gave the best current distribution (*3*). A zinc spool anode gave sufficient cathodic protection at a distance of more than 50 times the diameter of the pipe. Similar results were found by Groover and Peterson, (*4*) who showed that low-carbon steel pipes in stagnant sea water would be completely protected only when the diameters were larger than 2 in. (*4*). Cathodic protection was most effective in systems in which there was a slow flow rate of corrosive fluid.

MacKay and Grace designed a zinc anode assembly and tested it inside tanker pipelines containing stagnant sea water (*5*,p.345). The anode used inside a 14-in. steel pipe produced a current density of 14.5 mA/m^2 and provided cathodic protection over a length of 520 pipe diameters.

A study by Simpson and Robinson examined which coatings on steel pipes work best in conjunction with cathodic protection (*6*). The worst blistering was found to occur at the highest protective potentials. The best coatings proved to be epoxy and coal tar epoxy systems. These coating systems showed no deterioration after 4 years of exposure.

These studies represent the limited amount of literature that is available on the application of internal anodes to corroding systems. It is clear that this project can provide information that is very important to a better understanding of applying cathodic protection to corrugated steel pipe systems that have various types of coatings.

METHODOLOGY

This project was divided into two areas: (a) proving in the laboratory that it is possible to apply anodes inside of corrugated metal pipes and (b) installing cathodically protected and unprotected corrugated metal pipes in the field. Methods have been developed by which each of these areas could be studied.

J. D. Garber and J. H. Lin, University of Southwestern Louisiana, P.O. Box 44130, Lafayette, La. 70504. L. G. Smith, Corrosion Control, Inc., 197 Pat Street, Lafayette, La. 70506.

Laboratory Study Using Internal Anodes

Some experimental data in the literature have suggested that internal cathodic protection on pipes is achievable. The literature suggests that the current distribution improves with increasing pipe diameter. To determine whether anodes would work inside corrugated steel pipes, a test tank was constructed with dimensions of 2.5 × 24 × 12 ft. The tank was capable of holding five corrugated steel pipes that were 10 ft in length. A circulation system was designed to pump water through each pipe on a continuous basis. The flow rate through each pipe was set at 7 gal/min, which corresponds to a residence time of 35 min. The water contained 0.75 percent sea salt, which maintained the resistivity at 90 ohm-cm. The corrugated steel pipes used in this study were 2 ft in diameter and were completely filled with water. Figure 1 shows the tank and the water circulation system used to test the corrugated steel pipes. A 2-in. × 2-in. × 5-ft zinc anode was placed in the center of the pipe on a rubber mat to prevent electrical contact. The electrical connections were made on each of the 5-ft sections and the connecting metal band. The leads from the anode and pipes were connected across a 0.01-ohm shunt so that current flow versus time could be determined. Potential measurements were made using a copper-copper sulfate reference electrode. The current was measured each day, and the potential was measured at the mouth of each pipe at four positions: 12:00, 3:00, 6:00, and 9:00 with the anode connected. At the same time each day, the anode was disconnected, and, after approximately 2 hr, the potentials were measured again. The open-circuit potential of the zinc anode could be determined at that time.

After 30 days of this type of measurement, the tank was drained and the corrugated steel pipes were removed for examination. After this, the tank was reloaded with water and a new set of corrugated steel pipes were tested. The final test was on the polymer precoated black steel pipe, which was tested alone.

The test was designed to determine whether the corrugated steel pipes could be internally cathodically protected. The potential measurements verified that fact. Also, the current measurements through the 30-day period showed which corrugated steel pipe system required the minimum amount of current from the anode. The coatings that are less incompatible with cathodic protection show increased current output from the anode with time.

Field Installation of Corrugated Steel Pipes

On June 13 and 14, 1989, eight sets of corrugated steel pipes were installed at Pecan Island, La. (near the Fresh Water Bayou pontoon bridge). The Louisiana Department of Transportation installed eight 10-ft sections of corrugated steel pipes parallel to Highway 3147 at two different sites. Site 1, closest to the pontoon bridge, is where eight 10-ft sections of corrugated steel pipes were installed with zinc anodes on the inside and outside of each one. Site 2 is where eight 10-ft sections of the same corrugated steel pipes were installed without anodes. At each site there was a drainage ditch and the eight pipes were placed on the north side of the drainage ditch. The pipes are listed as follows with No. 1 being closest to the ditch at each site.

Pipe	*Pipe Type*
1	Polymer precoated black steel
2	Polymer precoated aluminized Type 2 steel
3	Polymer precoated aluminized Type 1 steel
4	Polymer precoated galvanized steel (Supplier 2)
5	Polymer precoated galvanized steel (Supplier 1)
6	Bituminous coated galvanized steel
7	Galvanized steel
8	Fiber-bonded bituminous coated galvanized steel

The intention of this experiment was to check the potential of the protected and unprotected section of pipe and to measure the current output of the zinc anodes.

The actual corrugated steel pipe installation took 2 days and used equipment and a crew of five men from the Louisiana Department of Transportation. Both of the 5-ft sections and the metal band were electrically connected. As in the laboratory test, the 2-in. × 2-in. × 5-ft anodes were placed on a rubber mat and then placed in the center of the pipe. The pipe was then lowered into the ditch and covered (see Figure 2). The external zinc anodes were pushed into the ground using a Gradall shovel (Figure 3).

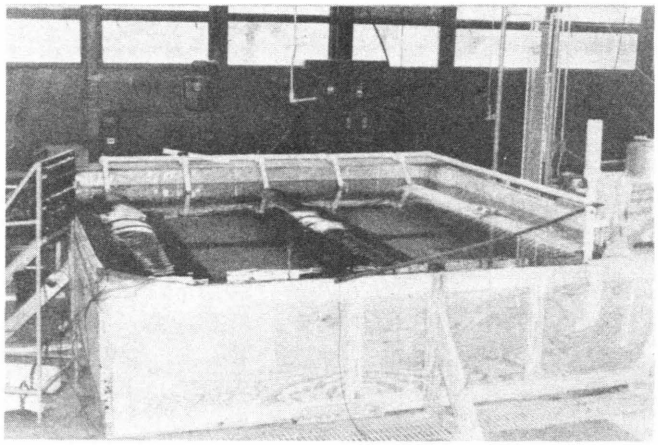

FIGURE 1 Large water tank with circulating water.

FIGURE 2 One of corrugated steel pipes is lowered into ditch.

FIGURE 3 External anodes are pushed into ground using Gradall shovel.

FIGURE 4 Unprotected steel pipe is lowered into ditch.

At Site 2, the process of installation was much simpler. It was necessary to run only one wire from the pipe so that potential readings could be made. Since anodes were not involved at this site, it was easier to install the pipes (see Figure 4).

DISCUSSION OF RESULTS

The two tests that were described previously have been performed on several different types of corrugated steel pipes to establish which type might be best to use in conjunction with cathodic protection.

Results of Laboratory Study

The large water tank test was very important for proving that zinc anodes would provide cathodic protection inside a 2-ft-diameter pipe. The circulation system pumped water through each filled pipe so that its volume was displaced every 35 min.

Eight pipes were tested in this manner. The following testing order was used in this part of the study:

Pipe	*Pipe Type*
1	Fiber-bonded bituminous coated galvanized steel
2	Bituminous coated galvanized steel
3	Polymer precoated galvanized steel (Supplier 1)
4	Polymer precoated galvanized steel (Supplier 2)
5	Galvanized steel
6	Polymer precoated aluminized Type 1 steel
7	Polymer precoated aluminized Type 2 steel
8	Polymer precoated black steel

Internal potential measurements were made on the pipes each 24-hr period. An example of the results of this 1-month test is presented in Figure 5. The potential of the fiber-bonded bituminous coated galvanized steel pipe was measured while

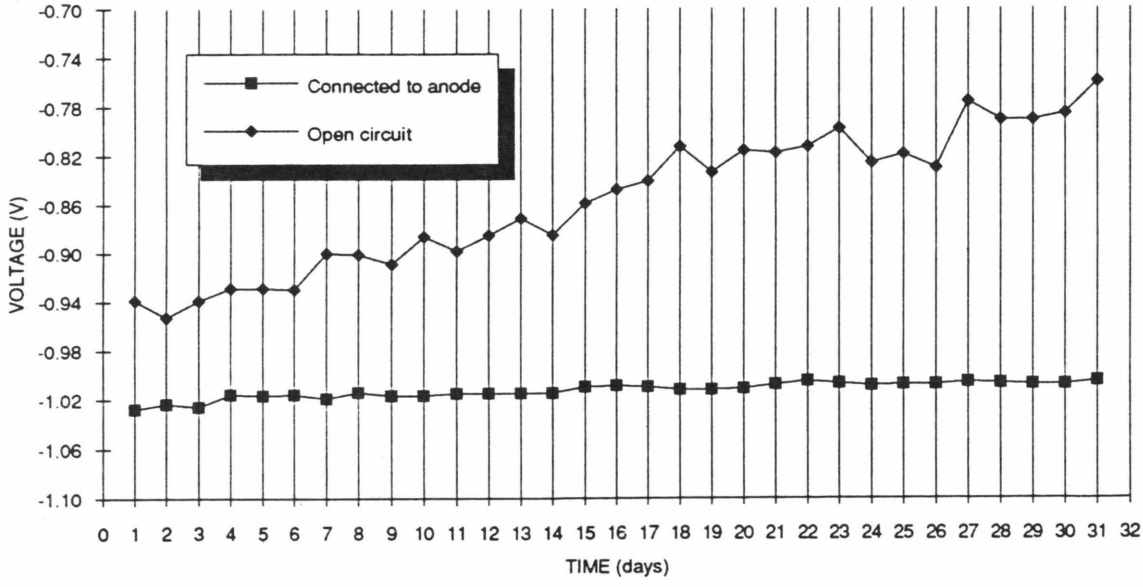

FIGURE 5 Connected and open-circuit potential of fiber-bonded bituminous coated galvanized steel in large water tank.

connected to the anode, as well as its potential 2 hours after being disconnected from the anode. The amount of current required to shift the potential of each pipe was measured each day. An example of these results is shown in Figure 6. Table 1 shows the ending voltage and current values of these corrugated steel pipes tested in the large tank. The fiber-bonded bituminous coated galvanized steel pipe showed the largest potential difference of 0.245 V while drawing 10 mA of current from the internal anode. The galvanized steel pipe shifted only 0.002 V and drew 1 mA of current. All of the polymer precoated pipes showed relatively low current draw—always 4 mA or less. The worst material appears to be the bituminous coated galvanized steel since it drew 44 mA and showed a potential difference of 0.152 V.

The potential difference between the closed-circuit value and the open-circuit value (after 2 hr) is very important since it shows which pipes depolarize the fastest. Rapid depolarization is generally an indication of a relatively poor coating. The results in Table 1 suggest that the two polymer precoated galvanized steel pipes should provide the best coating system to be used in conjunction with cathodic protection. In general, all of the closed-circuit potential values are well below the −0.85-V value required to protect the steel beneath the coating. The average open circuit potential of the zinc anodes used in this study was −1.093 V versus a copper-copper sulfate reference electrode.

Results of Field Study

Since installation on June 13 and 14, 1989, the test sites have been visited on 15 different occasions. Measurements of the resistivity of the water have been made on 10 of these occasions. The data suggest that the values are somewhat cyclic and range between 140 and 1,170 ohm-cm (Table 2). In general, the resistivities of the two sites tend to follow each other, and the average values are very close in magnitude. The soil resistivities were 428 ohm-cm for the protected site and 370 ohm-cm for the unprotected site. These soil values are not expected to change with time. During installation, samples of water were also tested for chloride and pH, yielding a pH of 7.7 and 0.22 percent Cl^- at the protected site, and a pH of 7.3 and 0.22 percent Cl^- at the unprotected site. The water level at the site also varies, and occasionally the pipes are not completely liquid filled.

Measurements of the potential of the protected and unprotected corrugated steel pipes have been made on both the inside and outside of the pipe during each visit. Figure 7 shows typical results obtained on the fiber-bonded bituminous coated galvanized steel pipe. Table 3 shows the internal potential values of the protected and unprotected pipes and the voltage difference that existed between these two numbers on June 13, 1991. The larger this potential difference, the more the structure is protected. This information suggests that the polymer precoated galvanized steel appears to have experienced the greatest potential shift. In fact, all of the polymer precoated pipes appear to be very well protected. The fiber-bonded bituminous coated galvanized steel and bituminous coated galvanized steel pipes show much less shift. This suggests that these pipes have few holidays (holes in the coating), and they are primarily being attacked on the ends where galvanizing is present.

It takes current from the internal and external anodes to maintain the potential differences shown. Figure 8 shows a typical graph of the internal and external current measurements that were made during the 15 visits since the installation. Table 4 shows recently obtained current values for the eight pipes in the field. The two polymer precoated galvanized steel pipes require the least amount of current and appear to be performing the best. The galvanized pipe requires substantially more current to be protected than any of the other pipes because it has no coating to help provide protection.

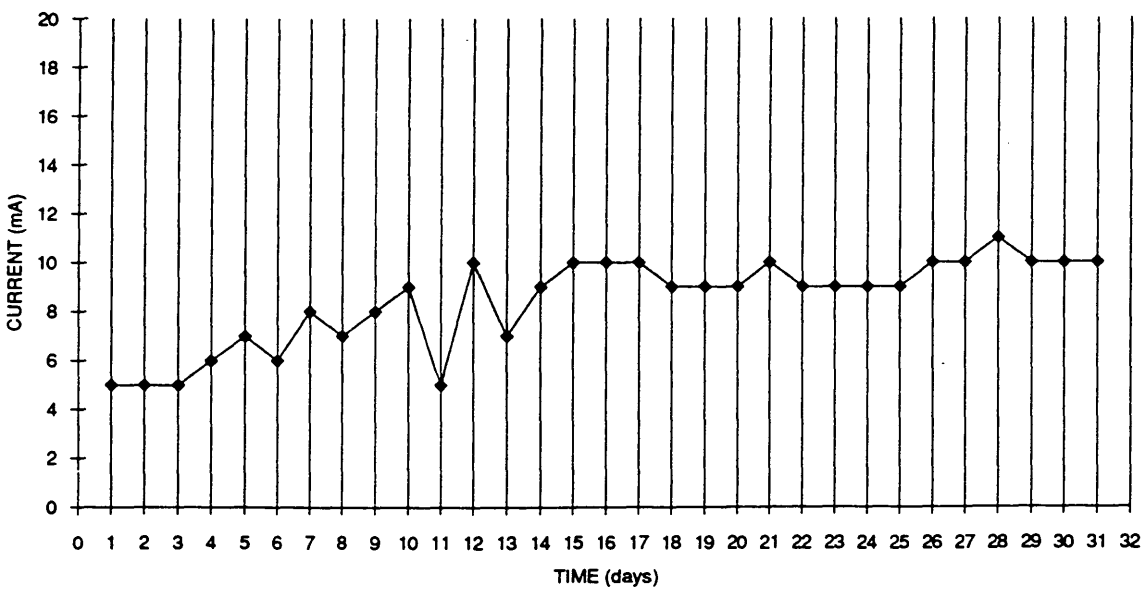

FIGURE 6 Current required to shift potential of fiber-bonded bituminous coated galvanized pipe in large water tank.

TABLE 1 Ending Potential and Current Values for Corrugated Steel Pipes in Large Water Tank Test

Pipe	Open Circuit Potential, V	Closed Circuit Potential, V	Potential Difference, V	Current ma
Fiber-Bonded Bituminous	-0.760	-1.005	0.245	10
Bituminous Galvanized	-0.808	-0.960	0.152	44
Polymer Precoated Galvanized (Supplier 1)	-1.008	-1.055	0.047	4
Polymer Precoated Galvanized (Supplier 2)	-0.962	-1.032	0.070	4
Galvanized	-1.064	-1.066	0.002	1
Polymer Precoated Aluminized Type 1	-0.885	-1.060	0.175	3
Polymer Precoated Aluminized Type 2	-0.900	-1.063	0.163	3
Polymer Precoated Black Steel	-0.913	-1.034	0.121	4

Open circuit potential values were measured two hours after being disconnected from the zinc anode using a copper-copper sulfate reference electrode.

TABLE 2 Resistance Readings at Field Test Sites

		Site 1 (Protected)		Site 2 (Unprotected)	
Date	Day	Soil	Water	Soil	Water
June 13, 1989	0		140		160
June 30, 1989	17		220		190
September 30, 1989	109	428	432	370	585
November 30, 1989	170		655		945
March 30, 1990	290		825		790
May 30, 1990	351		488		475
August 31, 1990	444		280		310
November 30, 1990	535		140		180
February 28, 1991	625		613		1170
June 13, 1991	730		815		712
Average Resistivity		428	460	370	552

Note: Values are in ohm-cm.

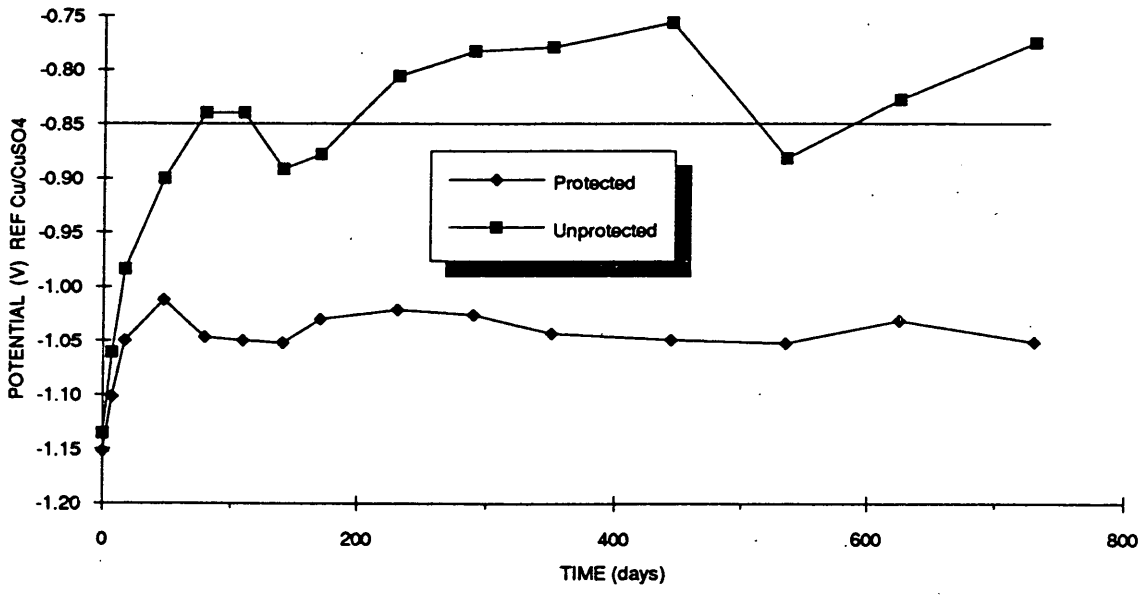

FIGURE 7 Internal potential readings of protected and unprotected fiber-bonded bituminous coated galvanized pipe.

The internal current requirements of all the pipes are fairly close in magnitude: they range from 8.5 to 28 mA. The outside current requirements are much larger values, and they range from 20 to 100 mA. These high external corrosion currents are somewhat of a surprise because at the start of the project it was unclear where the major corrosion action on a corrugated steel pipe was occurring.

These preliminary results show that, in general, the current requirement to protect any of the pipes is reasonable. To prove this point, the following calculation has been performed.

Calculate the pounds of zinc required to protect a 24-in., 10-ft polymer precoated aluminized Type 1 steel pipe, inside and outside, for 25 years. [The current requirement for this

TABLE 3 Internal Potential Readings Made June 13, 1991

Pipe	Protected Potential, Volts	Unprotected Potential, Volts	Difference Volts
Polymer Precoated Black Steel	-1.052	-0.651	0.401
Polymer Precoated Aluminized Type 2 Steel	-1.057	-0.662	0.395
Polymer Precoated Aluminized Type 1 Steel	-1.067	-0.690	0.377
Polymer Precoated Galvanized Steel (Supplier 2)	-1.077	-0.661	0.416
Polymeric Precoated Galvanized Steel (Supplier 1)	-1.069	-0.731	0.338
Bituminous Galvanized Steel	-1.063	-0.965	0.098
Galvanized Steel	-1.027	-0.931	0.096
Fiber-Bonded Bituminous Galvanized Steel	-1.052	-0.775	0.276

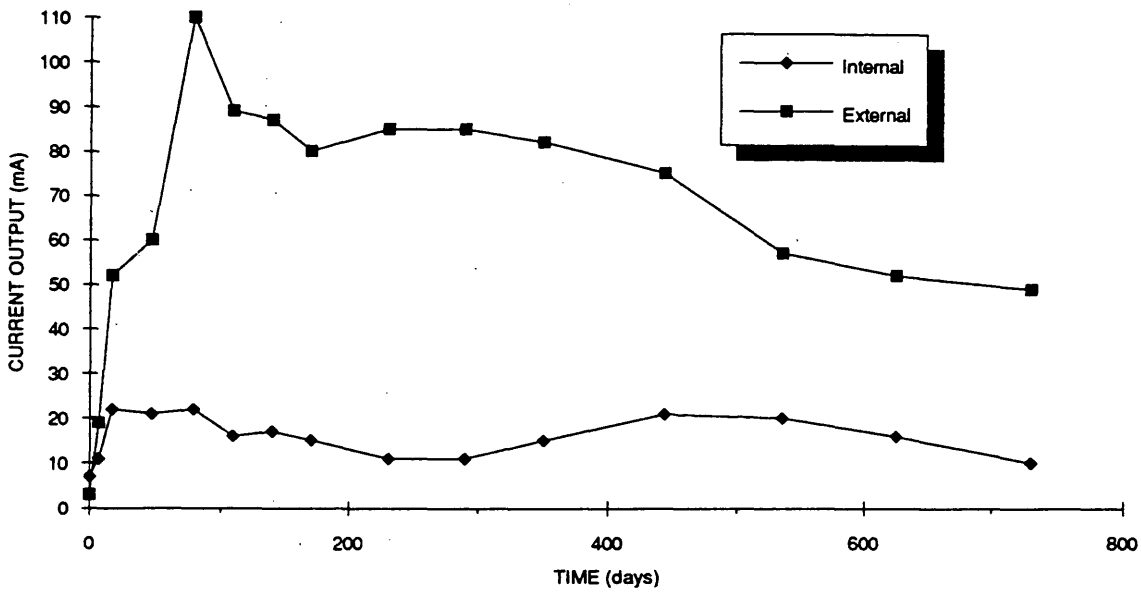

FIGURE 8 Internal and external current readings for fiber-bonded bituminous coated galvanized pipe.

pipe is 50 mA (Table 4).] Therefore, the pounds of zinc required for protection are

zinc = (0.050 amps) (25 years) (25 lb zinc/amp year)

= 31 lb.

A 30-ft pipe would require three times this amount, or 93 lb, of zinc; to protect this 30-ft pipe for 50 years instead of 25 years, it would require twice as much zinc, or 186 lb. If a polymer precoated galvanized steel pipe were used, this requirement would be reduced by about one-third because of the lower current requirement.

One estimate of the materials cost of installing a corrugated steel pipe in the Pecan Island, La., area is $85/ft; the pipes in that region historically have lasted for 25 years. Installation of the anodes required to protect these pipes for 50 years would cost approximately $1,000 and the pipes would be in like-new condition. This figure compares with that of two replacements of the pipes by the Louisiana Department of Transportation at an estimated present value cost of $2,600.

TABLE 4 Current Measurements Made June 13, 1991

Pipe	External Current ma	Internal Current ma	Total Current ma
Polymer Precoated Black Steel	60	11	72
Polymer Precoated Aluminized Type 2 Steel	48	15	63
Polymer Precoated Aluminized Type 1 Steel	38	12	50
Polymer Precoated Galvanized Steel (Supplier 2)	20	8.5	29
Polymer Precoated Galvanized Steel (Supplier 1)	30	16	46
Bituminous Galvanized Steel	41	17	58
Galvanized Steel	100	28	128
Fiber-Bonded Bituminous Galvanized Steel	49	10	59

This calculation assumes a 6 percent inflation rate and an 8 percent interest rate over that period and illustrates that cathodic protection on pipes is economically feasible.

CONCLUSIONS

1. All corrugated steel pipes in the field have successfully responded to both internal and external cathodic protection.
2. All coated corrugated steel pipes can be economically protected by cathodic protection. A calculation made on a polymer precoated aluminized Type 1 steel pipe shows that it would require 186 lb of zinc to completely protect a pipe 24 in. in diameter and 30 ft long for 50 years. This can be done at an estimated installed cost of $1,000. After the project is completed, more-conclusive economics can be obtained.
3. On the basis of measurements made after 2 years of exposure, it can be said that the polymer precoated galvanized steel pipe is requiring the least amount of current for protection. The bituminous coated galvanized steel pipe requires more current than the polymer precoated galvanized steel pipe, but only about half as much as the bare galvanized pipe.
4. The unprotected corrugated steel pipes in the field are losing whatever protection they may have had from their galvanized or aluminized coatings, and they are experiencing corrosion. This is known to be true because the potentials of the pipes are more positive than the −0.85-V potential value required for protection of steel.
5. Internal current requirements are lower than external values because there was less coating damage to the inside during installation and the natural soil stresses are causing coating damage on the outside of the pipes.
6. Even though the resistivity of the water at the protected culvert site varied from 140 to 825 ohm-cm, it was still easy for the zinc anodes to protect the pipes.
7. The field study has proven that a corrugated steel pipe disconnected from the anode can be readily identified. After reconnection to the anode, the potential and current values return to normal almost immediately.
8. The 30-day water tank test demonstrated that the corrugated steel pipes could be cathodically protected in the laboratory. All of the closed-circuit potentials were much more negative than the −0.85-V potential required for protection.
9. The large water tank proved that the polymer precoated galvanized steel pipes would not very readily depolarize and would have a low current requirement.

ACKNOWLEDGMENTS

The authors sincerely appreciate the contribution of the following people at Louisiana Transportation Research Center who have made helpful suggestions during the project: Steve Cumbaa, William Temple, and Kirk Clement. Also, a special thanks to Eugene Waguespack of the U.S. Department of Transportation (DOT) for providing the staff needed to bury the test pipes at the Pecan Island site.

Without the financial support of a grant from the Louisiana Department of Transportation and Development Research Center in cooperation with DOT, FHWA, this work could not have been performed.

REFERENCES

1. W. H. Temple, S. L. Cumbaa, and B. J. Gueho. *Evaluation of Drainage Pipe by Field Experimentation and Supplemental Laboratory Experimentation*. Report FHWA/LA-85/174. Louisiana Transportation Research Center, Baton Rouge, March 1985.
2. *Control of External Corrosion on Underground or Submerged Metallic Piping Systems*. Standard RP-01-69. National Association of Corrosion Engineers, Houston, Tex.
3. F. Q. Jensen and R. D. Tems. *Internal Cathodic Protection of Cement-Lined Steel Pipes*. National Association of Corrosion Engineers 88, Paper 25, St. Louis, Mo., 1988.
4. R. E. Groover and M. H. Peterson. *Cathodic Protection of Internal Surfaces of Pipes Containing Sea Water. Materials Performance*, Nov. 1984, pp. 24–29.
5. W. B. MacKay and L. R. Grace. Cathodic Protection of Pipeline Internals. *Proc., 4th International Congress on Marine Corrosion and Fouling*, Antibes, France, 1976.
6. V. P. Simpson and R. C. Robinson. Experimental Studies Relate Effect of Cathodic Protection with Certain Generic Coating Systems. Presented at Offshore Technology Conference, 1980.

Publication of this paper sponsored by Committee on Culverts and Hydraulic Structures.

Structural Performance of Perforated PVC Pipe

SHAD M. SARGAND, GAYLE F. MITCHELL, ROBERT KASTNER, AND JULIAN RUEDA

Plastic pipes are being used increasingly in transportation facilities and for other infrastructural applications. However, limited information is available on the performance of these pipes under live load. Furthermore, little is known about total deflections and their relationship to corresponding strains induced on the outside and inside surface of the pipe. Since laboratory tests cannot effectively model these variables, a field facility must be used to study these pipes. This paper presents information on the response and performance of a small-diameter pipe under field conditions. Unique instrumentation, developed for small-diameter pipes by the lead author, provided a means for installing strain gauges on the interior surface of the pipe. Analysis of the strains and deflections for 10 incremental loads up to a total load of 187 tons showed that the strains caused by the backfill and live load were not very large. However, at a total load exceeding about 80 tons, large changes occurred in the strain, particularly the transverse strain. Deflections during the application of the live load were small. However, deflections caused by the backfill alone were large, and the backfill process had an influence on the subsequent performance under application of load.

Plastic pipes, such as high-density polyethylene (HDPE) and polyvinylchloride (PVC), have become widely employed for infrastructure applications, for example, highway drainage, municipal sewers, water supply systems, and underground telephone conduit. They offer advantages in durability, application under various aggressive environments, ease of handling, and economics.

In design of these plastic pipes, the following factors are considered: deflection, ring bending moment, ring compression force, and buckling. None of the present procedures used for design considers the long-term performance of the plastic pipe. Generally, the strength of these pipes is determined by short-term tests, such as the parallel plate test. Janson suggests that long-term response be determined by deflecting pipes to strain values from 0.8 to 3.7 percent for 10,000 hr (*1*). As a short-term test he recommends testing to 5 percent strain in 3 min. In addition, when these pipes are employed in an undrained system they generally would have circular or slotted holes. It is obvious that this modification of the pipe wall will result in a severe stress concentration around the perforations. Also, most information about the performance of these pipes has been provided by the manufacturers, and not all manufacturers are familiar with loading conditions that occur in the field.

S. M. Sargand, G. F. Mitchell, R. Kastner, Department of Civil Engineering, Stocker Center, Ohio University, Athens, Ohio 45701. J. Rueda, Waste Management of North America, Inc., 303 Butterfield Road, Oak Brook, Ill. 60521.

PIPE PERFORMANCE

The current equations that are used in design of plastic pipe are summarized by Chambers et al. (*2*). Standard procedures that are currently in use do not incorporate the true properties of plastic pipe, such as viscoelasticity. No data are available as to whether small- and large-diameter pipe respond the same and so can be designed by identical procedures. Design procedures are not verified with sufficient field data. Also, investigators have suggested that design parameters, such as modulus of elasticity of the pipe material (E) in the Iowa culvert design formula, may be too conservative. The following discussion summarizes the major literature on the subject.

Adams et al. fully instrumented a 24-in.-diameter corrugated polyethylene (PE) pipe and buried it under a 100-ft-high embankment (*3*). They did not see any distress under 95 ft of embankment, noting that change in the horizontal diameter was less than 0.5 percent and the vertical diameter was reduced 3 to 5 percent. Gabriel investigated the performance of 4-, 6-, 8-, and 12-in.-diameter perforated HDPE pipe under simulated backfill 42 ft high (*4*). He predicted that pipe placed under poorly compacted fill would sustain an embankment exceeding 42 ft.

Horn reported on one study of three types of plastic pipe (PVC, PE, ABS) with diameters of 10, 12, and 15 in. and another dynamic test of slotted 4- and 6-in.-diameter PVC and PE pipe (*5*). The pipes were buried under shallow cover and tested under static and dynamic wheel loads. The loads were to simulate the type of conditions that would exist on runways at airports. The 10- and 12-in. PVC pipes performed well for all depths of cover tested in both pea gravel and lean clay. Two 6-in.-diameter PVC pipes installed 6 in. deep had permanent deflections greater than 5 percent but less than 8 percent. Under 12 and 18 in. of cover, 6-in. PVC had permanent deflections less than 3 percent; a 4-in. PVC pipe installed at 12 in. of cover depicted about 2.5 percent permanent deflection.

Watkins and Reeve investigated four specimens of 6-in.-diameter HDPE pipe in the Utah State University small soil cell to determine the performance under deep cover; this study was conducted for King County Solid Waste (*6*). One of these pipes was unperforated, one was perforated, and two were slotted. Under the load condition for this experiment, they reported that when the 6-in. pipe was buried in washed gravel it performed satisfactorily under 200 ft of fill simulated at 50 lb/ft^3. Deflection was less than 3.3 percent. They reported that there was no cracking or tearing close to the perforations, concluding that stress concentration in the per-

foration region is not very serious. The instrumentation employed in this study was very crude, particularly in determining the stress concentration and bending moment. Also, the loading condition was very close to a hydrostatic situation. In addition, Watkins et al. tested 24-in. corrugated PE pipes under compacted granular backfill and live load (*7*). On the basis of this study, he concluded that the ring compression should be the primary design parameter, and the effect of the ring deflection should also be included.

Since these pipes are generally very flexible, special attention should be given to their installation procedure. Field observations reported by Hurd indicated that there are several installations in Ohio in which flattening (15 percent deflection) and buckling (25 percent deflection) have occurred (*8*). He suggests installation procedures as the cause and recommends higher pipe stiffness as the remedy to this problem. Prevost and Kienow discussed buckling of six pipes—two thermoplastic, three thermoset, and one metal (*9*). They said that the principal buckling factor for low-stiffness pipe may be the result of the change of shape that occurs during the installation procedure. They recommended that to minimize changing the shape of the pipe, great care should be taken during installation.

Because various types of materials and wall profiles of plastic pipe are available, knowledge of strain and stress fields is necessary for proper application and analysis of these pipes. Strain is an essential part of design of plastic pipes, because stress is difficult to determine. Furthermore, little is known about total deflections and their relationship to corresponding strains induced on the outside and inside surface of the pipe. A limited number of studies have been conducted to compute the strain in small-diameter plastic pipe. Moore and Donaldson developed a profile meter to monitor the deflection of pipe having a diameter range of 0.6 to 1.5 m (*10*). The results recorded by this device were used to compute the strain. Some of the major concerns of this technique are that computed strains cannot indicate the local distress. In the profile of some of the plastic pipes there is discontinuity through the depth. Again, the predicted strains are not necessarily the actual interior strains. Furthermore, a profile meter will not operate properly when the deflection of the pipe exceeds 10 percent. Alternately, the procedure that is commonly used for computing the strain in small-diameter plastic pipe is an empirical technique such as the modified Iowa Formula.

This paper presents results from the performance of a small-diameter plastic pipe (PVC) installed in a field facility. Because a new technique was developed by Sargand et al. to install strain gauges inside of small-diameter pipe (*11*), performance is presented in terms of measured interior and exterior strains in conjunction with deflections.

PIPE DESCRIPTION, INSTRUMENTATION, AND INSTALLATION

Pipe Description

A 6-in.-diameter Schedule 80 PVC perforated pipe, 20 ft in length, was selected for the study. The perforations in the pipe are circular of diameter 0.5 in. spaced at intervals of 5 in., and the wall thickness is 0.436 in. Two lines of perforations are separated by an angle of 110 degrees. Laboratory testing of the pipe indicated that the average stiffness factor would be about 2,774 in.^{3}-lbf/in.-in. for 5 percent vertical deflection and 2,227 in.^{3}-lbf/in.-in. for 10 percent vertical deflection.

Instrumentation

A unique method of surface preparation and gauge installation, developed by Sargand et al. (*11*), was used to install eight biaxial strain gauges at the pipe interior midsection (10 ft from the pipe end). The interior of the pipe was cleaned, conditioned, and neutralized using an adapted method of surface preparation from Measurements Group, Inc. (*12*), for a PVC surface. A 10-ft-long piece of ⅜-in.-diameter steel tubing, fitted with a chuck on one end (so that an electric drill could be used to rotate the shaft) and a metal piece at the other end that secured an engine cylinder hone, was used to clean, hone, and prepare the inside of the pipe.

Eight biaxial strain gauges (KFG Series, KFG-5-120-D16-65 L3M 3S, 120 ± 0.8 ohms, Kyowa Electronic Instruments Co., Tokyo, Japan) were placed on the pipe interior surface using Type 10 curing agent mixed with Type AE adhesive resin. A 10-ft-long piece of copper tubing with a shutoff air valve on one end and a round disk with eight plungers on the other end was employed to install the strain gauges. The air hose was attached to the copper tubing applicator, and a pressure of 41 lb/in.^{2} was applied to provide a clamping pressure on the gauges while the adhesive was hardening. These gauges were located at the crown and invert, and at 45, 90, and 135-degree positions clockwise and counterclockwise on the crown gauge. Eight biaxial strain gauges (Micro Measurements, CEA-06-125WT-350, 350 ± 0.5% ohms, Raleigh, N.C.) were also adhered to the exterior of the pipe in the same locations as the interior gauges.

The deflection was monitored at the 20-ft pipe midsection with a profile meter that used a remotely triggered linear variable differential transducer (LVDT), secured to the end of an aluminum I-beam, which was held in position by a special holding stand. Voltage output from the counterclockwise rotating LVDT provided a determination of the angle of rotation, and a photoelectric eye, attached to the LVDT, detected each of eight tape marks on the inside circumference of the pipe during each sweep. Deflection, as well as the strain, were monitored concurrently using a portable data acquisition system.

Pipe Installation Procedure

At the field installation site, the pipe was installed in a rectangular trench that was excavated in the original soil, a lean clay. The trench dimensions were 26 in. wide × 240 in. long × 18 in. deep. A 20-ft-long geotextile (Trevira Spunbond nonwoven type 1125, Hoechst Celanese Corp., Spartanburg, S.C.) was placed on the bottom and sides of the pipe installation trench. Crushed limestone (AASHTO No. 3) was spread in the bottom of the trench for a 4-in.-thick bedding layer. The pipe was then positioned on this layer, and additional limestone material was placed on the sides and over the pipe to a depth of 18 in. A mound about 5 in. high at the top of

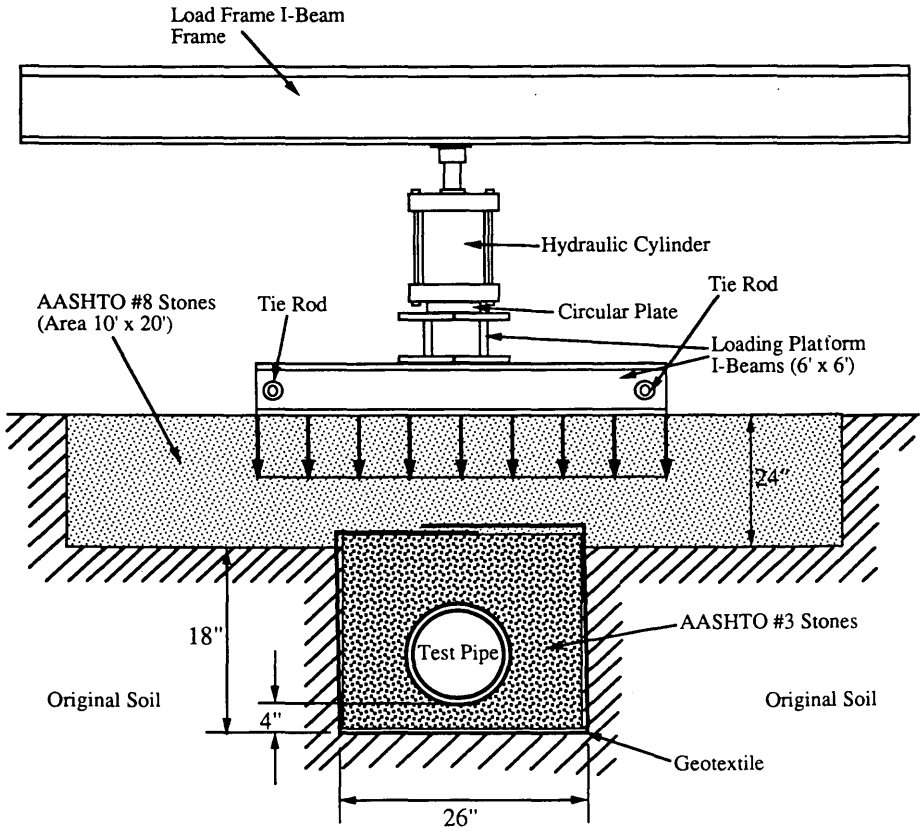

FIGURE 1 Schematic of test pipe setup.

the trench was made with river gravel (AASHTO No. 8 stones). Then, the geotextile was wrapped over this material with an overlap of 12 in. Finally, river gravel material was placed over the pipe in an area 10 by 20 ft to a depth of 24 in. The schematic of the profile is shown in Figure 1.

TEST FACILITY AND LOADING

The field facility used for testing the pipe is located on the Ohio University campus in Athens. This unique facility consists of four concrete columns, spaced approximately 25 ft from center to center, that serve as a support for a structural I-beam frame. The structural I-beam frame is tied to bedrock through a total of eight grouted tension rock anchors. Two 230-ton-capacity hydraulic cylinders, attached to the frame, apply the load. For this test a loading platform, covering an area 6 ft square, was assembled under the two hydraulic cylinders. The platform, weighing about 2.7 tons, applied an initial stress of 1.16 lb/in.^{2} over the backfill material. During the test, incremental hydraulic pressures of 200 lb/in.^{2} were used up to a maximum of 1,200 lb/in.^{2}. (The hydraulic power

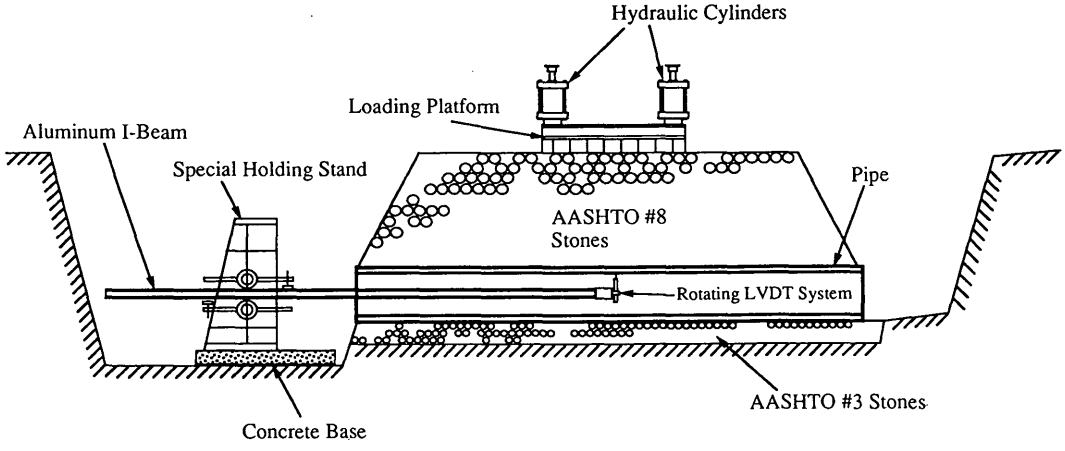

FIGURE 2 Schematic of loading profile with deflection measurement device.

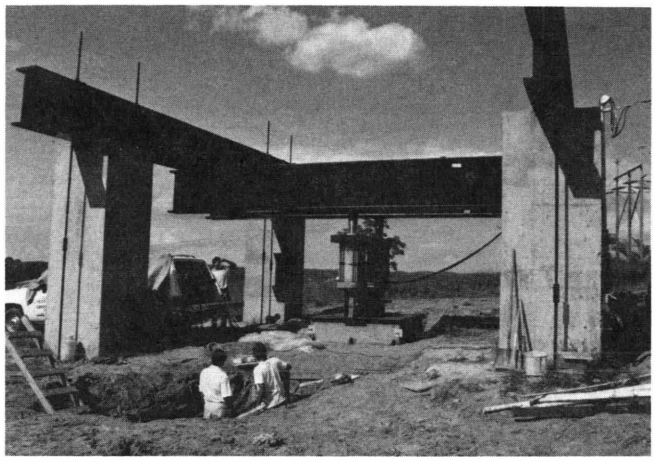

FIGURE 3 Load application to pipe system (hydraulic power system on right and loading platform at center).

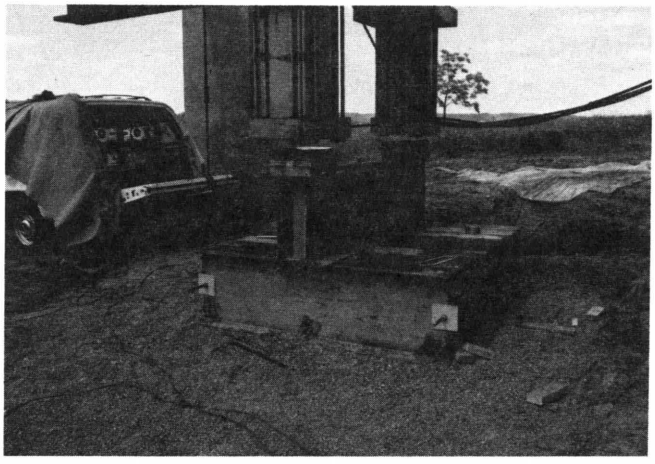

FIGURE 4 Hydraulic cylinders and loading platform with data acquisition system.

system can develop up to a 2,200-lb/in.^{2} pressure in each loading cyclinder.)

The schematic shown in Figure 2 illustrates the loading and deflection measurement device. The photographs in Figures 3 and 4 depict the loading of the pipe system during the test; the load was applied in an incremental process up to a total of 187 tons.

FIELD RESULTS

Deflection

At each load sequence, five sweeps or rotations of the LVDT system were performed. Results from the five sweeps were then averaged to arrive at the shape and dimensions of the pipe at each load condition. The data indicated antisymmetric behavior of the pipe, which was caused by the initial change in shape during the backfill process. This occurrence can be reduced by utilizing a pipe of higher stiffness or modifying the backfill process.

Figure 5 illustrates the change in diameter of the pipe from application of the backfill and the live load. The measured displacement is the vertical dimension and not necessarily the maximum value of the shortening of the diameter. Also, the change in shape was measured to an accuracy of 0.03 in. The diameter in the vertical direction decreased by 3.14 percent because of the backfill, whereas in the horizontal direction it increased by 1.57 percent. Moreover, due to the application of 157 tons loading the vertical and horizontal diameters changed 7.90 and 3.13 percent, respectively. This behavior indicates that a large amount of deformation can occur because of the construction sequence. When the load was removed at the end of the test, a permanent change in shape was noted.

Bending Moment and Thrust

The moment and the thrust were computed from the strains that were recorded in both the transverse and longitudinal directions during the application of live load. Table 1 presents the values obtained for the strains at the crown of the pipe at selected load increments. (The sign convention is positive for tension and negative for compression.) All the strains are calculated using as the initial conditions the completion of the backfill with the loading platform.

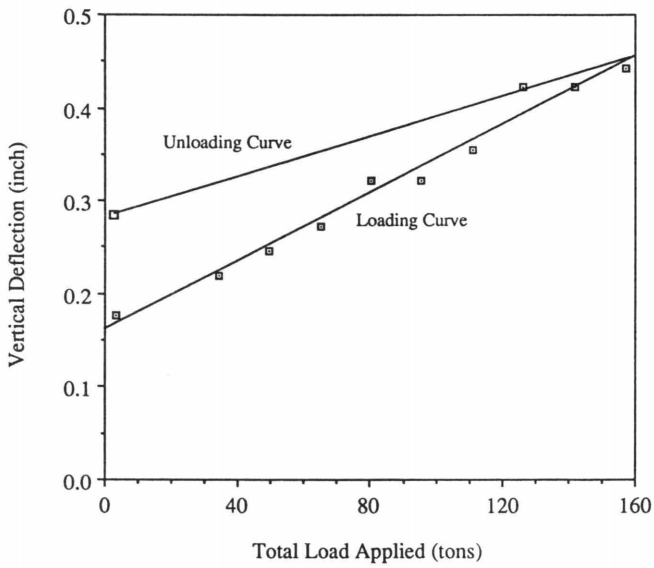

FIGURE 5 Vertical deflection versus total load curve.

TABLE 1 Strains at Crown of Pipe

Total Load (tons)	Transverse Strain (microstrain)		Longitudinal Strain (microstrain)	
	Outer	Inner	Outer	Inner
33.5	-1646.42	1454.48	8.47	137.73
48.9	-2098.36	1781.76	6.72	214.03
64.3	-2758.30	2225.89	8.36	332.08
79.7	-3369.85	2686.83	10.60	385.68
95.1	-4674.19	3988.36	25.37	442.89
110.5	-5947.56	4805.12	25.67	781.52

The strains in the transverse as well as the longitudinal directions generally were reasonable numbers. Most of the strains were very small compared with the limitations of the strain gauges. The strain values confirm the change in the shape of the pipe during the application of the load, as illustrated in Figure 6. The high values of transverse strain occur at the crown and invert of the pipe. The same antisymmetric trend noted in the deflection was observed also for the strain.

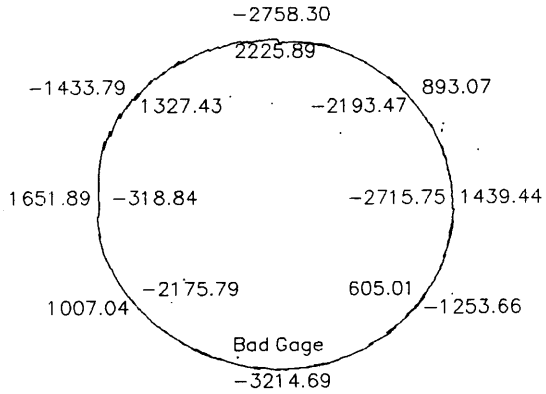

FIGURE 6 Deflection and transverse strain for 64.28-ton load.

Figure 7 presents the values for the moment calculated from field data using the value for modulus of elasticity of 400,000 lb/in.^{2} and Poisson's ratio of 0.38. A significant increase in the moment at the crown is noted for each incremental load increase. At the high level of loading, only two data points are shown for the moment, since the wires connected to some of the gauges were damaged by the backfill material before this loading sequence. Figure 8 presents the values of thrust for the upper half of the pipe. Surprisingly, the thrust was in tension on the left side of the spring. This thrust could be attributed to the initial distortion of the pipe caused by the installation process or local response to the backfill material, or both.

The pipe that was tested in this study typically will be used in a landfill. Since the material that will be used as backfill must have a high permeability value, the crushed limestone was applied around the pipe. With this type of backfill material it is difficult to obtain a uniform distribution of stress around the pipe. In addition, when the pipe was excavated, it was observed that the aggregate around the pipe was crushed by application of the heavy load. Also, numerous dents were made on the surface of the pipe, and, despite the fact that

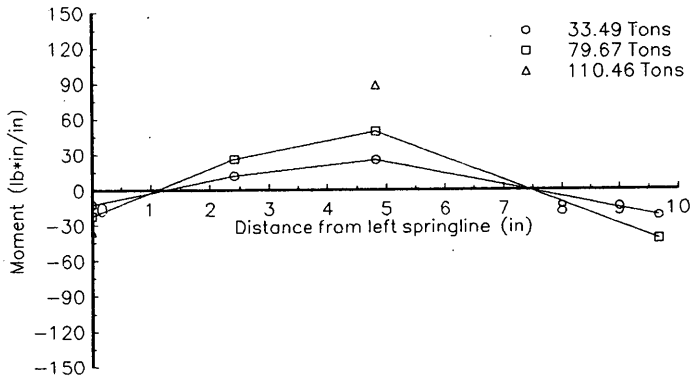

FIGURE 7 Bending moment in upper section of pipe.

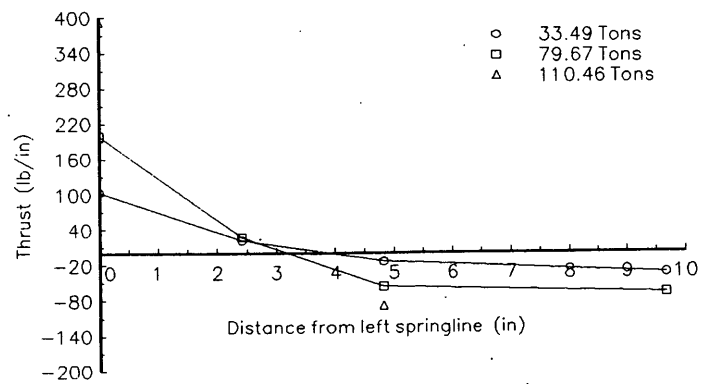

FIGURE 8 Thrust in upper section of pipe.

the gauges and wires were well protected, the wires connected to the gauges were damaged by the sharp edges of the stone.

SUMMARY AND CONCLUSIONS

On the basis of the performance of the pipe for this one test, the following statements can be made:

1. The strains caused by the backfill and live load were not very large.
2. Deflections caused by the backfill were large compared with the application of live load.
3. The change in shape of the pipe caused by the backfill process had an influence on the subsequent performance under the application of load.
4. The deformation of the pipe caused by the backfill process could be controlled by more careful installation procedures. Furthermore, deformation could be reduced by constraining the pipe segment(s) during installation of the backfill.
5. This pipe, overall, performed well during this test; however, it should be noted that this was the first time a study of this type has been conducted, and further verification is needed to extrapolate results to field application.

ACKNOWLEDGMENTS

This research was supported by Waste Management of North America, Inc., and the Ohio University Center for Geotechnical and Groundwater Research. The authors would also like to acknowledge the assistance provided by Robert C. Rogers and Teruhisa Masada, of the Ohio University.

REFERENCES

1. L. E. Janson. *Investigation of the Long-Term Creep Modulus for Buried Polyethylene Pipes Subjected to Constant Deflection*. VBB Consulting Group, Stockholm, Sweden, Aug. 1985, pp. 253–262.
2. R. E. Chambers, T. J. McGrath, and F. J. Hagar. *NCHRP Report 225: Plastic Pipe for Subsurface Drainage of Transportation Facilities*. TRB, National Research Council, Washington, D.C., Oct. 1980.
3. D. N. Adams, M. T. Muindi, and E. T. Selig. *Performance of High Density Polyethylene Pipe Under High Fill*. Geotechnical Report No. ADS88-351F. Department of Civil Engineering, University of Massachusetts, Amherst, April 1988.
4. L. H. Gabriel. *Deformation Response of ADS Perforated Pipes Under Embankment Fill*. California State University, Sacramento, March 1983.
5. W. J. Horn. *Field Tests of Plastic Pipe for Airport Drainage Systems*. Final Report. U.S. Army Corps of Engineers, Waterways Experiment Station, Vicksburg, Miss., Dec. 1979.
6. R. Watkins and R. C. Reeve. *Effect of Heavy Loads on Buried Corrugated Polyethylene Pipe*. Advanced Drainage Systems, Inc., Columbus, Ohio, March 1982.
7. R. K. Watkins, J. M. Dwiggins, and W. E. Alternatt. Structural Design of Buried Corrugated Polyethylene Pipes. In *Transportation Research Record 1129*, TRB, National Research Council, Washington, D.C., 1987, pp. 12–20.
8. J. O. Hurd. Field Performance of Corrugated Polyethylene Pipe Culvert in Ohio. In *Transportation Research Record 1087*, TRB, National Research Council, Washington, D.C., 1987.
9. C. R. Prevost and K. K. Kienow. Pipe/Soil Stiffness Ratio Effects on Flexible Pipe Buckling Thresholds. *Journal of Transportation Engineering*, Vol. 115, No. 2, March 1989.
10. C. A. Moore and C. F. Donaldson. Measuring Strains in Buried Flexible Pipes. *Geotechnical Testing Journal*, Vol. 13, No. 3, Sept. 1990, pp. 208–214.
11. S. M. Sargand, G. F. Mitchell, and R. C. Rogers. Monitoring of Strains in Small Diameter Pipe. *Experimental Techniques*, Jan.–Feb. 1992.
12. *Strain Gage Applications with M-Bond AE-10/15 and M-Bond GA-2 Adhesive Systems*. Instruction Bulletin B-137-13. Measurements Group, Inc., 1979.

Publication of this paper sponsored by Committee on Culverts and Hydraulic Structures.